The interaction of protein-based pharmaceuticals with interfaces under biopharmaceutical manufacturing

Ioanna Panagi

Submitted in accordance with the requirements for the degree of Doctor of Philosophy

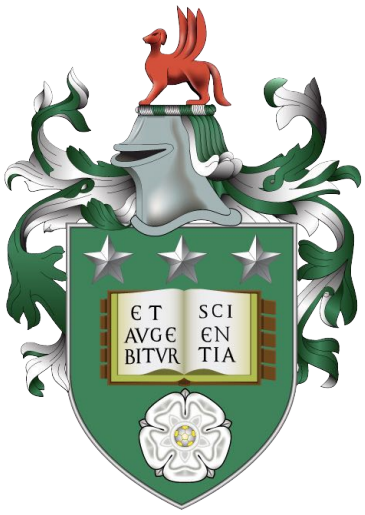

The University of Leeds

School of Mechanical Engineering

Astbury Centre for Structural Molecular Biology

February 2022

Declaration

The candidate confirms that the work submitted is her own and that appropriate credit has been given where reference has been made to the work of others.

This copy has been supplied on the understanding that it is copyright material and that no quotation from the thesis may be published without proper acknowledgement.

© 2022 The University of Leeds and Ioanna Panagi.

Acknowledgements

This journey would not be feasible without the help and support of people both professionally and personally throughout the years. Firstly, I would like to thank my main supervisor from the School of Mechanical Engineering, Prof. Nikil Kapur, for his amazing support and guidance throughout the project. I am really grateful to have worked with him, as he helped me to grow as a professional throughout his supervision. I want to acknowledge all the help and supervision from the team in the Astbury Centre from the School of Molecular and Cellular Biology, Profs. David Brockwell, Sheena Radford and Frank Sobott for giving me the opportunity to work in their group and collaborate with the rest of the team. It was great working with them and I thank them for all their support and supervision. My thanks also go to the Radford and Brockwell lab manager, Mr Nasir Khan for his kindness and endless help when I needed and of course for his delicious curry. Also, my thanks go to the lead technician Mr Tony Wiese and the mechanical service manager Mr Graham Brown, from the school of Mechanical Engineering, for their help whenever I needed.

Secondly, I wish to thank BBSRC for funding the project. I would also like to thank AstraZeneca for industrially sponsoring the project, and give my thanks to our industrial AstraZeneca partners: Drs Nicholas Darton, Paul Devine, Janet Saunders, Nick Bond and Richard Turner for their support and all the helpful discussions over the meetings. My thanks also go to Dr Katie Day, Dr Peng Ke and Ms Maria Bruque for supervising me over running experiments and using the laboratory equipments.

Thirdly, I gratefully thank all the current members of the "Squishers" team, Dr Leon Willis, Ms Samantha Lawrence and Mr Alex Page for being friends and colleagues, for all their help, the collaboration over the project and of course all the fan we had in the lab. I also want to thank the past "Squishers" members, Drs Amit Kumar and Lorna Kelly. It was a pleasure working with the team over this journey.

Finally, I would like to thank my parents Alexia, Panicos, my sister Martha, and my grandparents Andreas and Ioanna. This thesis is dedicated to them and to the memory of my grandparents Christophoros and Martha. Last but not least, many thanks to Rafael for his endless support throughout the years.

Abstract

The interaction of proteins with surfaces is fundamentally important to their function. Within the biopharmaceutical industry, the interfacial interaction during the manufacture and delivery can influence the stability of the protein, causing the proteins to unfold and aggregate. The removal or suppression of protein aggregation from biopharmaceuticals is desired as it has been linked with immunogenic reactions within the human body of the patient. Building on previous studies [1–3], using an extensional flow device mimicking the hydrodynamic forces that the biopharmaceuticals are encountered throughout their production, the current work simultaneously investigates the effects of surface wettability/protein formulation, and hydrodynamic flow on the aggregation of several biopharmaceutical molecules. The aim of the project is to understand how protein stability can be enhanced under the exposure of biopharmaceuticals to flow. The work, therefore, addresses the investigation of the extensional flow on the aggregation of antibodies by considering its application combined with other biophysical methods to study aggregation. Surprisingly, protein aggregation was found to show a complex dependence on surface wettability: surfaces with contact angles of 58° and 80° were able to suppress protein aggregation under flow while more hydrophobic surfaces (94°) yielded aggregation similar to borosilicate glass (47°). The protective effect of intermediate contact angle is compared to the use of formulation excipients, including surfactants, which appear to minimise aggregation via distinct surface and protein-mediated effects, respectively. The outcome of this work can shed light into understanding the science of biopharmaceutical aggregation, as well as the application of flow-based tools that can used during the development of protein-based medicines. The aim of the final form of these developed medicine molecules is to exhibit formulation properties which can withstand the fluid forces encountered during manufacture. Together, the data collected in the current work, could lead to the design of bioprocessing equipment and formulations which minimise flow induced aggregation of pharmaceutical proteins and further underlines the importance of both flow and surfaces in protein aggregation during manufacture.

Contents

List of Tables

List of Figures

Abbreviations

AFM Atomic Force Microscopy. iv, vi, xxi, 35, 36, 37, 38, 85, 90, 148

ANS 8-Anilinonaphthalene-1-sulfonic acid. xxvii, 18, 96, 107, 206, 207, 208

APTES Aminopropyltrimethoxysilane. xv, xviii, xx, xxi, 81, 82, 83, 85, 86, 123, 124, 125, 126, 128, 129, 130, 131, 132, 133, 134, 136, 137, 138, 139, 140, 147, 148, 149, 241

ASTM American Society for Testing and Materials. 96

Bis-ANS 4-4-Bis-1-phenylamino-8-naphthalene sulfonate. 18

BMI Background Membrane Image. xxiv, xxv, xxvi, 19, 111, 175, 177, 178, 179, 180, 181, 182, 183

BS3 Bis(sulfosuccinimidyl)suberate. 85, 86, 147

BSA Bovine Serum Albumin. xxi, 23, 25, 41, 85, 147, 148, 149, 152

C12E8 Octaethylene glycol monododecyl ether. 23

CAD Computer-aided design. xv, xvi, xvii, 73, 75, 95, 103

CFD Computational Fluid Dynamics. xiv, xxx, 3, 56, 57, 71, 98, 229

CHO Chinese Hamster Ovary. 10

CMC Critical Micelle Concentration. vii, viii, x, xxvii, xxix, xxx, 18, 20, 23, 95, 96, 107, 167, 202, 205, 206, 207, 208, 209, 211, 213, 214, 215, 218, 219, 221, 223, 246, 247

CVD Chemical Vapor Deposition. 81

DASP 5-Dimethylaminonaphthalene-1-sulfonamidoethyl] trimethyl ammoniumperchlorate. 18

DCVJ 4-(Dicyanovinyl)-julolidine. 18

DLS Dynamic Light Scattering. iv, vi, 16, 107, 108, 111, 120, 135, 212

DPI Dual Polarization Interferometry. 36

DTPA Diethienetriamine-pentaacetic acid. 20

EDTA Ethylenediaminetetraacetic acid. 20

EL Polyoxyl-35 castor oil. viii, ix, x, xxiii, xxiv, xxv, xxvi, xxvii, xxviii, xxix, xxx, 94, 95, 96, 167, 168, 169, 171, 172, 173, 174, 176, 177, 178, 179, 180, 181, 182, 183, 184, 185, 187, 188, 189, 190, 191, 192, 193, 195, 196, 197, 198, 199, 200, 201, 202, 203, 204, 207, 208, 210, 211, 215, 216, 217, 220, 221, 222, 223, 224, 245

FAS Fluoroalkylsilane. 81

FDTS Perfluorodecyltrichlorosilane. xv, xviii, xx, 81, 82, 83, 123, 124, 126, 129, 130, 131, 132, 133, 134, 135, 136, 137, 138, 139, 140

FPOP Fast Photochemical Oxidation of Proteins. iv, v, vi, viii, xi, xv, xvi, xvii, xxxii, 17, 18, 56, 67, 69, 70, 71, 73, 74, 75, 76, 77, 97, 98, 99, 100, 101, 103, 104, 249, 281, 282, 283, 284, 285

GCSF Recombinant human growth hormone. 23

HMDSO Hexamethyldisiloxane. 81

HPSEC High Performance Size-Exclusion Chromatography. iv, vi, 14, 111, 168, 175, 183, 190, 212

HS15 Polyoxyethylated12-Hydroxystearic acid. viii, ix, x, xxiii, xxiv, xxv, xxvi, xxvii, xxviii, xxix, xxx, 94, 95, 96, 167, 168, 169, 171, 172, 173, 174, 176, 177, 178, 179, 180, 181, 182, 183, 184, 185, 186, 187, 188, 189, 190, 191, 192, 193, 195, 196, 197, 198, 200, 201, 202, 203, 204, 207, 208, 210, 211, 215, 216, 217, 218, 220, 221, 222, 223, 224, 245, 246, 247

HSA Human Serum Albumin. 20, 23, 30, 31

HTS Hexyltrimethoxysilane. xv, xviii, xx, 81, 82, 83, 123, 124, 125, 126, 129, 130, 131, 132, 133, 134, 135, 136, 137, 138, 139, 140, 142, 241

IgG Immunoglobulin G. 2, 23, 58, 80, 96, 116, 135, 157, 205, 212, 224, 246, 247

LDH Lactate Dehydrogenase. 23

mAb Monoclonal Antibody. vi, viii, ix, xi, xviii, xx, xxxi, xxxii, 1, 2, 3, 8, 9, 10, 11, 23, 24, 40, 41, 42, 108, 116, 118, 119, 120, 121, 122, 124, 125, 129, 130, 133, 134, 135, 136, 137, 138, 143, 144, 219, 234, 235, 244, 247

MALS Multi-Angle Light Scattering. 16

mPEGMA Poly(ethylene glycol) methyl ether methacrylate. xviii, xx, 82, 84, 123, 124, 125, 126, 129, 130, 131, 132, 134, 136, 137, 143

NATA N-Acetyl-L-tryptophanamide. xxvii, 107, 209, 210, 211, 212

NR Neutron Beam. 36

OTS Octadecyltrimethoxysilane. 81

P188 Poloxamer 188. viii, x, xxiii, xxiv, xxv, xxvi, xxvii, xxviii, xxix, xxx, 95, 96, 167, 169, 171, 172, 173, 174, 175, 176, 177, 178, 179, 180, 181, 182, 183, 184, 185, 186, 187, 188, 189, 190, 191, 192, 193, 194, 195, 196, 197, 198, 200, 201, 202, 203, 204, 207, 208, 209, 210, 211, 215, 216, 217, 220, 221, 222, 223, 245

PAGE Polyacrylamide Gel Electrophoresis. iv, 16

PDI Polydispersity Index. 110

PEG Poly(ethylene glycol). 20, 40, 82, 240

PFS Prefilled Syringes. 23, 24

Phe Phenylalanine. 17

PLGA Poly Lactic-co-Glycolic Acid. 20

PMMA Poly(methyl methacrylate). xv, xvii, 74, 99, 100, 102

PNA N-phenyl-1-naphlhylamine. 18

PS20 Polysorbate 20. viii, ix, xxiii, xxiv, xxv, xxvi, xxvii, xxviii, xxix, xxx, 21, 77, 94, 95, 96, 143, 156, 157, 167, 168, 169, 171, 172, 173, 174, 175, 176, 177, 178, 179, 180, 181, 182, 183, 184, 185, 186, 187, 188, 189, 190, 191, 192, 193, 195, 196, 197, 198, 200, 201, 202, 203, 204, 207, 208, 209, 210, 211, 214, 215, 216, 217, 219, 221, 222, 223, 224, 227, 245, 246, 247

PS80 Polysorbate 80. viii, ix, x, xxiii, xxiv, xxv, xxvi, xxvii, xxviii, xxix, xxx, 21, 94, 95, 96, 167, 168, 169, 171, 172, 173, 174, 175, 176, 177, 178, 179, 180, 181, 182, 183, 184, 185, 186, 187, 188, 189, 190, 191, 192, 193, 195, 196, 197, 198, 199, 200, 201, 202, 203, 204, 207, 208, 209, 210, 211, 215, 216, 217, 218, 220, 221, 222, 223, 224, 245, 246, 247

PTFE Polytetrafluoroethylene. xvi, 91, 95

PVD Physical Vapor Deposition. xv, 80, 83

QCMD Quartz Crystal Microbalance with Dissipation. iv, vi, xiii, xvi, 35, 36, 37, 87, 89, 123, 144, 149, 150, 243

QELS Quasi-Elastic or dynamic Light Scattering. 108, 109

Re Reynolds number. v, 50, 53, 58

rhGH Recombinant human growth hormone. 23

rhTF220 Recombinant human tissue factor 220. 23

rhTF243 Recombinant human tissue factor 243. 23

SAMs Self-Assembled Monolayers. xv, 80, 81, 83, 84

SDS Sodium Dodecyl Sulfate. iv, 16, 89

SE Spectral Ellipsometry. 36

SEC Size-Exclusion Chromatography. 16

SPR Surface Plasmon Resonance. 36

ThT Thioflavin T. 18

TMAO Trimethylamine N-oxide. 20

TNS 2-(p-Toluidino)- naphthalene-6-sulfonic acid. 18

ToF-SIMS Time-of-Flight Secondary Ion Mass Spectrometry. 36

Tris 2-carboxyethyl)phosphine hydrochloride. 86

Trp Tryptophan. xxvii, xxviii, xxix, 17, 18, 104, 106, 107, 210, 211, 212, 214, 216, 217

Tyr Tyrosine. 17, 104

vWF von Willebrand Factor. xii, 32, 33

XPS X-ray Photoelectron Spectroscopy. 36

XRR X-Ray Reflectivity. 36

Chapter 1

Introduction

Therapeutic proteins, including monoclonal antibodies (mAbs), correspond to key products among biopharmaceuticals through the advancement of recombinant DNA technology [13]. Presently, mAbs, represent the most important class of biologics, with 27 new antibody-based drugs approved (out of 127 biologics) between 2016 and 2018 [34] with a market projection of $300 billion by 2025 [35]. mAbs are used in the treatment of a diverse range of diseases from rheumatoid arthritis to cancer [36]. Protein aggregation can have a critical effect on therapeutic efficacy and has been implicated in immunogenic reactions [37–39] and in delivery to the patient, for example through clogging of constrictions found in auto-injection devices [40]. Alongside the biopharmaceutical challenges that can be encountered due to the protein aggregation of pharmaceuticals, protein aggregation has been also associated with various human disorders. Specifically, the aggregation of proteins has been reported as a common molecular mechanism found in several neurodegenerative diseases including Alzheimer's disease (AD), Parkinson's disease (PD), Huntington's disease (HD), amyotrophic lateral sclerosis (ALS) and prion diseases [41].

During manufacture, and given the number of processing steps (up to 5000 [42], compared to 100s for a small molecule drug [43]), both understanding and controlling aggregation is vital in achieving efficient and viable manufacturing processes. Aggregation can take place at many stages in the overall process including fermentation, pumping [44, 45] freeze-thawing, purification by chromatography [46], fill-finish and storage [13, 47–50]. Proteins can accumulate at surfaces [51] at all the stages, the extent of which depends on surface characteristics such as hydrophobicity, charge and roughness [52, 53]. In the presence of hydrophobic interfaces, protein denaturation can be encountered by the exposure of protein's hydrophobic core, which can result in self-association and finally aggregation [51]. In addition to the adsorption of therapeutic proteins to surfaces affecting delivery into patients [12] (including pre-filled syringes [54–56]), such interactions may cause aggregation of proteins [57].

The interaction of proteins with multiple interfaces, in combination with the mechanical disruption of the interfaces under the application of mechanical stress throughout the production line, can be conducive to causing protein aggregation [12]. The association of proteins with several interfaces is also reported to be linked with the promotion and amplification of protein aggregation [24, 54, 58, 59]. Protein surface adsorption is an important phenomenon in biology, enabling their interaction with membrane surfaces [60] and the ability of a variety of organisms to resist hydrodynamic flow [61–63]. Conversely,

the fouling of surfaces with proteins is problematic both in vivo and in vitro. In the context of the biotechnology industry, the unfavourable interaction of pharmaceutical proteins with surfaces during and post-manufacture is of particular interest. Alongside the changes in surface, the nature of the hydrodynamic forces that biopharmaceuticals encounter, changes throughout their manufacturing process [58]. These include shear and extensional flows [1, 2, 58, 64], as well as cavitation and air-water interfaces [65, 66]. The specific interfacial stresses can be encountered throughout the stages of ultrafiltration/diafiltration (air/liquid interface, shear, cavitation), formulation/mixing (air/liquid interface, shear), filtration (filter/liquid interface, extensional flow), filling (air/liquid, solid/liquid, shear, cavitation), transportation (agitation, air/liquid interface) and storage (container/liquid interface) as summarised in [12].

Therefore, the stability of these biopharmaceuticals, is a desired attribute, and is a constant challenge, particularly considering the chemical modifications that the molecules can encounter throughout their complex steps involved during their manufacturing process [67]. Stability is also an important property during the formation of bispecific molecules, which are artificially engineered through the application of sophisticated molecular design and genetic engineering [68].

The type of hydrodynamic flow which is responsible for contributing to the promotion of protein aggregation is a controversial subject within the literature. Therefore, the understanding of the mechanisms under which the proteins can aggregate is crucial for developing and employing analytical methods that can be used to measure and identify the formation and presence of aggregation. Many previous studies have implicated the role of surface in flow-induced aggregation [12, 24, 58, 69–71]. An extensional and shear flow device (EFD), which subjects proteins to controlled flow environments which mimic those found in bioprocessing [58], has been previously developed in Leeds. Extensional flow has the ability to induce protein aggregation [1], with mAb biopharmaceuticals being particularly sensitive to these hydrodynamic forces [1–3].

In this work, the simultaneous role of surface, by modifying the surface of the EFD, and hydrodynamic flow is evaluated on the aggregation of four IgGs, mAbs and a bispecific molecule, corresponding to a total of five model proteins. Molecules include WFL (MEDI1912) which is a potent inhibitor of nerve growth factor (NGF) and is a mAb with known poor biophysical properties, including a propensity to aggregate under manufacturing [72]. mAb1 is a generic IgG1 of not known target and has been previously characterised, exhibiting moderate aggregation stability under flow, whereas STT (MEDI1912_STT) is a mAb with known stability properties against aggregation). MEDI8852 and a fifth bispecific molecule, MEDI3549, where both MEDI8852 and MEDI3549 have unknown aggregation propensity profiles under flow. Modifying the solid interfaces of the EFD to have a range of surface energies (interpreted through contact angle) allows the systematic

study into the interaction of hydrodynamic forces and surfaces on mAbs. Alongside the role of solid interfaces, the effect of liquid interfaces, using excipients, is corroborated through further formulation studies.

1.1 Aims

The work, presented here, investigates the aggregation propensity of protein-based pharmaceutical products using flow-based tools. Such devices enable the detection of parameters and conditions that affect the aggregation of proteins, which is crucial for the development of safe and cost-effective biopharmaceutical materials. Using flow-based devices, an understanding of the flow induced aggregation can be developed, along with understanding the effects of manufacturing conditions on proteins.

The aim of the project is to understand how protein stability can be enhanced under the exposure of biopharmaceuticals to flow, by employing strategies including the incorporation of interfaces. The incorporation of interfaces refers to the modification of equipment surfaces, as well as the formulation conditions of proteins. The current study builds on the work presented in previous studies [1, 2] in terms of the shear and extensional flow and by implementing new parameters and particularly the incorporation of interfaces and measurement techniques for studying the phenomenon of flow induce aggregation in the presence of interfaces. To achieve a deeper understanding of the aggregation propensity path, a set of objectives determines the strategy which will be followed in the present work.

1.2 Objectives

1. Use of Computational fluid dynamics (CFD) to simulate the shear and extensional flow which is expected to be applied on proteins within the extensional flow device (EFD) and microfluidic flow channels. Characterise the regions of low shear flow, extensional flow and high shear flow, understanding the forces applied from flow and evaluate the performance against literature and experiments.

2. Conduct experiments on the currently developed extensional flow device by introducing surface treatment on the components of the device. Select test proteins and suitable biophysical methods to determine aggregation propensity.

3. Expand the investigation to go beyond extensional and shear flows to include surface interactions.

4. Investigate the enhancement of stability of molecules using formulation strategies under flow, using excipients including arginine, sucrose, and surfactant molecules.

1.3 Contributions

The contributions of this thesis in the field of biopharmaceutical aggregation are:

1. The computational flow characterisation of the molecules within flow channels and the development of a microfluidic device which can be integrated in a current biophysical method to study the effects of shear and extensional flow on early unfolding events of proteins in a detailed level, which can identify the building blocks of proteins which are responsible for initiating the aggregation process (chapters 4 & 5).
   Outcome: The underpinning flow descriptions on which to build a more complex investigation into surface and flow (and used in contributions 2-4).

2. The investigation of the effects of a surface library and its role in the aggregation propensity of proteins during flow conditions, which are relevant to pharmaceutical manufacturing conditions (chapter 6).
   Outcome: Unpick mechanism of role of surface in aggregation.

3. The investigation of the effect of novel surfactant molecules and the characterisation of their effects on aggregation within a range of analytical techniques investigating their effects during the stages of manufacture and shipping of protein-based pharmaceuticals (chapter 7).
   Outcome: Insights into the role of surfactant molecules within the mechanism of flow induced aggregation.

4. The development of proof-of-concept studies that can be expanded in further work. The application of microfluidic devices that can be advantageous in the study of highly aggregation resistant molecules under flow as well as the further investigation of the role of interfaces in systems which can represent the action of sliding interfaces which can represent plungers and pistons, which are typically found throughout the production line of protein pharmaceuticals (chapter 8).
   Outcome: A road-map for extending the studies to include sliding interfaces in a way they can be "unpicked" from extensional flow.

1.4 Thesis structure

The current thesis consists of 9 chapters, which will be described briefly here. Chapter 1, introduces the reader to the motivations of the current work and the area of biopharmaceutical aggregation, along with the work's aims, objectives and contributions to the field. Chapter 2 introduces the area of biopharmaceutical aggregation by the presentation of methodologies and techniques that are typically employed in the field, as well as the studies which concern on the application of hydrodynamic flow and interfaces on the aggregation of various proteins. In chapter 3, a theoretical background around the mathematical

expressions that are employed to characterise the flow environment of protein within a range of devices is presented, which is then followed by the computational characterisation of the flow fields by the application of the theoretical expressions in chapter 4.

Next, in chapter 5, the experimental methods and materials are described, which are then followed by the surface effects on aggregation which are presented in chapter 6. The surface chapter is then followed by the surfactant chapter, presenting the effects of various surfactant formulations on the aggregation of molecules in chapter 7, followed by the proof-of-concept studies in chapter 8 presenting studies which can be further developed in the future. Lastly, the conclusions' chapter is then followed in chapter 9.

Chapter 2

Literature Review

In this chapter, a review of literature is presented, including the current studies conducted in the area of protein aggregation. The aggregation of biopharmaceuticals is a topic of interest, since it has been found to be linked with the immunogenic reactions in vivo, which results into a bad drug candidate in the biopharmaceuticals [10, 39]. Parameters that can be denoted as physical and chemical, are linked with the induction of aggregation. Hydrodynamic forces are considered to physically induce the aggregation of drugs during the manufacturing or administration process. Filtration and transportation leading to sample shaking can lead to the generation of hydrodynamic forces that initiate the aggregation [39]. The literature review summarises the manufacturing process along with the parameters that affect the formation of aggregates and highlights some of the studies found to examine the relation of hydrodynamic forces on various areas, including the interaction of a variation of interfaces.

Literature review structure

Analytically, an overview of the main topics which are covered within the literature review chapter is shown in figure 2.1. The motivation of this chapter is firstly to give an overview of the structure of an antibody which is the model protein investigated in this project in section 2.1, followed by the process in which aggregation is suggested to be induced in bulk conditions in section 2.2. The next section, 2.3, refers to the stages involved in the manufacturing process of biopharmaceuticals and the steps which are critical for potential aggregation. Then the factors that are reported to have direct effects on the formation of aggregation are introduced in 2.4, followed by the commonly used techniques developed in the literature, to study the phenomenon in 2.5, and the strategies which are followed in order to minimise or prevent aggregation in 2.6. Next, the review covers the effects of hydrodynamic forces on the aggregation and a variation of methods in which the hydrodynamic forces can be developed in 2.7, followed by the effect of interfaces present during their application in 2.8. Lastly, a summary of the literature is described, addressing the main focus of the current literature in section 2.9.

2.1 Antibody structure

The unique attributes of antibodies have led to their successful development as therapeutic molecules due to their properties. The high binding affinity, long circulation times in

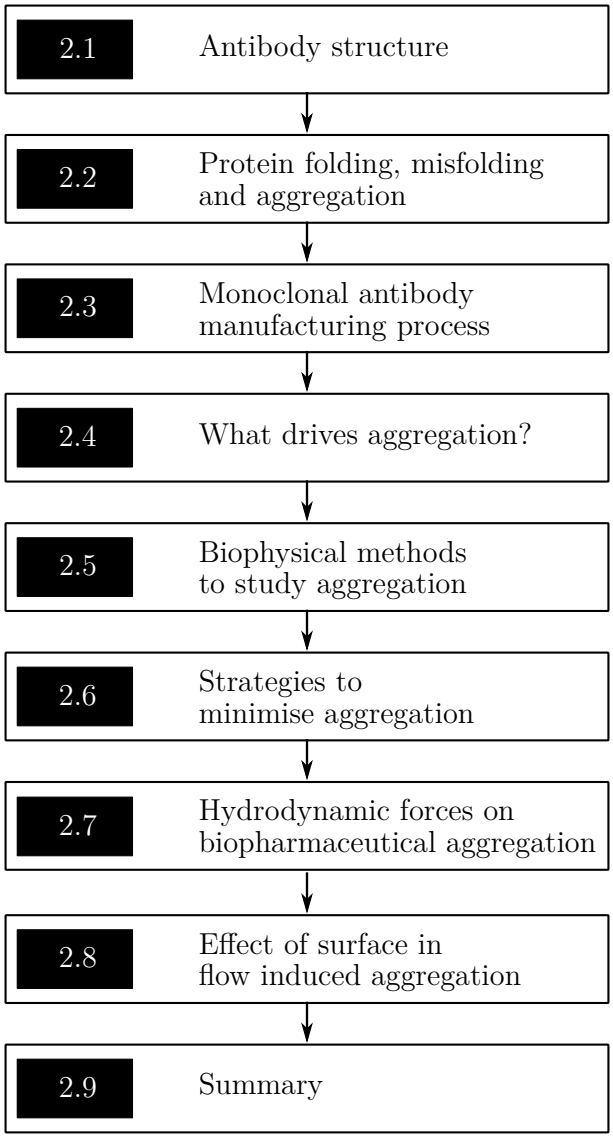

Figure 2.1: Overview of the main sections covered in the literature review chapter.

the blood stream, the well established methods for their identification, and the non-toxic nature of their building blocks, amino acids, make antibodies attractive molecules for treating disorders in the range of arthritis to cancer [73, 74].

A generic mAb structure consists of 12 domains, in four polypeptide chains, including two heavy chains consisting of four domains each and two light chains consisting of two domains that are connected via multiple disulfide bonds [9]. A folded monoclonal antibody (mAb), as shown in figure 2.2, consists of two antigen binding domains (F_{ab}), containing the amino acid sequences that provide the specificity and affinity of a given mAb to a given epitope [10]. They also consist of one conserved domain (F_c). The F_{ab} domains, which are referred to as antigen-binding fragments, correspond to the antibody "arms" and contain the variable domain of the heavy chain (V_H), first constant domain of the heavy chain adjacent to the VH domain (C_H1), variable domain of the light chain (V_L) and constant domain of the light chain (C_L) domains [9, 75]. The F_c domain, corresponds to the "base" of the antibody, containing two second constant domain of the heavy chain adjacent to the VH domain (C_H2) and two third constant domain of the heavy chain adjacent to the VH domain (C_H3) domains and is referred to as the crystallisable domain [9, 75]. A flexible hinge region connects the two domains, facilitating target binding providing conformational flexibility [76]. Complementarity-determining regions, (CDRs) mediate the antibody binding and are found in each variable domain, each containing three CDRs [75]. The variation of V_H and V_L domains determine most sequence differences between antibodies [75]. Depending on structure and function, antibodies are divided into five isotypes such as IgG, IgA, IgM, IgE, and IgD. Based on the number of disulfide bonds, especially in the hinge region, the IgG isotope can be divided into further four IgG subclasses [9]. The most commonly used subtype is IgG1 although IgG2, IgG3 and IgG4 may be found, with IgG4 having different anti-inflammatory mechanisms to be used for the design of immunotherapies [9, 75, 77]. The four IgG subtypes are functionally distinct because of different heavy chain genes, differ in their ability to fix complement (IgG3> IgG1> IgG2> IgG4) and bind Fc receptors [78]. The most dominant subclass corresponds to IgG1, up to 60-70% of the total IgG, followed by IgG2 (20-30%), IgG3 (5-8%) and IgG4 corresponds to the least frequent subclass (5%) [78].

2.2 Protein folding, misfolding and aggregation

When pharmaceutical products are under the stage of manufacture, it is expected to have the development of net irreversible aggregates in most of the therapeutic proteins and over time as products are stored, transported and/or administered to patients [10]. During the manufacturing process, proteins are exposed into many chemical and physical effects which can cause denaturation leading to aggregation. The aggregated proteins resulted from the conformational changes can have an impact on the patient where the final pharmaceutical

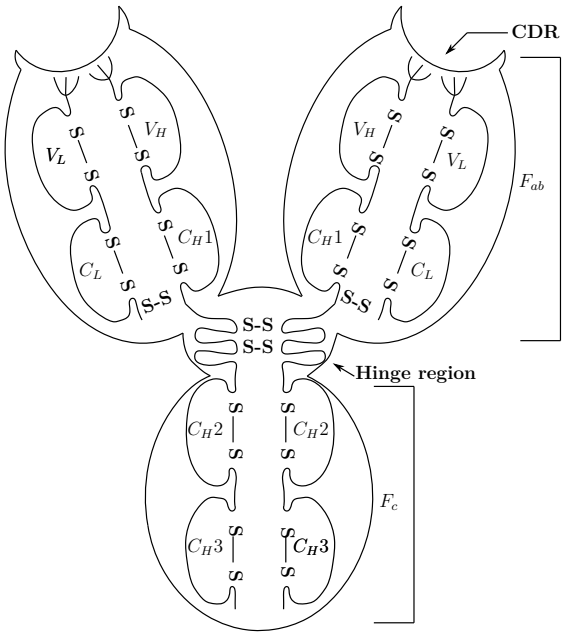

Figure 2.2: Antibody general structure. F_c, crystallisable fragment; F_{ab}, antigen binding fragment; V, variable domain; C, constant domain; L, light chain; H, heavy chain; S-S, disulfide bond. Adapted from [9].

product is delivered to. Serious health issues such as adverse immunological responses can be caused to the patient if even a small protein aggregate is within the delivery system [79]. Therefore, the molecular nature of how different aggregates form as well as which aspects of the proteins and their sample environments alleviate this process and whether the aggregation can be prevented is crucial. This could significantly reduce the cost to the patient and the market in general, as well as reducing and preventing potential immunogenicity of the future therapeutic products.

Protein aggregation can be defined as a term denoting the process by which protein molecules can be assembled and stick to each other, composing stable complexes consisting of two or more proteins [79]. The individual proteins, which can be denoted as the monomers, could be composed of a single folded chain, multiple protein chains that are disulfide bonded to one another such as with monoclonal antibodies (mAbs), or a natively multimeric complex [79]. There are several pathways in which a protein can aggregate, which can differ depending on the environmental conditions, including different types of applied stress. The representation of various types of aggregates formed by therapeutic proteins such as mAbs are illustrated in figure 2.3.

Monomers are composed of strong non-covalent bonds that require a degree of conformational change to distort in to unfolding or misfolding so as the amino acids can be stretched forming strong contacts that make up an aggregate between monomers as it can be seen in figure 2.3.

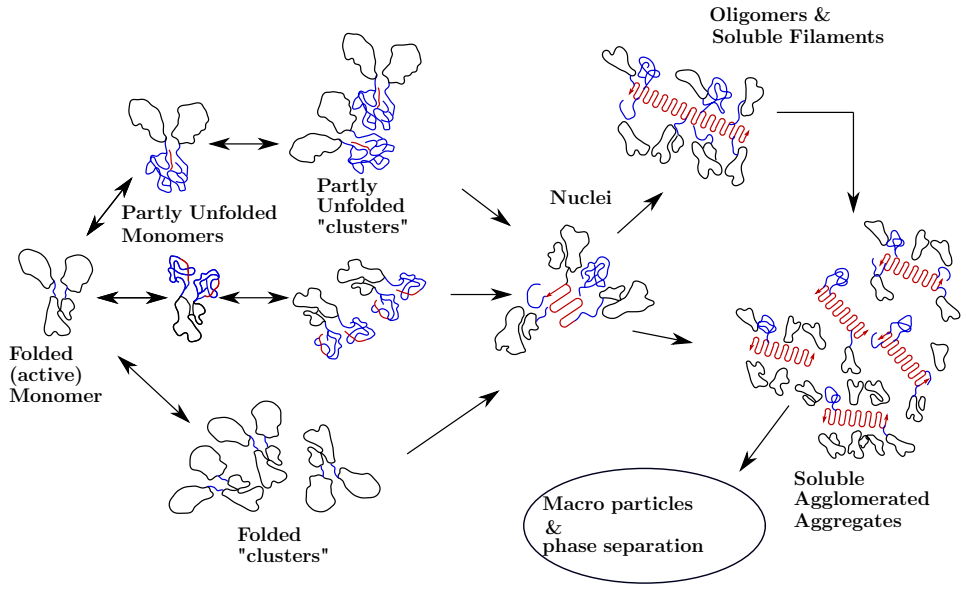

Figure 2.3: Schematic diagram illustrating multiple non-native aggregation pathways for a multi-domain protein such as a monoclonal antibody (mAb) composed of a single Fc fragment and two identical Fab fragments. Red strands denote hot spot sequences that are prone to form strong, effectively irreversible inter-protein contacts that stabilise aggregates, but are primarily hidden or buried in fully folded monomers. Double-arrows denote effectively reversible steps. Single arrows denote irreversible steps. Adapted from [10].

2.3 Monoclonal antibody manufacturing process

A typical manufacturing procedure is illustrated in figure 2.4. The production of biopharmaceuticals can be separated into two main processes, known as the upstream and downstream process. The manufacturing process of antibodies begins from the growth of mammalian cells in suspension culture in large bioreactors. The majority of antibodies is produced in eukaryotic cells such as Chinese Hamster Ovary (CHO) which is the most dominant growth choice [80]. Aggregation can happen during cell culture, where the aggregation process can be occurred within the cell and once the protein is secreted into the cell culture medium [39, 48]. The aggregation at this stage can be limited by the modification of cell culture conditions, such as the temperature and pH (among others) [39].

The manufacturing procedure corresponds to a process with multiple steps, in which the molecules are exposed to various interfacial stresses. Briefly, as reviewed in [11], the cell culture corresponds to the first step of the upstream process, which is expanded from a cell bank to a series of batch bioreactors of larger volume for cell expansion, and finally the production bioreactor for protein expression. This step is then followed by the centrifugation step required for the cell and cell debris removal, which is then followed by the depth and membrane filtration. The purification process is then followed, which corresponds to the downstream process of the manufacturing process as illustrated in figure 2.4. The

purification of mAbs is then conducted by protein A affinity chromatography, which provides >98% purity in a single step [11]. The next step, which is the viral inactivation step at low pH, inactivates viruses by the elution of the products from the adsorbents at low pH. Further removal of impurities is then conducted by two chromatography steps, cation exchange (CEX) chromatography and anion exchange (AEX) chromatography. The last step of the process corresponds to the subsequent step of ultrafiltration/diafiltration (UF/DF) which formulates and concentrates the final product.

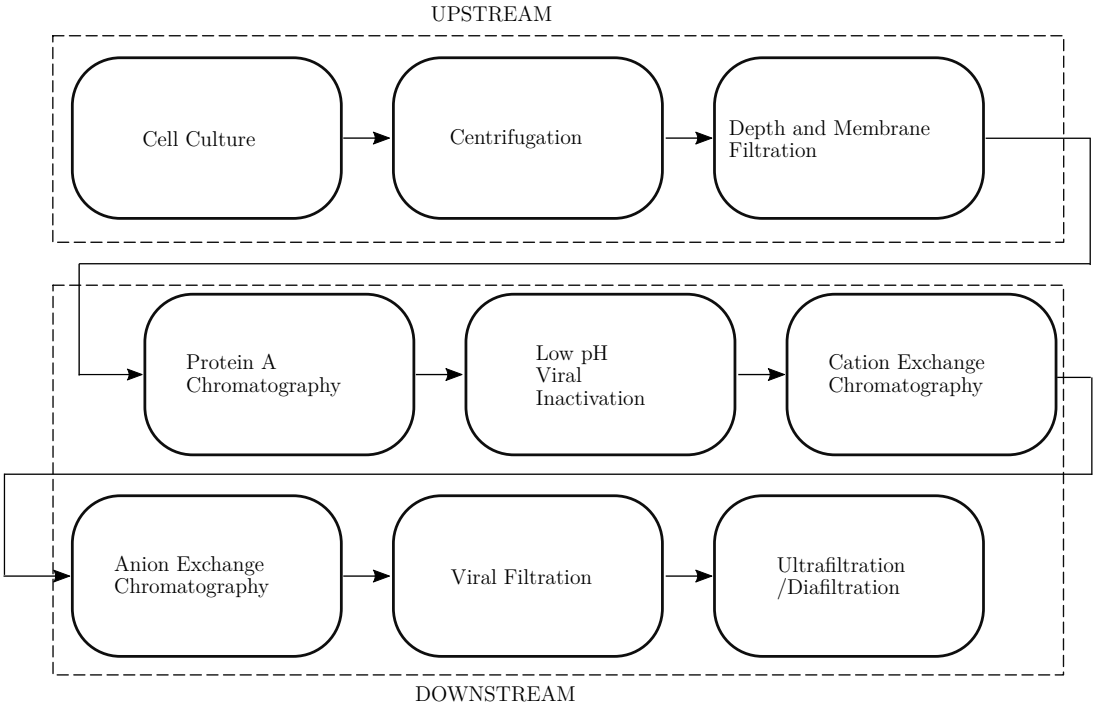

Figure 2.4: Flow diagram of the outline steps involved in a typical mAb manufacturing process. Adapted from [11].

As the manufacturing process is quite complex, the molecules are exposed to various types of interfacial stress that can be encountered throughout the stages of development, manufacturing and clinical administration [12]. Analytically, the interaction of the interfacial stress that can be found throughout the different stages of biopharmaceutical manufacturing is shown in figure 2.5. As reviewed in [12], during the drug substance process, the molecules are exposed to a range of solid/liquid interfaces such as columns, filters, processing equipment, container surface and ice during storage, involved in the steps of the protein isolation and purification. The interaction of molecules with air/liquid interface can be also found in the process of mixing and mechanical pumping operations. Moving to the drug substance manufacturing process, the steps of thawing and mixing with additional excipients induced the interaction of proteins with ice/liquid interface during thawing, air/water interface during mixing exposing the molecules to shear flow conditions before the filling process. In the steps of packing, transportation and administration, air/liquid interfacial stress is found within the container's headspace, agitation during transportation and stress during clinical administration. In the final stage of clinical use,

a range of solid/liquid interfaces are present from a range of surfaces and materials such as plastics of IV bags, infusion sets, in-line filters, silicone oil and metals.

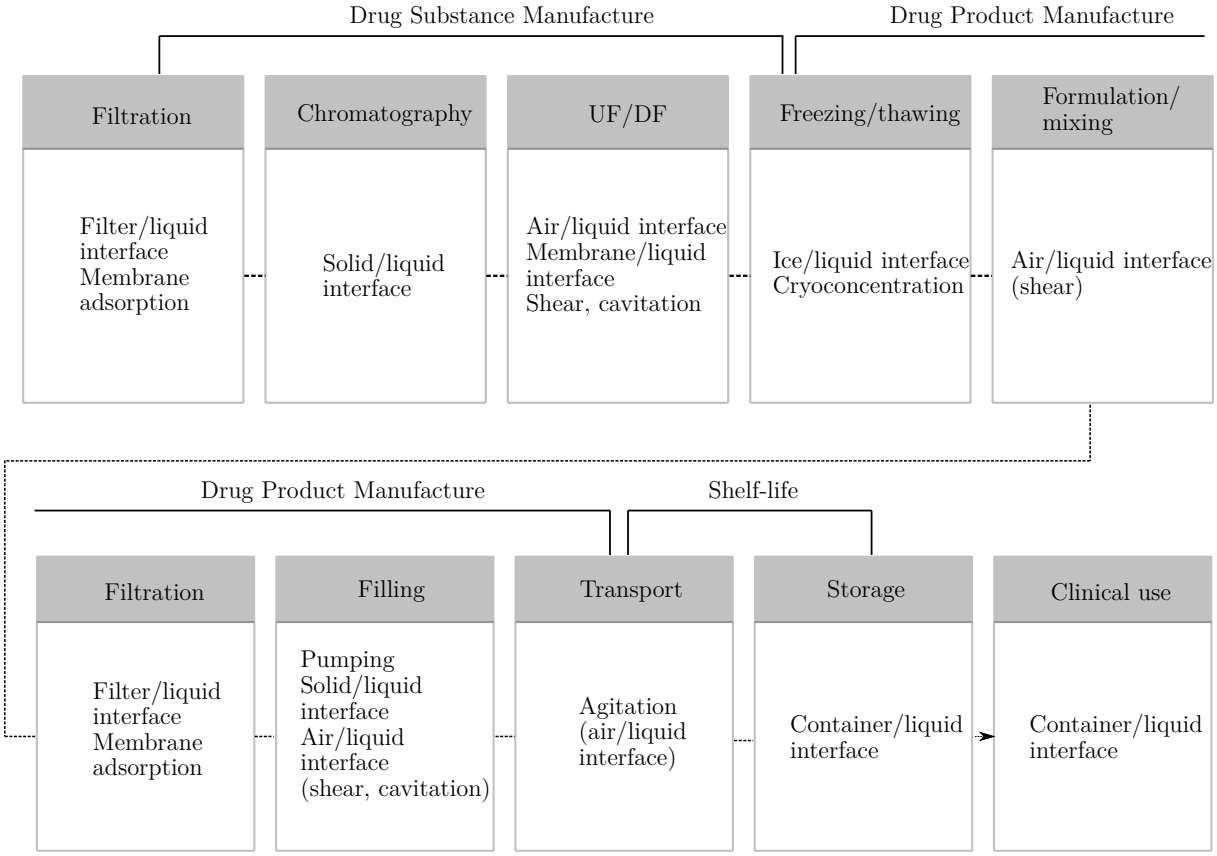

Figure 2.5: Flow diagram displaying the types of interfacial stress occurring during unit operations for drug substance, drug product manufacture, transportation and storage. Adapted from [12].

2.4 What drives aggregation?

The rate of aggregation has been found to be settled by several factors in vivo and ex vivo. Temperature, mechanical stress, pumping, freezing and formulation are some of the parameters which are found to induce aggregation [13]. Particularly, biopharmaceutical therapeutic proteins are exposed to a variation of stress conditions during the manufacturing, storage and shipping stages and their simultaneous interaction with flow-interface environments as shown schematically in figure 2.6, and have been described previously in section 2.3. Aggregation of biopharmaceuticals can be induced by process steps such as fermentation, purification, filling, shipment and storage [13]. Additionally, formulation parameters such as protein concentration, protein structure, temperature, pH and ionic strength can control the aggregation rate [13, 81]. Therefore, the parameters that are found to be related to inducing protein aggregation can be used as control means for monitoring the aggregation.

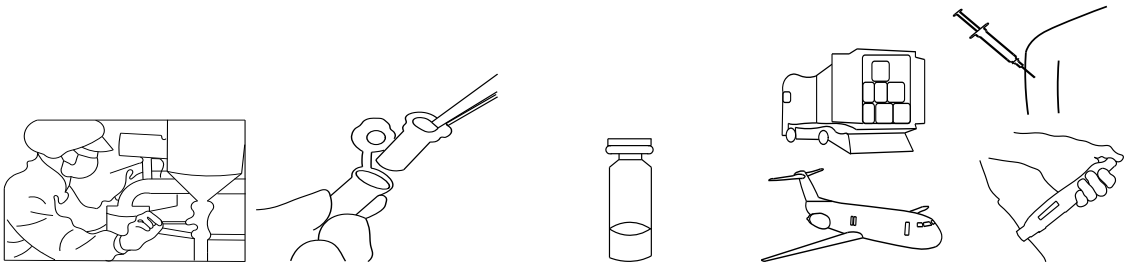

Figure 2.6: Interaction of biopharmaceuticals with flow-interface environments during equipment interaction under bioprocessing (2.6a), filtration (2.6b), storage (2.6c), transportation (2.6d), and administration conditions (2.6e).

2.4.1 Classification of protein aggregates

In literature, the classification of aggregates is commonly found since no precise understanding and definition of aggregates exist. The classification can be based according to the environment where aggregates can be formed based in broad categories such as in vivo versus in vitro [82] while the separation of aggregates is divided among others into soluble and insoluble categories [83, 84]. However, these terminologies according to authors are not clear and standard for everyone, therefore a more precise determination of the protein aggregate classification has been defined. The classification of aggregates has been found to be mostly based on the following categories [13]:

(a) by the type of bond: non-covalent aggregates versus covalent aggregates;

(b) by the reversibility: reversible versus irreversible aggregates [84];

(c) by size: small soluble aggregates (oligomers) versus large;

(d) by protein conformation: aggregates with predominantly native structure vs non-native structure (partially unfolded species)

2.4.2 Factors favouring aggregation

Temperature is a common parameter used to accelerate protein aggregation since the chemical reactions such as oxidation of biopharmaceuticals are accelerated under an increase in temperature. The temperature increase is related, having effects including an increase in protein diffusion and also enhancing the hydrophobic interactions which are necessary for the occurrence of physical protein aggregation [85].

pH parameter can impact the behaviour of protein aggregation. This is due to the fact that pH precepts the type and distribution of surface charges on proteins, affecting both the intramolecular folding and intermolecular protein-protein interactions [85]. Related to pH, ionic strength is also an important factor for monitoring protein aggregation. Different conformational states can be induced by the interactions between positive and negative

ions, which bind or interact electrostatically with proteins, as they can be affected by the ionic strength. This can lead to the generation of different aggregation behaviours and morphologies [85]. Protein concentration has also been reported in literature for having an effect by enhancing the formation of protein aggregates. As it is referred in [85] increased aggregation and precipitation due to solubility limit is induced by the increase in protein concentration.

Protein denaturation which implies the low conformational stabilities of protein can be prone to aggregate and can be achieved under the addition of chaotropic agents (among other conditions and substances) such as guanidinium ion and urea [86]. Chaotropic agents are reported to alter the stability of proteins by either direct binding to them or modifying the solvent properties [87]. Guanidinium ion and urea, are the most commonly used protein denaturants, as their association with denaturation lies in the increase in the solubility of nonpolar substances in water. The ability to disrupt hydrophobic interactions is stemmed from the effectiveness of the denaturants [86].

The phenomenon of aggregation can be also found during the manufacturing process of biopharmaceutical products as a part of purification, formulation, shipment and storage [13]. The fluid drag which is associated with the shear flow resulting from the mechanical agitation of proteins, is linked with the denaturation and subsequent aggregation due to the destabilised native structure of protein molecules [17]. This implies that the understanding of the influence of fluid forces on the structural integrity of aqueous protein systems, is important, as the shear flow is commonly found to be associated with protein denaturation/aggregation, which simultaneously accompanied by the molecule interaction with multiple interfaces.

2.5 Biophysical methods to study aggregation

The analysis of protein aggregation is an increasing challenge in the biopharmaceutical industry. Since the morphology and structure of proteins vary from protein to protein, there is no single analytical method that can be used for analysing the entire range of pharmaceutical proteins. The encounter of artefacts between methods can be also observed, as samples may be prone to stick to column membranes. Therefore, combination of analytical methods can be applied for the aggregation detection. The detectable size range of aggregates using a range of techniques is summarised in figure 2.7.

2.5.1 High Performance Size Exclusion Chromatography, HPSEC

The detection and quantification of protein aggregates (particularly used for monoclonal antibodies), can be achieved using one of the most common analytical methods, which is the size exclusion chromatography [88]. This method is used in literature to separate proteins

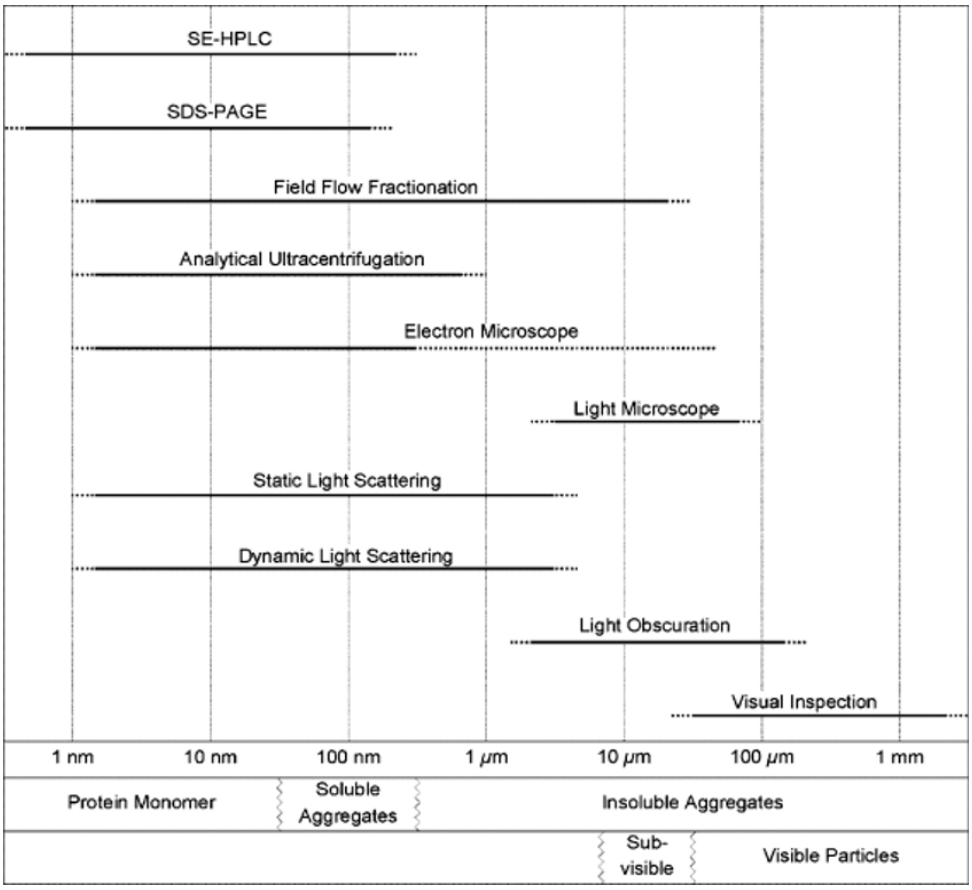

Figure 2.7: Schematic representation of the approximate range of detectable protein sizes (diameter) of various analytical methods [13].

by their hydrodynamic volume, and its primary application is the protein monitoring and aggregation [13]. Protein aggregates can be separated via a column material based on their shape and size as they travel through a solid phase (gel) matrix. The separation is achieved as a molecule enters a pore in the stationary phase; hence, bigger molecules will elute first, having the shortest time to pass through the chromatography column. The coupling of SEC with multi-angle laser light scattering (SEC-MALS), has been used for the characterisation of the extent of aggregation and degradation (among others) by the increase or reduction in molecular weight and the change in monomer amount [88]. The combination of the two methods can be done since the amount of light scattered is proportional to the weight molar mass, and macromolecule concentration [88]. A major drawback of this technique is that it does not provide an exact estimation of molecular mass [88]. Additionally, in [13] it has been reported that insoluble aggregates cannot be detected using SEC because of a possible removal using filtration by the column or by the sample preparation using centrifugation

2.5.2 SDS-PAGE

The estimation of protein size, identification of protein, sample purity can be achieved by the gel electrophoresis chromatography. This method is a traditional technique for the separation of different proteins based on their size and charge [13]. However, the detection of protein aggregates is limited with a weight range of 5 and 500 kDa. Nevertheless, the SDS technique is a method which has been considered by the authors to be useful for analysing small size aggregates and differentiating reducible from non-reducible aggregates [13, 89].

2.5.3 Dynamic light scattering, DLS

The size distribution of protein aggregates can be estimated using dynamic light scattering. In particular, particles with a size distribution in the diameter range of 1-2 nm to 3-5 μm can be detected (figure 2.7). In the DLS method, the fluctuations of the concentration of molecules, particles or aggregates which are suspended in a tested solution, scatter light which is recorded during the measurement [90]. The rate of diffusion of the scattered species in the sample is indicated by the rate of decay of the fluctuations of scattered light [90]. The major advantage of this method is the re-use of the sample for further characterisation of protein solutions, since it is a non-destructive technique [91]. Moreover, the volume required for conducting a DLS analysis can be very low as a few μL [91]. However, it has been reported that large particles or samples with contamination may cause the divergence of the laser beam before the sample passes through, leading to results that are imprecise [13]. Therefore, the output results can be determined to be qualitative and not quantitative [91].

2.5.4 Analytical Ultracentrifugation, AUC

Analytical ultracentrifugation is commonly used for the determination of aggregates‘ presence in solution. Among the advances of this method is that protein aggregates can be detected without the need of sample manipulation in their formulation buffer [91]. AUC depends on the property of mass, size and shape and the fundamental laws of gravitation and the results obtained using this method do not depend on the comparison of those with standard values/results [13]. Nevertheless, the reproducibility of the results has been highlighted in literature to be relatively poor, where determining a threshold of detection for aggregates is difficult mainly due to the cell(mis)alignment and quality of centrepieces [91]. Moreover, in terms of cost, it has been determined in [13] as a method which requires expensive and specialised equipment. In general, due to the difficulty of reproduction of the results, this method could be recommended to be used as a qualitative and not as an absolute quantitative method [91].

2.5.5 Fast Photochemical oxidation of proteins, FPOP

Fast photochemical oxidation of proteins, FPOP, is a method which has multiple uses around the assessment of protein structure, folding and aggregation. This method provides information into biomolecular structures and interactions and the extent of the modification of proteins at peptide and amino-acid levels [92]. The modification level resulted from the chemical reactions can determine the level of hydrophobicity of the peptide bonds. This method is a type of hydroxyl-radical based protein footprinting which makes use of a pulsed KrF laser (248 nm) to allow the hydrolysis of hydrogen peroxide, producing hydroxyl radicals which can then modify the proteins in situ as it shown in figure 2.8. Authors highlight the high sensitivity of this method detecting the alterations in protein structures. A flow system consisting of a capillary placed perpendicular to the laser beam is used where the protein is mixed with hydrogen peroxide and a radical scavenger and then the solution is irradiated by the laser which produces the hydroxyl radicals [14]. The flexibility of this method is that it can be combined with flow-based tools such as microfluidics to further investigate in deeper level the aggregation propensity.

2.5.6 Fluorescence Spectroscopy

The detection of structural changes of proteins during the aggregation process can be determined using fluorescence spectroscopy. The high sensitivity of the technique to the local environment makes it a commonly used tool to observe protein conformational events [93]. The detection of fluorescence is achieved throughout the contribution of three amino acids found in proteins, which are phenylalanine (Phe), tyrosine (Tyr) and tryptophan (Trp). Due to its higher extinction coefficient and quantum yield, Trp is the most valuable probe used to investigate protein conformation [93]. Excitation at the wavelength of 295

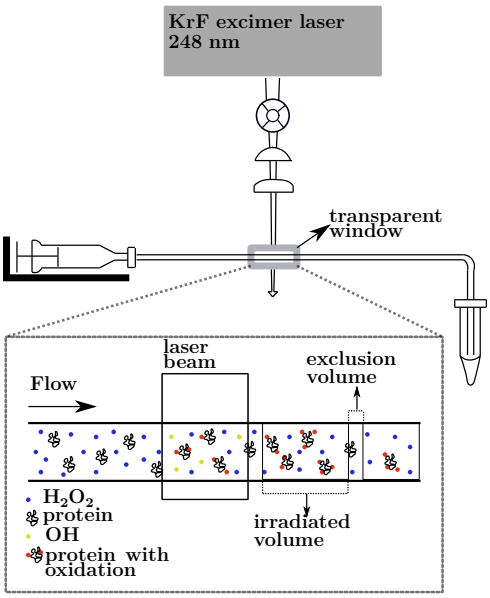

Figure 2.8: Schematic illustration of an FPOP experimental setup, adapted from [14].

nm allows the emission of Trp to be detected specifically from the contribution of the Trp amino acid. The detection of unfolding events can be achieved by emission intensity spectra of Trp which as a hydrophobic aromatic residue is found to be fully or partially buried inside a protein core [93]. During an unfolding event caused by a conformation disruption, Trp becomes exposed to the surrounding environment [93], leading to its emission at longer wavelengths [94]. Therefore, the variation of Trp emission spectra arise from the structure of the protein, and it can also be used to investigate the binding events of surfactants to proteins as shown in [95].

During the process of misfolding and self-assembly of protein leading to the formation of aggregates, the use of a range of fluorescence probes such as 8-Anilinonaphthalene-1-sulfonic acid (ANS), 4-4-Bis-1-phenylamino-8-naphthalene sulfonate (Bis-ANS), 4-(Dicyanovinyl)-julolidine (DCVJ), and Thioflavin T (ThT), allows the detection and characterisation of the different states involved within the aggregation pathway [96]. The binding of surfactants to a range of fluorescent probes including N-phenyl-1-naphlhylamine (PNA), 2-(p-Toluidino)- naphthalene-6-sulfonic acid (TNS), ANS, 5-Dimethylaminonaphthalene-1-sulfonamidoethyl] trimethyl ammoniumperchlorate (DASP) [97] and pyrene [98] can be used to determine their critical micelle concentration (CMC) which can be determined by the enhancement in the emission spectra as investigated in [97].

2.5.7 Sub-visible particle analysis

The aggregation characterisation in terms of particle analysis can be employed using sub-visible particle analysis as the presence of micron or nanometer-sized protein molecule aggregates (particulates) is considered as critical quality attribute as they impose effects on the efficacy and safety of biopharmaceuticals. To ensure safety and control for clinical use,

a microscopic particle counting and light obscuration method for injectables is described in United States Pharmacopeia, USP<788> (Particulate Matter in Injections general chapter) and European Pharmacopoeia as suitable for subvisible particle measurements [99]. A variation of techniques has been explored within the area of sub-visible particle analysis including light obscuration, microflow imaging and more recently background membrane imaging (among others). Firstly, light obscuration (LO) is a technique where as the particles flow through a beam of light, the loss of light intensity which occurs through their exposure to the beam, is measured and related to the cross-sectional area of the particle [99]. However, there are several drawbacks reported, including the inability of the technique for accurate particle counting in high viscosity formulations as well as assessing particle morphological information [99, 100]. Alternative to LO, the detection and characterisation of particles is well studied using micro-flow imaging (MFI) which was shown to provide high sensitivity in particle detection using image filtering [101]. The technique is based on a flow microscopy setup where samples continuously pass through a flow cell and bright field images are captured in successive frames [101].

Background membrane imaging (BMI), which is a recently developed technique, is based on image subtraction of a reference from the measurement image [99]. Using an image analysis software, a background membrane image before loading the samples is aligned and subtracted from the actual measurement images which are created with the final image showing the isolation of the actual particles [102]. With the vacuum suction applied after the samples are loaded on the membrane rings, the liquid phase is removed from the samples with the particles left on the membrane to be analysed, eliminating the inclusion of air bubbles that artificially increase particulate concentrations in flow microscopy and LO techniques. The low sample volume requirements, with the minimum sample volume at 20 μL, and the ease of handling, make the technique a valuable alternative for formulation screening. The comparison between a variation of subvisible particle imaging techniques have been conduced in investigating the performance of MFI, BMI, LO on protein particles generated through freeze-thaw stress, indicating that control and stressed samples analysed using BMI, were either not significantly different from MFI [99].

2.6 Strategies to minimise aggregation

The formulation aspect of protein-based pharmaceuticals is crucial for developing molecule stability. Apart from stability, formulation aims in manufacture of the dosage form, control or target the delivery in the body or provide tonicity (predicting changes in cell volume at equilibrium after exposure of the cell to a solution [103]) minimising patient's pain upon injection [4]. The addition of excipients/additives in the protein preparation is a commonly applied method to provide the inhibition of protein aggregation by changing proteins' environmental properties. As shown in table 2.1, a variation of additives including buffer

agents, surfactants, salts, polymers and amino acids (among others) has been linked with the protein stabilisation by preferential interactions [47, 104, 105]. The mechanism of these formulation agents has been also reported to address increased rate of protein folding [47, 106, 107], reduction of solvent accessibility and conformation mobility [47, 108] and increase in solvent viscosities [47, 109].

Table 2.1: Overview of commonly used formulation agents of biologic drugs [4, 5].

Formulation agent	Purpose of action	Example
Buffers	pH modulator	Citrate, acetate, histidine, phosphate, tris
Surfactants	Surface adsorption inhibitors	
	Interfacial stabilisers	Polysorbate-20 and 80, pluronic-188
Salts	Tonicifiers	
	Stabilisers/destabilisers	Sodium chloride, potassium chloride, sodium sulfate
Preservatives	Inhibitors of microbial growth	Phenol, m-cresol
Antioxidants/chelators	Free radical scavengers	
	Inhibitors of metal-induced degradation	EDTA, DTPA, methionine, ascorbic acid
Osmolytes/sugars	Tonicifiers	
	Cryoprotectants	
	Stabilisers (preferential hydration)	Sucrose, trehalose, sorbitol, TMAO
L-amino acids	Stabilisers	
	Antioxidants	
	Tonicifiers	
	Rheology modulators	Arginine, glycine, proline, lysine, methionine, histidine
Bio-/polymers	Sustained release/extended half-life,	
	Surface adsorption inhibitor,	
	Bulking agents	HSA, PLGA, PEG, cyclodextrins
Polycations	Condensing agents for nucleic acids	Cationic lipids, spermidine, tetra-arginine
Metal ions	Viscosity modifiers, cofactors, cell stabilisers	Calcium, magnesium, manganese

2.6.1 Surfactants

Surfactants can be described as amphiphilic compounds consisting of a hydrophobic tail which is insoluble in water and a hydrophilic head which is water-soluble. Due to the nature of their structure, and having water diffusing properties, interacting with interfaces and offer solubilisation to hydrophobic compounds in water, they are used within a range of industrial applications such as agrochemical, agriculture, food, pharmaceutical and cosmetic industries as well as therapeutic and oral-health related applications [110]. The potential mechanisms of surfactants are reported in literature with two possible descriptions. One suggesting the tendency of surfactant through displacement during their competition with protein to adsorb at interfaces, with their protective effect commonly correlated with the critical concentration in which they form micelles (CMC) [4]. As shown in figure 2.9, from their micelle aggregate state they can release monomers to an air-water interface in the absence of protein, that they dissociate from the aggregate and migrate through the liquid in order to adsorb [15].

The other description is their direct interaction and potential binding to hydrophobic patches of proteins, offering coverage and protection by preventing their interaction with other protein molecules and interfaces [4]. The protein can promote the micelle aggregate disruption, increasing the concentration of surfactant monomers promoting the adsorption or forming stable surfactant-protein complexes with little or no effect on

surfactant adsorption rate [15].

In regard to the pharmaceutical sector, and particularly the biological manufacture of protein-based pharmaceuticals, the molecule stability can be affected by a range of interfaces present during the complex manufacturing steps. As their name suggests, surfactants, which correspond to surface-active agents, can interact with interfaces which could correspond to molecule interfaces such as proteins, air-liquid and solid-liquid interfaces. The most commonly used surfactants as shown in table 2.2 are polysorbates and particularly polysorbates 20 (PS20) and 80 (PS80) promoting protein stability. However, it has been reported that the chemical structure of polysorbates can lead to degradation through autoxidation and hydrolysis pathways which can be encountered due to their storage conditions involving increased temperatures and parameters including solution pH, presence of oxygen, peroxides, heat, UV light and metal ions [111].

Their ability to offer stability against protein unfolding and aggregation has been reported in literature and attributed to correspond to their competitive adsorption properties at interfaces, as summarised in table 2.2 . The interaction of surfactants with protein interfaces is well studied in literature by employing surface tension experiments. The common observation among authors, is the tendency of surfactants to interact with proteins indicating suppression in the surface tension, presenting their interaction with protein interfaces [15, 112–114]. Alongside the interaction of surfactants with protein molecules, authors suggest the competition of protein-surfactants for interfacial area, which is an important parameter leading to the protein molecules to be controlled between their interactions. The effect of surfactants has been also identified in terms of the protein aggregation propensity in their presence in protein formulations during flow conditions. Particularly in [89, 112, 115] agitation induced aggregation, studies have determined the efficiency of surfactants to suppress the aggregation formation when compared to protein formulations alone. In these studies, the agitation has been induced via shear flow configurations.

2.6.2 Other excipients

Alternative excipients, such as sugars including sucrose and thehalose, are employed as formulation additives as they are preferentially excluded from the protein's surface, promoting conformational stability [119]. The suggested protection mechanism of sugars is reported, as they can stabilise the native protein structure and reduce the extent of denaturation by preferential hydration of the unfolded state [119, 120]. Their protection mechanisms have been also shown under mechanical agitation, where sucrose and trehalose (among others), stabilised therapeutic proteins during agitation using an orbital shaker when combined with surfactant in the sucrose formulation buffer [121] and exposed to high shear using a capillary rheometer [58]. Interestingly, in the studies conducted in

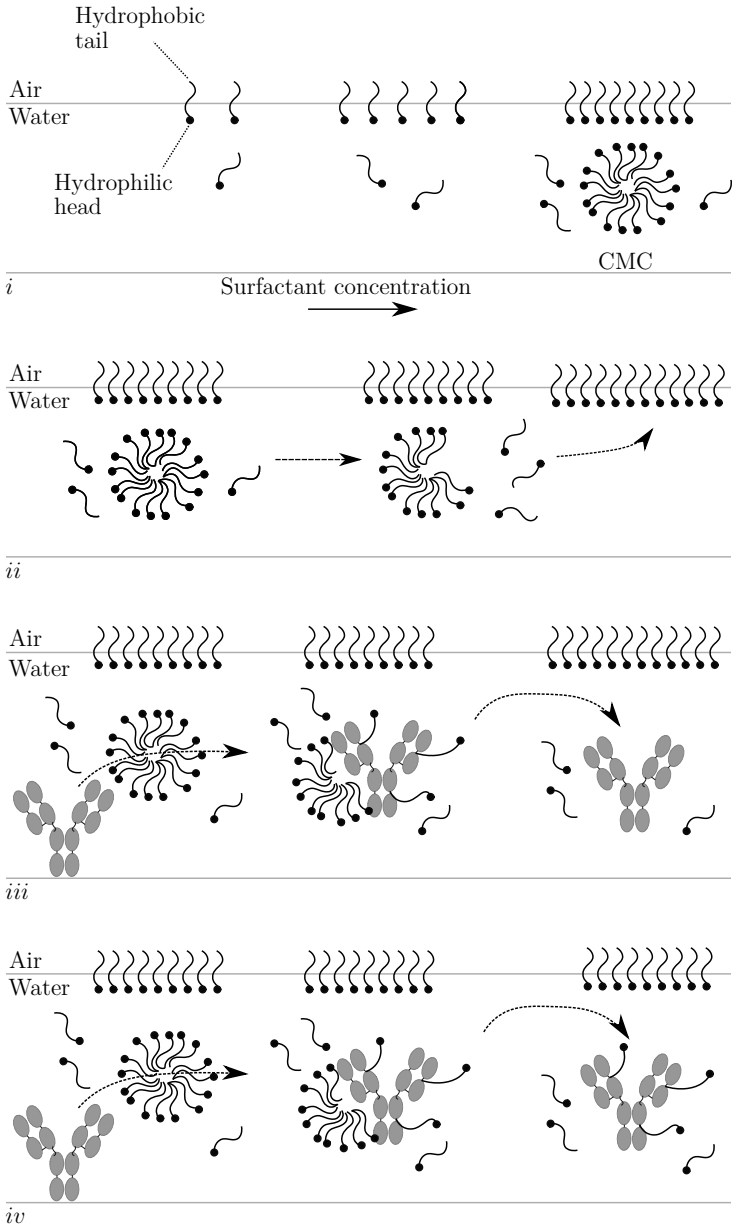

Figure 2.9: Schematic illustration of surfactant and surfactant-protein interactions in the presence of an air-water interface. Surfactants consist of hydrophobic and hydrophilic components, a hydrophobic tail and a hydrophilic head. The hydrophobic components drive an interaction with air-water interfaces as well as between the surfactant molecules themselves in solution, driving the assembly of micelles at concentrations above the critical micelle concentration, CMC (i). In the absence of protein (ii), surfactant monomers must dissociate and migrate through the liquid in order to adsorb. The presence of protein may facilitate aggregate disruption, leading either to an increased concentration of surfactant monomers thus enhancing adsorption (iii), or to the formation of stable, surfactant-protein complexes having little or no effect on surfactant adsorption rate (iv). Adapted from [6, 15].

Table 2.2: Example of surfactants used to research surfactant-protein interactions, adapted from [6].

Non-ionic surfactant investigated	Model protein	Interaction proposed
16-Doxyl stearic acid, Brij, PS20, PS40, PS80	rhGH, rhIFN-γ	N/A
PS20, Brij 35, Brij 78	α and β-lactoglobulin	N/A
C12E8	rhTF220, rhTF243	N/A
PS20 and PS80	Albutropin	Interaction leading to increase of free energy of unfolding
PS80	LDH	PS competes with protein at interface
PS20 and PS80	IgG and HSA	Negligible binding with IgG
PS20, PS40, PS80	LDH	Competitive displacement mechanism driven by surface pressure
Dodecyl dimethyl phosphine oxide	β-Casein	Competitive displacement at interface
PS20, PS40, PS80	LDH	Weak hydrophobic interaction
PS20 and PS80	BSA	Binding model for BSAsurfactant binding
PS20 and PS40	Lysozyme	Hydrophobicity driven preferential tween adsorption
PS80	Recombinant factor VIII	Competitive displacement at the interface
PS20 and PS40	Fibrinogen	Adsorption and packing phenomenon
PS80	BSA	Aggregation inhibition of partially or fully denatured monomer
P188, PS20, PS80	Recombinant factor VIII	Colloidal stabilisation and competitive interfacial adsorption
P188, PS20, PS80	Lysozyme, GCSF	Disruption of surfactant aggregates
PS80	HSA	Hydrophobic interactions
P188, PS20, PS80	Fc-fusion	Competitive adsorption but, poor displacement of protein
P188, PS80	Fc-fusion	Competitive adsorption
PS20, PS80	BSA	Hydrogen bonding, van der Waals, and hydrophobic interactions
PS20	IgG	PS20 above CMC protects the air-water interface from mAb adsorption [113]
PS20, P188	IgG	Competitive adsorption at interfaces [116]
P188	IgG	Competitive adsorption of mAb and P188 from solution [117]
PS20	IgG, lysozyme	PS20 adsorption on interface [118]

[52, 121], sucrose formulation showed enhanced aggregation under mechanical agitation. Authors suggested that the enhanced aggregation levels were due to the sucrose effect in increasing the free energy of unfolding of protein molecules in the bulk solution, but apparently decreased the protein's conformational stability at the air-water interface [52]. Additionally, the enhanced aggregation levels in the presence of sucrose indicated the formation of a strong interfacial gel formed at the air-water interface [121].

Some amino acids, including arginine, are added as excipients influencing mAb stability. It has been shown that arginine can increase protein solubility, protecting the molecule from photo-induced and thermal-induced aggregation alongside unfolding protection [122]. The stabilising effects of arginine as a formulation agent, have been investigated under flow condition experiments, where the aggregation has been suppressed from 86% with buffer formulations including histidine, acetate, succinate, and phosphate to 20% in arginine succinate formulation buffer [2].

2.6.3 Syringe lubrication

Syringe lubrication, as a part of the fill-finish process of biopharmaceutical production, aims to improve efficiency in the administration process. The use of prefilled syringes (PFS) as an alternative administration mean, can be used to provide accuracy and safety compared to traditional parenteral administration [123]. With the use of PFS increased accuracy and safety can be achieved as the dosing can be direct as well as reduced contamination risks [124]. A typical pre-filled syringe system consists of various interfaces including syringe needle, syringe barrel and plunger head. Silicone oil is used as a lubricant, to facilitate smooth movement of plungers within the barrel as well as on exterior surfaces of hypodermic needles to reduce the frictional drug and pain during the

administration process through the tissue [54]. However, silicone oil among other syringe components (adhesives, leachables from rubber stoppers and tip caps) has been evaluated and identified as a potential source of incompatibility for biologics, as reported in [125]. The interaction of biopharmaceuticals with silicone oil interfaces has been investigated in various studies, highlighting the formation of aggregates during agitation [54, 126, 127]. To overcome this phenomenon, other studies suggest alternative approaches, implying into the surface modification of PFS. Particularly, in the study conducted in [125] a novel cross-linked silicone coating was shown to improve the stability of the mAb samples compared to lubricated syringes, resulting in fewer silicone oil droplets sloughing off into the solution.

2.7 Hydrodynamic forces on protein aggregation

The term of 'shear flow' has been extensively used in literature, describing all the forces applied to a fluid. However, this term is usually defined with a generic meaning where its definition has multiple meanings as it is used by the authors in literature. Therefore, there is a need for differentiating the stress arising from mechanical shear with the stress causing damage to proteins arising from changes in protein's secondary structure through unfolding, or by disruption of the quaternary structure of a protein [128]. 'Shear' in the fluid mechanical sense can be determined to be caused by velocity gradients in moving liquids [128]. The term is also used to describe extensional flow events; therefore, this leads to the extensive use of the term shear rather than extensional flow, which is not clearly defined in literature. In this chapter, the development and effect of hydrodynamic flow will be described alongside studies focusing on monoclonal antibodies as well as on other proteins.

2.7.1 Development of hydrodynamic flow

The development of hydrodynamic flow can be found in studies in the literature by employing devices with geometric configurations to allow effects in fluid's velocity, allowing the flow phenomena of shear, extension and rotation to be developed. The direction of velocity streamlines for each flow configuration is shown in figure 2.10.

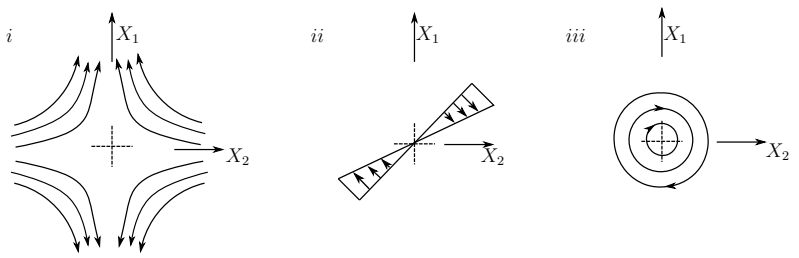

Figure 2.10: Streamline schematics of stagnation point flow fields. (i) Extensional flow, (ii) Shear flow, (iii) Rotational flow. Adapted from [16].

A range of different devices as summarised in table 2.3 have been used in the literature for generating hydrodynamic flow and investigating the aggregation propensity of various proteins.

Table 2.3: Studies of the shear stability of protein system using a variety of shear devices.

Device	Protein model	Result	Reference
Four roll mill	Lysozyme, BSA, Alcohol dehydrogenase	Aggregation	[129]
Capillary	Cytochrome c, BSA	no change, aggregation	[18]
Couette	insulin, von Willebrand factor	unfolding and aggregation, unfolding	[130]
Microfluidic cell	Von Willebrand factor	unfolding, aggregation	[131, 132]
Miniature reactor	Human growth hormone (hGH)	aggregation	[133]
Miniaturised cone and plate shear cell	Von Willebrand factor	Unfolding	[134]

In experimental studies, the shear flow can be generated by subjecting protein solutions under velocity gradients, which can be uniform or heterogeneous. Heterogeneous velocity fields can be generated by stirring or shaking [17]. However, the authors suggest that heterogeneous velocity gradients provided poorly controlled shear conditions. Protein studies found in literature have been conducted using capillary and rotational devices, which are the two main device categories for experimental analysis of proteins. Such devices are ideal for studying the protein aggregation since they can be used to create velocity gradients which can provide well-controlled stress conditions. A capillary flow within a capillary/microfluidic device (figure 2.11) is where a fluid is forced through a channel by applying a pressure difference between the inlet and outlet of the channel. Rotational flow devices that are commonly used for shear controlled conditions on proteins correspond to cone and plate, parallel plate and concentric cylinder viscometers as shown in figure 2.12.

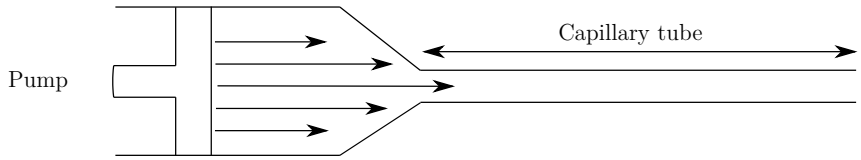

Figure 2.11: Schematic of a simple extrusion glass capillary viscometer. The arrows show the direction of flow. Adapted from [17].

Four roll mill apparatus

Four roll apparatus has been used previously as a means for generating shear flow by generating different flow defined configurations to investigate protein aggregation. The apparatus consists of four cylindrical rollers which can rotate either in opposing or parallel pairs as shown in figure 2.13. The particular configuration allows the development of a two-dimensional laminar flow, which can be used to create extensional flow regions to "stretch" protein molecules. Particularly, in [129] protein aggregation has been investigated using the four mill apparatus using experimental and computational methods. Using the particular device and computational fluid dynamics simulations, the authors predicted

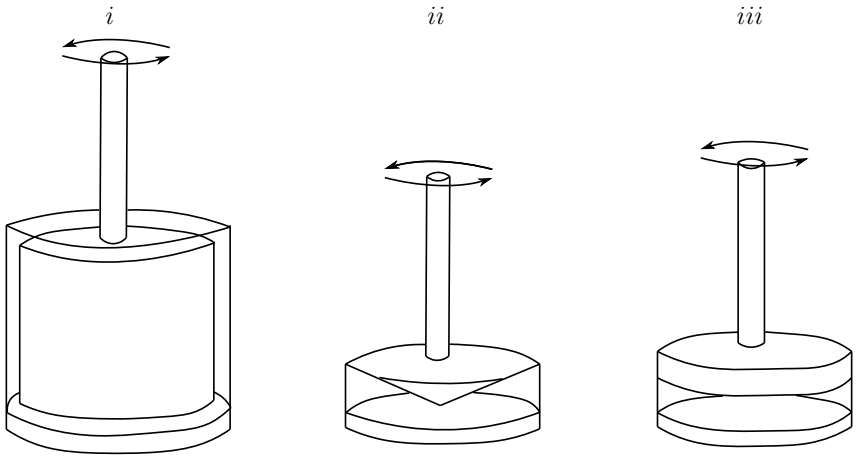

Figure 2.12: Common rotational flow devices: Concentric cylinder (i), cone and plate rheometers (ii), parallel plate (iii). Adapted from [17].

the generation of elongation and shear stress with increasing the roller speed and also observing the maximum shear arising at the rotating roller walls. It was found that with an increase in rotational speed, the light absorbance of the protein solution increases, indicating the formation of higher amount of aggregates and larger particles [129]. Using the four roll mill, different velocity profiles can be generated for elongation, hybrid and rotational flow configuration. The development of elongation/extensional flow was found to have a higher effect on the formation of larger aggregate molecules within the device compared to the rest of the flow profiles generated.

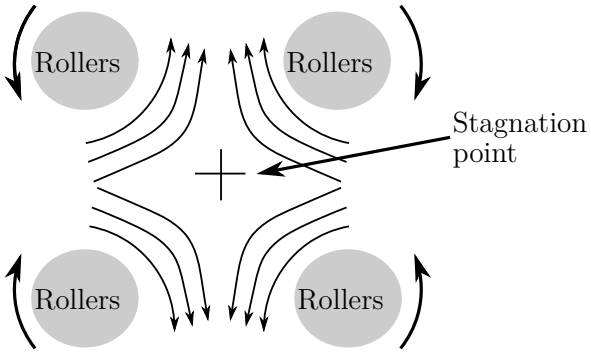

Figure 2.13: Schematic illustration of the four-roll mill flow configuration for fluidic applications. Adapted from [16].

Cross slot

Cross slot geometry, as shown schematically in figure 2.14, is a method which is used extensively in literature for generating extensional flow for various applications. A cross slot geometry involves multiple channels which intersect at the centre of the configuration. A stagnation point at the centre of the geometry can be developed, where a pure elongation flow is created under equal flow rates [16]. Cell damage to mammalian cells was investigated using a cross slot geometry which was implemented in a microfluidic device, to characterise mechanical cell damage by an extensional stress field [135].

The implementation of the particular configuration has been previously used for stretching DNA molecules using planar extensional flow [136]. The stagnation point, which is created using the particular configuration, is used to trap and elongate the molecule along the extensional axis. The interest in trapping and controlling particles using cross slot geometry can be used as method for developing aggregates where their aggregation performance can be correlated with the variation of micro particles sizes and shapes. This can be useful for the development of new biological assemblies [16].

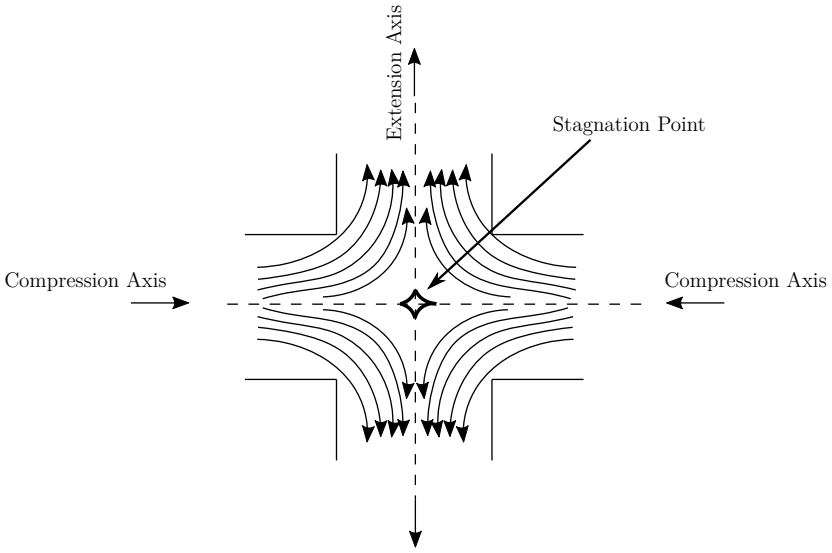

Figure 2.14: Microfluidic cross slot geometry setup, adapted from [16].

Opposed Jets

This method, as shown in figure 2.15, is used to create a stagnation point by the configuration of the device in which two co-axial, counter flowing streams impinge against each other at relatively high relative velocities [137]. This apparatus geometry can be used to generate compressional and extensional flows. The particular arrangement of flow can be useful and it can be considered to be advantageous in terms of its ability to generate relatively large velocity gradients. Its implementation in literature has been done for studies concerning the stability of diffusion flames, producing a flame at the junction between them [16]. Additionally, the application of the generated flow has been used in the production of very thin solid films, studying the purely homogeneous kinetics of endothermic reactions. The application of the stagnation point generated by either extensional or compressional flow has been found to be used in studying polythene birefringence in xylene solution as a function of temperature. This setup has also been expanded upon doing viscosity measurements showing the dependence of extensional viscosity to strain rate [138] and polymer solution [139].

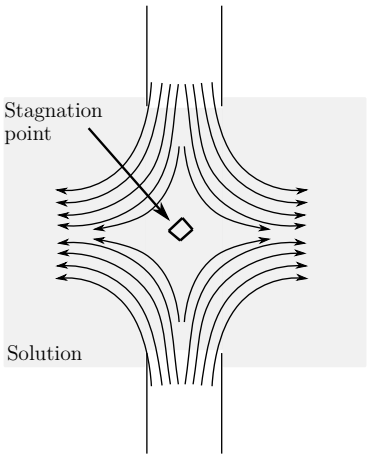

Figure 2.15: Schematic illustration of an opposed-jets apparatus in "push mode", generating an uniaxial compressional flow along the stagnation point axis. Adapted from [16].

2.7.2 Shear and extensional flow effects on aggregation

Extensional and shear flow describe the common flow fields found in "shear" studies. The extensional flow is also called elongation flow or stretching flow, and can be characterised by a linear velocity gradient along the direction of flow (figure 2.16a). Simple shear flow can be characterised by a velocity gradient which is perpendicular to the direction of flow. Shear flow can de determined as the velocity gradient perpendicular to the direction of flow, inducing rotational events (figure 2.16b).

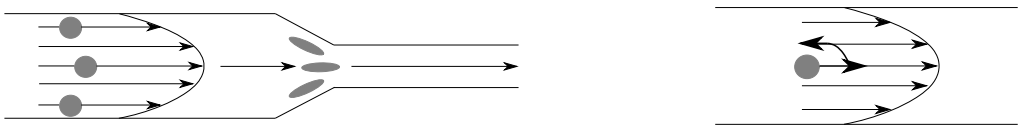

(a) Extensional Flow **(b)** Shear Flow

Figure 2.16: Representation of extensional fow (2.16a) indicating protein stretching at the point of the contraction and shear flow indicating protein molecule rotation (2.16b).

The fluid flow pattern of shear flow was examined in the study conducted in [129] using computational fluid dynamics in a four roll apparatus under steady state conditions. Using the specific four-roll mill device, different well-defined flow configurations (shear, elongation and hybrid) have been developed, investigating their effects on the aggregation of lysozyme. From the particular work, authors highlighted the significant role of elongation flow configuration which is defined by the roller direction (figure 2.13) among shear and hybrid, for partial protein unfolding of lysozyme, which is indicated by the highest content of lysozyme aggregates formed.

There are various experimental studies concerning the flow effects on protein structures using shear flow. The magnitude and type of hydrodynamic flow is debated in the literature, with multiple studies investigating the flow induced aggregation of various

proteins. Authors have identified several hydrodynamic magnitude values, which are typically termed as shear rate and strain rate, and they have identified the flow magnitudes in which they can induce conformational changes to protein structure leading to protein aggregation.

Jaspe and Hagen [18], investigated the protein aggregation of a small globular protein, cytochrome C, under shear of up to 2 $\times 10^5$ s^{-1} where they observed no changes in protein conformation. The authors developed a theoretical model suggesting that only in high levels of shear in the order of 10^7 s^{-1} the configuration of small globular proteins can be destabilised. In the same study, the authors have conducted the theoretical model by which the protein denaturation under extensional flow is proposed by the approximation of protein molecules as a necklace of N spherical beads, as shown schematically in figure 2.17. Under elongational flow, the protein denaturation is encountered by the division into two roughly spherical clusters of radius a, with the clusters separated by a linker of n beads. The resulting difference in the viscous force on the two clusters creates a tension in the linker which is shown to be related with the viscosity of the solution, which is proportional to the tension applied on the linker as given by the equation 2.1. The viscosity parameter is shown to be correlated with the unfolding force as a part of the unfolding pathway.

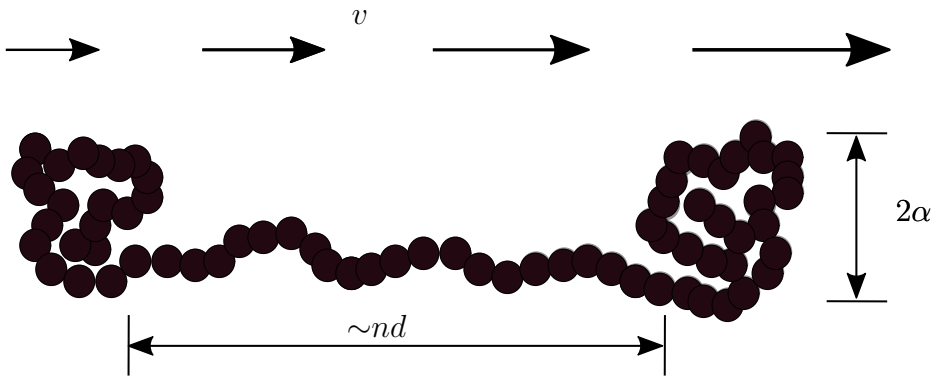

Figure 2.17: Shear denaturation model of a protein by an elongational flow, where a protein of N residues (small spheres, with centre to centre separation d) divides into two clusters of residues, separated by a linker of $\sim n$ residues and length $\sim nd$. The heterogeneity of the velocity field v leads to a tension in the linker, as shown from equation 2.1. Adapted from [18].

$$T \approx 6\pi\eta\alpha(v_2 - v_1)/2 = 3\pi\eta\alpha\dot{\gamma}nd \tag{2.1}$$

where:

$T =$ tension resulted from viscous force difference

$\eta =$ dynamic viscosity of the fluid

$\alpha =$ radius of spherical cluster

$(v_2 - v_1) =$ difference in flow velocities at the two clusters

$d =$ centre to centre distance between consecutive beads

$\dot{\gamma} =$ elongational flow

$n =$ number of linker beads

Similar observation has been made in the study carried out by Szymczak and Cieplak [140], where the conformational dynamics of a single protein molecule (considering two proteins: ubiquitin and integrin) is studied using Brownian dynamics simulations. Partially and fully unfolding of proteins happen at shear rates in the order of 10^7 s^{-1} in agreement with the proposed order of shear rates suggested by the authors in [18]. In the study conducted by Duerkop et al. [66], a computational method has been developed, to predict the maximum shear rate under which the aggregation of HSA (human serum albumin) was investigated. Even higher shear rate has been reported by the particular study, calculating a maximum and average shear rate values in the orders of 10^8 s^{-1} and 1.2 $\times 10^6$ s^{-1} respectively, where the authors support that the aggregation was caused by the increased surface area due to cavitation-mediated bubble growth, and not mechanical stress.

On the other hand, lower order of magnitudes of shear rates, in the order of $\sim 10^1$ and $\sim 10^2$ s^{-1}, have been linked with shear-induced structural changes of lysozyme, using a flow cell, as investigated by Ashton et al. [141]. These low range shear rates, are also reported by Bekard and Dunstan [130], where structural disruption of bovine insulin protein was detected for shear rates in the order of $\sim 10^2$ (200-600 s^{-1}). In other study, conducted by Lippok et al. [134], shear unfolding of the recombinant fusion protein rVWF-eGFP is defined by experimental and simulation studies, which is indicated at a shear rate of 10^3 ($\sim$5,000 s^{-1}). Protein aggregation of a monoclonal antibody as investigated by Kalonia et al. [59], it was shown that in extremely high shear rate values in the order of 10^4 ($\sim$25,000 s^{-1}) there was severe sub-visible particle formation indicating protein aggregation.

In the study conducted by Chantre et al. [142], it is found that extensional and shear rates, which are distinguished as terms by the authors, generated in rotary jet spinning device in the order of 1.2 $\times 10^5$ s^{-1} and 3 $\times 10^5$ s^{-1} respectively, are found to be important in producing nanofibre scaffolds. The differentiation of the two flow configurations, has been also acknowledged in the study conducted by Grigolato and Arosio [24], where the authors indicated that both flow configurations are important in promoting protein aggregation within a range of shear and elongational (strain) rates up to 2.6 $\times 10^5$ s^{-1} and 5 $\times 10^4$ s^{-1} respectively. From these studies, it can be observed that the extensional flow has gained an increased interest from authors in literature who are starting to address both or distinguish the types of shear and extensional flow.

As an overall observation, the magnitude of hydrodynamic flow in studies focusing on the flow induced aggregation, is reported to be induced within a broad range with several

orders of magnitude, with shear rate values reported from 10^1 up to 10^8 s^{-1}. The general tendency from literature studies is to report both shear and extensional flows with the term shear rate, whereas the term strain or elongational rate describes the extensional flow configuration. The extensive use of shear rate as a generic term, to describe the magnitude of hydrodynamic flow, corresponds to disorienting the clear effects of shear and extensional flow. Therefore, this also contributes to a broader range of hydrodynamic magnitude values, which are reported in inducing protein aggregation.

Additional to the generic use of the term, the broad range of hydrodynamic flow magnitudes, corresponds to the various types of proteins that have been studied, with different molecular weights and formulation conditions. Specifically, cytochrome c protein which was studied as a model protein by Jaspe and Hagen [18] is a protein with a small molecular weight (∼12 kDa) compared to an intermediate molecular weight of HSA (∼66 kDa), which is also compared to molecules with even higher molecular weights of that of antibodies (∼150 kDa) and fibronectin (Fn) (∼440 kDa). Alongside the differentiation of the model proteins, the formulation conditions in which the experimental studies have been conducted is another parameter which can contribute to the variation of the hydrodynamic flow magnitudes responsible for unfolding. For example, in the study investigating the aggregation of lysozyme by Ashton et al. [141], the authors have highlighted the different aggregation profiles of the molecules when lysozyme was studied in water and glycerol formulations. Several buffer formulations have also been used in the other studies, including sodium phosphate and sodium chloride [66], histidine [59], sodium citrate dihydrate [24], hydrochloric acid [130] (among others), with several pH values which is also a reported parameter which drives protein aggregation [13].

The several studies have also employed different equipment configurations and materials (glass, aluminium, stainless steel) in which exposed the molecules to several magnitudes of hydrodynamic flow and interfaces (solid-liquid, air-liquid) present. Moreover, the time in which the samples were exposed to flow conditions in these studies is also a significant parameter that defines the flow induced aggregation observed. The specific exposure times to shear, and extensional flow configurations (for a single exposure/pass number), vary between studies, as well as the duration of the total experiment including multiple passes/sample recirculation. Single exposure times have been reported to 0.5 s for each sample recirculation, as mentioned in [66], corresponding to a total time of 19.5 s for 39 sample circulations. In the study conducted in [18], exposure times to samples within two different sizes of capillary tubing, have been reported as residence times of 5.4 $\times 10^{-3}$ s and 4.2 $\times 10^{-3}$ s. For a range of syringe setups as investigated in [24], the exposure times to hydrodynamic flow have been reported to 0.71 s, 3.55 s and 4 $\times 10^{-3}$ s at the maximum flow rate, with a total experimental time of 3, 6 and 12 hours. On the other hand, the single exposure time for samples exposed to multiple passes has not been reported in [59], whereas the total number of passes investigated has been reported (0-20 passage number),

which makes the time parameter challenging for comparison between the studies.

Studies in microfluidics

Microfluidic devices can be an extremely useful tool for conducting experimental studies within very small scales. Therefore, their use can be helpful in protein-based studies. Among the advantages of microfluidics is the significantly reduced time and cost for conducting experimental studies, where the amounts of sample and reagents needed are also reduced. Consequently, there is an extensive interest in their implementation in studies in a range of areas such as chemical technology and biotechnology. In the literature, they have been widely used in studies considering the tumbling dynamics of DNA and platelet aggregation. Microfluidic devices have been also used in the study conducted in [143] for examining the parameter necessary for assembly of spider silk proteins. The application of controlled mechanical stress has been also investigated using microfluidic platforms, inducing the fibre formation from phase separated liquid condensates [144]. Moreover, the inducing of aggregation in microfluidic devices has been also studied (among other studies) for the self-assembly of insulin monomers [145], analysing of Alzheimer's β amyloid aggregation [146] and for observing the conversion of amyloid growth to fibrillar nanostructures [147]. However, in the latter three studies, the induction of aggregation has been investigated without the application of extensional or shear flow. On the other hand, the referred studies [143, 144, 148, 149] investigate the study of proteins in microfluidic devices under shear and extensional flow, which is the main focus of the current review of literature.

2.7.3 Other applications of hydrodynamic flow on proteins

The hydrodynamic flow has also been studied in literature including the stretch and fragmentation of DNA molecules, investigating platelet aggregation as well it can be found in nature during spider silk development. In the process of blood clotting, the unfolding event of a force sensitive protein in the human body, von Willebrand Factor (vWF) is crucial as it is found to cause bleeding disorder (von Willebrand syndrome). The overall structure of vWF was shown to unfold under different kinds of stresses. The encounter of hydrodynamic flow can be developed in vessel stenosis as bleeding occurs as shown in figure 2.18, inducing extensional flow events. The significance of extensional flow event into platelet aggregation was investigated by mimicking the vessel stenosis in constricted flow geometries adapted in microfluidic systems. As it is shown in [132], platelet aggregation occurred immediately downstream of the stenosis and induced the conformation unfolding of vWF under a strain and elongational stress of blood flow, reaching a peak strain rate at 28,000 s^{-1} as it was characterised computationally. The effect of stenosis was also correlated with the application of rapid and extreme phases of shear acceleration, with peak strain rates approaching 1 $\times 10^6$ s^{-1} leading to platelet aggregation [150]. The effect

of stenosis level inducting extensional flow events as characterised computationally, it was shown to play a significant role in the shear rate acceleration towards shear flow development inducing the increase in shear rate 34.6 and 41.0-fold respectively as stenosis level was increased from 30 to 95% [151].

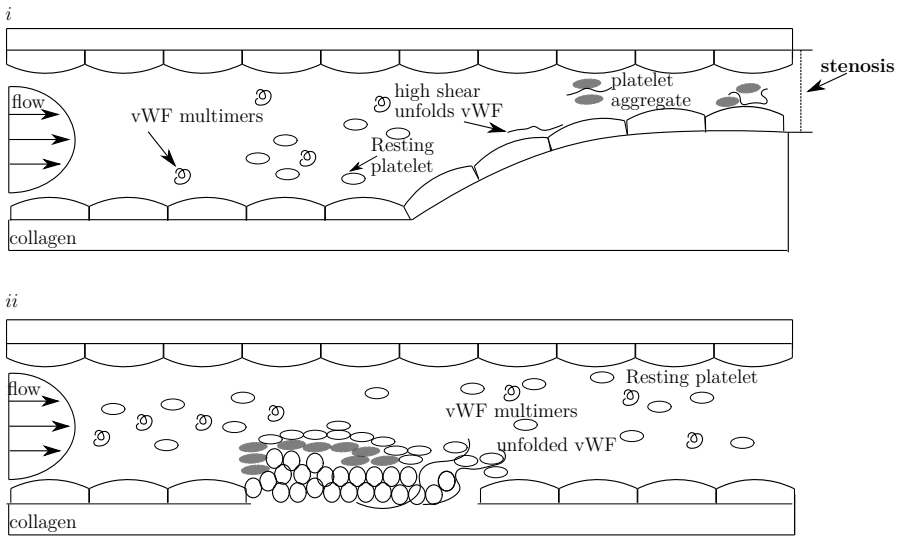

Figure 2.18: Platelet interaction during clot formation. Hydrodynamic forces and the mechanical microenvironment affect each of these platelet-ligand interactions. vWF regulation and vWF-dependent platelet aggregate formation at high shear rates. (i): Under pathological high shear stress, at the site of stenosis, vWF multimers are unfolded by hydrodynamic forces to switch to an extended conformation, thus causing platelets to bind and form aggregate. (ii): Clot formation at the vessel injury site. vWF multimers adhere to exposed collagen and adapt an unfolded conformation due to wall shear stress. Adapted from [19].

The application of extensional flow can be found in nature under the production of silk by spiders. The extreme toughness of spider silk given with its biological properties of degradability and biocompatibility, make it a desired material for technical and medical applications [152]. The spider silk is produced by a process-structure-function loop as shown in figure 2.19, where the rapid reeling during silk formation induce the development of mechanical forces promoting tiny crystalline domains, providing greater tensile strength [20]. The orientation and dispersion of the β-sheet nanocrystal, embedded within its domain, can control the silk strength over extensibility [20].

Due to the properties of natural silk, the mimicking of silk production is studied in literature by investigating the variables incorporated into the process. During natural spinning, parameters such as chemical changes, pH and mechanical stress have been identified to be important as a part of the natural process. With flow being identified as the primary energetic input for silk fibre formation [153], the effect of flow into silk fibre formation has been extensively studied in literature. With the application of extensional flow in a microfluidic geometry with gradual constricted flow path, silk suspensions have been highly orientated along the fibre axis [154]. The authors are suggesting that during the flow

process, molecules have been transformed to an oriented conformation of β-sheet structure. Moreover, the suspension alignment was shown to be improved under increasing fluidic flow. Constricted flow geometries allowing the mechanical elongation in the production of artificial spider silk has been also applied in [155] using a straining flow spinning method allowing the incorporation of other processing conditions.

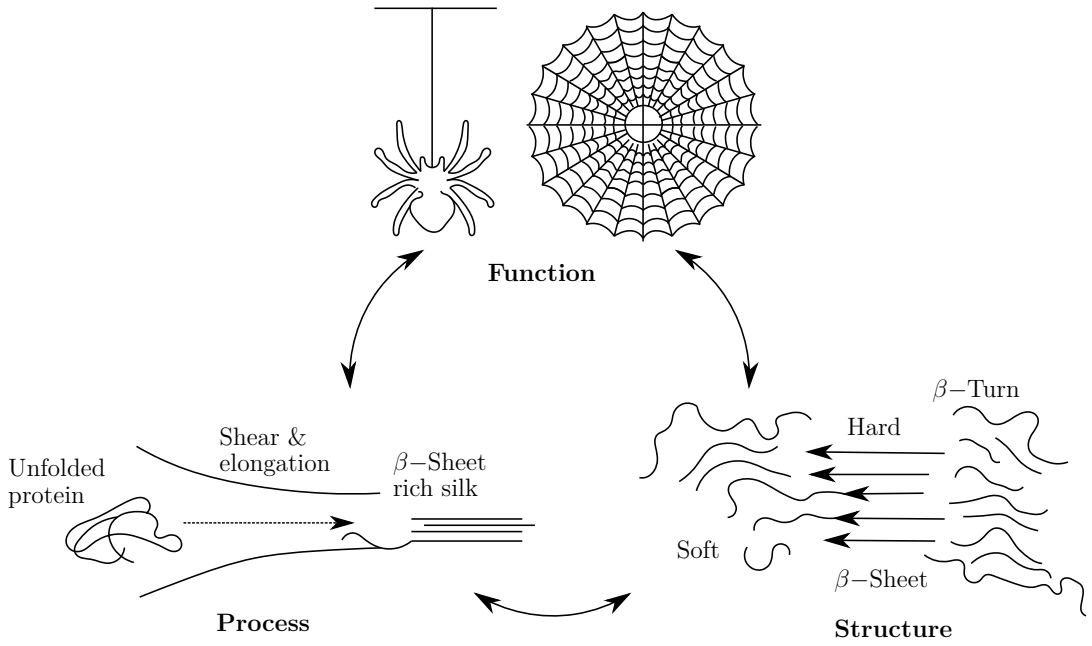

Figure 2.19: Process-structure-function. The silk production process of spiders involves the transformation of unfolded proteins into ordered, beta-sheet nanocrystals through shear and elongation. Adapted from [20].

The application of extensional flow can be implemented into studies involving the manipulation of DNA involving DNA extension for DNA mapping and fragmentation for gene sequencing [21]. DNA fragmentation is a critical step in part of gene analysis and can be determined to be a useful tool for DNA microarray analysis. Hydrodynamic shearing is defined to be among the most robust methods on fragmentation for the development of small fragment length and low sheared length variation [149]. A microfluidic device was developed as part of the study carried out in [149] investigating the DNA fragmentation on a LOC (lab on chip) microfluidic system. The microfluidic channel consisting of constricted regions was used to induce long DNA molecules. The DNA fragmentation can be achieved by the extension of the DNA molecules through the channels' constriction as indicated in figure 2.20, under the extensional and shear flow developed by the contraction part. Other studies implementing microfluidic platforms have identified that parameters including the magnitude and the distribution of the extension rate were crucial for the DNA fragmentation, with the extension rate at the microscale being the dominant factor [21]. Similar observation was made in the study conducted in [149] where shorter DNA fragments have been achieved at increased flow rates correlated with increased hydrodynamic flow fields, alongside the increase in exposure time to hydrodynamic flow fields. From this study, it

has been concluded that the minimum fragmented DNA can be achieved using either long constriction channels or recirculate DNA particles through shorter constrictions but for multiple times. As a more efficient method, the authors suggest to use smaller constrictions for multiple times since the pressure requirements are lower compared to using longer constrictions. This is suggested because the pressure requirement which will be responsible for damaging the DNA is relatively low for shorter constrictions.

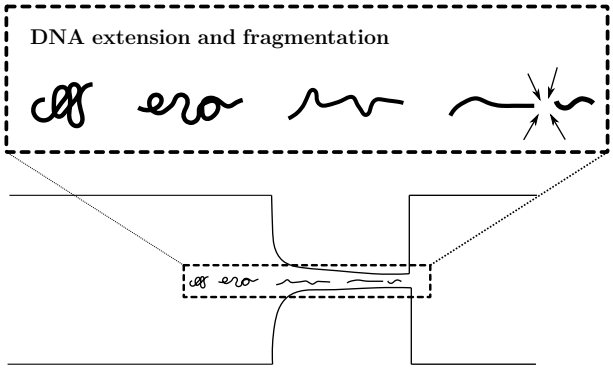

Figure 2.20: DNA extension and fragmentation induced by fluid force in a micro-funnel. The flow heads from left to right. Adapted from [21].

The effect of constriction for stretching DNA molecules has been also conducted in [156]. In this study, the shape of constriction was altered for four different contraction shapes by changing the time where the DNA will experience shear and extensional flow. Particularly, the influence of the strain rate profile on a DNA was determined by the shapes of the funnel. The highest strain rate applied to protein has been achieved for the increasing strain rate funnel, yielding a highly extended conformation on the DNA. The increasing strain rate funnel corresponds to the shape among the four used in the study, having the longest strain rate region between the low and high shear region (before and after the constriction). It is also found that the efficiency of stretching DNA has been improved by increasing the strain rate [156]. Therefore, this finding suggests that the elongation flow rather than shear flow is responsible for the conformation changes to the DNA, which is then stretched and elongated through the sudden contraction. This is also shown in [157] where shear flow rather of extensional flow is applied using rotational rheometers, where authors could not observe severe DNA fragmentation under the application of this flow configuration.

2.8 Effect of surface in flow induced aggregation

The interaction of proteins with interfaces is extensively studied in the literature, with the range of techniques employed to study antibody interaction on surfaces to be summarised on table 2.4. Among this set of techniques, QCMD and AFM will be briefly described as they have been employed in this work, with their further description as applied experimentally to be followed and can be found in subsections 5.3.1 and 5.3.2 respectively. The effect of

interfaces on protein aggregation under flow conditions, will be also presented in subsection 2.8.3 by literature review of studies focusing on the aggregation of antibody proteins.

Table 2.4: Literature overview of commonly used methods in surface analysis for investigating antibody, adapted from [7].

Technique	Input	Output	Information	Reference
XPS	Monochromatic x-rays	Photoelectrons	Elemental and chemical	[158–162]
SE	Elliptically polarised light	Change in light phase or intensity	Thickness, refractive index, surface roughness	[163–168]
DPI	Laser light	Evanescent wave change	Mass, film thickness, refractive index, density	[169–171]
SPR	Monochromatic multiangle laser light	Change in reflected and absorbed light	Refractive index, film thickness	[172–175]
NR	Neutron beam	Change in reflection of neutron beam	Refractive index, film thickness, surface roughness	[176–179]
AFM	Feedback driven cantilevered tip	z-height in 2D and tip/surface force	Surface roughness, phase information, imaging	[175, 180]
QCMD	Resonance frequency of microbalance	Change in frequency and amplitude	Mass of adsorption, bioaffinity	[181, 182]
ToF-SIMS	Ionised metal clusters, primary-ions	Ionised sample fragments, secondary-ions	Semi-quantitative elemental, chemical and molecular	[183–190]
XRR	X-rays	Intensity of reflected X-rays	Growth behavior of thin films (thickness, roughness, density)	[114, 191]

2.8.1 Quartz Crystal Microbalance with Dissipation, QCMD

For investigating protein interactions with surfaces, QCMD, which is a nanogram sensitive technique, is a well established for the detection of small molecules to micro-sized objects, including bacteria attached to surfaces [192]. It is also used to investigate protein adsorption, lipids and membranes, cells, DNA and carbohydrates [192]. The working principle of this method is the utilisation of acoustic waves generated by the oscillation of single crystal quartz, which is related to quartz's inherent property of piezoelectricity [193]. Piezoelectricity, as the name suggests, is the electricity generated by the pressure to measure adsorbed mass. The application of alternating electric fields on the quartz induces an alternating contraction and expansion to the quartz [193]. QCM quartz crystal consists of the quartz which is sandwiched between two metal electrodes as indicated schematically in figure 2.21a. The detection of mass information can be determined by the monitor of frequency, (Δf) of the crystal, which is decreased as mass is added to the oscillating sensor [192]. Viscoelastic properties of the adsorbed layer can be extracted by the monitor of the dissipation shifts, (ΔD) during the binding events, where the dissipation parameter is correlated with the energy loss in the system [193]. Comparison studies, alongside a commonly used technique in the field, surface plasmon resonance (SPR), indicated the sensitivity of both techniques measuring peptide-antibody binding capacity [194]. However, both techniques cannot be directly compared as they are based on different operating principles [194]. SPR measures the change in refractive index, which is proportional to the concentration of the interacting molecules during their binding and dissociation with the surface [194]. QCMD protein adsorption studies investigating the effect of material surfaces [195], identifying adsorption types such as reversible or irreversible adsorption [196], effect of increased protein concentrations [59] as well as surfactant effects on surface

and proteins [197], are some of the application areas of the technique around protein adsorption studies.

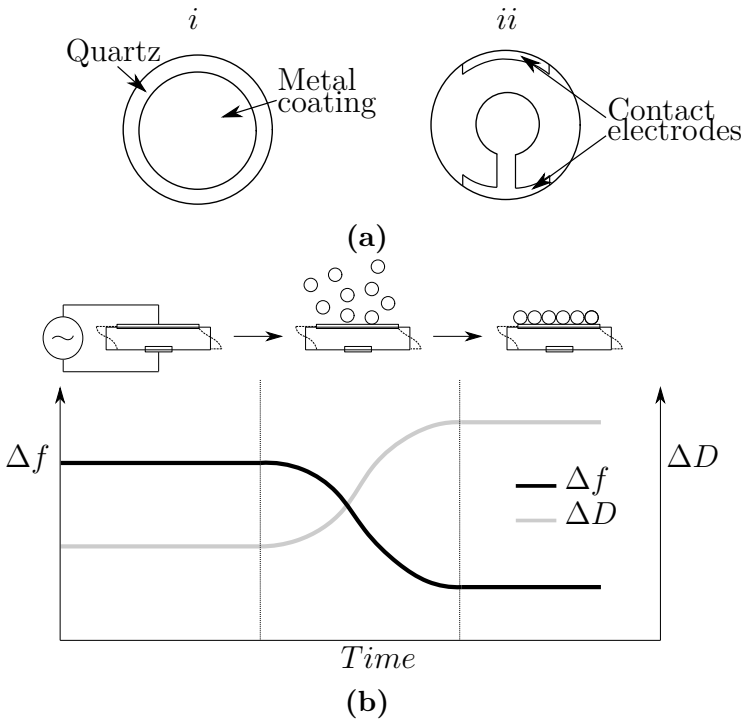

Figure 2.21: QCMD experimental components along with the raw data during the experiment. 2.21a: Schematic illustration of quartz crystal with electrodes, top view (i) and bottom view (ii). 6.26: Representation of raw experimental data during the conduction of the experiment. Initially stable baselines of Δf and ΔD are detected on a bare surface, as molecules are introduced onto the surface the frequency decreases and dissipation increases indicating the mass uptake and energy loss and the frequency and dissipation responses are then stabilised when the surface uptake has been completed. Adapted from Biolin Scientific (The working principles of QCM and QCM-D technology).

2.8.2 Atomic Force Microscopy, AFM

The topographical analysis of samples across a surface can be determined using, AFM which performs surface scanning using a nanoscale tip as shown in figure 2.22. The flexibility of the technique, to operate in liquid environments and at ambient temperature, makes the technique a versatile tool with applications analysing biomolecules and cells at (sub-)nanometre resolution [22]. Combined with other techniques, such as infrared spectroscopy (IR), was also used to provide physical along chemical composition information of samples [144].

The characterisation of solid substrates is commonly determined using contact mode AFM (figure 2.22i), however its application on biological sensitive systems, must be careful by adjusting the force applied to the tip scanning the surface. This direct contact with the surface might impose surface damages and, referring to biological systems such as proteins, that could cause reversible or even irreversible deformations [45]. Particularly, as reviewed

in [198], forces within the range of ∼15-300 pN were found to cause the unfolding of a range of proteins. To minimise structure effects on samples during scanning, the tapping mode AFM can be used by the cantilever oscillation as shown in figure 2.22ii, close to the resonance, with the tip touching at the very end of its downward movement, also minimising friction contributions [45]. The adsorbed orientation of proteins on surface is well studied by their immobilisation on surface, as shown in various studies in literature using antibodies as model proteins [175, 199].

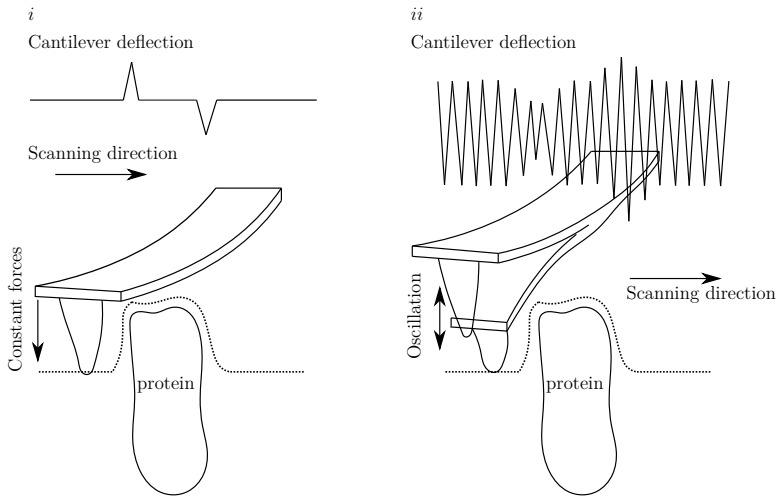

Figure 2.22: Schematic illustration of the basic principles of contact (i) and dynamic (tapping) (ii) AFM imaging modes. In contact mode, the cantilever deflection is kept constant (constant force) by adjusting the relative height between tip and sample. A topographic height change alters the cantilever deflection. The dynamic mode oscillates the cantilever close to or at resonance frequency. Adapted from [22].

2.8.3 Presence of interfaces

The structural perturbations of proteins along their interactions with the presence of an interface is suggested to be consisted of a cascade of microscopic molecular events, as shown schematically on figure 2.23a. The protein adsorption on the surface can induce possible effects on the molecular conformation of proteins, promoting nucleation and growth of aggregates and their eventual release from the surface to the bulk [23], (figure 2.23b). The incorporation of hydrodynamic flow can trigger the aggregation by enhancing the mass transport processes, as shown in figure 2.23c, which are related to the detachment and renewal of surface-adsorbed protein films [23].

The enhancement of protein aggregation has also been correlated with the interaction of proteins with interfaces under the simultaneous exposure of molecules to hydrodynamic flow/mechanical stress. Mass transport phenomena relating to the detachment and renewal of surfaces adsorbed protein films can be greatly enhanced under the interaction of hydrodynamic flow [23]. In the study conducted by Zhou et al. [200], the hydrodynamic mixing it was shown to highly promote amyloid aggregation by the formation of amyloid

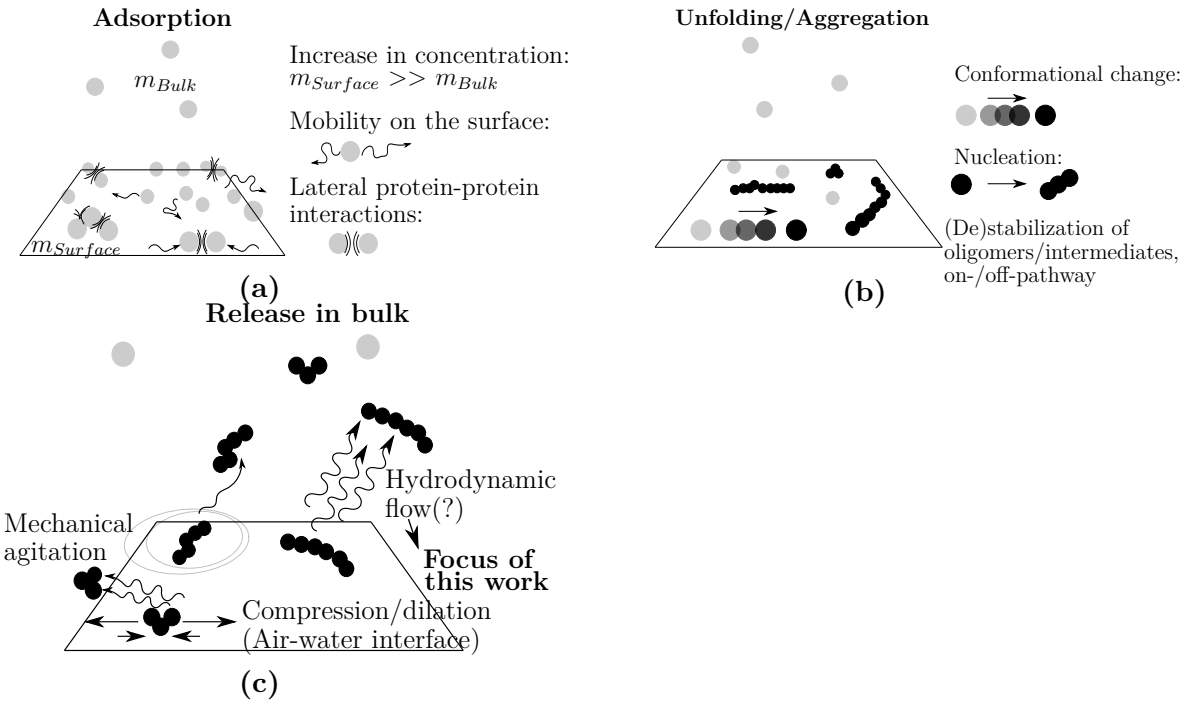

Figure 2.23: Schematic illustration of the set of microscopic molecular events underlying surface-catalysed protein aggregation. 2.23a: the process involves protein adsorption on surface, 2.23b: the subsequent possible change in their molecular conformation inducing unfolding/aggregation, the nucleation and growth of aggregates and 2.23c: the eventual release of the species from the surface to the bulk. The main focus of this work is the synergistic effects of hydrodynamic flow and interfaces on protein aggregation. The major challenge in protein aggregation studies is unpicking the exact molecular mechanisms involved, including the potential presence of interfaces and mechanical agitation or hydrodynamic flow. Adapted from [23].

fibrils both in the presence and absence of an air-water interface, where in the presence of a moving airwater interface, a further increase in the rate of primary nucleation was observed. Similar observation was made in other studies by Zhou et al. [201], Adam et al. [202], Maa and Hsu [203], supporting the enhancement of aggregation under increased shear flows in the presence of air-water interface, triggering the aggregation of α-synuclein, human insulin and recombinant human growth hormone (rhGH) respectively.

Apart from the presence of air-water interface, the effect of interfaces in the form of nanoparticles was also investigated under the simultaneous interaction of hydrodynamic flow, where it was shown that surfaces and mechanical agitation have a combined effect on the aggregation of human insulin, as shown by Grigolato et al. [69]. On the contrary, in the study conducted by Hoehne et al. [204], the authors showed the adsorption of monoclonal antibodies in the presence of glass nanoparticles suspended in the formulation buffers; however, the authors suggest that the adsorption to the nanoparticles had no destabilisation effects to the native structure of the antibodies. This observation can be explained by the type of shear flow configuration the authors used to conduct the experiments, which was a gentle mixing by end-over-end rotation. The enhancement of aggregation in the presence of stainless-steel microparticles was investigated by Bee et al. [205] showing the mAb degradation due to their adsorption with the stainless-steel particle, in the absence of any mechanical stress.

The effects of solid interface on the aggregation propensity of antibodies have been also investigated in literature corresponding to the interaction of molecules with solid interfaces, such as equipment and container surfaces. In the study conducted by Movafaghi et al. [206], the effect of containers surfaces under a variation of mechanical stress flow conditions was investigated. The particle concentration was shown to be enhanced among the most hydrophobic surface, with PEG-treated surface showing the suppression of particle formation. The authors suggest the particular surface as desirable; however, it should be noted that in the particular study an air water interface was also present as the solutions were stored in vials, inducing bubble formation leading to cavitation during mechanical stress. Therefore, for a more clear understanding of the contributing effect of each surface, the parameter space involved must be carefully controlled or limited.

The effect of aluminium and ceramic surfaces within pumps have been investigated by Defante et al. [45] and shown to have distinct effects on particle concentration. Authors have identified the ceramic piston surface as efficient in suppressing the particle formation. Stainless-steel effect on particle formation was also observed in the study conducted by Kalonia et al. [59] where the authors observed substantial amount of particle formation from stainless-steel surface than alumina with the formation to be pronounced under the application of shear stress within a flow cell observing the synergistic effects of flow and surface. To suppress the effect of stainless-steel surface, modification of the surface is

investigated by Chang and Hsiao [207], using a polycaprolactone coating, where the coating was shown to effectively suppress BSA adsorption compared to bare stainless-steel surface; however, this study does not incorporate the introduction of shear flows, henceforth the protective effect of this surface might also be depended on along its interaction with flow. As reviewed in Grigolato and Arosio [24], the contribution effects of pure shear flow has been investigated with its effect on a range of protein molecules with the authors indicating that the surface parameter alongside flow incorporation have effect on the aggregation as shown in figure 2.24. As the focus of the current work, is the aggregation of biopharmaceutical proteins, table 2.5, summarises a selection of studies investigating the aggregation of therapeutic proteins (mAbs) during their interaction with flow and interfaces.

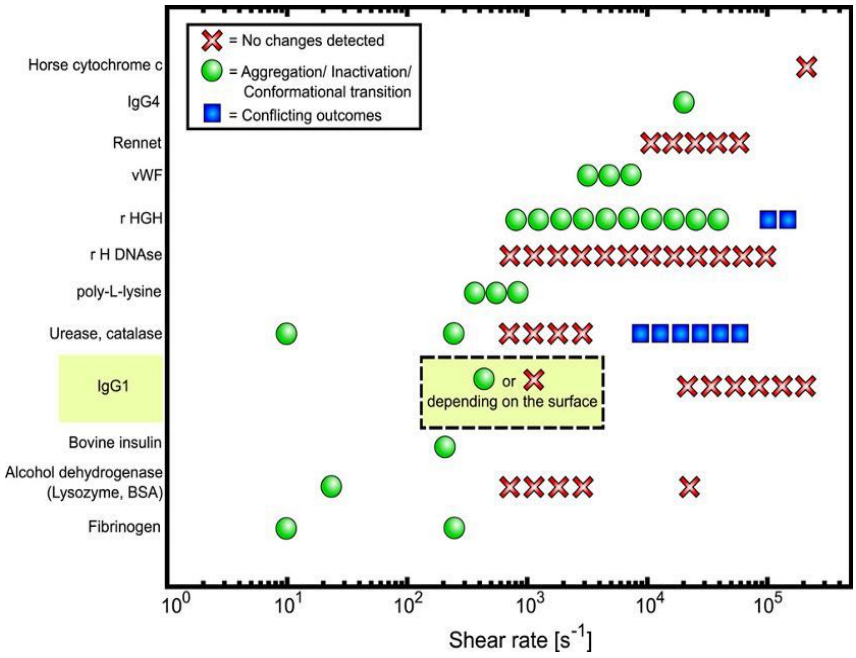

Figure 2.24: Overview of literature studies along with the author outcomes about the effects of hydrodynamic flow on various proteins along the magnitude of hydrodynamic flow applied in each study. Taken from [24].

The majority of studies investigates the aggregation of several proteins by the application of shear flow by using instruments such as rheometers, pumps and shakers. The application of extensional flow is less established for antibody aggregation studies. Additionally, the incorporation of interface effects is mostly focused into the incorporation of the liquid phase which in some studies is combined with air-liquid effects, with the actual effects of each interface to be difficult to be excluded in order to be identified. Studies investigating the effects of solid interfaces are introducing shear flow environments with the study conducted by Grigolato and Arosio [24] using extensional flow events to characterise interfacial aggregation, highlighting the synergy between flow and interface. This implies that the investigation of the simultaneous effects of extensional flow and interfaces is a topic which is currently under investigation in the literature, as the study of aggregation

Table 2.5: Overview of literature studies investigating the effects of flow and interfaces on the aggregation of monoclonal antibodies (mAbs), along with the suggested study outcomes by the authors.

Model protein	Flow	Interface	Suggested outcome	Reference
mAb	Shear	NPs, PS80	Protein destabilisation by interfaces is amplified by mechanical agitation.	[71]
mAb	Shear	Stainless-steel, alumina	mAb concentration and interface material had a significant effect on SVP formation.	[59]
IgG4	Shear	PS80, stainless-steel, aluminum oxide	Amount of adsorbed protein plays a role in surface-induced protein aggregation at the solid-liquid interface.	[45]
IgG1,IgG2	Entensional	SiO_2 NPs, glass, polypropylene	Synergistic effects of hydrodynamic flow and liquid-solid interfaces.	[24]
IgG1, IgG4	Shear	Air, PS20, PS80, silicone oil	Air/liquid interfacial stress generated sub-visible and visible aggregates.	[127]
mAb	Shear	Silicone, polypropylene, PS20, PS80, P188, Brij L-23	Substantial levels of particles in the presence of surfactants and from potential material shedding from the tubing.	[208]
mAb	Shear	Stainless-steel, ceramic	Aggregation is initiated by protein adsorption on pump surfaces and the propagation by mechanical and/or hydrodynamic disruption of the film.	[209]
mAb	Shear	Air, PS80	Synergistic effect of cavitation and agitation.	[210]

is currently conducted based mainly on the shear flow aspect.

For studies concerning the aggregation of monoclonal antibodies, the shear flow is mainly applied to induce protein aggregation, followed by the incorporation of air, solid and liquid interfaces. Overall, the synergy between the contributions of hydrodynamic flow and interfaces is also acknowledged in other literature studies. In the study conducted by Kopp et al. [71], the authors investigated the effects of shear flow and liquid interfaces (nanoparticles) where the protein destabilisation was amplified by mechanical agitation. The synergistic effect of cavitation and mechanical agitation was also shown by Torisu et al. [210], with the same effect to also suggested by Sreenivasan et al. [127], where the air liquid interfacial stress generated aggregates. The material shedding from equipment tubing is also reported to contributing to the aggregation under hydrodynamic flow as suggested by Sreenivasan et al. [127], even in the presence of surfactant molecules. The material type in which molecules interact under their exposure to hydrodynamic flow is also acknowledged to be important into the flow induced aggregation of the molecules in the studies conducted by Grigolato and Arosio [24] (glass, polypropylene), Kalonia et al. [59] (stainless-steel, alumina) and Roffi et al. [209] (stainless-steel, ceramic).

2.9 Summary

2.9.1 Literature emphasis and gaps

The majority of studies around biopharmaceutical aggregation are focused into the application of shear flow and its impact on aggregation. Fewer studies address the effect of extensional flow and its importance into affecting the aggregation pathway of samples exposed to it. Apart from the nature of the flow field, samples throughout their production, formulation transportation and administration, are exposed to and interact with interfaces which happens simultaneously under these steps. The distinct effects of solid interfaces where the samples are interacting with equipment and storage interfaces is less addressed. Most studies investigate the presence of air and liquid interfaces with regard to formulation additive interfaces present in the final formulation as well as storage interfaces incorporating air-liquid interfaces. Studies also investigate the effects of interfaces by addressing the incorporation of nanoparticle interfaces represented as liquid interfaces [69, 71, 204, 211].

Overall, the aggregation phenomenon is quite complex from the perspective of parameter space involved to affect the pathway of aggregation, the natural state and properties of each independent molecule. This implies that the combination of the parameter space with each independent molecule, makes aggregation studies challenging, but also useful to identify the strategies suppressing aggregation and enhancing molecule stability. From literature studies, a set of parameters have been identified to be crucial for ensuring

molecule stability. The protein primary structure and molecular weight, magnitude of hydrodynamic flow and the duration of its application [1] as well as formulation properties have been identified as important factors contributing to aggregation propensity of the molecules. The material of the solid surface in which the molecules are interacting with, is also an important parameter which is currently addressed in the literature. Therefore, for a complete understanding of the flow induced aggregation pathway, this set of parameters needs to be considered during the design of biopharmaceutical process ensuring molecule stability and functionality.

Chapter 3

Theoretical background

Chapter structure

In this chapter, the flow characterisation equations, Navier-Stokes equations, employed to describe and simulate the behaviour of proteins within flow-driven systems, are described, with an overview of the main sections covered in the current chapter summarised in figure 3.1. Initially, as the project addresses the effect of shear flow environments on how proteins can unfold and aggregate, shear flow equations describing shear and extensional flow fields are presented in 3.1. It is important to acknowledge the distinct effects of shear and extensional flow on protein's orientation under the exposure to the respective flow fields. Mathematically, shear flow can be described by the shear rate equations and extensional flow by the strain rate tensor equation, which will be described in 3.2, followed by the basic principle equations in microfluidics in section 3.3. Additional to the mathematical equations to describe the fluid's motion, analytical solutions to the Navier-Stokes equations, are developed to validate the simulation results in 3.4, which will be presented in the following chapters. The pressure drop along a geometry with a sudden contraction is then described in 3.5. The sudden contraction geometry is the flow environment where the experiments are conducted, inducing extensional flow events into proteins. Lastly, a summary of the chapter is described in section 3.6.

3.1 Shear and extensional flow field

The shear in fluids can be developed when the fluid is in motion, where its molecular particles move relative to each other having different velocities. The different velocities of the fluid's particles are responsible for causing a deformation of the original shape of the fluid, which then becomes disordered [25]. As it is shown in figure 3.2, deformation of the fluid occurs as the shear force, F has been applied tangentially to the fluid element. Therefore, the shear stress, τ, given by equation 3.1, can be defined mathematically as the force (F) per unit area, (A) causing the material to deform from ABCD to AB′C′D′.

$$\tau = \frac{F}{A} \tag{3.1}$$

The shear strain can be defined as the deformation of the fluid in terms of the angle of deformation, ϕ which is proportional to shear stress, and it keeps increasing with time as the fluid flows. For a particle moving through a distance x in time t and if E is a

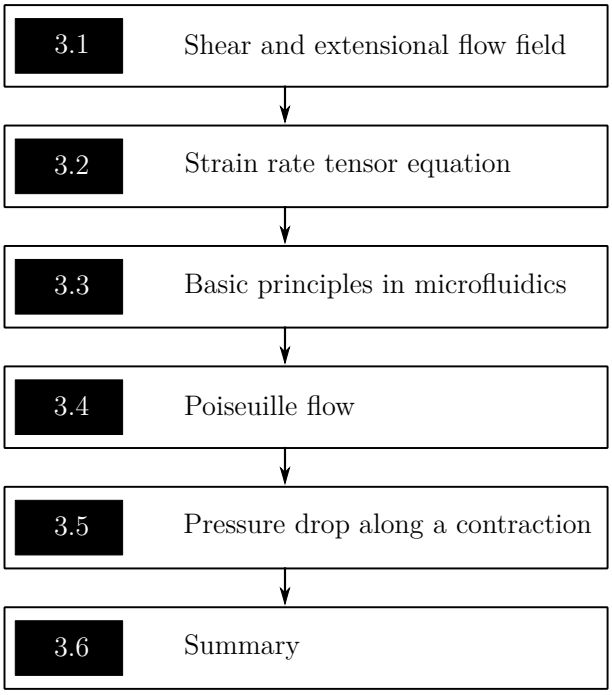

Figure 3.1: Overview of the main sections covered in the theoretical background chapter.

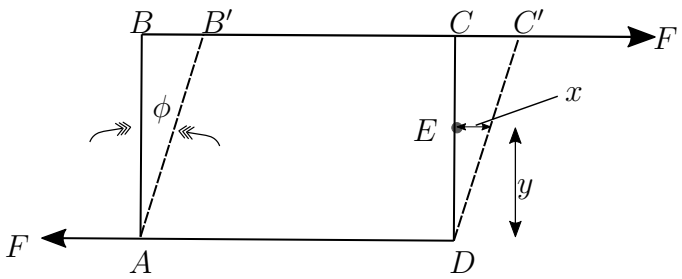

Figure 3.2: Deformation caused by shear forces, adapted from [25].

distance y from AD then for small angles shear strain and rate of shear strain can be defined as:

$$\phi = \frac{x}{y} \tag{3.2}$$

$$\text{Rate of shear strain} = \frac{x}{yt} = \frac{u}{y} \tag{3.3}$$

Assuming that shear stress is proportional to shear strain then,

$$\tau = \text{constant } \cdot \frac{u}{y} \tag{3.4}$$

The proportionality constant of the fluid, known to be the dynamic viscosity of the fluid, hence the final form of equation 3.4 becomes:

$$\tau = \mu \cdot \frac{u}{y} \tag{3.5}$$

The shear flow field can be interpreted as the orientation change of the plane as shown in figure 3.3, which acts perpendicular to the direction of flow over time, whereas the extensional flow can be determined as the velocity gradient in the direction of travel (figs. 3.3a and 3.3b).

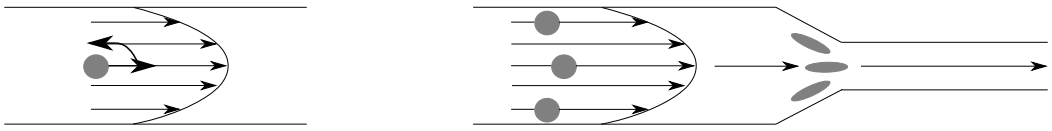

(a) Shear Flow **(b)** Extensional Flow

Figure 3.3: Representation of shear (3.3a) and extensional flow (3.3b).

For a Newtonian fluid flowing through a straight tube, the velocity develops a parabolic profile where it is greatest at the centre and decreases at the walls, as it is shown in figure 3.4. The slope of the line connecting the 0-velocity point at the wall and the tip of the near wall velocity vector (arrow) illustrated in figure 3.4b is the wall shear rate. Mathematically, it can be defined as the near wall velocity, v(y) divided by y, given by equation 3.6.

$$\dot{\gamma} = \frac{v(y)}{y} \tag{3.6}$$

In a Poiseuille flow, the wall shear rate is given by equation 3.7 [26].

$$\dot{\gamma} = \frac{32Q}{\pi D^3} \tag{3.7}$$

where:

$Q =$ Volumetric flow rate (m^3/s)

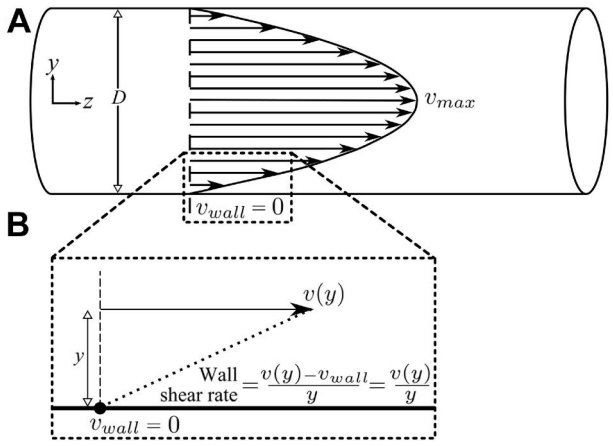

Figure 3.4: Shear rate. (A) Flow in a straight tube (Poiseuille Flow) characterised by a parabolic velocity profile. The arrows indicate the velocity vector as a function of y across the vessel.(B) Near the wall the velocity is > 0. The near wall velocity divided by the distance from the wall defines shear rate, taken from [26].

$D =$ Vessel diameter (m)

3.2 Strain rate tensor equation

Strain in general can be used for the determination of the change of a fluid's element configuration to another configuration under change of time [212]. The deformation of an element, allows determining how material points close to each other change their relative positions. This is important for understanding how the elements containing proteins change their relative positions, leading to the deformation on the protein which is linked with aggregation. The deformation of the neighbour of particle, P, can be characterised by the strain tensor, which is given by equation 3.8.

$$E = \begin{bmatrix} \frac{\partial u_1}{\partial x_1} & \frac{1}{2}\left(\frac{\partial u_1}{\partial x_2} + \frac{\partial u_2}{\partial x_1}\right) & \frac{1}{2}\left(\frac{\partial u_1}{\partial x_3} + \frac{\partial u_3}{\partial x_1}\right) \\ \frac{1}{2}\left(\frac{\partial u_1}{\partial x_2} + \frac{\partial u_2}{\partial x_1}\right) & \frac{\partial u_2}{\partial x_2} & \frac{1}{2}\left(\frac{\partial u_2}{\partial x_3} + \frac{\partial u_3}{\partial x_2}\right) \\ \frac{1}{2}\left(\frac{\partial u_1}{\partial x_3} + \frac{\partial u_3}{\partial x_1}\right) & \frac{1}{2}\left(\frac{\partial u_2}{\partial x_3} + \frac{\partial u_3}{\partial x_2}\right) & \frac{\partial u_3}{\partial x_3} \end{bmatrix} \tag{3.8}$$

Unit elongations, i.e., normal strains, are given by the diagonal elements of E in the x_1, x_2 and x_3 directions. The shear strain which corresponds to the decrease in angle between elements, given by the off diagonal elements of E. If $\nabla\ \vec{u}$ is antisymmetric, then E=0, and we have an infinitesimal rigid body rotation, Ω, which is given by equation 3.9.

$$\Omega = \frac{1}{2}\{(\nabla\vec{u}) - (\nabla\vec{u})^T\} \tag{3.9}$$

where:

$\nabla\ \vec{u} =$ displacement gradient

$$(\nabla \vec{u})_{ij} = \frac{\partial u_i}{\partial a_j} \tag{3.10}$$

Because of the symmetric strain tensor E, there exist at least three mutually perpendicular directions, $\vec{n_1}$, $\vec{n}_2$, $\vec{n}_3$ with respect to which the matrix of E is diagonal [212].

$$[E]_{\vec{n1}\vec{n2},\vec{n3}} = \begin{bmatrix} E_1 & 0 & 0 \\ 0 & E_2 & 0 \\ 0 & 0 & E_3 \end{bmatrix} \tag{3.11}$$

where:

E_1, E_2, E_3 = principal strains of E, correspond to the eigenvalues of E, and they include the maximum and minimum normal strains [212].

The Cartesian matrix representation of the velocity gradient tensor, can be written as shown in equation 3.12, and it can be then decomposed into the sum of its symmetric and antisymmetric parts, given in equations 3.14 and 3.15.

$$[\nabla \vec{v}] = \begin{bmatrix} \frac{\partial v_1}{\partial x_1} & \frac{\partial v_1}{\partial x_2} & \frac{\partial v_1}{\partial x_3} \\ \frac{\partial v_2}{\partial x_1} & \frac{\partial v_2}{\partial x_2} & \frac{\partial v_2}{\partial x_3} \\ \frac{\partial v_3}{\partial x_1} & \frac{\partial v_3}{\partial x_2} & \frac{\partial v_3}{\partial x_3} \end{bmatrix} \tag{3.12}$$

$$\nabla \vec{v} = D + W \tag{3.13}$$

$$D = \frac{1}{2}\{(\nabla \vec{v}) + (\nabla \vec{v})^T\} \tag{3.14}$$

$$W = \frac{1}{2}\{(\nabla \vec{v}) - (\nabla \vec{v})^T\} \tag{3.15}$$

where:

D= rate of deformation tensor, or strain rate tensor

W= spin tensor

The rate of change of a material's length and direction issuing from material point, P, located at $\vec{x}$ at time t can be determined by the rate of deformation tensor in matrix form D, given by the equation:

$$[D] = \begin{bmatrix} \frac{\partial v_1}{\partial x_1} & \frac{1}{2}(\frac{\partial v_1}{\partial x_2} + \frac{\partial v_2}{\partial x_1}) & \frac{1}{2}(\frac{\partial v_1}{\partial x_3} + \frac{\partial v_3}{\partial x_1}) \\ \frac{1}{2}(\frac{\partial v_1}{\partial x_2} + \frac{\partial v_2}{\partial x_1}) & \frac{\partial v_2}{\partial x_2} & \frac{1}{2}(\frac{\partial v_2}{\partial x_3} + \frac{\partial u_3}{\partial x_2}) \\ \frac{1}{2}(\frac{\partial v_1}{\partial x_3} + \frac{\partial v_3}{\partial x_1}) & \frac{1}{2}(\frac{\partial v_2}{\partial x_3} + \frac{\partial v_3}{\partial x_2}) & \frac{\partial v_3}{\partial x_3} \end{bmatrix} \tag{3.16}$$

Similarly to E, the diagonal parts of the matrix correspond to the rates of elongation, i.e., extension rates in the x_1, x_2 and x_3 directions. The rate of decrease in angle between elements, i.e., shear rate, given by the off diagonal elements of D.

3.3 Basic principles in microfluidics

The microfluidic development and technology has been particularly significant in the last decade due to the rapid development of lab on chip systems. The technological applications are driven by the field of the lab on a chip, which describes the application and adaptation of entire bio/chemical laboratories on the surface of silicon or polymer chips [27].

3.3.1 Reynolds number, Re

Several studies concerning the protein aggregation around the biopharmaceutical industry, have been conducted using microfluidic systems. The wide use of microfluidic devices can be found in literature due to a variety of advantages arising from scaling down standard laboratory setups achievable within a microfluidic system. The microscale of such systems enables the conduction of fast analysis, where the use of bio/chemical handling and analysis systems can be performed on compact and portable experimental condition. Liquids, such as proteins, can be handled within those systems, where its deformation can happen under the action of external forces. The type of flow that travels within the device can be characterised by the Reynolds number, Re, which is given mathematically by the equation 3.17.

$$Re = \frac{LV_{avg}\rho}{\mu} \tag{3.17}$$

where:

$L =$ length scale (m) (Typically for a channel taken as 4A/P where A: cross-sectional area, P: wetted perimeter of the channel; for circular cross-section this reduced to diameter D)

$V_{avg} =$ average velocity of the flow (m/s)

$\rho =$ fluid density (kg/m^3)

$\mu =$ fluid dynamic viscosity $(Pa \cdot s)$

3.3.2 Governing Equations

The flow of fluid through a control volume can be characterised by the Navier-Stokes equations, which are derived from the conservation of mass, momentum, and energy principles [213]. The simulations of the current study are conducted in a microfluidic

channel, where the Laminar Flow interface found in COMSOL's physics is suitable for simulating in low Reynolds numbers. The interface of the Laminar flow can solve the Stokes equations for conservation of momentum and the continuity equation for conservation of mass, as it is shown in equation 3.18.

$$\begin{aligned} \rho(u \cdot \nabla)u = \nabla \cdot [-pI + \mu(\nabla u + (\nabla u)^T) + F] \\ \rho \nabla \cdot u = 0 \end{aligned} \tag{3.18}$$

where:

$u =$ fluid velocity

$p =$ fluid pressure

$F =$ external forces applied to fluid

3.4 Poiseuille flow

The pressure driven, steady state flows in channels also known as Poiseuille flows or Hagen Poiseuille flows, correspond to a class of analytical solutions to the Navier-Stokes equation. The fluid is driven along a straight and rigid channel, by imposing a pressure difference between the two ends of the channel. Originally, channels with circular cross-sections have been studied by Hagen and Poiseuille, as these channels are easier to produce. In the area of microfluidics, other shapes of cross-sectional channels have been encountered.

Pressure-driven flow is one of the two most common ways in which the fluid is actuated to flow within the microchannels [213]. With the particular method, the fluid is pumped through the micromodel via the displacement of syringe pumps. For the pressure-driven flow, a parabolic velocity profile is expected to be developed by the flow with a no slip boundary condition imposed at the wall. The fluid velocity, can be therefore estimated analytically via the pressure difference which is specified between the inlet and outlet of the channel. Channel shapes other than round are encountered within microfluidic systems [27]. Particularly, circular and rectangular cross-sections will be considered in this section since these shapes will be considered for experimental and computational analysis, and are relevant to the studies described within this thesis.

3.4.1 Circular cross-section

A relation between the flow rate of the fluid entering the channel and applied pressure difference between the two channel ends can be obtained by a formal expression relating the two for circular and rectangular cross-sections, among other shapes. Initially, an elliptic cross-section can be considered where the major axis of length "a", and the minor

axis of length "b", are parallel to the y-axis and z-axis, as it shown in figure 3.5. The boundary ∂C of the ellipse is given by the expression:

$$\partial C : 1 - \frac{y^2}{a^2} - \frac{z^2}{b^2} = 0 \tag{3.19}$$

Using as a trial solution the following equation, and by substituting it into the left-hand side of the Navier-Stokes equation for an elliptical cross-section, the final form corresponds to the equation 3.20.

$$[\partial_y^2 + \partial_z^2]u_x(y,z) = -2u_0(\frac{1}{a^2} + \frac{1}{b^2}) \tag{3.20}$$

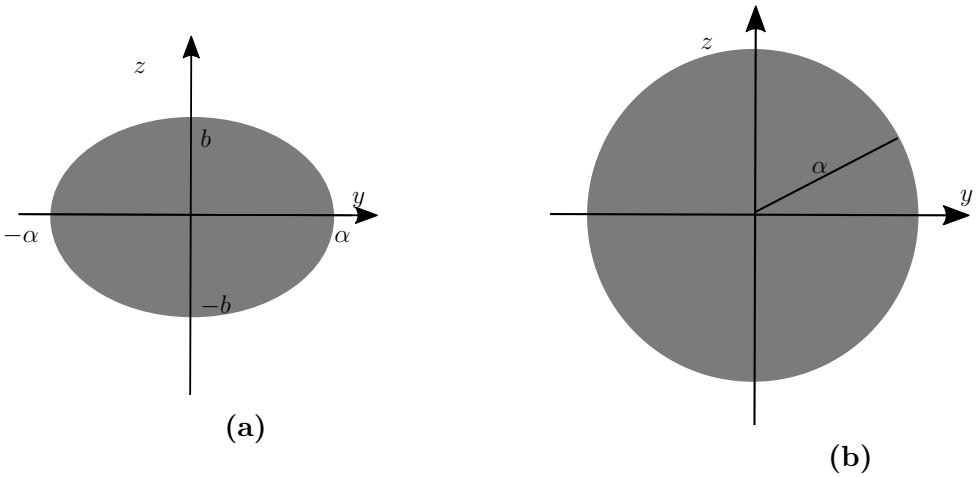

Figure 3.5: Cross-sectional shapes for the Poiseuille-flow problem in long, straight channels. The ellipse (3.5a) with major axis "a" and minor axis "b", the circle (3.5b) with radius "a". Adapted from [27].

The flow rate, Q, for the elliptic channel is then calculated by evaluating a 2D integral in an elliptically shaped integration region. In particular, for the circular cross-section is the case where a=b of the ellipse and the final form of the equation is given by the equation 3.21.

$$Q = \frac{\pi}{8}\frac{\alpha^4}{\eta L}\Delta p \tag{3.21}$$

where:

$\alpha =$ channel radius (m) (Defined as D/2)

$\eta =$ dynamic viscosity (Pa s)

$L =$ channel length (m)

$\Delta p =$ pressure difference (Pa)

3.4.2 Rectangular cross-section

Regarding the rectangular cross-section, the relation between the flow rate and pressure difference is approximated using a Fourier sum representing the solution.

$$Q \approx \frac{h^3 w \Delta p}{12 \eta L}[\,1 - 0.630\frac{h}{w}]\,, \quad for \quad h < w \tag{3.22}$$

where:

$h =$ channel height (m)

$w =$ channel width (m)

According to Bruus [27], the approximate result in eq. (3.22) can be considered to be a good approximation; for the case of a square cross-section (h=w), the approximation is given with an error of just 13%, whereas with an aspect ratio of a half, h=w/2, the error is further reduced to 0.2%.

3.5 Pressure drop along a contraction

When the flow passes along the sudden contraction, the velocity distribution undergoes development until it is fully developed at some distance down the contraction. Therefore, the pressure gradient in the region where the flow is fully developed is different from the flow development region. The pressure difference at the region where the flow immediately passes the contraction and starts to develop a velocity profile can be given by the equation 3.23, as it is proposed by Holmes in [214].

$$\Delta P = \frac{\rho V^2}{2}[\,K + \frac{K'}{Re}] \tag{3.23}$$

where:

$K =$ Hagenbach correction (dimensionless)

$K'/Re =$ Couette correction (dimensionless)

The dimensionless parameters of K and K', have been reported in several literature studies which indicate their values, as determined either theoretically or experimentally as summarised in [214] as a function of Re. The pressure loss that is developed along the sudden contraction occurs as a result of the eddies formed as the flow expands from the vena contracta up to the full cross-section of the downstream tube, as it is shown in figure 3.6.

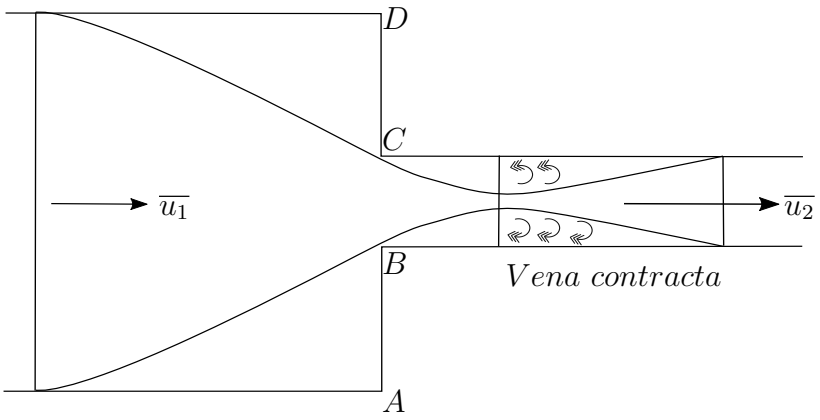

Figure 3.6: Flow separation due to contraction of a tube. The point of the smallest flow rate is the vena contracta, adapted from [25].

3.6 Summary

To investigate the effects of flow on protein unfolding pathway, a mathematical background is presented describing the theoretical equations implied to simulate, predict and characterise the flow behaviour on proteins required for the conduction of flow simulations. The following chapter, chapter 4, addresses the flow characterisation computationally, by employing the theoretical equations of fluid motion described in this chapter. The theory, presented here, will be applied to describe the flow in extensional devices designed to induce response of proteins to flow environments. Their response to the generation of flow fields will be characterised computationally and experimentally in the following chapters 6, 7 and 8.

Chapter 4

Computational approach to assessing flow within extensional flow devices

Computational method structure

In this chapter, the methodology applied for the flow characterisation within a range of different systems is presented, with an overview of the main sections to be covered schematically shown in figure 4.1. The aim of the particular chapter will be firstly introduced in section 4.1, followed by a description of the software used for the conduction of the simulations (COMSOL) in section 4.2. A description of simulation studies performed for a range of devices, for creating controlled flow conditions including the extensional flow device, sliding interface and microfluidics is then presented in sections 4.3, 4.4 and 4.5. Lastly, a summary describing the main aspects addressed in the simulation studies is presented in section 4.6.

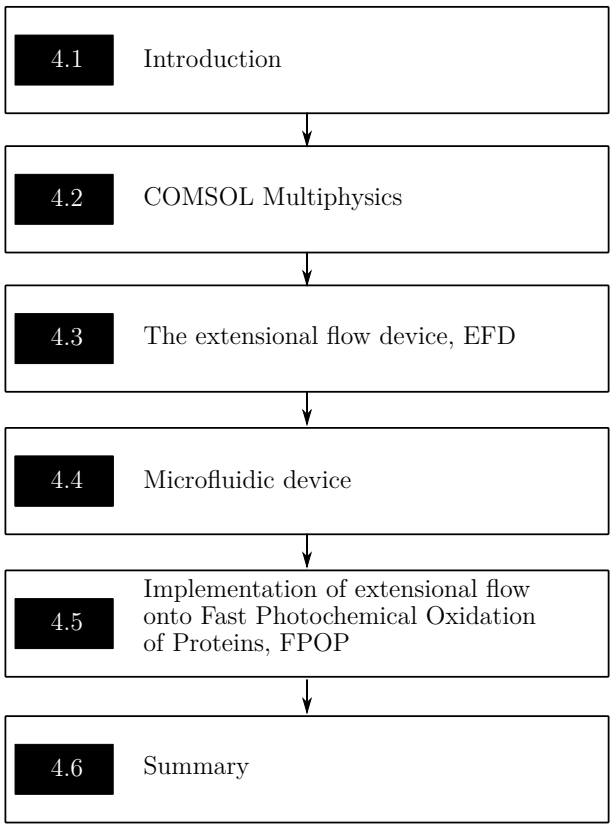

Figure 4.1: Overview of the main sections covered in the computational method chapter.

4.1 Introduction

CFD is employed here, for the study of fluids in a variety of flow devices used to better understand protein response to flow induced forces. The technique uses governing equations and associated boundary conditions to describe the fluid motion. More generally, the application of CFD can be found both in applied research or industrial fluid-engineering applications, for example in the fields of aerospace, automotive, biomedical, civil, chemical and biomedical engineering [215]. The application of such a tool in the current project allows the flow characteristics to be linked with the unfolding events, which form the basis of the subsequent aggregation pathways of protein-based pharmaceuticals. In addition, characterisation of potential designs is used to optimise equipment performance.

The computational part of the project determines the flow properties which are important in inducing the unfolding or partial unfolding event which is essential for the protein structure perturbation leading to aggregation. The sudden contraction within the geometry allows the development of an extensional flow field which is responsible for the elongational event which affects the amount of force applied on the molecules; this is expressed as the rate of strain. The effect of the shear flow which is also present in the system for the straight flow channel is also considered to be important for affecting the aggregation. Simulations will be able to characterise each flow field component and the amount of force applied; this can be used to better understand the experimental data. The controlling parameters, affecting the effects of force on the aggregation of the molecules, can be also explored by simulation studies.

A design optimisation study has also been performed to establish the design specifications which meet the requirements of a microfluidic channel which is intended to be used in a current biophysical technique known as FPOP, focusing primarily on the early stages of protein unfolding. Simulations are conducted, identifying the design characteristics that allow the duplication of the amount of force which is developed within the extensional flow device. This takes design from milliscale to microscale dimensions.

Computational work has also been conducted to support the investigation of the fluid properties on the aggregation mechanism. The viscosity of protein solution is a parameter related to the protein concentration and which has also been explored to identify the effect on the aggregation at the constricted part of the geometry. The link between viscosity and hydrodynamic force is important for determining the contribution of a range of factors that are all simultaneously exposed to the molecules throughout the production, transportation and administration processes.

4.2 COMSOL Multiphysics

COMSOL is a multiphysics simulation software, finite element analysis and solver which allows the physics-based user interfaces with coupled systems of partial differential equations. The modelling workflow consists of the geometry definition, material properties, the physics which describe specific phenomena depending on the application, solver and post-processing models. The software offers the flexibility to apply models for fields including solid mechanics, acoustics, fluid flow, heat transfer, chemical species transport and electromagnetics as the platform is pre-installed with a set of core physics interfaces [216]. The simulations conducted for the flow characterisation as well as the design optimisation as a part of this project have been performed in COMSOL Multiphysics 5.5. The steps required for the modelling process are shown in the form of a framework analysis, as shown in figure 4.2 consisting of three main sections corresponding to pre-processor, solver and post-processor. The simulations are firstly set in the pre-processor section where the model geometry is defined followed by the material properties. Physics definition is then followed by specifying the fluid transport equations, followed by the assignment of boundary conditions of the model and mesh discretisation. Then the solver settings are defined by defining the solver type to be used for the simulations as well as by determining a stationary, time-dependent or a parametric study. The last step of the analysis, in the post-processor part, is the visualisation of the desired results via qualitative or quantitative means, via contour plots and graphs respectively.

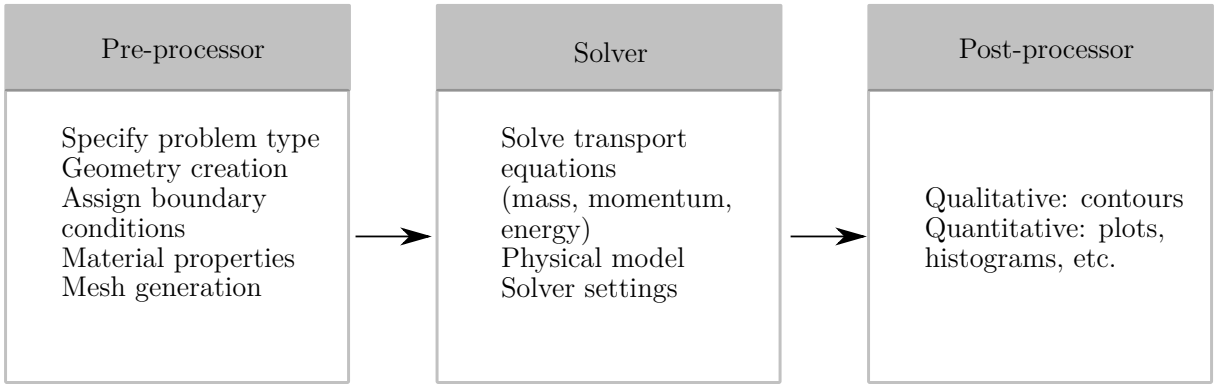

Figure 4.2: CFD analysis framework.

4.3 The extensional flow device, EFD

The computational characterisation of flow field environments and their link to protein aggregation are conducted using a previously defined extensional flow device [1], which consists of a sudden contraction geometry to allow extensional flow and shear flow events to be developed. The flow within the extensional flow device can be characterised by conducting CFD simulations. Regions of high and low shear can be identified to determine

the flow environment in which the proteins are exposed to within the device, and through experimentation understand how this is related to aggregation. A geometry with a sudden contraction can be modelled to simulate the extensional flow from a wide tube section, which corresponds to a syringe connected with a narrower tube as the capillary [1].

4.3.1 Model geometry

The flow through this particular device can be modelled with a 2D axisymmetric model, which can be viewed as a 3D model when it is revolved around the axis of symmetry. This is achieved by designing the half geometry of the device around the axis of symmetry, as it is shown in figure 4.3. The extensional flow has been designed with the actual dimensions of the device used in the study described in [1]. The syringe and capillary diameters correspond to 4.61 mm (bore diameter) and 0.3 mm (inner diameter), respectively. The geometry of the channel is simplified into a 2D axisymmetric simplification, which is more computationally efficient.

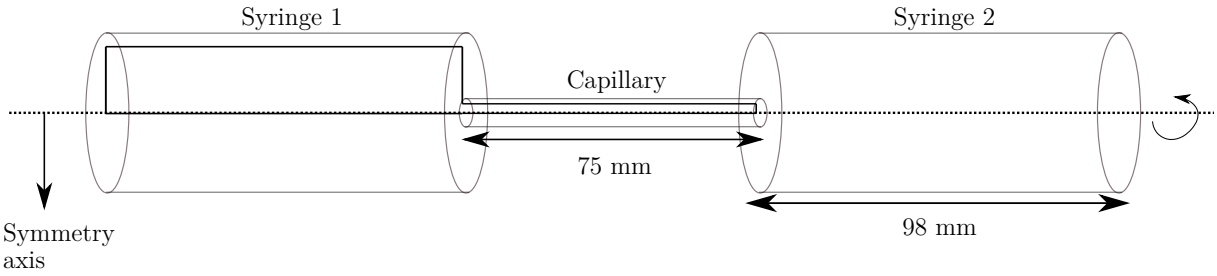

Figure 4.3: Schematic illustration of the extensional flow device geometry model indicating the model to be designed indicated in bold line corresponding to a single syringe along the constricted flow channel representing the capillary.

4.3.2 Boundary Conditions

The simulations are conducted using COMSOL Multiphysics v.5.5 using the Laminar flow interface, which is used to solve the Navier-Stokes equations. Laminar flow interface is selected because the flow developed within the extensional and then microfluidics devices corresponds to low Re numbers, Re<1,000 (as calculated in sections 4.3.4 and 4.4.3 respectively). As a part of the flow module, the setup of the boundary conditions is required for determining the initial conditions that describe the model at the preprocess stage of the computational procedure. The boundary conditions can be schematically seen in figure 4.4 and the fluid properties are those of water. This is appropriate for low concentration protein solutions (i.e., for an IgG at 2 mg/mL) with a reported mass density of ∼1.4 g/mL [176], which is similar to the water density ∼1 g/mL. The flow conditions are defined to be laminar with an inlet flow velocity entering the syringe, a pressure point constraint is also set at the outlet of the geometry, whereas the walls are characterised by the no slip condition.

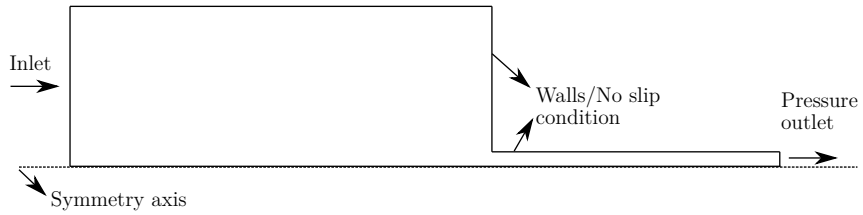

Figure 4.4: Schematic illustration of the geometry model indicated with the boundary conditions.

Sliding interface

The sliding interface corresponds to a variation of the extensional flow device where the geometry consists of a single syringe with the absence of the contraction in the flow environment, as shown schematically in the figure 4.5a. In the particular setup, the sample is loaded in the single syringe, where it is exposed to multiple flow events by the slide movement of two plungers. The geometry representing the particular experimental setup is illustrated in figure 4.5b, which is modelled as a 2D axisymmetric model revolved around the axis of symmetry. The boundary conditions including the incorporation of moving wall representing the liquid motion of the samples which is induced by the forward and backward repetitive syringe movement is shown in figure 4.6.

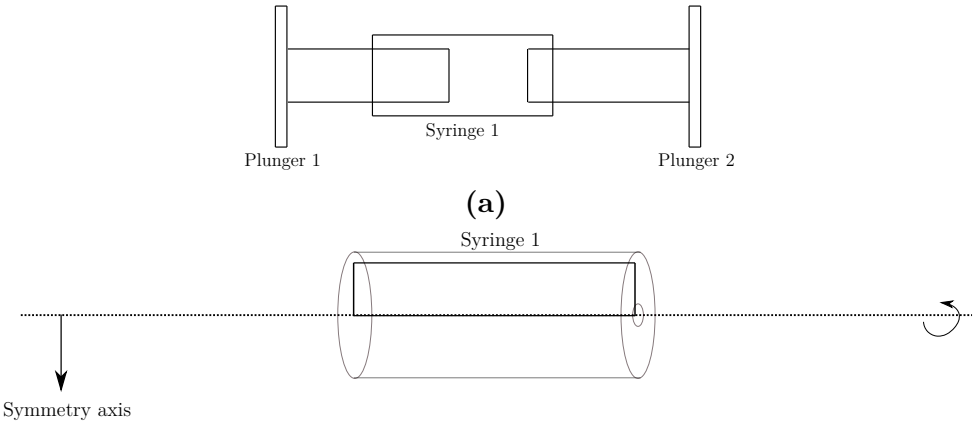

Figure 4.5: Schematic illustration of the sliding interface device (4.5a) and geometry model indicating the model to be designed, indicated in bold line corresponding to a single syringe (4.5b).

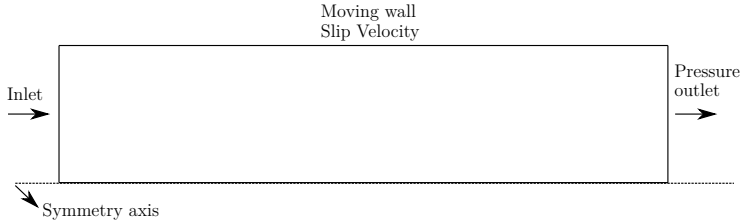

Figure 4.6: Schematic illustration of the geometry model indicated with the boundary conditions.

4.3.3 Model discretisation

The model is then discretised into smaller elements before the post-process stage of the simulation procedure, as it shown in figure 4.7. To ensure that the accuracy of the simulation results can be considered to be sensible, a mapped mesh has been selected, allowing a uniform refinement in element size across the domain of the geometry.

The suitability of the mesh size has been also investigated by conducting grid independence study as shown in figure 4.8, for a local point of interest (i.e., point of the contraction) (figure 4.8a) and globally along the whole domain geometry (figure 4.8b). A mesh consisting of 4,750 edge elements (axisymmetric model) corresponding to a total of 9,500 edge elements (full model geometry) has been selected as the appropriate to converge the output result of interest, with <1% change on maximum velocity compared to a mesh with double the element count. The simulation time for the particular model with the specific edge element size is 2,690 seconds (44 minutes, 50 seconds) and the computing power is 6.65 GB and 15.16 GB for physical and virtual memory respectively.

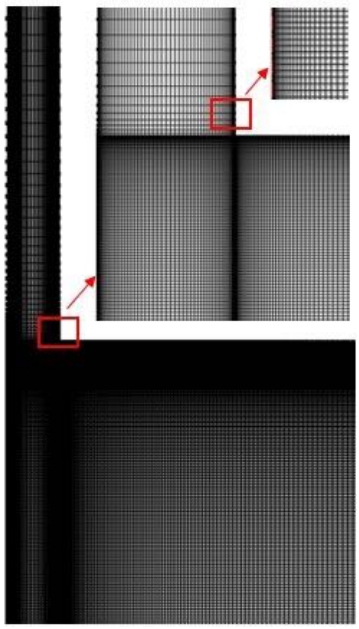

Figure 4.7: Mesh representation with a zoomed view of clustered elements and boundary element.

4.3.4 Model verification

The quality control of the computational results can be determined by the validation and verification process. Model validation is carried out to ensure that the computational model represents accurately the real world from the perspective of the intended uses of the model [217]. Model verification investigates the accuracy of the solution to a computational model by comparison with known solutions [217]. The conduction of a verification process is followed to to determine the degree of accuracy of the results by the comparison between

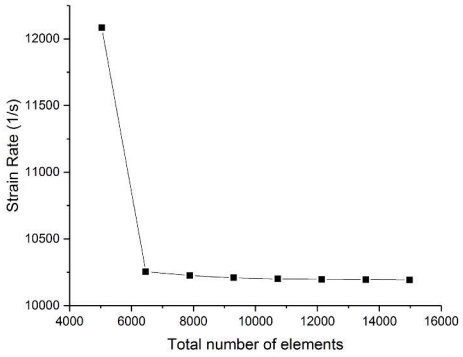

(a) Strain rate at point (0,74)

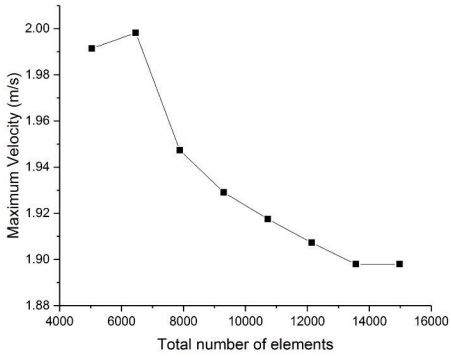

(b) Maximum velocity along the model domain

Figure 4.8: Extensional flow device, (EFD) mesh sensitivity tests.

the pressure difference (ΔP) obtained from the simulations and hand calculations. The total pressure of the model can be calculated by employing analytical equations for the pressure difference along the domain, with the inclusion of the pressure difference obtained from the sudden contraction of the geometry. The pressure difference across the syringe and capillary can be calculated by rearranging the Hagen-Poiseuille equation (equation 3.21), as it is previously mentioned in chapter 3, into equation 4.1.

$$\Delta P = \frac{8Q}{\pi}\frac{\eta L}{\alpha^4} \tag{4.1}$$

The mass flow rate, Q, entering the domain inlet, can be determined by equation 4.2:

$$Q = \pi \times {r_s}^2 U_s \tag{4.2}$$

$$Q = \pi \times (0.00231)^2 \times 0.008 \implies Q = 1.3411 \times 10^{-7}\ m^3/s$$

The average flow within the capillary can be then calculated using the equation 4.3 as follows:

$$U_c = \frac{Q}{\pi r_c^2} \tag{4.3}$$

$$U_c = \frac{1.3411 \times 10^{-7}}{\pi \times 0.00015^2} = 1.897\ m/s$$

The Reynolds number along the capillary can be then calculated (equation 3.17):

$$Re = \frac{997 \times 1.897 \times 0.0003}{8.9 \times 10^{-4}} = 637.5$$

Pressure drop over the capillary for the half geometry (axisymmetric model) is calculated based on the Hagen-Poiseuille equation (equation 3.21):

$$\Delta P = \frac{1.3411 \times 10^{-7} \times 8 \times 8.9 \times 10^{-4} \times 0.075}{\pi \times (0.00015)^4}$$

The pressure loss across the capillary is calculated as:

$$\Delta P_{overall} = 45,028Pa \implies \Delta P_{capillary} = 22,514\ Pa$$

The additional pressure loss induced by the presence of the geometrical contraction can be then calculated for the half geometry (axisymmetric model) using the equation 3.23. K=2.4 and K'=295, based on the contraction ratio of the model, as taken from [214].

$$\Delta P = \frac{997 \times (1.897)^2}{2} \times [2.4 + \frac{295}{637.5}] \implies \Delta P_{contraction} = 2,568\ Pa$$

The total pressure loss is then calculated as:

$$\Delta P_{total} = \Delta P_{capillary} + \Delta P_{contraction} = 25,082\ Pa$$

Total pressure drop from computational simulations suggest ΔP =26,621 Pa. A percent error calculation is conducted to quantify whether the error is significant.

$$\%error = |\frac{26621 - 25082}{25082}| \times 100 = 6\%$$

This suggests that the hand calculations and computational results are similar within a difference of 6% in the pressure field.

4.3.5 Effect of high viscosity

In respect of the formulation properties and their effects on aggregation, the effect of viscosity is investigated within the flow field using the extensional flow device geometry as a system of reference for the simulations. The effect of formulation viscosity can be correlated with the protein concentration, as it is reported that viscosity exponentially increases with protein concentration [218–220].

As proposed by Jaspe and Hagen [18] and previously mentioned in chapter 2 (section 2.7), the theoretical model interpreting the effects of elongational flow on protein unfolding,

corresponds to a tension force, affecting the unfolding phenomenon, and it is characterised by the viscosity parameter. To further investigate the significance of this parameter and its effect on the flow fields, simulations are designed for investigating the effects of viscosity over a range of shear rates, and on particular flow parameters such as the flow velocity and strain rate. Highly concentrated protein solutions can express shear-thinning flow behaviour, which leads to a reduction in viscosity with increasing shear rate [8, 221]. The Carreau model, which is described by equation 4.4 and was previously used in [8] to determine the shear thinning effect of protein solutions, is used here. The model demonstrates a viscosity-shear rate profile of protein solution by combining viscosity data obtained from plate/cone rheometer with data modelled by the Carreau model, with the corresponding fitting model parameters summarised in table 4.1.

Here, the model can be applied to the extensional flow device system by combining the experimental data and fitting parameters taken from 4.1 and allowing highly concentrated protein solutions (120-225 mg/mL) expressed as shear-thinning flows with the model to investigate the potential effects on the flow environment within the device.

$$\eta = \eta_\infty + (\eta_0 - \eta_\infty) \times (1 + \Gamma^2 \dot{\gamma}^2)^{(n-1)/2} \tag{4.4}$$

where:

$\eta_\infty =$ infinite shear rate viscosity $(mPas)$

$\eta_0 =$ zero shear rate viscosity $(mPas)$

$\Gamma =$ time constant

$\dot{\gamma} =$ shear rate (s^{-1})

$n =$ power law index

Table 4.1: Rheological parameters of mAb1 (25 ℃) taken from [8]. ($c_{protein}$=protein concentration, η=dynamic viscosity at 2 x 10^3 s^{-1}, n=power law index, Γ=time constant).

$c_{protein}$ (mg/mL)	η (mPa s)	n (dimensionless)	Γ^{-1} $(10^3 s)$
120	4.4	0.84	33 ±10
170	13.1	0.82	57 ±67
210	26.3	0.68	41 ±5
225	46.0	0.57	31 ±2

4.4 Microfluidic device

To determine the differences in terms of the hydrodynamic forces generated between the extensional flow device and microfluidics, the flow is characterised within various microfluidic designs. The models are initially designed and then simulated in 3D using

COMSOL Multiphysics v.5.5. The intent to generate an extensional flow along the device geometry is achieved by introducing contractions as a part of the geometry.

4.4.1 Model definition

The characteristic in the design of the chips is the repetition of multiple contractions, which corresponds to multiple extensional flow events. The boundary conditions in this case differ from the EFD model, consisting of one contraction. For the microfluidic models, the periodic flow condition is applied as shown schematically in figure 4.9. The periodic flow condition corresponds to the geometry which is a part of a larger geometry; therefore, a model consisting of one contraction has been designed as the initial geometry to which periodic conditions have been applied. As it is shown in figure 4.9, the boundary conditions selection is sorted between a source and destination group, where a pressure difference between the two groups can be set up to evaluate the flow rate after the completion of the simulation. Multiple contraction in series have been designed with 1 (figure 4.10a), 2 (figure 4.10b) and 4 (figure 4.10c) contractions respectively.

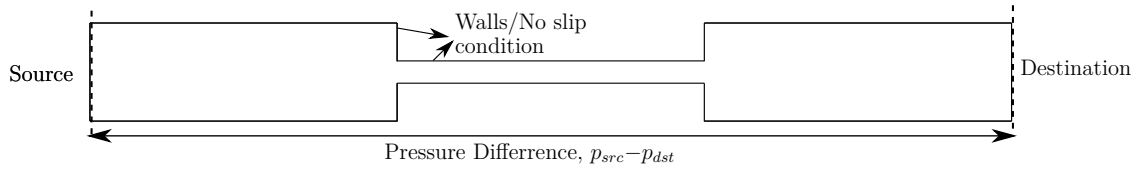

Figure 4.9: Schematic illustration of the microfluidic device with a single constriction (N-1) indicating periodic flow conditions.

(a) 1 contraction **(b)** 2 contractions **(c)** 4 contractions

Figure 4.10: N1 simulated chip designs with multiple contractions: 1 (4.10a), 2 (4.10b) and 4 (4.10c) using periodic flow conditions.

4.4.2 Model discretisation

The microfluidic 3D model is discretised using swept mesh, where it consists of uniform rectangular elements. Mesh refinement is carried out close to the corners and close to the contraction area, as shown in figure 4.11. The total mesh consists of 140,200 elements which is found to be suitable where the maximum velocity converges at 0.67 m/s and strain rate at 10,100 s^{-1}. The mesh was selected after the conduction of grid independence study as shown in figure 4.12. The mesh sensitivity test was conducted locally investigating the

strain rate (figure 4.12a) and globally along the maximum velocity that the flow can reach within the geometry (figure 4.12b).

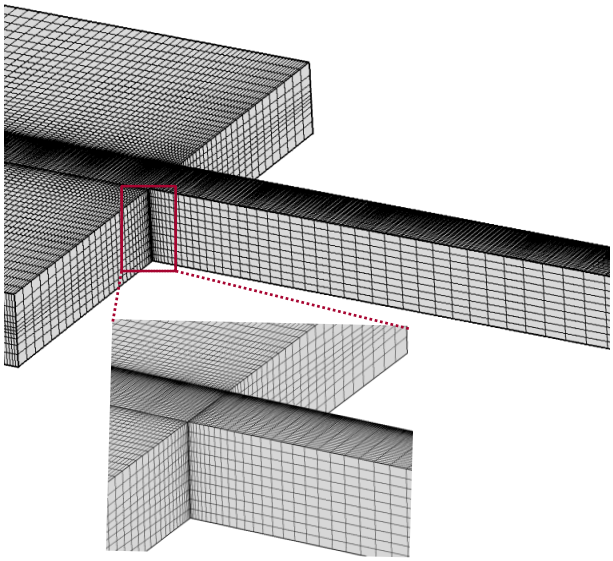

Figure 4.11: Mesh representation with a zoomed view of clustered elements and boundary element.

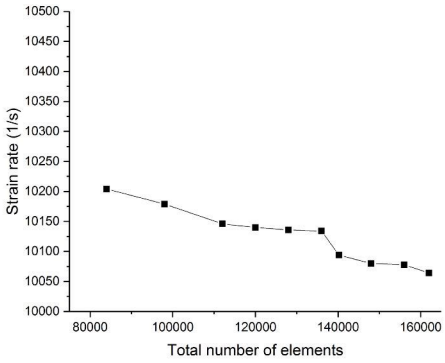

(a) Strain rate at the centreline

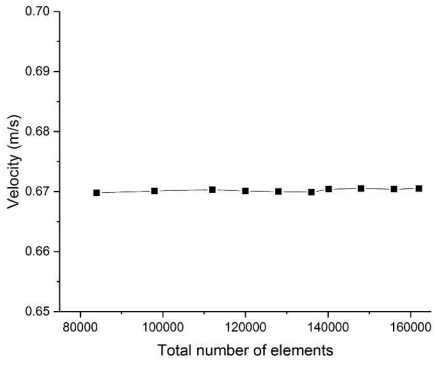

(b) Maximum velocity along the model domain

Figure 4.12: Microfluidic mesh sensitivity tests.

4.4.3 Verification

To ensure that the mathematical representation of the model is solved accurately, the pressure difference along the model for a rectangular cross-section can be calculated by rearranging the equation 3.22 into equation 4.5.

$$\Delta P = \frac{12 \times Q \times \eta \times L}{h^3 \times w \times [1 - 0.630\frac{h}{w}]} \tag{4.5}$$

The periodic flow condition has been set based on the pressure difference along the model, which is set to ΔP = 2,500 Pa. The flow rate calculated in COMSOL corresponds to the value of 3.98× 10^{-9} m^3/s. The velocity under which the flow enters the inlet domain can be calculated using the cross-sectional area of the channel, A. The cross-sectional dimensions of the rectangular channel correspond to channel width, w = 1 × 10^{-3} m and channel height, h = 0.125 × 10^{-3} m.

$$V = \frac{Q}{A} = \frac{3.98 \times 10^{-9}}{1 \times 10^{-3} \times 0.125 \times 10^{-3}} = 0.032\ m/s$$

$$Re = \frac{997 \times 0.032 \times 0.0002}{8.9 \times 10^{-4}} = 7$$

The pressure drop can be then calculated using the equation 4.5:

$$\Delta P = \frac{12 \times 3.98 \times 10^{-9} \times 8.9 \times 10^{-4} \times 100 \times 10^{-3}}{(0.125 \times 10^{-3})^3 \times 10^{-3} \times [1 - 0.630 \times \frac{0.125 \times 10^{-3}}{10^{-3}}]} = 2,362\ Pa$$

The additional pressure loss induced by the presence of the geometrical contraction can be then calculated using the equation 3.23. K=2.4 and K'=295, as taken from [214].

$$\Delta P = \frac{997 \times (0.032)^2}{2}[2.4 + \frac{295}{7}] \implies \Delta P_{contraction} = 23\ Pa$$

The total pressure loss is then calculated as:

$$\Delta P_{total} = 2,362 + 23 = 2,385\ Pa$$

The percent error is then calculated as shown below:

$$\%error = |\frac{2500 - 2385}{2385}| \times 100 = 5\%$$

This indicates that computational results can be considered to be an accurate representation with an error of 5% compared with the hand calculations.

4.4.4 Sensitivity tests

Sensitivity tests investigating the effect of the design on the extensional field have been conducted by coupling computational and experimental work. The experimental work has been previously conducted by Dr. Amit Kumar investigating the aggregation propensity for each chip design. The experiments have been conducted using the extensional flow device, where the capillary part was replaced by the microfluidic chip. The models used for the conduction of the experiments were first designed and then simulated in COMSOL are shown in figure 4.13. The presence of a series of contractions along the chip length allows the generation of the extensional flow. This is investigated for a microfluidic chip with repeated contractions; hence the boundary conditions differ from those used in the extensional flow device. The determination of the most efficient chip suitable for achieving maximum protein unfolding is done by coupling both the experimental and computational results. Each microfluidic design has been simulated under the same flow rate, and the maximum strain rate under which the flow is exposed at the flow channel's centreline is determined. The protein unfolding can be also investigated from the time perspective, demonstrating how much time the protein can be exposed into the extensional and shear region. The following table groups each microfluidic chip by the variation of the parameter conducted in the experimental part, so as to be also characterised computationally. The simulations have been based on the set of the previously experimental work conducted, by organising the set of experiments according to the number of extensional events depending on the chip design and experimental parameters such as plunger speed as shown in table 4.2.

Table 4.2: Experimental and computational test of microfluidics in groups.

Group	Test protein	Device	Plunger speed mm/s	Protein volume, μL	No of Passes	No of extensional events
A	mAb1	N11	1,2,4,8,12	700	100	1
B	mAb1	N11, N12, N14	4	700	100	1,2,4
C	mAb1	N11,N12,N14	4	700	100,50,25	1,2,4
D	mAb1	N11	4	400,600,800	100	1
E	WFL	O121	4	700	1	21
F	WFL	P121	4,8	700	1	21
G	mAb1	R110	4	700	2,10,20,40	10
H	mAb1	S110	4	700	2,10,20,40	10

4.5 Implementation of extensional flow onto FPOP

The flexibility to implement a microfluidic chip into current and new biophysical methods, is a powerful tool for achieving a multiple characterisation of aggregation propensity using multiple techniques. Fast Photochemical Oxidation of Proteins, FPOP is the biophysical method of interest here, where a microfluidic chip can be integrated into the currently used setup with the chip designed to give strain rates of the order which is found to cause aggregation for the previously studied proteins in [1–3]. As previosuly described in

(a) N1-1 (1 contraction)

(b) N1-2 (2 contractions)

(c) N1-4 (4 contractions)

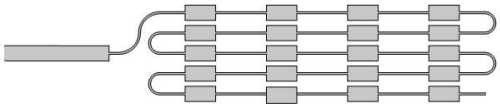

(d) O-21 (21 contractions)

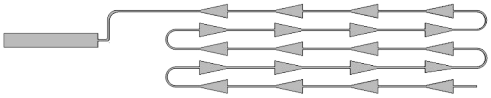

(e) P1-21 (21 contractions)

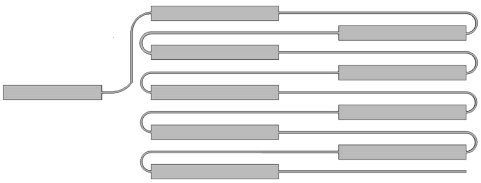

(f) R1-10 (10 contractions)

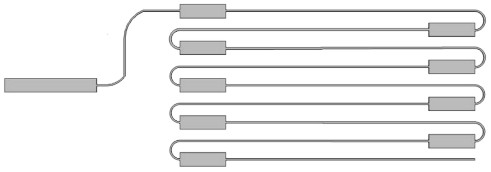

(g) S1-10

Figure 4.13: Microfluidic chip designs with a range of contractions in series.

chapter 2, section 2.5.5, the particular method can be employed to provide information into the biomolecule structures and interactions of proteins which can be encountered under unfolding events. As mentioned earlier, this method is a type of hydroxyl-radical based protein footprinting which makes use of a pulsed KrF laser (248 nm), which produces hydroxyl radicals which can then modify the proteins in situ [14]. The experimental procedure is based on a flow system where the protein solution is loaded into a continous capillary which is placed perpendicular to the laser beam. The laser then labels the protein solutions so as to capture in peptide or residue level, the protein building blocks which are affected during the partial unfolding of proteins.

Since this method is based on a continuous flow system, the aggregation via extensional flow can be explored by the implementation of microfluidic chips onto an established FPOP setup at the University of Leeds. The full equipment description and methodology conducted for the integration of the device into the current FPOP setup is described in the next chapter 5, section 5.5. This will allow the aggregation propensity induced by hydrodynamic forces to be studied in amino acid peptide bonds or residue levels in real time by the reacting hydroxyl radicals. Therefore, this will give new insights into the aggregation behaviour under flow by the combination of protein footprinting method and hydrodynamic forces arising from flow. The incorporation of the microfluidic device, will also provide the flexibility to select the areas which are important for capturing the unfolding events, allowing laser spots to be introduced at multiple regions within the flow channel as schematically shown in figure 4.14. Additionally, simulation studies are also performed determining the desired laser frequency for the sufficient sample labelling, by the adjustment of the laser spot size.

4.5.1 Microfluidic design requirements

The successful integration of a microfluidic chip within the current used FPOP setup requires designing to a set of parameters which are encountered within the FPOP technique. Analytically, a set of the currently used parameters for the FPOP can be found in table 4.3. A series of geometry sensitivity tests has been conducted to determine a suitable microfluidic chip dimensions for the FPOP application. The suitable chip dimensions must be based on a set of requirements such as laser specification and generating a strain rate in the range of 10,000 to 11,000 s^{-1} which has been previously found to induce aggregation to the proteins of interest [1]. The development of the target strain rate will need to be linked with the flow rate, which is correlated with the laser frequency, such as the pulsed laser can label the protein samples efficiently. Additionally, another requirement is that the design will require that the protien samples are introduced into the flow channel for a single pass (once) at minimum flow rates. This is desirable to ensure that the conformational state of the protein is not altered as the FPOP experiment addresses the early stages of protein unfolding and not the aggregation of the molecules. Therefore, the suitable chip

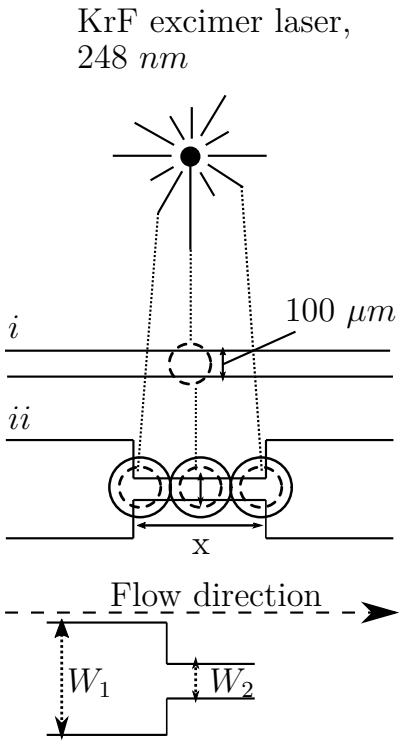

Figure 4.14: Schematic illustration of the transition from the capillary geometry with internal capillary diameter of 100 μm (i) to the microfluidic flow channel (W_1/W_2=contraction ratio), allowing the laser spot position (x) along the x-axis, and laser spot size variation (dashed and solid circles) using a translational stage (ii).

dimensions for its integration within the FPOP must meet three critical requirements as listed below:

- Achieve a strain rate of order 10,000 s^{-1}.
- Ensure the flow rate is such that the pulsed laser can label the flow efficiently.
- Minimise flow rates for the once through design.

4.5.2 Flow rate-laser frequency effect

The combination of the target strain rate and required laser frequency within the laser's wavelength range will determine the suitable microfluidic design for its application into the FPOP setup. The laser of the experiment which is used to label the samples, has a given frequency of operation at the standard experiments which is 15 Hz and it can reach a mamimum frequency of 50 Hz (table 4.3). The required laser frequency F, is then calculated by the laser spot size S, and the velocity entering along the contraction U_c, using the equation 4.6:

$$F = \frac{U_c}{S} \tag{4.6}$$

Table 4.3: FPOP laser specifications used at the existing FPOP experimental setup at the University of Leeds.

Parameter	Value
Laser wavelength	248 nm
Laser frequency	15 Hz
Max. repetition rate	50 Hz
Flow rate	20 ul/min
Transparent width	3 mm
Inner capillary diameter	100 μm
Max. pulse energy	150 mJ
Max. average power	7 W
Pulse duration	20 ns

With the flexibility of the FPOP, the suitable microfluidic chip design can be developed, so it can be incorporated into the FPOP setup. Various chip designs have been examined regarding the required laser frequency needed for the laser in relation with the achievable centreline strain rate. This set of results describes the design of an FPOP setup. The calculated relationship between the strain rate and required laser frequency is represented on figures 4.15a and 4.15b. It can be seen that there is a linear relationship between the strain rate and required frequency for the laser. CFD simulations have been conducted by varying chip thickness, t, in a range of 0.025 - 0.125 mm and contraction ratios, W_1/W_2, in the range of 10 - 14. Simulations have predicted that all of the chip dimensions examined, can achieve a strain rate close to ∼11,000 s^{-1} which is the target strain rate, as it has been previously found to promote aggregation for the proteins [1]. It has been also shown that by increasing the laser spot size from 3 mm to 6 mm (transparent width, table 4.3), the required frequency decreases, whereas the opposite happens when the spot size is decreased (figures 4.15a and 4.15b). As it is shown from figure 4.15b, the target strain rate is feasible to be obtained at the maximum laser frequency of the instrument which is 50 Hz, suggesting the maximum sample labelling at the target strain rate of ∼11,000 s^{-1} for a laser transparent width of 6 mm. However, the increase in laser spot size is an optimisation that could be conducted in the future. Standard FPOP experiments are conducted at a constant laser spot size of 3 mm, whereas it is shown from figure 4.15a, the target strain rate would correspond to a required laser frequency of 100 Hz, however as this exceeds the instrument's capabilities, the samples will need to be conducted at the maximum frequency of 50 Hz. This will imply that the as the strain rate can be determined by the flow rate and contraction ratio, the laser frequency at 50 Hz will imply to the 50% sample labelling.

4.5.3 Pressure drop-contaction ratio (W_1/W_2) effect

For the determination of the suitable chip design that can be first manufactured, the pressure drop can be also considered as a part of the decision process for the suitable chip. From the simulation results, it can be observed that the target strain rate is achievable

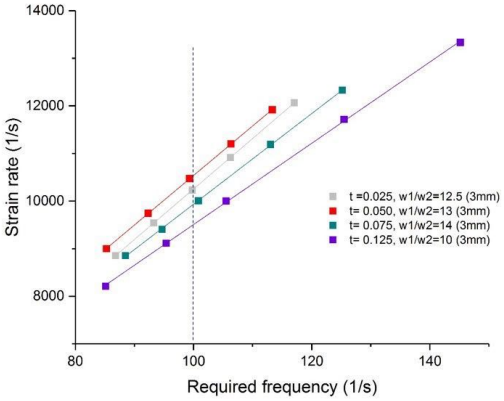

(a) Strain rate relation between required laser frequency for 3 mm spot size

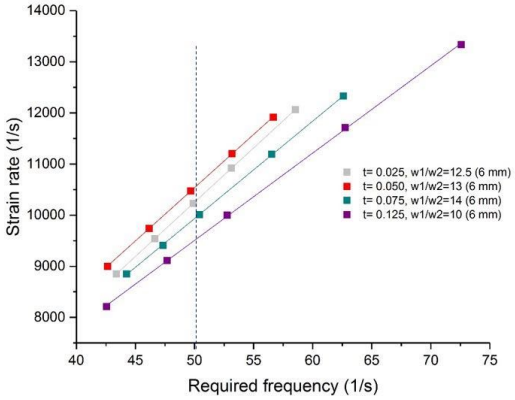

(b) Strain rate relation between required laser frequency for 6 mm spot size

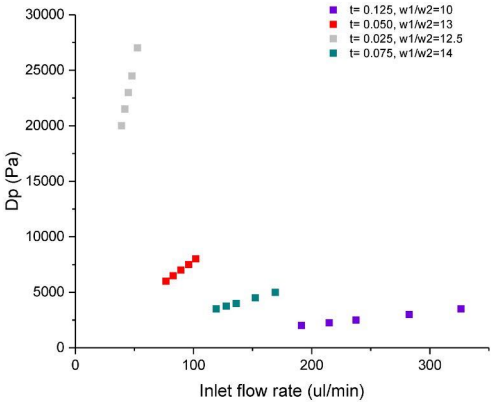

(c) Pressure difference (Dp) against inlet flow rate

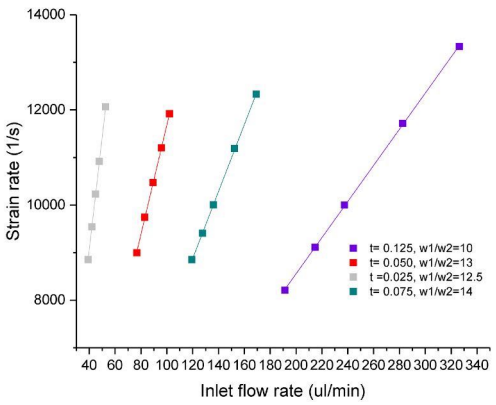

(d) Strain rate relation between inlet flow rate

Figure 4.15: Design optimisation studies investigating the effects of microfluidic dimensions on the strain rate, and pressure drop, Dp developed within the flow channel. 4.15a and 4.15b: Strain rate against required laser frequency for laser spot sizes (transparent widths) of 3 mm and 6 mm respectively. 4.15c: Pressure drop, Dp against inlet flow rate. 4.15d: Strain rate against inlet flow rate. Flow channel thickness, t and contraction ratio W_1/W_2 parameters have been investigated as sets: t=0.125 mm & W_1/W_2=10, t=0.05 mm & W_1/W_2=13, t=0.025 mm & W_1/W_2=12.5, t=0.075 mm & W_1/W_2=14.

for all the chip dimensions investigated. Hence, the pressure drop as well as the inlet flow rate, shown in figures 4.15c and 4.15d can be used for the determination of the suitable microfluidic chip design. Comparing the different chip dimensions, it is clear that each microfluidic design imposes different pressure and flow rate requirements. A balanced pressure drop and inlet flow rate combination can be determined as the basis

for determining the suitable chip for manufacture. Based on these set of requirements, the chip with t=0.05 mm and W_1/W_2=13 shown in red, best satisfy the requirements, achieving the target strain ∼11,000 s^{-1} at a flow rate of 90 μL/min. The selected flow channel is schematically shown as a CAD model in figure 4.17. Alongside the effect of channel thickness on the development of the target strain rate, the distinct effect of the contraction ratio on the development of strain rate was also investigated. An asymptotic fitting between contraction ratio and strain rate is shown, with the target strain rate to be achieved at contraction ratios (W_1/W_2) starting from 8, based on flow channel with thickness of 0.075 mm, as shown in figure 4.16.

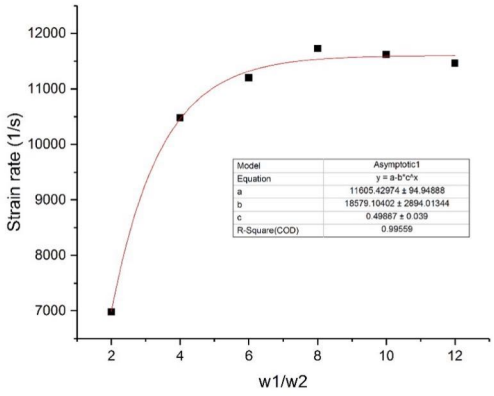

Figure 4.16: Effect of contraction ratio (W_1/W_2) on the development of the strain rate for a flow channel thickness, t =0.075 mm.

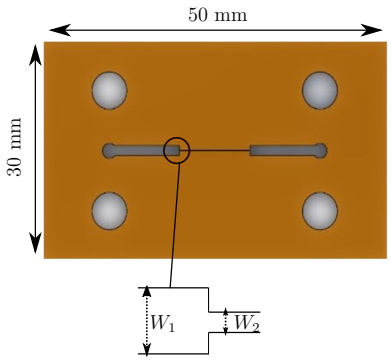

Figure 4.17: CAD model of the FPOP polyimide (kapton) flow channel with dimensions of 50 ×30 mm flow channel and with the contraction ratio (W_1/W_2) 13 (W_1=1.3 mm, W_2=0.1 mm) and channel thickness (t) 0.05 mm.

The design of the prototype device was conducted with the full components of the device to be presented in the next chapter, section 5.5. Computationally, the device is designed as a CAD model with a "sandwich" configuration (figure 4.18a), indicating its components as well as its mounting on the translation stage allowing the horizontal movement of the channel so as the laser labelling can be conducted at various channel locations (figures 4.18b, 4.18c), along with aluminium protection masks with wider and narrower window openings (figures 4.18d, 4.18e).

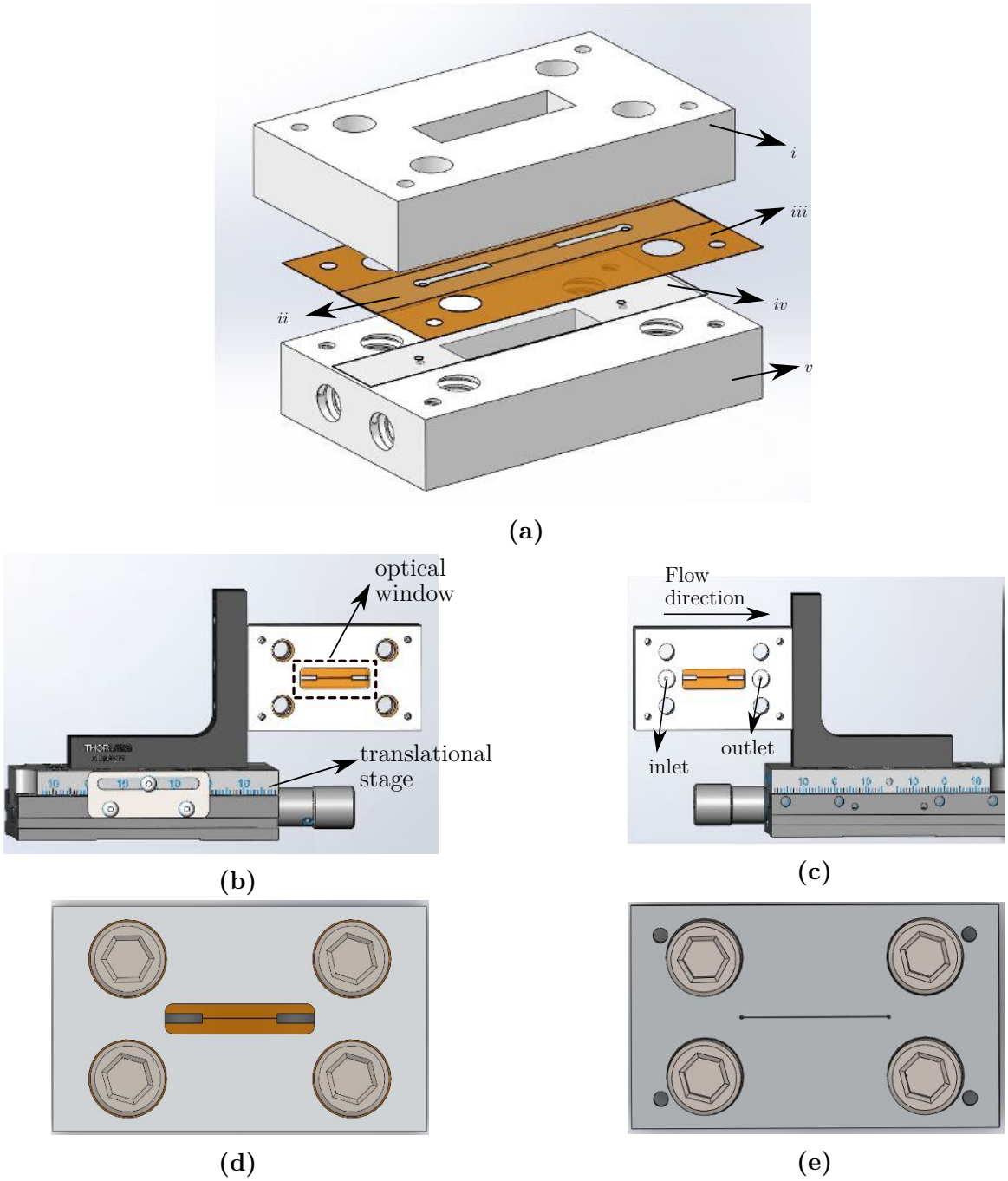

Figure 4.18: CAD model indicating the design of the FPOP microfluidic device. 4.18a: CAD model of the FPOP microfluidic prototype device annotated with its components including PMMA top part with optical window (i), UV glass window (ii), polyimide (kapton) flow channel (iii), UV- glass window with inlet and outlet openings (iv) and PMMA bottom part with optical window (v). 4.18b: CAD model of the integration of the FPOP microfluidic device with the optical window where the laser can be exposed, mounted on a translational stage, showing the front view. 4.18c: back view of the microfluidic device annotated with the sample inlet and outlet along with flow direction. Aluminium mask models with a 4 mm (4.18d) and 90 μm wide optical windows (4.18e).

With the use of a syringe pump, the samples will be introduced on the back side of the device using tubing fittings. The optical window, allows the visualisation of the channel to be exposed to the laser, which is sandwiched between two UV- glass slides compatible with the laser wavelength of 248 nm.

As the desired dimensions have been determined, the experimental setup can be then modified to accommodate the microfluidic device as schematically shown in figure 4.19, by aligning the flow channel with the capillary position to allow the laser modification to be conducted at the same vertical orientation as the capillary.

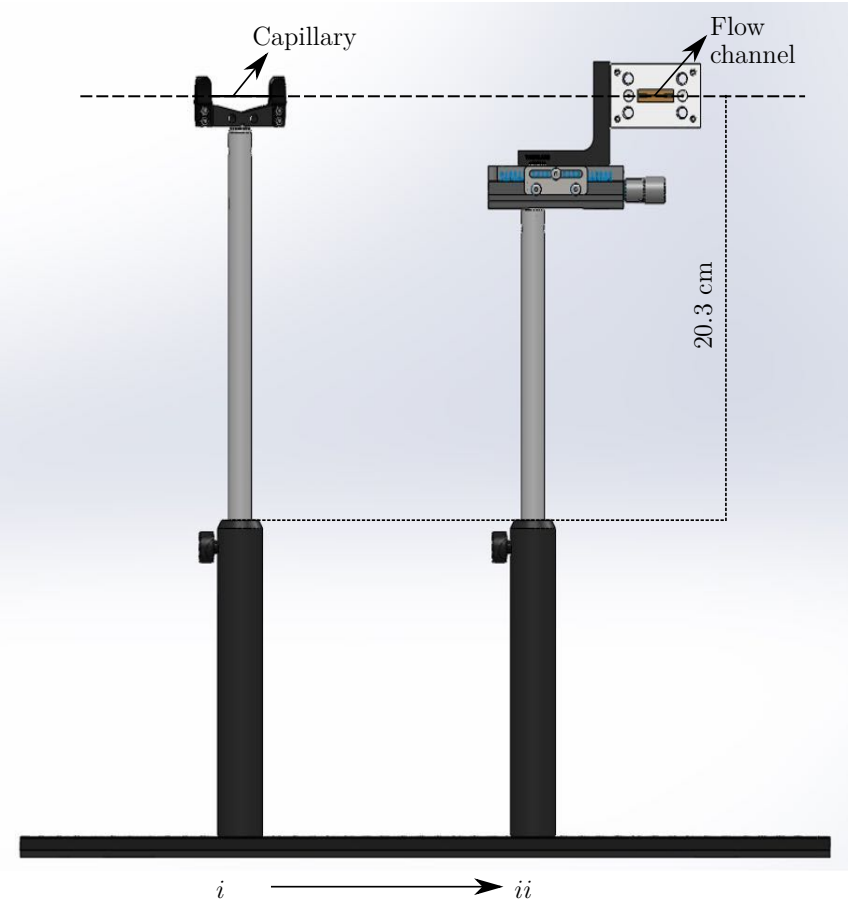

Figure 4.19: CAD model of the FPOP experimental setup, indicating the transition from the single capillary (i) typically used for the conduction of FPOP experiments, to the microfluidic device (ii). To ensure the laser is aligned to the sample, the capillary and flow channel are consistent at 20.3 cm in height by adjusting the optical post for the microfluidic device.

4.5.4 Timescale for laser labelling

Lastly, to ensure that the particular design will fit the experimental requirements, the time in which the laser labels the samples needs to be correlated with the time in which the samples are expected to spend within the extensional flow event where the flow rapidly accelerates. Based on the laser specifications, the laser pulse duration corresponds to 20

ns (0.02 μs), as previously shown in the table 4.3. The time in which the molecules are expected to spend within the extensional flow event for a range of strain rates is shown in figure 4.20. For the range of strain rates investigated, the expected time lies within a range of ∼200-280 μs, a 1000-fold increase with the respect to the pulse duration of the laser. Specifically, for the desired strain rate of ∼11,000 s^{-1} the molecules are expected to spend ∼210 μs within the extensional region. This implies that the time where the molecules will spend in the sudden contraction is suitable, allowing the laser to sufficiently label the samples.

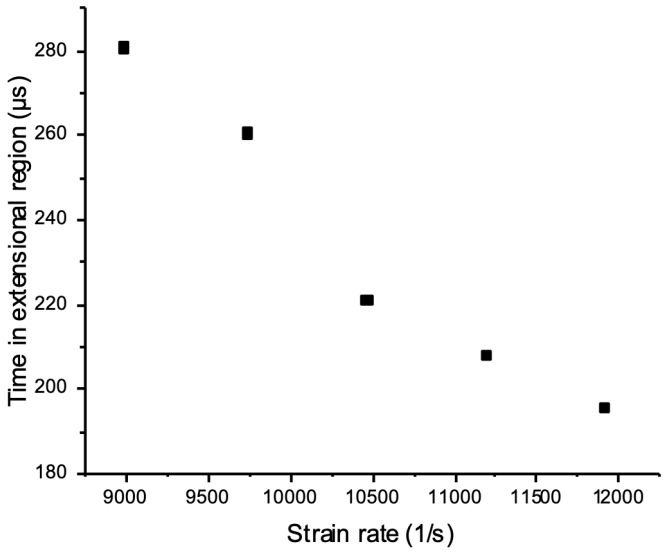

Figure 4.20: Calculated time in which the sample is expected to spend in the extensional point at the sudden contraction over a range of strain rate values. Time calculations are determined based on the selected flow channel with contraction ratio W_1/W_2=13 and channel thickness, t=0.05 mm.

4.6 Summary

In this chapter, the methodology followed for the computational characterisation of flow within a range of geometries is described. Firstly, flow is characterised within the extensional flow device consisting of the sudden contraction, allowing the extensional flow fields to be developed. A series of microfluidic geometries was also designed, allowing the multiple extensional flow events to be developed along the flow channel. In the last section of the chapter, the design and optimisation of a microfluidic device was described with the aim to be incorporated into biophysical techniques and particularly within an FPOP experimental setup, allowing the investigation of extensional flow events on the early stages of the unfolding pathway of proteins. Alongside the computational methods, experimental methods are described in the next chapter.

Chapter 5

Experimental methods

Chapter structure

In this chapter, the detailed description of the methodology followed, as well as the experimental setups used for the conduction of the experiments, are presented. The main sections covered are schematically shown in figure 5.1. The chapter firstly introduces the methodology which is followed for the protein preparation, followed by the surface treatment procedure in sections 5.1 and 5.2. Experimental techniques are then conducted by firstly investigating the protein adsorption on the various treated surfaces in the absence of flow contributions in section 5.3. Then the flow parameter is introduced by conducting experiments investigating the simultaneous effects of surface and flow in section 5.4. The next section, section 5.5, presents the development of a microfluidic device and its integration within a biophysical method (Fast Photochemical Oxidation of Proteins), which aims to investigate the early stages of protein unfolding under flow. The upcoming sections 5.6 and 5.7, describe the methodology conducted for the flow-induced aggregation characterisation, followed by a formulation characterisation section by the conduction of rheology experiments. Lastly, an overview of the main sections covered within the current chapter are summarised in the section 5.8.

5.1 Protein preparation

The preparation of protein-based pharmaceuticals involves their formulation into the desired buffer systems, and concentrations. Their preparation in the desired buffers ensures the limitation of pH changes that can be encountered during storage and handling, as the ability of various buffer systems to modulate pH variation has been reported in literature [222]. The antibodies used in the project, mAb1, WFL (MEDI1912), STT ($MEDI1912_{STT}$), MEDI8852 and MEDI3549 were all provided by AstraZeneca PLC, Cambridge UK and were stored at -80 ℃ as supplied, before use. Antibody solutions of mAb1, WFL and STT were prepared by dialysing thawed stock protein into filtered (0.22 μM PVDF membrane filters (Durapore, Sigma)) and degassed 150 mM ammonium acetate solution, pH 6.0 (Sigma) for three hours at 4 ℃, using a 3 kDa MWCO dialysis tube (Generon).

For those studies involving different formulation conditions, including Tween 20 (PS20), the dialysis procedure was performed as above, except the antibodies were dialysed into

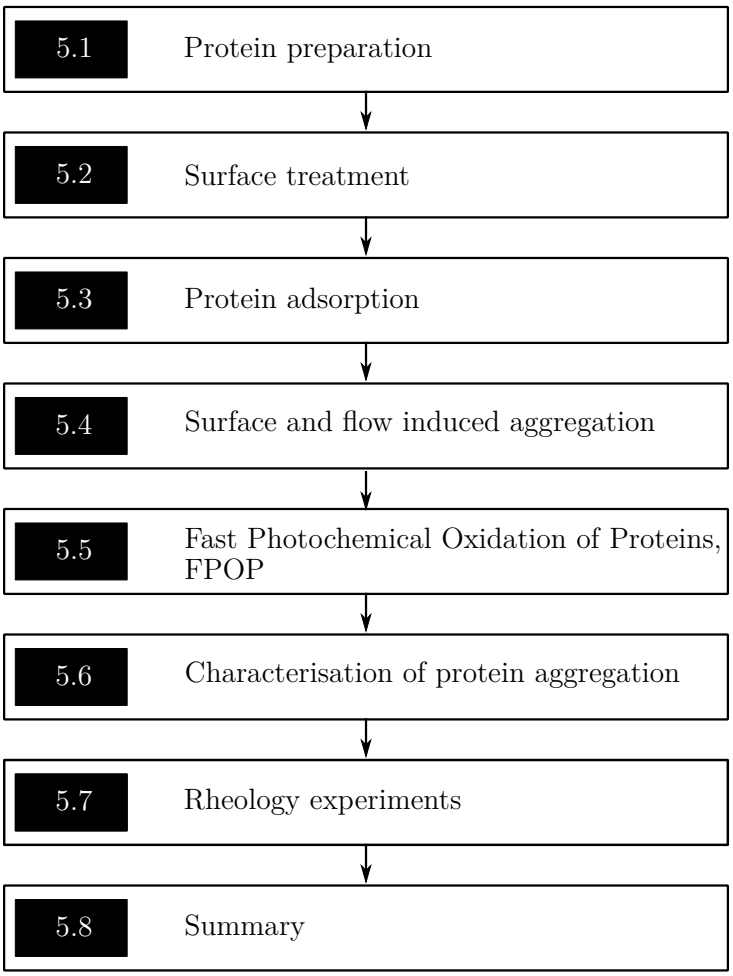

Figure 5.1: Overview of the main methodologies followed in experimental methods chapter.

filtered (0.22 μM) and degassed 150 mM ammonium acetate + 0.1% (v/v) Tween (R) 20 (UltraPure: National Diagnostics), pH 6.0 or 125 mM L-arginine (Acros Organics) + 20 mM sodium succinate (Sigma) pH 6.0. Protein samples were then filtered through a 0.22 μM syringe filter and kept on ice. The concentration of the solutions was determined using UV-visible spectrometry (UV-1800, Shimadzu, UV spectrophotometer) using the molecular weight values and extinction coefficients, ϵ_{280} as shown in table 5.1. The samples were then adjusted to a final concentration of 0.5 mg/mL, where most experiments were carried out.

For studies involving higher concentrations (>0.5 mg/mL), using MEDI8852 and MEDI3549 as model proteins, samples were prepared in the desired concentrations by the dilution of their initial stock concentrations (50 mg/mL) using 235 mM Sucrose (Fisher Scientific), 25 mM Histidine (Sigma), pH 6.0 into the desired sample concentration of 5-40 mg/mL.

Table 5.1: Summary of molecular weight and extinction coefficients of samples provided by AstraZeneca.

Protein	Molecular weight, (Da)	Molar extinction coefficient at 280 nm, ϵ_{280}, $(M^{-1}cm^{-1})$
mAb1	147,483	207,360
STT	148,107	228,440
WFL	148,422	239,440
MEDI8852	149,170	231,214
MEDI3549	204,466	321,012

5.2 Surface treatment

The surface modification will give insights into the understanding of whether the surface affects the aggregation process and whether the aggregation is induced by the combination of surface interaction and hydrodynamic forces.

To further investigate that, a surface modification of the parts where the proteins come in contact within the device (syringes, plunger, capillary) are modified by vapour (silanisation) and liquid deposition methods, which is described in the following section 5.2.1. Alongside the surface silanisation, the particular section explores another set of experiments, where the surface was modified by the covalent attachment of protein molecules on the equipment surface, which is then followed in section 5.2.2. Surface characterisation of silanised and protein labelled surfaces, is then followed by contact angle (θ) measurements, which will be described in section 5.2.3. Therefore, this section explores two types of experiments; experiments involving silanised surfaces inducing the change in the hydrophobicity of the surface (increasing the contact angle, θ), and experiments involving the modification of surfaces with protein attachment on the surface. The surface silanisation investigates the effect of the surface hydrophobicity-surface wettability, on the aggregation propensity

under flow. On the other hand, the protein attachment on surface experiment, investigates whether the conformational state of a protein which is already landed on the surface equipment, affects the aggregation propensity of the proteins while they are exposed to flow. As previously examined in [1, 2], the aggregation behaviour of various IgGs at the same concentration and buffer conditions has been examined using the extensional flow device. The intent of the particular set of experiment is to identify and compare any key differences regarding three proteins: STT, mab1 and WFL. The surface and flow effects are also investigated for a bispecific molecule, MEDI3549, with the largest molecular weight between the model proteins. The surface treatment process consists of three main steps including the surface cleaning step by the plasma treatment of the surfaces, followed by the surface modification via liquid or vapour deposition methods, and the characterisation of the surfaces via contact angle measurements as the final step of the process. The procedure is summarised schematically in figure 5.2.

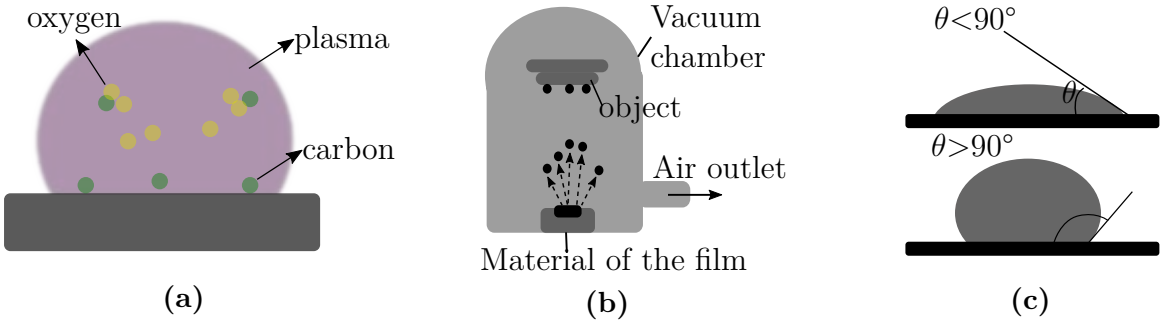

Figure 5.2: Surface treatment process schematic. Firstly, the surface is plasma treated (5.2a), then treated using PVD within a vacuum chamber (5.2b) and finally is characterised by contact angle measurements (5.2c).

5.2.1 Self Assembled monolayers, SAMs

The generation of monomolecular films of molecules on a range of substrates can be carried out by the method of Self-Assembled Monolayers (SAMs). The field was first reported by Zisman [32, 223] where the formation by adsorption of a surfactant monolayer onto a metal surface was firstly published. Following studies since then have focused on the underlying formation process and characterisation of surface properties [223]. The understanding of self-organisation, structure-property correlations and interfacial phenomena can be developed through the use of SAMs. As reported in [32], due to the flexibility of the variation between head and tail groups of SAMs systems, phenomena involving intermolecular competition, interactions between molecular-substrates/solvent interactions including growth, adhesion, lubrication and corrosion can be better understood.

Silanes are important in the preparation of SAMs as they can be used into the attachment to various substrates such as silicon and glass which contain hydroxyl or oxide groups [224]. Organosilane SAMs are significantly stable mechanically, thermally and chemically

due to the strong immobilisation through siloxane bondings [223–226]. The preparation of SAMs can be performed by immersion in solution and also by Chemical Vapor Deposition (CVD) methods encountered by the adsorption from the gas phase in a vacuum chamber [227]. The preparation at the solid/liquid interface is most commonly used, but besides the liquid phase, self-assembly at the vapour-solid deposition method is also an alternative method. Particularly, for the conduction of the experiments which will be described in the next sections, the vapour deposition method was applied for the surface modification experiments. The advantage of vapour deposition method is the reproducibility of homogeneous, covalently bonded and high density functionalised silane films. Vapour phase method corresponds to a cleaner approach as the surface is not exposed to impurities contained in solution, allowing also the control of the amount of moisture in the deposition chamber, which limits the self-polymerisation of the silane [31]. The one exception is where a liquid deposition method is applied, when using PEG solution, where the substrates are immersed into the solution.

Silane selection

The surface library, was constructed based on the degree of hydrophobicity of reported silane agents, as summarised in table 5.2. The selection of the desired silanes was based on various levels of hydrophobicity, allowing the aggregation propensity of proteins to be investigated in a range of surfaces exhibiting either hydrophilic or hydrophobic profiles. Based on the most commonly used silanes as found in literature, the most hydrophilic silane agent corresponds to APTES with reported contact angle, θ within a range of 41-59°. Alternatively, the most hydrophobic silane agents with increased contact angle corresponds to various silane agents including dodecyltriethoxysilane (θ=102°), FDTS (θ=100-110°), OTS (θ=100°) and FAS (θ=100-110°).

Table 5.2: List of most commonly used silanes found in literature along with their wettability properties-contact angle values.

Silane	Contact Angle, θ (°)	Reference
Hexamethyldisiloxane (HMDSO)	75-90	[228]
Dodecyltriethoxysilane	102	[229]
3-Aminopropyltriethoxysilane, (APTES)	41-59	[230], [231]
(3-Isocyanatopropyl)triethoxysilane	65-72	[232]
(3-Glycidyloxypropyl)triethoxysilane	49	[233]
Perfluorodecyltrichlorosilane, (FDTS)	100-110	[234]
Poly(dimethylsiloxane)	97	[235]
n-Hexyltrimethoxysilane, (HTS)	90	[236]
Methyltrimethoxysilane	80-87	[237], [236]
n-Octyltriethoxysilane	80.4	[236]
Octadecyltrimethoxysilane, (OTS)	100	[238]
Fluoroalkylsilane, (FAS)	100-110	[234]

Three silanes of interest have been then selected, and the surface library constructed to

investigate the surface effect under flow is shown in table 5.3. The choice of the particular silane agents corresponds to hydrophilic and hydrophobic surfaces. The surface library consists of the silane with the smallest contact angle as reported in literature corresponding to APTES (Silane A), FDTS (Silane C) as the silane agent with the maximum contact angle, and HTS (Silane B) corresponding to a surface with an intermediate contact angle (θ=90°) between the lower and upper contact angles of Silane A and silane B respectively. The library also includes a PEG agent, mPEGMA exhibiting hydrophilic properties. PEG has been extensively used as a protein surface-resistant coating material. According to the manufacturer (Sigma), poly (ethylene glycol) methyl ether methacrylate (mPEGMA) is often used to create PEG modified surfaces and surface grafted polyethylene glycol (PEG) prevents protein absorption. It is also reported in literature that the passivation of microfluidic systems with the particular coating is desired, as it is a high biocompatible material, and rejects protein adsorption among others (platelets) efficiently [239].

Table 5.3: Surface library constructed for the investigation of surface-flow interactions.

Surface	Chemical agent additive	Chemical formula
PEG	mPEGMA	$H_2C{=}C(CH_3)CO_2(CH_2CH_2O)nCH_3$
Glass	-	SiO_2
Silane A	APTES	$H_2N(CH_2)_3Si(OC_2H_5)_3$
Silane B	HTS	$CH_3(CH_2)_5Si(OCH_3)_3$
Silane C	FDTS	$C_{10}H_4Cl_3F_{17}Si$

Vapour deposition

The surface treatment procedure, which is shown schematically in figure 5.3, includes the surface cleaning by plasma treatment removing any hydrocarbon contamination from the untreated surface, which is then chemically functionalised by surface reactions using the selected silane agents shown above (table 5.3). The borosilicate syringes, capillaries, and float glass slides (for contact angle measurements) were cleaned by exposure to air plasma (using a Gala Instruments-PlasmaPrep2 cleaner) for 10 minutes to ensure the removal of contaminants and to introduce hydroxyl groups (-OH) onto the bare glass surface prior to modification. Surfaces were derivatised with silane A (3-Aminopropyltriethoxysilane APTES 98%; A10668, Alfa Aesar)), B (n-Hexyltrimethoxysilane, (HTS 97%; L03576, Alfa Aesar), or C (1H,1H,2H,2H-Perfluorodecyltrichlorosilane, FDTS 96%; L16584, Alfa Aesar) via evaporation of the silane solution under vacuum. The procedure followed to conduct the silanisation of the surfaces is based on the silanising glassware protocol found from current protocols in molecular biology [240].

Each was prepared by adding 1 mL of silane to a 5 mL beaker located within a desiccator containing the surfaces (syringes and capillary) along with a flat glass slide. The system was then evacuated by attaching a vacuum pump to the desiccator for a period of 5 minutes. The vacuum pump was then detached, and the system was left under vacuum

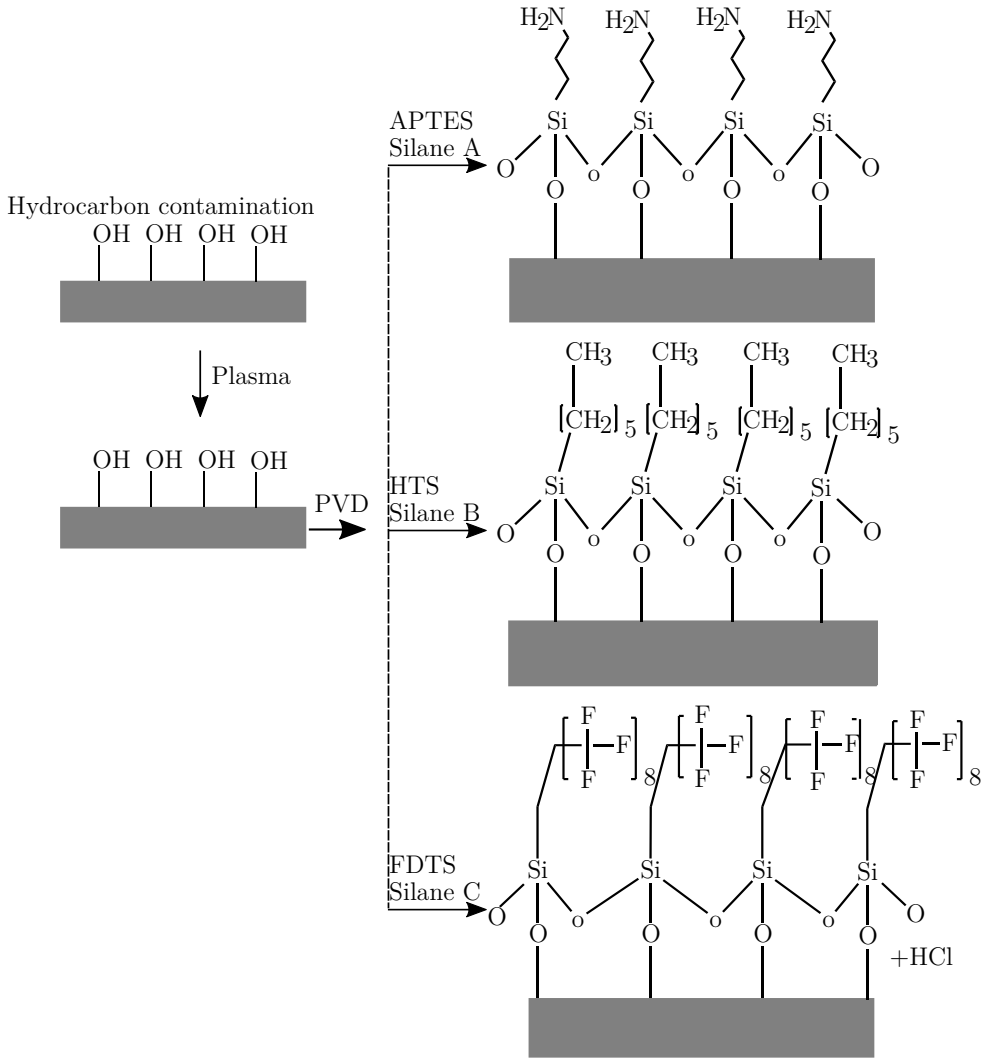

Figure 5.3: Schematic illustration of the surface treatment by contamination removal via plasma treatment. Surface cleaning has been accompanied by PVD followed by the preparation of chemically functionalised SAMs surfaces by surface reactions, using APTES (Silane A), HTS (Silane B) and FDTS (Silane C). Adapted from [28–31].

overnight.

Liquid deposition

For the surface treatment using the mPEGMA solution, a liquid deposition procedure is followed, which is schematically shown in figure 5.4. The formation of the particular SAMs is conducted by the immersion of the desired substrates into the solution of the surface-active mPEGMA. For mPEGMA (Poly(ethylene glycol) methyl ether methacrylate; 457876, Sigma Aldrich), surfaces were incubated in the PEG solution (50 wt.% in H_2O) overnight by simple immersion as indicated in figure 5.4. Samples were then removed, washed with 2% (v/v) Hellmanex II solution (Hellma analytics) and then rinsed with Milli-Q ddH_2O and characterised by contact angle measurements, described in the next section 5.2.3.

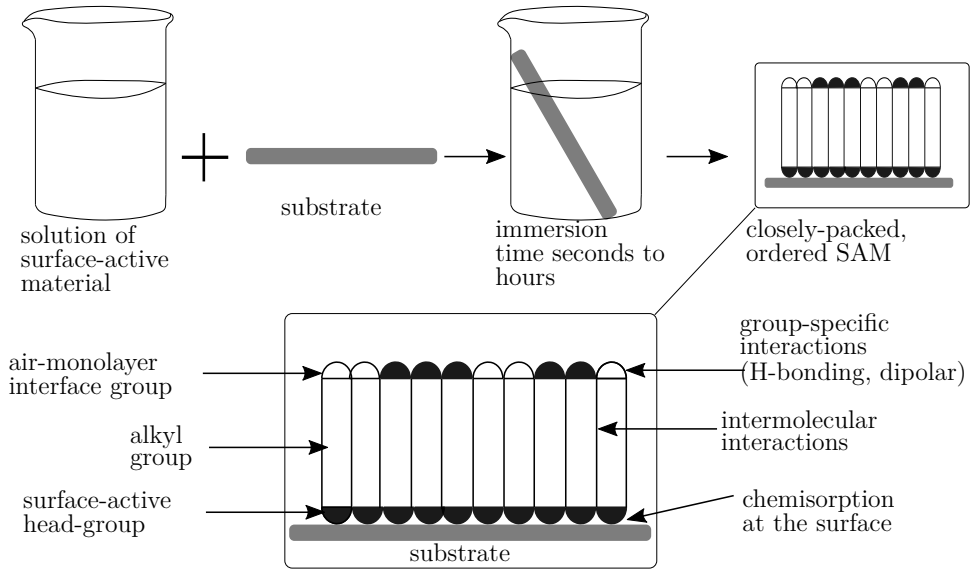

Figure 5.4: Formation of SAMs by simple immersion of the substrate into a solution of the surface-active material. The driving force for the formation of the assembly includes chemical bond formation with the surface and intermolecular interactions. Adapted from [32].

5.2.2 Antibody binding on surface

The determination of surface's role into the aggregation pathway can be established by the investigation of protein-surface and protein-protein interactions. The surface modification was previously described by the use of silanes and polyethylene glycol solutions, with a view to investigate the protein-surface interactions. Moving forwards, the protein-protein interactions in the presence of various underlying substrates can be established by the protein attachment on surface.

Physical adsorption

Protein immobilisation on the surface can be established by physical adsorption and chemical modification. Physical adsorption corresponds to the simplest method for immobilisation of antibodies with the limitation in the control of the antibody orientation, and it is usually correlated with poor binding and denaturation [7, 241]. The occurrence of the physical adsorption between antibodies and solid substrates is based through hydrophilic, hydrophobic and van der Waals forces [7, 242, 243]. Typical solid substrates include plastic (polystyrene and silicone), membranes and various metallic surfaces [243].

Chemical modification

Protein immobilisation on the surface can also be established by chemical means, including the formation of strong covalent bonds between the protein and the substrate of interest. The attachment between the protein and the substrate is characterised as efficient and irreversible through the bonds formed between the functional groups located at protein's surface and properly modified substrates [244].

Covalent protein attachment on surface

To investigate whether the surface wettability or the conformational state of the protein is responsible for inducing aggregation under flow conditions, covalently attachment of STT and BSA proteins is performed on the equipment surface. STT protein has been selected for its covalent labelling on the equipment surfaces due to its previously characterised aggregation resistant profile [1]. As reported in [7, 241], during the immobilisation of antibodies on surfaces, there is limited control of the antibody's orientation on the surface, which is linked with potential denaturation. As the particular protein has been previously characterised and showed that it exhibits enhanced molecular stability under flow, it is selected as a suitable protein for the covalent attachment on surface under flow. BSA is also selected as it is the most common protein used as a passivation technique reducing unspecific binding of biomolecules [239], and it is also among the most common model proteins for the study of the organisation of biomolecules on functionalised surfaces [245]. The experimental procedure for the covalent attachment, which will be described next, has been conducted by Dr Leon Willis.

The surface functionalisation was conducted on surfaces (glass slides and syringes) which were firstly treated with APTES (Silane A). Glass slides were also functionalised for their further surface characterisation using AFM which will be described in section 5.3.2. STT and BSA were covalently attached to APTES glass slides by dialysing both proteins into 20 mM sodium phosphate (Sigma Aldrich), 400 mM NaCl (Fisher Scientific) pH 7.2 overnight, then diluting the filtered stocks to a concentration of 0.5 mg/mL. A 50 mM stock of BS3 cross linker (XL) (Thermo Scientific) was prepared in double-distilled water,

ddH_2O according to the manufacturer. To functionalise the APTES syringes (which were prepared by the author and previously described in section 5.2), XL was added to the protein solutions such that the final [BS3] was a 50x molar excess. After mixing, 1 mL of the solution was drawn into each water-rinsed syringe and laid on ice for two hours. The remaining solutions were respectively pipetted onto two APTES-functionalised glass slides (in a tray on ice), covered over and left for two hours on ice. After two hours, 150 μL of 1M Tris was drawn into the syringes and the syringes inverted several times to mix and quench the reaction. In the slides case, the Tris was pipetted onto the reaction solution with repeated aspiration. The quenching reactions were left at room temperature for 15 mins. The solutions were discarded, with the glass components and syringe barrels rinsed extensively with ddH_2O, before drying under nitrogen gas. STT protein was then exposed to the covalently modified surfaces under extensional flow. All samples, stressed in the extensional flow device, were subjected to 0-500 passes at a plunger velocity of 8 mm/s. The quiescent control was incubated for the longest experimental time at 500 passes, corresponding to 50 minutes (3,000 s, 1 pass = 6 s). Samples were quenched after stress by placing them on ice.

5.2.3 Contact angle characterisation

As a part of the project is based on the modification of surfaces within the flow-based device that come in contact with proteins, the contact angle is useful to determine surface characteristics. Contact angle, is usually used to express the wetting behaviour of solid surfaces by a liquid. It can be expressed mathematically by a thermodynamic equilibrium between surface tension faces corresponding to solid, liquid and gas, given by Young's equation, equation 5.1.

$$\gamma_{LV} \cos\theta = \gamma_{SV} - \gamma_{SL} \tag{5.1}$$

where:

γ_{SV}= solid - vapour interfacial tension

γ_{SL}= solid - liquid interfacial tension

$\cos\theta$= contact angle

The degree of wetting of a solid surface can be detected by the contact angle measurements between the solid and liquid interaction, as it is shown schematically on figure 5.5. High wettability implies when the contact angle is considered to be small, ($<<90°$) whereas large contact angles ($>>90°$) correspond to low wettability.

Surface derivatisation was validated by quantifying the wetting behaviour of each surface by a water contact angle measurement. Static contact angles of a 20 μL water droplet at

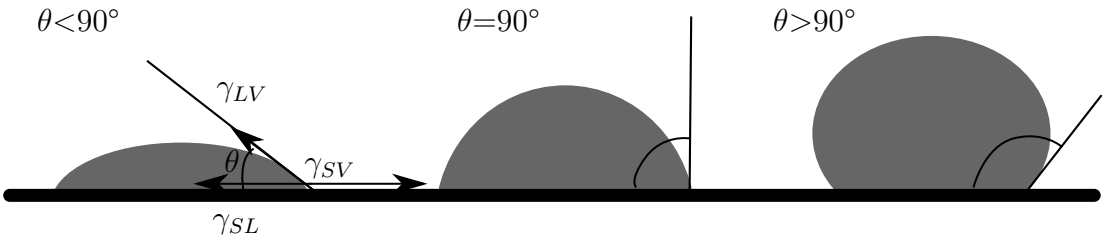

Figure 5.5: Contact angle illustration on a smooth homogeneous solid surface. Adapted from [33].

pH=7 placed on the surface of each derivatised float glass slide (soda-lime glass, 631-1552; VWR) were measured using a goniometer (CAM 200, KSV Instruments LTD), as shown in figure 5.6 at room temperature. The data were analysed using the CAM2008 software supplied with the instrument, and the final contact angle was taken from the average of ten independent measurements.

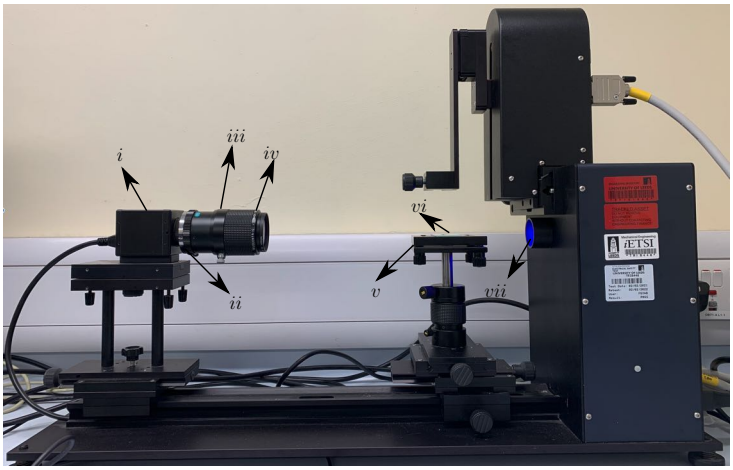

Figure 5.6: CAM 200 goniometer with annotated physical features including real-time FireWire camera (i), lens aperture adjustment (ii), camera zoom lock (iii), camera lens zoom adjustment (iv), sample stage (v), sample (vi) and LED light source (vii).

5.3 Protein adsorption

To understand the effects of surface modification on protein interactions, adsorption experiments have been conducted in the absence of any flow events. Here in this section, the experimental investigation of protein affinity on the various surfaces is described.

5.3.1 Quartz Crystal Microbalance with Dissipation, QCMD

Surface adsorption has been determined using the Quartz crystal microbalance with dissipation technique (QCMD), which allows the determination of protein mass and thickness under the oscillation of the quartz crystal. The technique measures the frequency and dissipation shifts as mass starts to adsorb on the QCM sensor. The resonant frequency

of the crystal decreases as the mass adsorbed on the surface increases. For evenly distributed adsorbed layers which are thin and sufficiently rigid without dissipating energy and having small mass relative to the crystals mass, the adsorbed mass can be described by the Sauerbrey model [246]. The adsorbed mass Δm, under the referred conditions, is proportional to the frequency shift of the crystal, as it is shown in equation 5.2.

$$\Delta m = -\frac{C\Delta f}{n} \tag{5.2}$$

where:

$\Delta f =$ resonance frequency change (Hz)

$C =$ mass sensitivity constant ($\frac{ng}{cm^2 Hz}$)

$n =$ overtone number

Based on this equation, the calculation of the thickness of the layer can be determined. As for the case here where investigating the adsorption of proteins, the adsorbed layer does not represent a rigid oscillation as the system dissipates energy and the Sauerbrey equation is not a suitable model. Proteins tend to be hydrated as they are adsorbed on the surface as well as being highly viscoelastic; therefore they are not completely rigid [246]. Raw data was then analysed based on the Voigt viscoelastic model using mathematical equations to automatically fit the raw data of frequency and dissipation shifts to the parameters of interest such as protein thickness. The Voigt viscoelastic model, which was analysed in [247], is described by equation 5.3 and corresponds to a spring and a dashpot arrangement under no slip conditions. In this system, the quartz plate is treated as a harmonic oscillator described by a wave equation for bulk shear waves propagating in a viscoelastic medium.

$$G^* = G' + iG'' = \mu_1 + i2\pi f \eta_1 \tag{5.3}$$

where:

$G^* =$ complex shear modulus

$G' =$ storage modulus

$G'' =$ loss modulus

$\mu_1 =$ shear elasticity

$f =$ resonance frequency

$\eta_1 =$ viscosity

The model relates the QCMD responses of frequency (Δf) and dissipation (ΔD) shifts to the thickness and viscoelastic properties of the adsorbing layer. The developed equations linking the parameters of interest with the raw experimental data are extensively described in [247].

For the QCMD experiments, a Q-SENSE E4 (Biolin Scientific Holding, AB., Stockholm, Sweden) was used as shown in figure 5.7, with samples loaded using a four channel peristaltic pump (Ismatec IPC-N 4) onto silicon dioxide layer sensors (QCM 5 MHz; 14 mm; Cr/Au/SiO_2; Quartz Pro, Sweden). The silicon dioxide coated layer sensors were selected in order to correspond to the chemistry of the syringe glass surface of the EFD device, which is borosilicate glass (with silicone dioxide composition of ∼74% [248]). For the surface modification experiments, QCM sensors were modified as described in section 5.2. The frequency and dissipation measurements have been recorded using QSoft software for number of overtones (n= 3, 5, 7, 9, 11, 13).

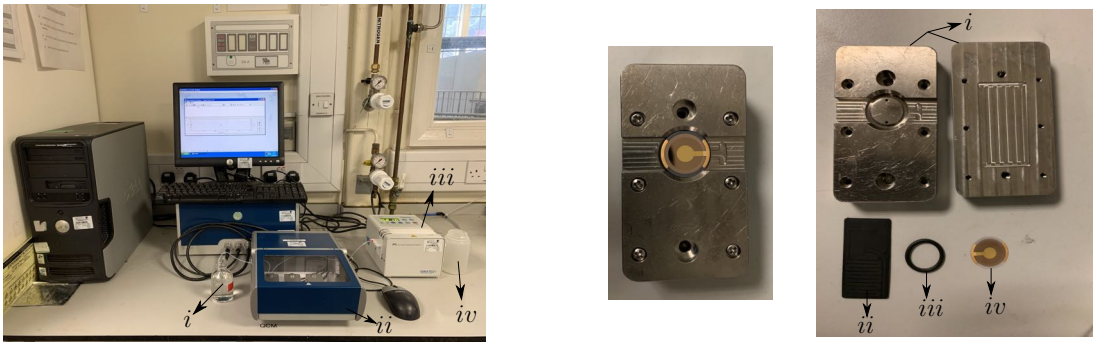

(a) **(b)**

Figure 5.7: QCMD experimental setup with annotated physical features. 5.7a: inlet sample (i), Q-SENSE E4 analyzer (ii), peristaltic pump (iii) and outlet-waste collection tube (iv). 5.7b: flow module metal pieces (i), sealing gasket (ii), o-ring (iii) and QCMD sensor (iv).

Firstly, the buffer solution was injected and allowed sufficient time to stabilise, for at least 10 minutes. After obtaining the buffer baseline, 0.5 mL of protein sample was introduced onto the sensor's surface. The sensor was then rinsed with fresh buffer until the baseline was re-established. All the measurements were conducted at a constant protein concentration (0.5 mg/mL) at a controlled temperature (25 ℃) at a flow rate of 0.21 mL/min. Raw data was then analysed using QSense Dfind software, using the Voigt viscoelastic model described above. New QCM sensors were used for each experiment to reduce contamination effects. Thorough cleaning was also conducted on the flow module by the immersion of all flow parts (fig. 5.7b) (metal piece, sealing gasket, o-ring) in 2% (v/v) Sodium Dodecyl Sulfate (SDS; 10%; Severn Biotech Ltd), followed by immersion in an ultrasonic cleaning bath (U100H; Ultrawave) in the 2% (v/v) Sodium Dodecyl Sulfate solution for 10 minutes at a maximum controlled temperature of 40 ℃.

5.3.2 Atomic force microscopy, AFM

Atomic force microscopy experiments (Multimode, MM2; Bruker) have been performed to characterise the surfaces modified with the cross-linked proteins as described in section 5.2.2 and used to establish the surface topography. Glass slide samples were firstly cut into smaller pieces to allow their fit to the sample stage of the instrument. Samples were then attached to 15 mm AFM specimen discs (AGF7003, Agar scientific) with epoxy resin and allowed to sit until the epoxy adhesive was cured (∼30 minutes). Samples attached with the metal disks were then mounted to the magnetic sample holder of the instrument. With the sample in place, the AFM head was mounted securely. Once the head was installed, the microscope of the instrument was then aligned on the translational stage at the bottom of the AFM base. The probe holder was then mounted, and the microscope was then adjusted in order to bring the tip into the optical microscope field of view. The microscope was then focused on the sample surface and the sample stage was then adjusted such as the sample was closer to the tip surface.

The laser was then aligned on the cantilever tip and the laser spot was then directed to the end of the cantilever using the laser adjustment knobs located on the top of the AFM head. The laser alignment was also ensured by monitoring the SUM signal display of the instrument. As the laser spot approaches the AFM probe (RTESP-300; Bruker), the SUM reading was increased. The laser mirror was then adjusted using the mirror tilt lever to maximise the SUM signal reading, which indicates the total voltage generated by the position sensitivity photodetector. The voltage value changes according to how much of the beam falls on the photodetector. The photodetector was then aligned by adjusting the photodetector knobs to reduce the values of the vertical deflection (VERT) and horizontal deflection (HORZ) close to zero. The mode of the instrument was then adjusted to tapping mode by enabling the TM AFM (tapping mode) option.

The experimental steps required for the imaging were then set using the NanoScope software by specifying the cantilever type and operation mode. The cantilever was then tuned by modifying the drive frequency, which was set lower than the resonance peak of the cantilever, as it has been found that the microscope produces better data in tapping mode by setting the drive frequency lower than the resonance peak of the cantilever, as reported in the "Bruker MultiMode 8, Standard Operating Procedure" laboratory manual. The drive frequency was set such that it coincides with ∼10% decrease in the vibration amplitude. After the cantilever tuning, the imaging properties were configured by specifying the scan size (5 μm), scan rate (0.992 Hz) and samples/line (768). Once all the parameters were checked and configured, the AFM platform was raised away from the table. The tip was then engaged to the sample surface and image scanning was started until the desired sample image scan was collected.

Samples have been imaged on air in tapping mode and data analysis was performed

in Nanoscope analysis software. The experimental procedure was conducted using the NanoScope software (NanoScope 8.15) where the experiment in air was selected.

5.4 Surface and flow induced aggregation

5.4.1 EFD experimental setup

The extensional flow device (figure 5.8) which has been previously developed in Leeds as a part of the study conducted in [1], shown in figure 5.8b consists of two modified borosilicate Hamilton syringes which are connected by a borosilicate glass capillary. A second device (figure 5.8a) has also been developed within this project to allow the conduction of multiple experiments in parallel by users. The extensional flow is developed by the sudden contraction between the syringes and capillary. Therefore, samples stressed within the device will be under the exposure of both hydrodynamic forces of shear and extensional flow.

The operation of the device has been handled by the use of an Arduino microcontroller, which has been programmed to determine the number of passes where the syringes will expose protein samples under shear and extensional events at constant plunger speed. The syringes are moved in both directions for one cycle using a lead screw stepper motor to achieve a linear motion of the syringes which is parallel to the direction of flow. For a single pass to be completed, the protein solution is shuttled from one syringe to the other until the final sample volume of 0.5 mL is loaded to the second syringe.

The device consists of two borosilicate Hamilton gas-tight syringes with an inner diameter of 4.6 mm connected via a borosilicate glass capillary (Sutter Instruments) with 0.3 mm inner diameter along with o-ring and compression fitting components, to allow flow sealing during the conduction of the experiment as shown in figure 5.8c. The full description of the EFD components can be found in detail under the caption of figure 5.8. The original surface of the device is made of borosilicate glass for the syringes and capillaries, polytetrafluoroethylene (PTFE) for the syringe plunger, and stainless steel for the syringe cap. A stepper motor controlled by an Arduino microcontroller was used to drive the syringe plungers for the desired number of passes and at a given plunger speed. The stressing experiments were conducted using the original untreated glass syringes and capillaries, as well as the modified glass syringes and capillaries.

The effect of hybrid equipment surfaces on the aggregation of proteins was also conducted, by the combination of multiples surfaces between equipment parts. The combination of surface treated surfaces corresponds to the rearrangements of the various surface components, which are the two syringes and capillary, in an array of device surfaces exhibiting multiple hydrophobic profiles. For clarification purposes, table 5.4 summarises the two sets of experiments employed for the construction of hybrid devices. The aim of

the construction of these hybrid equipment surfaces is to investigate the effect of surface within particular flow types found in syringes, before flow acceleration (low shear) and capillary, post flow acceleration (high shear). To investigate the effect of high shear flow region, the high flow region represented by the capillary is treated based on the surface library constructed and shown previously in table 5.3, whereas both syringes remained untreated (experiment 1). To investigate the surface effect of low shear region (syringes) the two syringes were treated based on the surface library whereas the capillary surface remained untreated (experiment 2).

Table 5.4: Construction of hybrid equipment surfaces (syringe 1, syringe 2 and capillary) of the extensional flow device. Experiment 1 investigates the effect of capillary surface (flow region of high shear). Experiment 2 investigates the effect of syringe surface (flow region of low shear).

Experiment	Syringe 1	Syringe 2	Capillary
1	Untreated	Untreated	Treated
2	Treated	Treated	Untreated

To carry out an experiment, a filtered protein sample was loaded into the device, avoiding the infusion of any air bubbles. The protein solution was shuttled between the two syringes via the borosilicate glass capillary at the desired number of passes and speed. Control samples (which can be also referred to as native or quiescent) were loaded into the EFD and incubated at ambient temperature for the length of the flow experiment, e.g., 100 passes takes 10 minutes. Once the control and stress experiments were complete, solutions were expelled from the syringes and stored on ice before quantification. Prior to the conduction of each experiment, the syringes were washed using a Hellmanex solution-II, followed by a buffer wash before the loading of protein samples.

5.4.2 Sliding interface

The contribution of shear flow effects on the aggregation, has also been investigated using a sliding interface setup, which is a partial modification of the EFD device as shown in figure 5.9. The variation of the sliding interface compared to the EFD is the absence of sudden contraction in the flow geometry, allowing the exclusive effect of plunger action on the flow induced aggregation to be investigated. The sliding interface consists of the same syringes as the EFD that have been modified by Yorlab supplier to accommodate a syringe plunger at the inlet part of the syringe additional to the outlet, as shown in the experimental setup in figure 5.10.

Experiments have been conducted using STT and WFL which represent molecules with extreme aggregation profiles, with STT having an aggregation resistant profile whereas WFL an aggregation prone profile. The samples have been both exposed to the sliding interface at the same plunger velocity (8 mm/s), however the experimental time in which

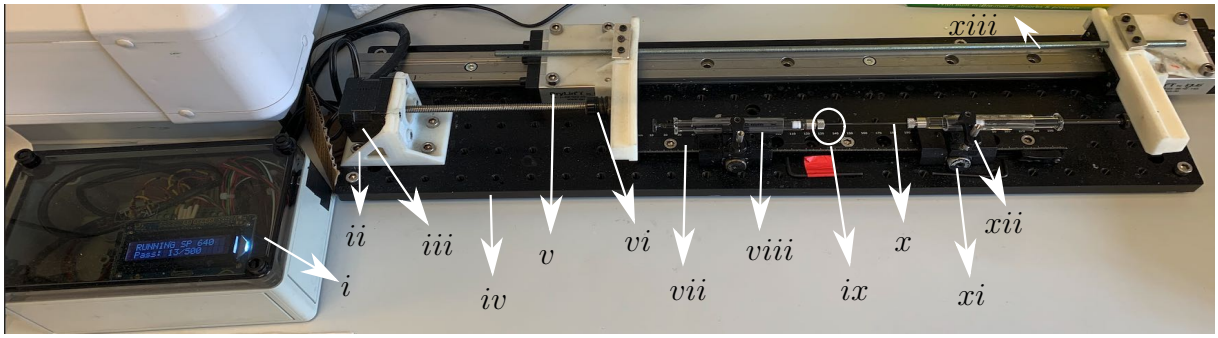

(a)

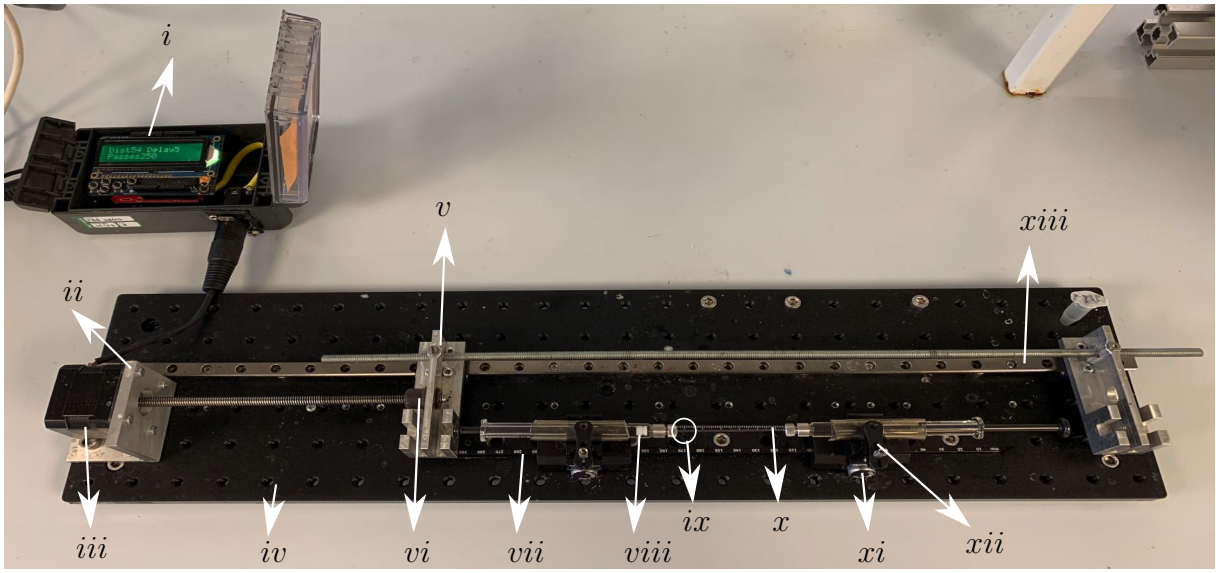

(b)

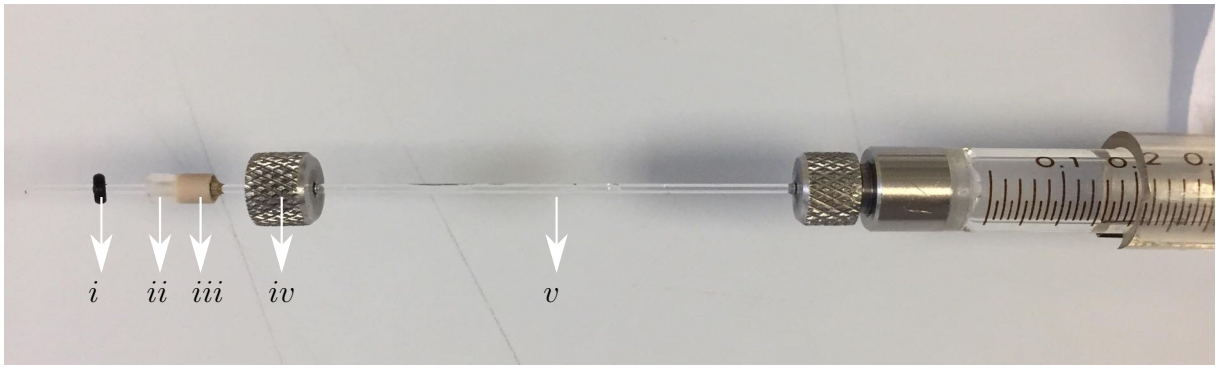

(c)

Figure 5.8: Extensional flow devices (EFDs) with annotated components and features. 5.8a & 5.8b: Project box with Arduino board (UNO) and LCD interface (i), motor mount (ii), stepper motor (Haydon Switch and Waterbury CT Instrument Co) (iii), mounting board (MB1560/M; Thorlabs) (iv), linear guide carriage (RS; Igus TW-01-20) mounted with syringe bracket as shown in 5.8a and syringe bracket shown in 5.8b (v), lead screw of the stepper motor (vi), dovetail rail (RLA300/M; Thorlabs) (vii), 1 mL syringe (1001 RN SYR; Hamilton) (viii), sudden geometry contraction (ix), borosilicate capillary (x), dovetail rail carrier (RC2/M)(xi), syringe clamp (VC1/M; Thorlabs) (xii), linear guide rail (5.8a: RS; Igus TS-01-20-600 T) (xiii). 5.8c: Rubber O-ring (P10; Gilson)(i), ferrule compression fittings (Hamilton) (ii &iii), stainless steel syringe cap (iv), borosilicate capillary (B100-30-7.5HP; Sutter instruments) (id=0.3 mm, length=7.5 cm) (v).

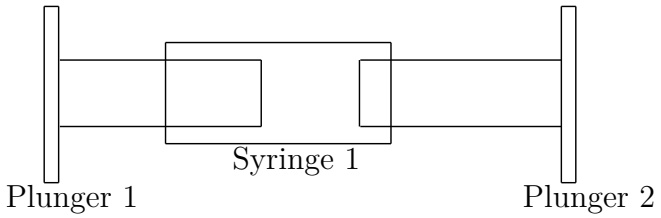

Figure 5.9: Schematic illustration of the sliding interface design consisting of a single syringe which is customised such as to accommodate two plungers in both sides.

they were exposed to the flow environment was 10 minutes for STT corresponding to 100 passes as it is resistant to aggregation, and 5 minutes corresponding to 50 passes for WFL as it is an aggregation prone molecule under flow. Sample preparation including surfactant formulation using PS20 has been followed as previously described in section 5.1. For further sealing support of the flow in the equipment consisting of a single syringe and to overcome any sample leak, plunger holders have been 3D-printed and integrated into the experimental setup for each plunger. Plunger holders have been first mounted to ensure that the setup is appropriate for the conduction of the experiment. To test the efficiency of the supporters, 100 passes have been conducted successfully using water as sample (0.5 mL) with no leaking observed using the plunger lock setup without the use of the upper parts of plunger supporters. The code controlling the stepper motor has also been modified to match the experimental time with the standard extensional flow experiment, using 2 s lag time between each pass.

5.4.3 Model protein formulation

Formulation studies investigating the interaction of protein and surfactant under extensional and shear flow have been performed at AstraZeneca (Cambridge) and Leeds. As a part of the collaboration between the University of Leeds and AstraZeneca, formulation studies are conducted in AstraZeneca (formulation department) using EFD as a flow test alongside other stress conditions found during shipping, which will be described in section 5.11. Initially, the studies have been performed in AstraZeneca using a library of surfactant molecules, as summarised in table 5.5. The surfactants have also been used at the same concentration of 0.02% (w/v) and spiked into the formulation buffer (235 mM Sucrose, 25 mM Histidine) from initial stock dilutions of 10% (w/v). The model protein for the conduction of the experiments was MEDI3549 (bispecific) which was diluted to a final concentration of 0.5 mg/mL from initial sample stock concentrated at 50 mg/mL.

For the studies conducted in Leeds, the pure surfactants as provided by the manufacturer, have been prepared at an initial surfactant stock dilution of 10% (v/v) or (w/v) (depending on the physical state of the surfactant as shown in table 5.5). To ensure accurate surfactant concentration needed for the experiments, pure surfactants at their initial physical state as supplied by the manufacturer, PS20 PS80, EL and HS15 have been heated on a hotplate

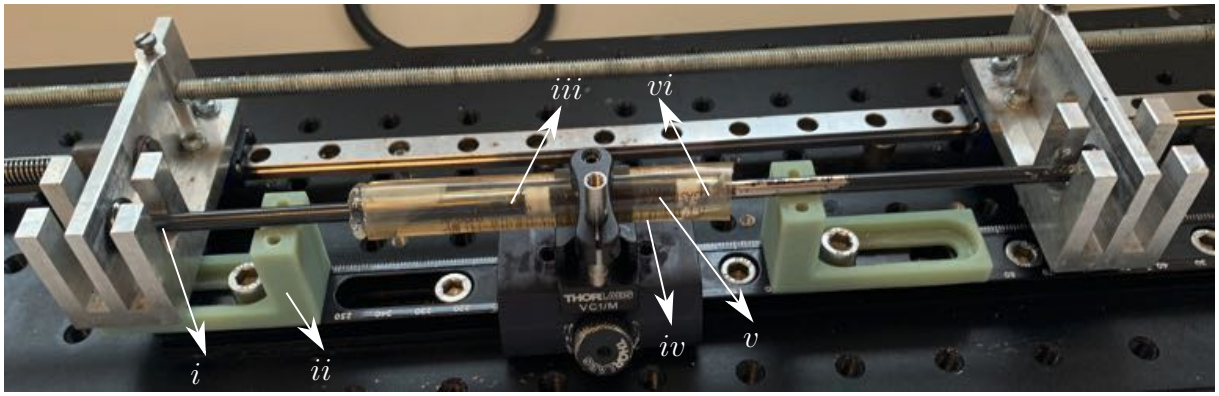

(a)

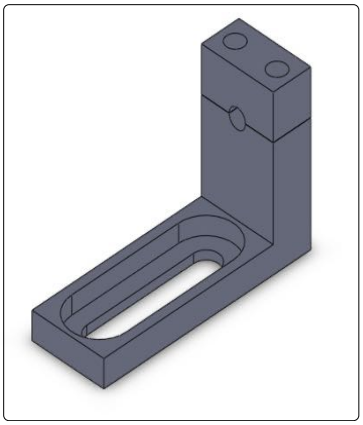

(b)

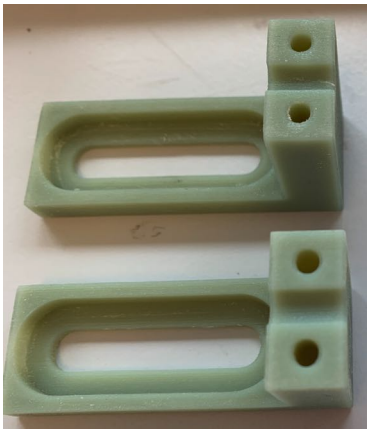

(c)

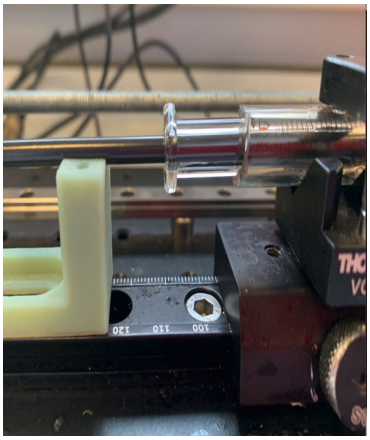

(d)

Figure 5.10: Sliding interface setup with annotated physical features and integrated plunger holders. 5.10a: plunger locked in syringe bracket for better alignment (i), 3D-printed plunger supporters (ii), PTFE plunger 1 (iii), modified borosilicate syringe barrel (iv), sample (v), PTFE plunger 2 (vi). 5.10b: CAD model for the plunger supporters, 5.10c: 3D-printed plunger holders and 5.10d: side view of plunger holder along with the syringe plunger.

Table 5.5: Surfactants along with their molecular weight (MW) values used for the conduction of the experiments in AstraZeneca along their determined CMC ratio relative to the concentration (c) used. Their physical state as received from the manufacturer is also stated. Polysorbate 20, PS20 (Tween (R) 20, UltraPure; National Diagnostics), Polysorbate 80, PS80 (4117-02; JT Baker), Kolliphor P188 (K4894; Sigma), Kolliphor HS15 (42966; Sigma), Kolliphor EL (C5135; Sigma).

Surfactant	c=0.02% (w/v)	MW (Da)	Physical state
PS20	∼3 × CMC	∼1228	liquid
PS80	∼20 × CMC	∼1310	liquid
P188	∼1 × CMC	∼8400	solid
HS15	∼2 × CMC	∼854	paste
EL	∼1 × CMC	∼3000	liquid

(SH2D; Stuart Scientific) until their viscosity is reduced, and until their initial state has been transformed into a liquid state, i.e., from paste (HS15). The dilution stock of P188 has been prepared as 10% w/v as its initial state is solid. 10% (w/v or v/v) dilution stocks are then prepared and thoroughly stirred to ensure a good mixing until the surfactant is evenly diluted and then filtered using 0.22 μL filters and stored at room temperature. Surfactants at the desired concentration were spiked into the formulation buffer of 235 mM Sucrose, 25 mM Histidine, pH 6.0. Three surfactant concentrations have been selected representing protein excess, equal proportion of surfactant and protein molecules and higher concentration representing excess of surfactant molecules at concentration closer or above to their CMCs as summarised in table 5.6. The protein excess ratio has been determined based on ANS experiments using fluorescence spectroscopy which will be described in section 5.6.3 and used to determine the CMC of the molecules formulated in the buffer used for the conduction of the flow experiments. Model protein for the conduction of the experiments was MEDI8852 (IgG1) which was diluted to a final concentration of 0.5 mg/mL from initial sample stock concentrated at 50 mg/mL.

Table 5.6: Surfactant concentrations used for the conduction of protein-surfactant flow experiments (MEDI8852 (0.5 mg/mL)-surfactants). Surfactant concentrations are also expressed as surfactant to protein ratio, S:P. Three surfactant concentrations have been used for each surfactant molecule representing protein excess (0.2:1), equal molecule proportion between surfactant and protein (1:1) and surfactant excess, (>CMC:1).

Surfactant	Surfactant concentration, (μM)	Respective surfactant to protein ratio (S:P)
PS20	0.67	0.2:1
PS20	3.35	1:1
PS20	67	20:1
PS80	0.67	0.2:1
PS80	3.35	1:1
PS80	67	20:1
P188	0.67	0.2:1
P188	3.35	1:1
P188	134	40:1
HS15	0.67	0.2:1
HS15	3.35	1:1
HS15	335	100:1
EL	0.67	0.2:1
EL	3.35	1:1
EL	83.8	25:1

5.4.4 Shipping simulator

Shipping simulation studies were performed according to the American Society for Testing and Materials (ASTM-D4169) which refers to the Standard Practice for Performance Testing of Shipping Containers and Systems. The shipping simulation studies have been kindly performed with Maria Bruque in AstraZeneca. For the conduction of the

experiments, 0.5 mL of sample (0.5 mg/mL MEDI3549) has been used in various surfactant formulations. EFD tests are performed in parallel along shipping simulator experiments. Samples, which have been packed and kept on ice, have been exposed to shipping simulator as shown in figure 5.11 (1000 TTV2 Vibration test system; Lansmont) at Truck Level II intensity of 0.517 Grms (2 hours) and Air level II intensity 1.052 Grms (2 hours). The study involved two cycles of Truck-Air-Truck for a total running time of 12 hours.

Figure 5.11: Shipping simulator.

5.5 Fast Photochemical Oxidation of Proteins, FPOP

Early stages of protein unfolding leading to further aggregation can be studied by FPOP. FPOP is a method which has multiple uses around the assessment of protein structure, folding and aggregation. To assess the protein structure and interaction during the exposure of proteins to extensional and shear flows, the application of FPOP can be employed, as it offers multiple advantages around protein structure elucidation. The technique allows the protein oxidation via the photolysis of H_2O_2 which is laser triggered. H_2O_2 and a scavenger (usually a free amino acid) are firstly mixed with the protein solution, before their laser irradiation. When the protein solution is laser irradiated, the photolysis of H_2O_2 produces hydroxyl radicals, OH in a nanosecond scale, which induce the hydrogen abstraction from the protein [14]. The detection of modified amino acids that can be considered to be important in possible conformational changes of the protein, results into the addition of

+16 Da mass additions induced by the reaction of the hydroxyl radicals with potentially any solvent accessible amino acid side chains [249]. The sample is then collected into a quenched solution containing catalyse and free methionine in buffer to remove leftover H_2O_2 and preventing post-footprinting oxidation artefact from any remaining reactive species [14].

The current setup of the FPOP experiment involves a flow system in which a fused silica tubing (FPOP capillary, figure 5.12), containing the sample of interest which is typically loaded at a flow rate of 20 μL/min, is placed perpendicular to a Compex 50 Pro KrF excimer laser beam (Coherent Inc., Ely, UK) at 248 nm. The laser gives a 3 mm irradiation window (transparent width) for the sample to be oxidised, with a firing frequency of 15 Hz and a pulse duration of 20 ns. Laser power was kept constant at 110 mJ. The choice of laser at the particular wavelength is due to the low absorbance of water and most proteins at 248 nm [14]. The sample is then collected in an Eppendorf tube containing quench solution.

This section describes the development of the current FPOP setup with a custom build microfluidic prototype device. The manufacture of the device was based on CFD simulations optimising the dimensions best accommodated the requirements of the particular experimental setup as previously described in chapter 4 (subsection 4.5.1). The manufacture of the microfluidic aimed to investigate and the ability of a microfluidic device to be accommodated into a current FPOP setup.

5.5.1 FPOP microfluidic experimental setup

The implementation of microfluidic chip devices into the FPOP method, will give insights into information regarding the aggregation behaviour during specific areas within the chip such as low shear, extensional and high shear region. FPOP allows the specification of the area under which the laser will shoot and modify the sample. With the flexibility of the FPOP, the suitable microfluidic chip design has been developed, so it can be incorporated into the FPOP setup.

Requirements for the microfluidic design

Various chip designs have been examined by performing CFD simulations as presented in the previous chapter (subsection 4.5.1), linking the laser frequency needed for high labelling from the laser in relation with the achievable centreline strain rate. This set of results described the design of the FPOP setup. Based on the simulation results where a variation on the dimensions of the chip has been performed and by comparing the different chip dimensions, it was shown that a balanced pressure drop and inlet flow rate combination can be determined as the basis for determining the suitable chip for manufacture. Based on these set of requirements, the chip with dimensions of channel thickness (t), t=0.05 mm

and contraction ratio (W_1/W_2) W_1/W_2=13, satisfied best the experimental requirements. From the computational simulations, it was shown that designing the device with the particular chip dimensions, the desired strain rate of ∼11,000 s^{-1} can be developed, which is the same amount of strain rate developed in the experiments using the extensional flow device. The simulations indicated that the flow rate required to achieve the desired strain rate, is 90 μL/min. Therefore, this ensures that the experimental setup is completed by identifying all the experimental conditions. Based on the computational simulations, it was also shown that the time in which the molecules will spend within the extensional flow region is calculated to be ∼210 μs which is longer than the duration of the laser pulse which is 20 ns. Thus, this ensures that the timescales of the molecules in which they can travel within the extensional flow region lies within the timescales of the laser irradiation.

Microfluidic components and experimental integration

Based on the referred requirements, and building from the computational simulations, the microfluidic prototype device has been manufactured and integrated within the current FPOP setup. The microfluidic device corresponds to a sandwich configuration consisting of multiple parts including an upper and bottom PMMA plate, the polyimide (kapton) flow channel which is covered by an upper and bottom glass slide (Spectrosil). The sandwich configuration, allows the integration of multiple layers, into the device, as well as the flexibility for their local treatment and allowing the replacement of the flow channel with other flow channels with desired dimensions and flow configurations depending on the experimental requirements. The use of hybrid devices, consisting of multiple layers, has been applied in in diverse applications, including the detection of infectious diseases and cellular studies [250].

The PMMA material, due to its low cost of manufacturing, easy of use and fabrication, is widely used in the fabrication of lab-on-a-chip microfluidic devices [250], and it is also selected as a component of the microfluidic device presented in the current work. The flow channel is introduced as a polyimide (kapton) sheet, due to the several reported advantages of polyimide. These include the high service temperatures, chemical stability, low water uptake and good biocompatibility [251]; as well as their bending flexibility properties allowing their integration into bent configurations as shown in [252]. The Spectrosil glass slide, is selected based on its transmission properties as given by the manufacturer (UQG Optics) reaching ∼90% transmission intensity (for a 10 mm thick sample) at the particular laser wavelength (248 nm). The full description of the device components, with the respective component dimensions, can be found in appendix A, figure A.1.

Initially, the FPOP setup consisted of a thin capillary shown in figure 5.12, where the flow channel (FPOP capillary) was then replaced with the microfluidic device as shown in figure 5.13 along its components as shown in figure 5.14. The microfluidic device

was designed to be incorporated into the current experimental setup, to configure the material properties needed to withstand the laser requirements of the instrument; therefore, biological experiments using the device were not conducted.

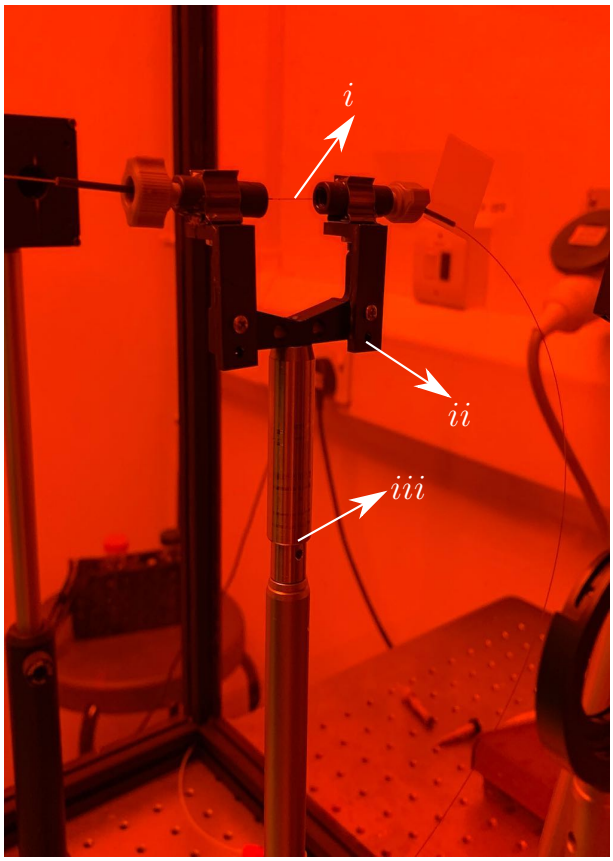

Figure 5.12: Typical FPOP experimental setup. Samples are loaded into a thin fused silica capillary (inner diameter: 100 μm) (i), supported by a stackable holder (Thorlabs) (ii) mounted on an optical post (Thorlabs) (iii).

The final flow channel dimensions of polyimide film were: 50×30×0.05 (mm). To expose molecules to extensional flow events, the flow channel was designed such as the flow is accelerated through a sudden contraction in the flow geometry, as annotated in figure 5.14a.

Mask alignment

As supplementary parts of the device, the design of aluminium masks as shown in figure 5.15 allow the laser protection of the PMMA top plate. The initial aluminium mask, as shown in figure 5.15a, is designed with an optical window of 4 mm, which is then updated to a thinner optical window. The full dimensions of both exterior masks can be found in appendix A, figure A.2. The update of the design has been done for the aluminium mask by ensuring the laser will be irradiated directly on the sample channel and not on the kapton sheet. The updated window size of the mask with the channel window corresponds to 90 μM as shown in figure 5.15b. The thinner optical window masks were designed

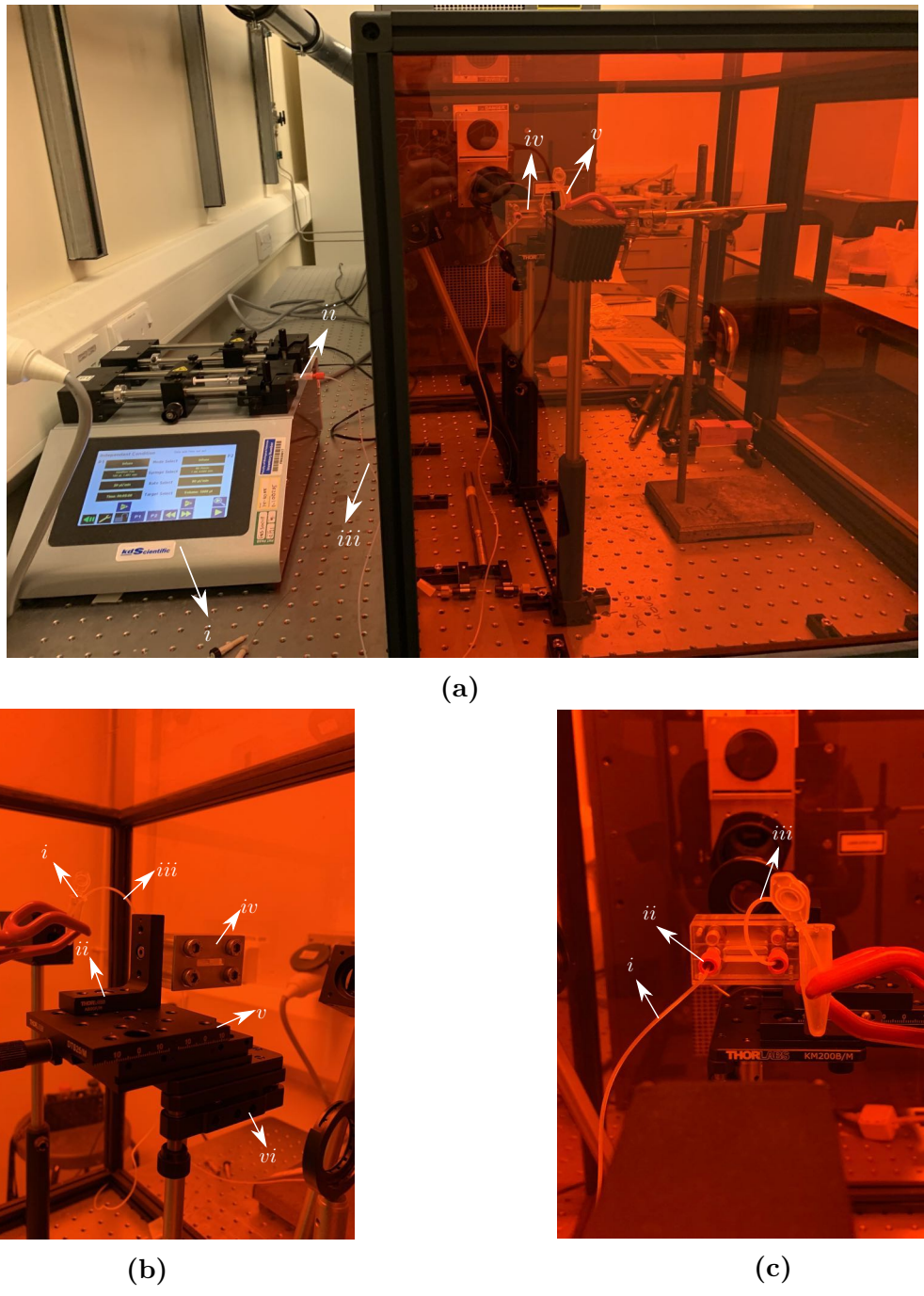

(a)

(b)

(c)

Figure 5.13: Implementation of the microfluidic prototype device into FPOP experimental setup. 5.13a: Syringe pump (KD Scientific) (i), sample (ii), inlet tubing (iii), microfluidic device (iv), waste collection (v). 5.13b: front side of the microfluidic annotated with physical features, including the waste collection tube (i), slim right-angle bracket (AB90F/M; Thorlabs) (ii), outlet tubing (iii), microfluidic device (iv), dovetail translation stage (DTS25/M; Thorlabs) (v), kinematic platform mount (KM200B/M; Thorlabs) (vi). 5.13c: back side of the microfluidic indicating the inlet tubing (i), tubing fittings (ii), outlet tubing (iii).

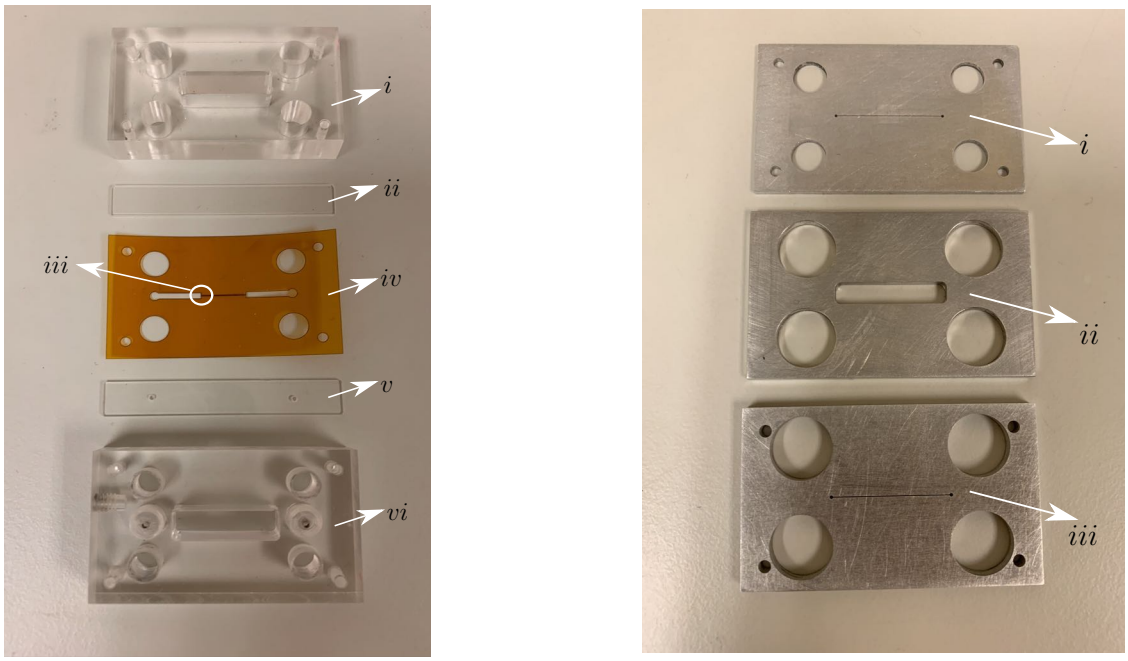

(a) **(b)**

Figure 5.14: Microfluidic layers and components. 5.14a: PMMA top part with optical window (50×30×10 mm), UV glass plate (50×8×0.5 mm) (Spectrosil 2000; UQG Optics) (ii), sudden geometry contraction (iii), polyimide channel sheet (50×8×0.05 mm) (536-3952; RS)(iv), UV glass plate (50×8×0.5 mm) with openings for sample loading (Spectrosil 2000; UQG Optics) (v), PMMA back part with tubing fitting openings (50×30×10 mm) (vi). 5.14b: Aluminium protection masks. Polyimide protection mask (50×30×0.8 mm) with a 90 μm window opening (i), PMMA protection mask with wider 4 mm (50×30×2 mm) (ii) and thinner 90 μm window openings (50×30×2 mm) (iii).

and developed such as they can be integrated as a protective cover at the exterior of the microfluidic device, as well as it can be integrated within the sandwich configuration of the microfluidic device. Full description of the interior aluminium mask dimensions can be found in appendix A, figure A.3. The integration of the aluminium mask within the microfluidic sandwich configuration will ensure that the polyimide (kapton) flow channel can be protected during the laser irradiation. The alignment of the aluminium kapton mask, which is integrated within the microfluidic device, is investigated in a microscopic level as shown in figure 5.15c ensuring that the kapton flow channel (orange in colour) is not visible, and therefore it is covered by the mask.

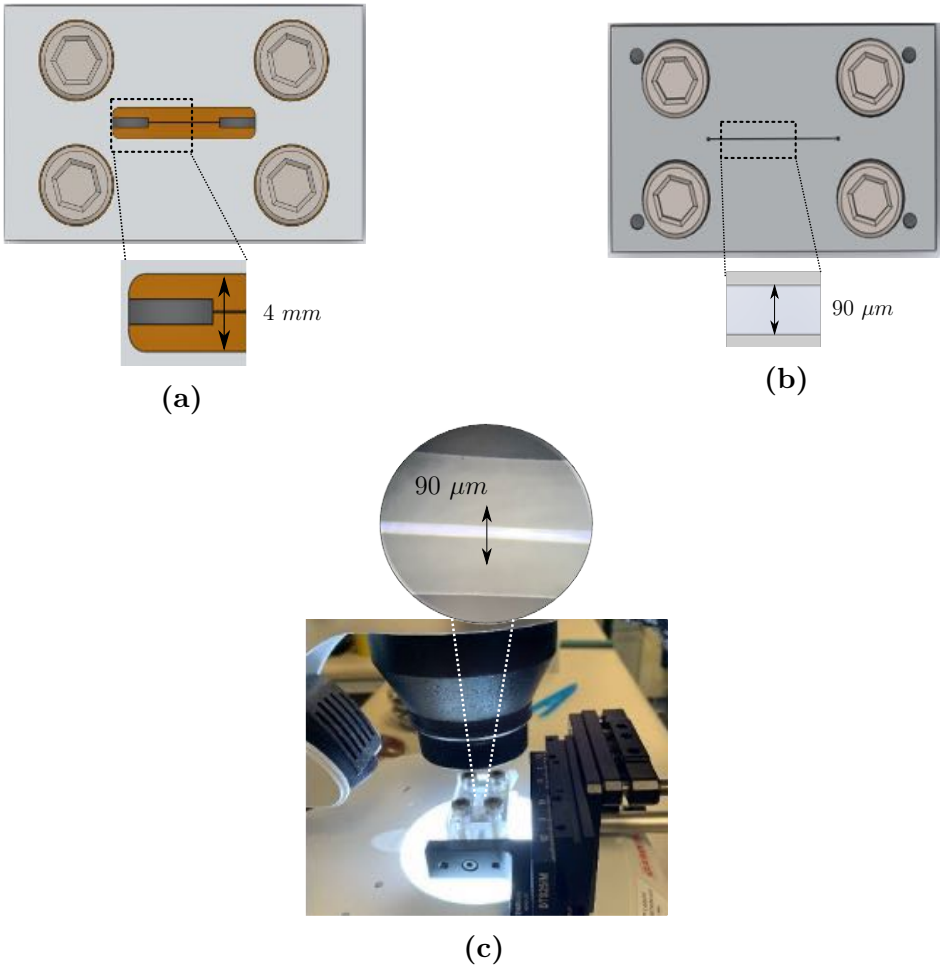

Figure 5.15: FPOP microfluidic mask alignment. 5.15a: CAD model indicating the aluminium mask at the exterior of the microfluidic device with a wider optical window (4 mm). 5.15b: CAD model indicating the aluminium mask at the exterior of the microfluidic with optical window smaller than the flow channel (90 μm). 5.15c: Alignment check of the interior mask using a microscope.

Laser alignment

The microfluidic device was integrated at the same height of ∼20.3 cm as the capillary of the typical flow experiment to ensure that the microfluidic channel is aligned with the laser. After the integration of the device into the current experimental setup, the laser was then

aligned between the typical capillary and the microfluidic device with the protective mask. Both setups were tested in water by using the standard laser specifications which is the laser firing at 15 Hz, at a flow rate of 20 μL/min. The alignment was conducted with the use of a paper piece which was positioned at the back side of the capillary and protective mask arrangements as shown in figure 5.16. The laser alignment was conducted to ensure that the laser is aligned at the desired locations between the two setups, corresponding to the capillary (figure 5.16a) and microfluidic optical window (mask opening) (figure 5.16b). For both experimental setups, the laser is aligned as indicated by the appearance of the laser beam profile silhouette on the paper.

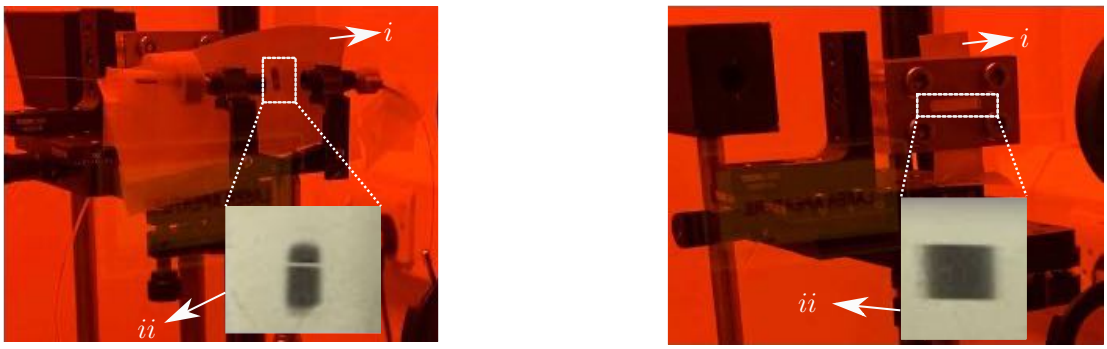

(a) **(b)**

Figure 5.16: Laser alignment using a paper piece (i) behind the capillary 5.16a and the FPOP microfluidic setups 5.16b as indicated by the appearance of the laser beam profiles on the laser papers (ii).

5.6 Characterisation of protein aggregation

5.6.1 UV Spectroscopy

Quantification of aggregation was conducted by the pelleting assay which will be described in the next section, 5.6.2. The pelleting assay is based on the UV absorbance of proteins. UV spectroscopy is mainly used for concentration measurements. The UV absorbance also depends on the molecule's environment. Biological events, including protein unfolding, can be interpreted by change in the spectrum with environment. Absorbance of two aromatic amino acids of tryptophan (Trp) and tyrosine (Tyr) (and to a small extent the absorbance of cystine) cause proteins to show absorption maxima between 275 and 280 nm [253]. The protein concentration was calculated by absorbance measurements using the Lambert-Beer law. The absorbance (A) is related to the light intensity before (I_0) and after (I) passage through the protein solution by equation 5.4, and the absorbance depends linearly on concentration according to the Lambert-Beer law as shown in equation 5.5.

$$A = -log_{10}(I/I_0) \tag{5.4}$$

$$A = \epsilon c l \tag{5.5}$$

where:

$c =$ molar concentration

$l =$ pathlength (cm)

$\epsilon =$ molar absorption coefficient (L mol^{-1} cm^{-1})

Absorbance values were measured in triplicates (at a wavelength of 280 nm, using the absorption coefficient ϵ_{280}, for all proteins taken from table 5.1), and the average absorbance value was used for the calculation of the final protein concentration using equation 5.5. For measuring protein concentration and also determining aggregation using absorbance, 120 μL of sample was loaded into the quartz curvets (105.250-Ultra-Micro cells, Hellma), where the corresponding solvent buffer was subtracted from each sample.

Optical density, OD350

For the protein-surfactant experiments, turbidity evaluation of the samples was conducted to investigate whether the range and concentration of the surfactant library, previously described, can affect the aggregation profiles under flow. Increased scattering of light can cause the opalescent/turbid appearance of solutions, indicating protein aggregation [254]. Optical density at 350 nm (OD350) of surfactant formulated samples was measured, before and after their exposure to extensional and shear flows. 200 μL of samples were measured in duplicates (2×200 μL per sample) out of 0.5 mL sample volume, in UV-transparent cuvettes (STARSTEDT), where the corresponding solvent buffer was subtracted from each sample. All the UV measurements described in this section were conducted using UV spectrophotometer (UV-1800, Shimadzu) as previously mentioned in section 5.1.

5.6.2 Pelleting assay

The extent of flow induced aggregation was quantified using an insoluble pelleting assay. Initially, 0.5 mL of protein solution was loaded within the extensional flow device and stressed for the desired number of passes at a defined plunger speed. For control comparisons, a second sample was left within the syringe and capillary bodies, for the length of the stressing experiment, but without exposure to flow. 200 μL of control and stressed protein samples were centrifuged at a speed of 30,000 rpm (∼35,000 g in a TLA100 rotor) at 4 ℃, in Beckmann Coulter Optima TLA 100 ultracentrifuge for 30 minutes. The centrifuged samples were then separated into the supernatant and pellet fractions. A total volume of 150 μL was removed from the 200 μL centrifuged sample corresponding to the supernatant samples, with the remaining 50 μL corresponding to the pellet sample. After the separation of pellet and supernatant tubes, 200 μL of 6M Guanidine hydrochloride

buffer (pH 6) (Sigma) was added to the 50 μL pellet sample, which includes the insoluble solid parts of the protein aggregates. The same volume of buffer was added to 50 μL of supernatant, ending up with pellet and supernatant samples of a total volume of 250 μL. Samples were then incubated overnight at 4 ℃. The sample concentration was then quantified using UV-visible spectroscopy as described in 5.6.1. The final percentage of insoluble protein corresponding to protein aggregates is determined using equation 5.6. Data analysis was performed in Microsoft Excel (v16.52) and Origin (2021).

$$\%protein\,in\,pellet = (\frac{([P]-[S])}{([protein]_0)}) \tag{5.6}$$

where:

$[P]$ = concentration of the protein in pellet fraction

$[S]$ = concentration of protein in the supernatant fraction

$[protein]_0$ = initial protein concentration

An updated pelleting assay protocol was followed for the latest experiments (i.e., surfactant formulations) based on optimisation studies, which have been conducted by Ms Samantha Lawrence and Dr Leon Willis. The appropriate sample volume required for the best accuracy of the results was investigated. A total volume of 150 μL was shown to provide the most of the accuracy between the samples and for minimising experimental errors, samples were then loaded in triplicates. Based on the protocol optimisation, 150 μL of control and stressed protein samples in triplicates (3×150 μL per sample) were centrifuged as described above, and a total volume of 100 μL was removed from the 150 μL centrifuged samples, corresponding to the supernatant samples, with the remaining 50 μL corresponding to the pellet sample. The protocol procedure remained the same after the sample centrifugation as it is described above.

5.6.3 Fluorescence spectroscopy

To determine the suitable formulation candidates that will enhance and conserve the stability of the proteins under flow, fluorescence spectroscopy experiments were employed. Fluorescence spectroscopy was employed as it is a sensitive tool, which allows the monitoring of structural perturbations of the proteins in the various surfactant formulations. Structural perturbation can be monitored in the absence and presence of extensional and shear flow conditions based on the intrinsic fluorescence from the Tryptophan (Trp) residue of proteins. The particular technique is desired, as it is sensitive to polarity changes in environment induced from the protein conformation or from the hydrophobic or hydrophilic microenvironment caused by surfactants binding to the protein structure [95]. Fluorescence emission spectra can be used to report information about the interaction of the solvent and a molecule where a fluorophore it is either exposed to, or buried from the solvent. A buried

fluorophore from the solvent refers to the condition where the fluorophore of interest (i.e., Trp) is buried in a macromolecule such as a protein (protein's interior), and it is usually inaccessible to water [94]. Whereas, exposed to the solvent refers to the arrangement of the fluorophore close to the protein's exterior, which is accessible to water [94].

Fluorescence experiments are conducted using PTI (Photon Technology International QM-1) spectrofluorimeter. The experiments were performed after the lamp of the instrument was turned on and left for at least 30 minutes until the voltage was set to 75 W. The instrument boxes were then turned on from top to bottom (motor driver MD-5020, BryteBox, temperature control TC-125, shutter control SC-500). Temperature was set at 22 ℃, using the temperature control, and left until the temperature was reached. Hardware configuration was then followed by initialising the configuration menu, ensuring that the monochromator wavelengths on the front and rear side of the instrument correspond to those reported on the computer screen. Data acquisition is then followed using the Felix32 Analysis Module software by selecting the emission scan mode to be performed and specifying the excitation wavelength.

CMC experiments of the surfactant library, previously shown in table 5.5, have been performed using ANS dye (A-1028; Sigma). Surfactant formulations at a concentration range of ∼0.001-1 mM were prepared in 40 μM ANS, 235 mM Sucrose, 25 mM Histidine, pH 6.0. Quiescent samples of 0.5 mL have been loaded into the quartz cuvettes (114F-Semi-Micro cells, Hellma), and excited at 389 nm. For single peptide-surfactant studies, (NATA-surfactants) surfactant concentrations have been spiked in 40 μM NATA (Sigma), 235 mM Sucrose, 25 mM Histidine, pH 6.0. Quiescent samples in the absence of extensional flow at a volume of 0.5 mL were loaded into the cuvettes and excited at 295 nm. For protein-surfactant studies (MEDI8852-surfactants), MEDI8852 was used as model protein at 0.5 mg/mL and the samples have been excited at the wavelength of Trp at 295 nm. Samples have been prepared in different surfactant concentrations as previously described in section 5.4.3 (table 5.6). The slit widths for NATA-surfactants and MEDI8852-surfactants were set to 4 nm. Samples were firstly exposed into the EFD (100 passes, 8 mm/s) and along with their respective controls were loaded into the cuvettes for fluorescence characterisation.

For all the studies described above, emission scans were recorded between 300-400 nm and three spectra were recorded for each sample. All the spectra have been recorded along their respective formulation buffer for each experimental case. The final spectra have been analysed by subtraction of their respective formulation buffer from each sample.

5.6.4 Dynamic light scattering, DLS

The effect of surface modification was investigated using DLS. Samples of mAb1 and WFL proteins at 0.5 mg/mL, which have been previously exposed to EFD along with their

respective controls, were analysed by batch-mode DLS (Wyatt miniDawn TREOS). The samples have been exposed to the EFD treated surfaces (surface modification described in section 5.2, surface library in table 5.3) at the standard flow conditions of 8 mm/s plunger speed, stressed for 100 passes.

Alongside the effect of surface modification, the effect of a wait time within the experimental procedure, was investigated on the size distribution of samples exposed to shear and extensional flow using DLS. The addition of a wait/lag time within the experiment, will allow a "dead" time in which protein samples can interact with the equipment surface at different time points within the experiment (i.e., before, after, during the experiment) as well as with different duration. Model protein for the particular experiment is mAb1 at a concentration of 0.5 mg/mL, where the samples have been stressed for 20 passes under the presence of a wait time which corresponds to the time where proteins allowed to interact with the equipment surface in the absence of flow effects. The variable parameter in the particular experiments was the position and duration of the wait time within the experiment. The presence of a wait time with the combination of the extensional flow within the device has been examined for the cases of: (a) wait time before extensional flow experiment (10 minutes), (b) wait time in between extensional flow experiments (30 seconds between each cycle of two passes) and (c) wait time after extensional flow experiments (10 minutes).

The DLS instrument was firstly thoroughly cleaned by injecting ∼1 mL 1 M filtered and degassed nitric acid, followed by ∼1 mL double-distilled water, ddH_2O. After the system was cleaned and the baseline was reached (i.e., when the trace shown on miniDawn reaches a number in four decimal places), ∼1 mL of the formulation buffer of the sample was injected, ensuring that the baseline was being maintained for ∼5 minutes before starting the experiment. The experiment was then recorded using the Astra software 6.1. The buffer baseline was then collected for ∼5 minutes, and 250 μL of the sample was then loaded and data was collected for ∼5 minutes. The formulation buffer was then loaded again, and data collection was continued for ∼5 minutes. After the data collection was completed, a washing step of the instrument was performed by injecting ∼1 mL of filtered and degassed nitric acid, ∼1 mL water and ∼1 mL 20% EtOH. All the samples injected into the instrument have been filtered using 0.22 μm filters.

Depending on the disparity of the species present in samples, the model for analysis is applied accordingly. The correlation function displays the intensity correlation curve for a single slice of Quasi-Elastic or dynamic Light Scattering data, which is the raw dynamic light scattering data from which the hydrodynamics properties are derived [255]. The theoretical analysis conducted to detect the hydrodynamic radius of the particles is fully described in the Astra (User's Guide) software manual (v5.3.4) [256]. Based on the software manual, the key equations required for the detection of particle size are

summarised next.

A second order correlation function which is shown in equation 5.7 is the result of a QELS measurement. The brackets indicate averaging over all t. The correlation function depends on the delay τ, that is, the amount that a duplicate intensity trace is shifted from the original before the averaging is performed.

$$g^{(2)}(t) = \frac{\langle I(t)I(t+\tau)\rangle}{\langle I(t)\rangle^2} \tag{5.7}$$

where:

$I(t) =$ intensity of the scattered light at time t

$\tau =$ time delay

The correlation function for a monodisperse sample can be analysed via the equation 5.8.

$$g^{(2)}(t) = B + Ae^{(-2\Gamma\tau)} \tag{5.8}$$

where:

$B =$ the baseline of the correlation function at infinite delay

$A =$ the correlation function amplitude at zero delay

$\Gamma =$ is the decay time

By the application of a nonlinear least square fitting algorithm by the ASTRA software, to the equation 5.8, the correlation function decay time Γ, can be retrieved. Finally, the diffusion coefficient, D of the particle is obtained by Γ, which is the decay time, via equation 5.9.

$$D = \frac{\Gamma}{q^2} \tag{5.9}$$

where:

$q =$ magnitude of the scattering vector

The magnitude of the scattering vector q, is then given by the equation 5.10.

$$q = \frac{4\pi n}{\lambda_0} sin(\theta/2) \tag{5.10}$$

where:

$n =$ solvent index of refraction

$\lambda_0 =$ vacuum wavelength of the incident light

$\theta =$ scattering angle

The diffusion coefficient can be interpreted as the hydrodynamic radius R_h for a diffusing sphere via the Stokes-Einstein equation, equation 5.11.

$$R_h = \frac{kT}{6\pi\eta D} \tag{5.11}$$

where:

$k =$ Boltzmann's constant

$T =$ temperature

$\eta =$ solvent viscosity

The fit of a single exponential decay to the correlation function data using the equation 5.12, can be employed to determine the hydrodynamic radius R_h, assuming that the sample is monodisperse. The degree of the fit can indicate the presence of aggregation based on R^2, leading to low R^2.

$$y = y_0 + Ae^{\frac{-(x-x_0)}{\tau}} \tag{5.12}$$

where:

$y_0 =$ y axis intercept

$A =$ amplitude

$x_0 =$ x axis intercept

$t =$ time

The previous equations do not address the effects of polydispersity on the correlation function, and they provide the tools for analysing a correlation function from a monodisperse sample. The cumulants method can be used to analyse data from polydisperse samples. For narrow monomodal distributions, the cumulants model is applicable to determine the intensity average hydrodynamic radius (R_h) and its main use is to calculate polydispersity index (PDI) shown in equation 5.13. The method estimates the width of the distribution as well provides an average diffusion coefficient of the species [257].

$$PDI = \frac{\sigma^2}{z^2} \tag{5.13}$$

where:

$\sigma =$ width of average z-radius (nm^2)

$z =$ z-average radius, R_h (nm^2)

Opposed to the assumption of monomodal distribution of species using the cumulants model, the regularisation analysis is one of the most sophisticated methods for analysis [256]. For polydisperse systems of bimodal size distributions assuming aggregated species of various sizes, the regularisation method can be applied. The method determines R_h of species in the sample which is based on the selection of the distribution function with the least detailed distribution that agrees with the data, resulting in narrower distributions [258]. Therefore, the regularisation method has been applied on the DLS data presenting the size distribution of aggregated species, as presented in the following chapter, chapter 6 (subsections 6.1.3 and 6.2.2).

5.6.5 Visual inspection

Visual inspection was conducted in AstraZeneca to visualise by naked eye the presence of any aggregated particles and investigate the effect of the various surfactant formulations on the particle formation. The inspection was carried out using an apparatus consisting of a box with a white and a matt black panel. The assessment of sample condition is done based on the formation of particles before and after their exposure to stress tests, using the black panel as the background under the exposure to a white light source (lamp). The visual inspection was conducted immediately after the samples (0.5 mg/mL; MEDI3549) were exposed to both EFD and shipping simulator, along with their respective control samples.

5.6.6 High Performance Size-Exclusion Chromatography, HPSEC

High Performance Size-Exclusion Chromatography, HPSEC experiments have been kindly conducted by Maria Bruque in AstraZeneca. Quantification of protein aggregation experiments conducted in AstraZeneca using HPSEC (Conan, 1260 Infinity II LC System; Agilent). Firstly, the samples (MEDI3549, 0.5 mg/mL) were exposed to EFD (8 mm/s, 100 passes) and shipping simulator (along with their respective controls) and were spun at 13 rpm for 1 min. Samples were then loaded in duplicates (2×100 μL) and the average monomer fraction was determined for each stress flow condition.

5.6.7 Subvisible particle analysis

Aggregation quantification has also been determined via quantitative sub-visible particle analysis using background membrane image (BMI) (Horizon; Halo Labs) in AstraZeneca. The technique involves the background image of the membrane to be subtracted from the experimental image to identify the particles which are filtered through on the membrane

under vacuum and captured under filtration. The membrane is then re-imaged with the particles on the surface. The final image is detected with the background image been aligned with the measure image and then subtracted on a pixel by pixel basis so that the background texture is eliminated and particles are revealed.

The technique requires low sample consumption (as little as 25 μL per test) so that multiple measurements can be made and averaged (loaded in triplicates). The flexibility with the specific technique is found in the wide working range: measured particles from 2 μm to 4 mm with high reproducibility. The accommodation of 96 samples in a single plate is achieved for each experimental run, and air bubbles are not counted as particles.

Samples were run in the instrument by Maria Bruque in AstraZeneca. 25 μL of samples (0.5 mg/mL MEDI3549) previously exposed to EFD and shipping simulator respectively, are loaded in triplicates (3×25 μL volume per sample) on the membrane. Samples have been formulated using the surfactant library as previously described in 5.4.3. Quantification of particle concentration on the membrane surface is then obtained both qualitatively and quantitatively via membrane images and particle concentration (expressed in particles/mL).

5.7 Rheology experiments

The fluid properties of pharmaceuticals are important, as they can affect how these protein-based pharmaceuticals can be processed, as well as their ease of use. Their exposure to flow can be encountered during their production, processing, purification and in dispensing by subcutaneous or intravenous injection [259]. The flow characterisation in terms of formulation, processing and dispensing prospectives can be achieved by the rheology analysis. Particularly, it has been reported that during the development of high concentrated protein formulations, this can correspond to formulations with high viscosities [259]. It is therefore important to consider the high viscosities of the formulation into the injectability of the pharmaceuticals as the resistance of the fluid to injection and thus the force required for the pharmaceutical injections is viscosity-dependent [259]. At higher concentrations, there can be interaction between neighbouring proteins. These structure the solution (getting increase to viscosity) but can be affected by flow itself. Therefore, to investigate whether the effects of shear are significant, viscosity measurements as a function of shear rate were recorded. Rheological characterisation of high concentrated solutions has been conducted using a rheometer (Kinexus; Malvern).

The viscosity profiles of samples of MEDI8852 and MEDI3549 at 0.5, 5, 10, 20 and 40 mg/mL were measured using shear viscosity ramps in a cone geometry (CP4/40) with a 40 mm diameter and 4° angle cone and a plate geometry with 55 mm diameter (PLS55) with 0.15 mm gap height. Initially, the optimisation of experimental parameters regarding the

duration of the experimental runs, has been performed using the working buffer (235 mM Sucrose, 25mM His, pH=6). A run time of 30 minutes was selected based on literature comparison of measured sucrose solutions; more details will be mentioned in section 7.1. Quiescent samples in volume of 1.2 mL were then loaded into the plate of the rheometer and their viscosity profile was measured using the rSpace software (v1.73), for 30 minutes at shear rate range of 0.1-1,000 s^{-1}, performed in logarithmic shear rate scale using 100 points of measurement. Measurements have been recorded at a temperature of 25 ℃.

5.8 Summary

In this section, a detailed description of the methods and the experimental setups were presented. Methods included protein preparation and formulation of the desired buffers and surfactants. Regarding the equipment surfaces, surface treatment method was presented using silanisation via vapour deposition methods as well as liquid deposition and the covalent attachment of proteins to surface which is followed by contact angle measurements as well as surface topography for the characterisation. Quantification methods also described to characterise the flow induced aggregation for each set of experimental condition. Quantification analysis involved protein adsorption, pelleting assay, optical density, size distribution, monomer fraction, particle concentration, fluorescence spectroscopy and visual inspection. Finally, flow properties such as viscosity by performing rheology experiments was described. Alongside these experiments, the manufacture of a microfluidic device was presented, indicating its implementation into a current experimental method. In the next section, the aggregation characterisation results will follow based on the set of the methods descried in this section.

Chapter 6

Characterising the surface and flow induced aggregation

Chapter structure

An overview of this chapter's main sections that will be discussed can be found in figure 6.1. In this chapter, the flow induced aggregation in the presence of surfaces is presented. Initially, an overview of the extensional flow device will be described in section 6.1, as it is the flow tool used to expose the molecules to controlled flow environments which are computationally characterised. The role of surface in the extensional flow induced aggregation is then investigated and will be described in section 6.2. The effects of particular flow regions within the extensional flow device under the effects of surface is then explored by investigating the effects of high and low shear regions in section 6.3. Surface effects combined with additional strategies to suppress aggregation through protein formulation are then investigated in section 6.4. Lastly, the flow induced aggregation is then explored by protein cross-linking on the extensional flow device components, investigating protein-protein interactions under flow, followed by a chapter summary in sections 6.5 and 6.6 respectively.

6.1 The extensional flow device, EFD

To explore the influence of the surface in flow-induced aggregation, flow-stressing experiments were performed using the extensional flow device, EFD as schematically shown in figure 6.2. Previously, the device was used to characterise the flow induced aggregation of three molecules (among others) [1–3], which will be also used in this chapter as the model proteins. The use of the extensional flow device allows the application of shear and extensional flow forces into the molecules in controlled conditions. The device consists of two syringes connected via a glass borosilicate capillary. Molecules are exposed to shear flow events with distinct magnitudes depending on the developed flow velocity. The flow velocity is rapidly increased as the molecules flow through the sudden contraction of the geometry, which induces the development of the extensional flow event. This implies that the velocity of the molecules experienced before the sudden contraction will correspond to a low shear region which is then followed by a high shear region, after the flow passes the sudden contraction. Typically, under a base set of operating conditions, molecules are expected to spend 5 s within the low shear region per pass, 18 μs within the extensional

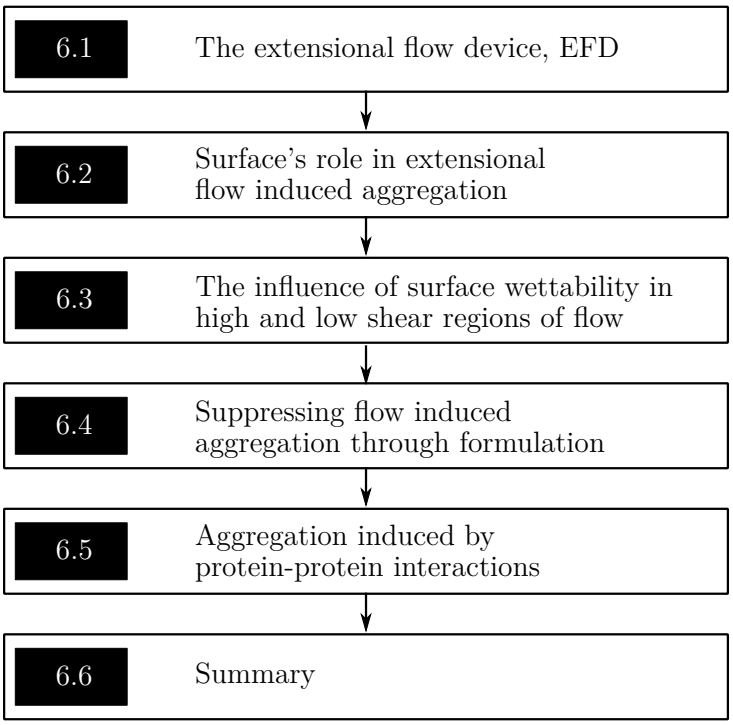

Figure 6.1: Overview of the main sections covered in the surface and flow induced aggregation chapter.

flow region and 40 ms within the high shear region as shown in figure 6.2.

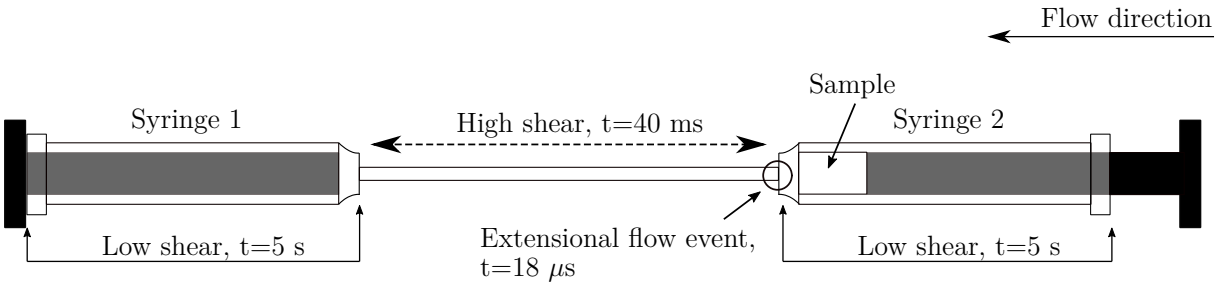

Figure 6.2: Schematic of the extensional flow device (EFD) along with the flow regions and the corresponding time frames when the sample is exposed to a single pass. Sample is exposed to low shear for 5 s, extensional point for 18 μs and high shear for 40 ms.

The novelty found using the particular device is the flexibility to control its components and investigate the effect of a range of parameters of interest. Strain rate, which describes the magnitude of the extensional force, can be controlled by the plunger speed. Additionally, the duration of the high shear region can be also controlled, as in previous study in [2], where it was shown that the duration of the high shear region can be modified by the capillary length, which significantly affected the aggregation propensity of an aggregation-prone molecule (WFL). The total duration of the application of forces to the molecules can be also controlled by the number of passes, which corresponds to the number of cycles where the protein molecule passes through the sudden point of contraction. As the device is programmed and driven by an Arduino microcontroller, it can be easily programmed

to the desired speed of the plunger, or introducing wait time events between passes or within any point throughout the conduction of the experiment. Thus, it can be used a flow-based tool for multiple flow induced aggregation experiments, investigating the aggregation performance of protein-based pharmaceuticals.

The main focus of the current thesis, is to explore a parameter using the extensional flow device, which has not previously investigated. The surface of the components of the device will allow investigating whether the surface in which the molecules interact during their direct contact with equipment surfaces under flow, can affect their propensity to aggregate. This chapter focuses on the surface effect on the aggregation propensity of three IgGs: WFL, STT and mAb1, all provided by AstraZeneca. WFL also mentioned as MEDI1912, is anti-nerve growth factor (NGF) antibody. During its bioprocessing, WFL was found to be colloidal instable, inducing protein precipitation, opalescence, phase separation and adsorbing to filter membranes [72]. Due to its aberrant biophysical and solution properties, the product development of the molecule was conducted by AstraZeneca to improve its poor biophysical properties, engineering the STT molecule. STT was engineered from WFL with mutations W30S, F31T and L56T, found in the variable region of the heavy chain of the antibodies [72]. mAb1 is also used as a model protein, and corresponds to a generic molecule used as an internal standard by AstraZeneca with no known target and favourable biophysical properties [260]. As WFL and STT are "relative" proteins, with WFL corresponding to the molecular "parent" of STT, they have a sequence identity of >99%. mAb1 is also related to these proteins, where WFL and STT have a sequence identity of 72% with mAb1 [2].

These molecules, have been stressed under previously characterised flow conditions of 100 passes at a plunger velocity of 8 mm/s (see section 6.1.1 for the corresponding flow characterisation). Their aggregation propensity has been previously characterised where it was shown that they exhibit different responses to flow [1, 2]. mAb1 was characterised as a molecule with intermediate aggregation propensity when exposed to flow. On the other hand, WFL was characterised as a high aggregation prone molecule, compared to STT characterised as the most aggregation resistant molecule, among the three exhibiting high stability to the flow conditions.

6.1.1 Computational characterisation of the flow environment

The hydrodynamic forces under which the flow is exposed within the devices have been explored. The parabolic velocity profile developed as the flow accelerates through the contraction is shown in figure 6.3. The development of flow rate along the centreline is presented in figures 6.4 and 6.5. The simultaneous behaviour of strain rate and velocity profile are shown in figure 6.5. Maximum strain rate is achieved at the point of the contraction where the fluid accelerates. The strain rate is found to be approximately

11,000 s^{-1}, which is in the same order of magnitude with previous related publications investigating the aggregation of platelet within a microfluidic device. As it is previously discussed in chapter 2, a more dominant platelet aggregation in the study conducted in [132] was observed for strain rates higher than 10,000 s^{-1}. This agreement suggests that the device is able to expose protein under reasonable strain rate values, as previously used by authors investigating flow induced aggregation. Relating to biopharmaceutical manufacturing procedures, the strain rate to which the molecules are exposed during the filtration process is reported to be in the range of 1,000 to 10,000 s^{-1} during cross-flow filtration, with the maximum shear rates expected during normal processing operations reach to 20,000 s^{-1} [58]. This implies that the extensional flow device exposes the molecules within the range of forces reported to be found during the industrial procedures.

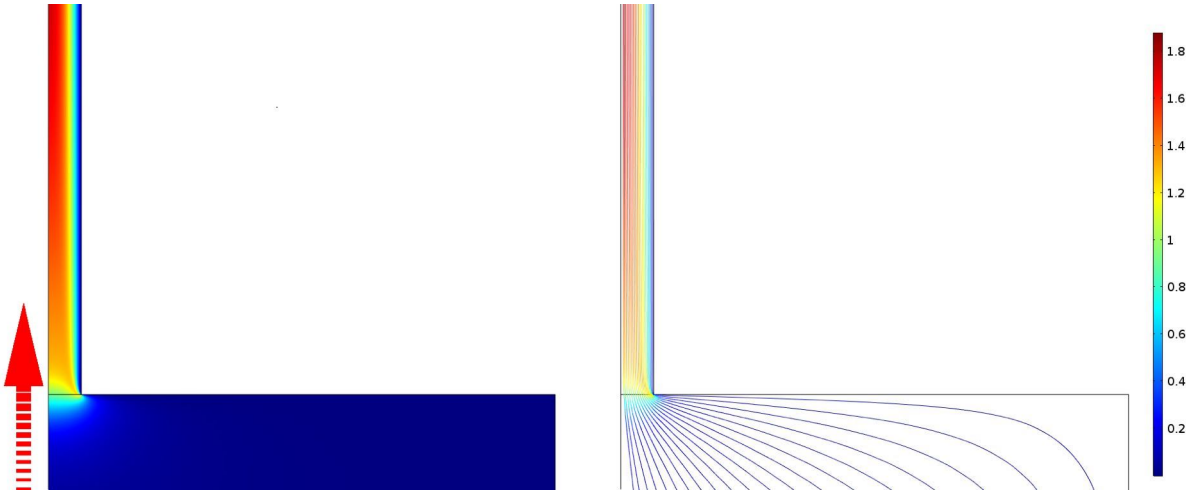

Figure 6.3: Velocity profile (m/s) contour and streamline plots within the extensional flow device, at a plunger velocity of 8 mm/s. Flow direction is indicated with a red arrow.

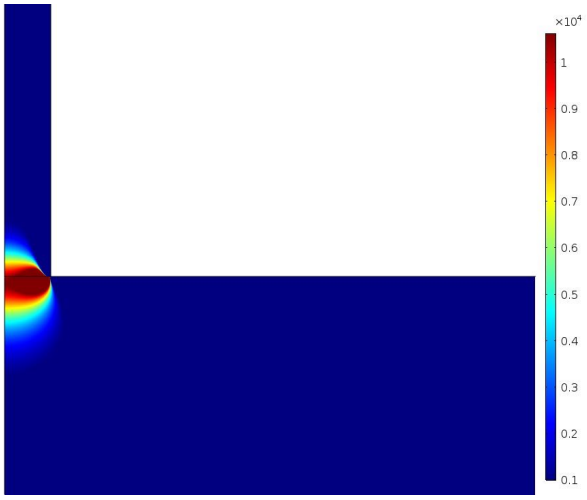

Figure 6.4: Strain rate (s^{-1}) contour plot at a plunger velocity of 8 mm/s.

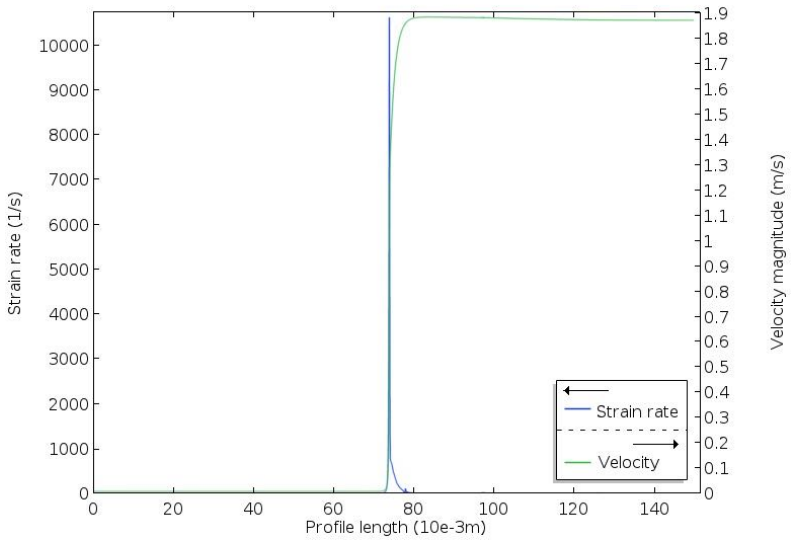

Figure 6.5: Strain rate (shown in blue) and velocity (green) profiles across the horizontal length of the device at a plunger velocity of 8 mm/s.

6.1.2 Number of passes effect - aggregation behaviour

The quantitative determination of mAb1 aggregation behaviour is obtained by performing the pelleting assay, where a percentage of insoluble protein can be calculated. Initially, the characterisation of mAb1 protein has been determined by investigating the effects of number of passes, as it is shown in figure 6.6. The aim of the particular experiment is to validate the expected correlation between the number of passes and aggregation propensity, as it has been previously shown in [2]. The results suggest that as the number of passes increases, the exposure time to hydrodynamic flows of shear and extensional flow increases, resulting in a maximisation of the aggregation propensity of mAb1 behaviour. As the number of passes through the device under which the samples are introduced increases, the time under which the protein is exposed under the hydrodynamic forces present within the extensional flow device is prolonged.

Based on previous work using the extensional flow device as a tool to investigate the aggregation propensity of proteins, a flow induced aggregation mechanism has been also proposed as shown in figure 6.7 as taken from [2]. Based on the proposed mechanism, the initial state of proteins, which are in their native state prior to the exposure to flow effects, is perturbed after the exposure to extensional and shear flow events. The unfolding pathway leading to irreversible insoluble aggregation is driven by multiple series of activation steps where the proteins are perturbed into an aggregation-prone state which can be either refold to the native state or proceed along the aggregation pathway. The rate of which the molecules can form or reform to the aggregation-prone state is driven by the rate constants k_f and, k_r respectively. Apart from the formation/refolding rates, the aggregation pathway is also proposed to be driven by concentration dependent rate of oligomer formation and unimolecular off-rate for oligomer dissociation, k'_f and k'_r, where

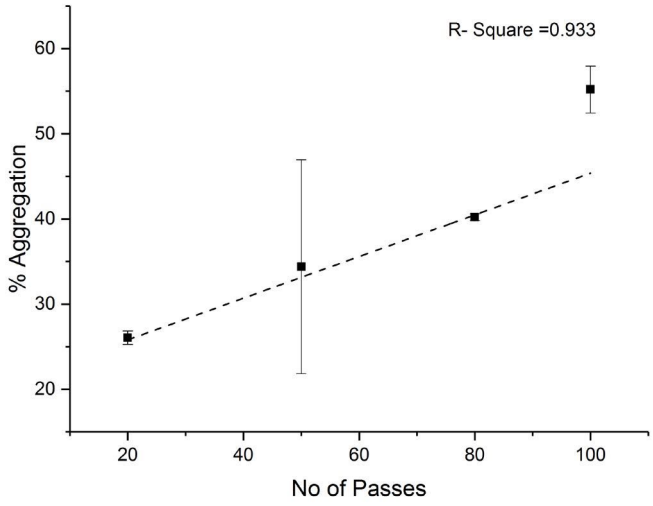

Figure 6.6: Plot of percentage of insoluble mAb1 as a function of the pass number.

the particular rate constants are currently not determined yet.

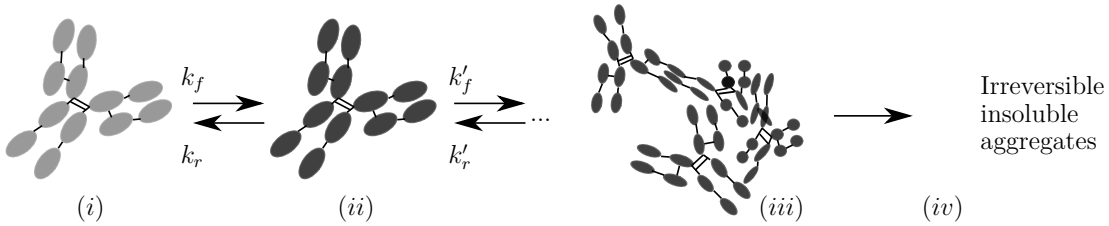

Figure 6.7: Proposed mechanism of flow-induced mAb aggregation. (i) The native protein (light grey) is perturbed into an aggregation-prone state (dark grey), the relative level of which is dependent on the fluid field and the protein studied. (ii) This can either refold to the native state or proceed along the aggregation pathway (iii) to form irreversible, insoluble aggregates (iv). k_f and k_r represent the rate of formation/refolding of the aggregation-prone state, while k'_f and k'_r represent the concentration-dependent rate of oligomer formation and the unimolecular off-rate for oligomer dissociation, respectively. These rate constants remain to be determined. Adapted from [2].

A range of flow parameters has been previously investigated, and correlated with the aggregation. Particularly, the effect of pass number has been explored and shown to be critical depending on the aggregation profile of molecules. In the study conducted in [2], aggregation landscapes have been constructed, highlighting which parameters are more significant in inducting protein aggregation, when molecules are exposed to extensional flow device. As previously shown in [2, 260], each protein investigated presented a unique aggregation landscape profile. The previously characterised aggregation profiles have shown that WFL which is an aggregation-prone molecule presented a strain-dependent as well as pass-depended aggregation profile. An intermediate aggregation-prone molecule, mAb1 presented a linear response to increased pass number with less propensity for aggregation compared to WFL. On the other hand, the most aggregation resistant protein among the

three proteins of interest, STT has previously shown a low aggregation "plateau" region for plunger speeds in the range of 2-8 mm/s at 100 passes with the aggregation to be significantly enhanced at the double pass number (200). Significant STT aggregation is proposed to occur at extreme plunger speed, 16 mm/s, at 200 passes. Based on these aggregation landscapes, all molecules possess pass-number effect behaviour at constant plunger velocity (i.e, 8 mm/s). This suggests that the duration in which the molecules are exposed to shear and extensional flow events, is crucial for affecting the aggregation profile of molecules. Pass number corresponds to the total experimental time in which the molecules are exposed to the controlled flow fields, inducing aggregation. The investigation of the parameter of a time delay in different stages along the conduction of the experiment will give insights into which stage of the experiment is crucial for inducing aggregation. Therefore, the effect of a wait time is investigated in the next section, section 6.1.3.

6.1.3 Wait time effect - mAb1 size distribution

The purpose of the initial stressing experiments is to identify the effects of the generated shear and extensional flow on the protein aggregation. Initially, the discrepancy of the aggregated mAb1 protein samples have been investigated under the presence of a wait time using DLS. mAb1 was selected as a model of interest for the particular experiment, as it corresponds to an intermediate aggregation-prone molecule. The combination of both extensional flow and wait time supports the kinetic understanding of aggregation pathways. Therefore, the distribution of the samples has been plotted for the cases where a wait time is introduced within the extensional flow device experimental procedure. The aggregation behaviour of mAb1 was examined under a plunger speed of 8 mm/s at a constant number of passes, in this case 20. The variable parameters in the particular experiment were the position and duration of wait time within the experiment. The results obtained can be shown analytically in figure 6.8.

The native aggregation of mAb1 shown in figure 6.8e is used as a control, where the native aggregation is detected by leaving the sample on the bench for the longest experimental time (10 minutes). In native aggregation, aggregates are formed by protein monomers with no disruption in structure, whereas the flow induced aggregation achieved within the EFD alters the protein structure determined as non-native aggregation. It can be seen that the wait time has a significant effect in the size distribution of aggregated samples, where in particular a broader size distribution is observed when the wait time is present between the flow event, which is similar to the distribution obtained when no wait time is introduced as a part of the experiment. This observation indicates that the wait time of 30 s which is introduced between the flow process is not significant in affecting the size distribution. However, a narrower distribution is obvious when the wait time is introduced either before or after the experiment. The total wait time of 10 minutes is enough to create discrepancies in the size distribution of aggregated samples. While the protein samples

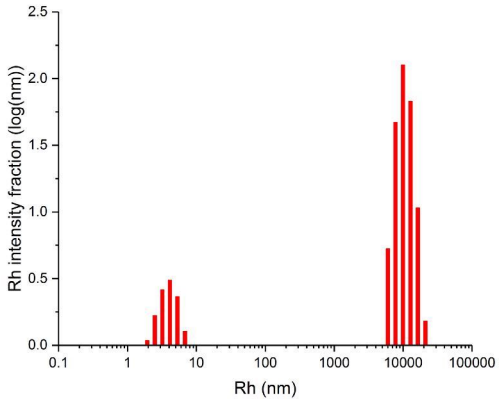

(a) Wait time before flow event

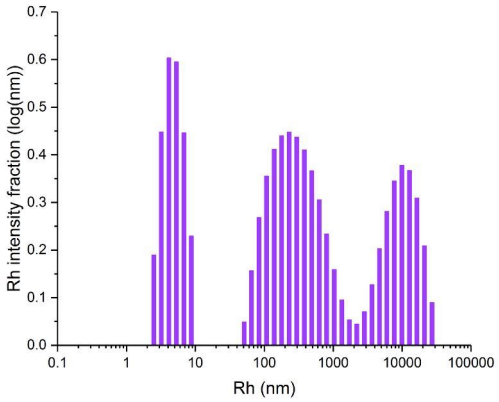

(b) Wait time in between flow event

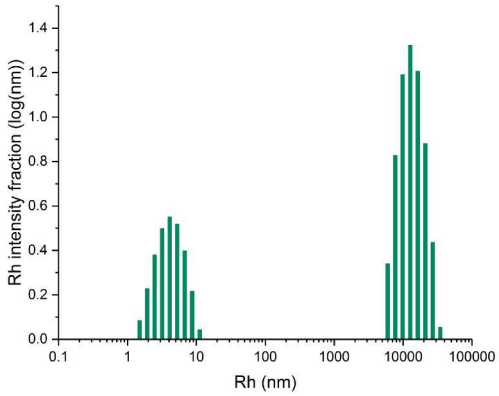

(c) Wait time after flow event

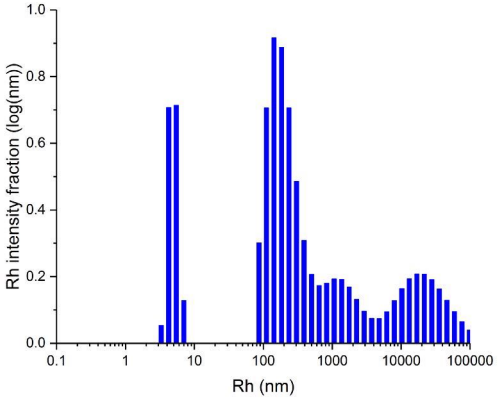

(d) Flow event with no wait time

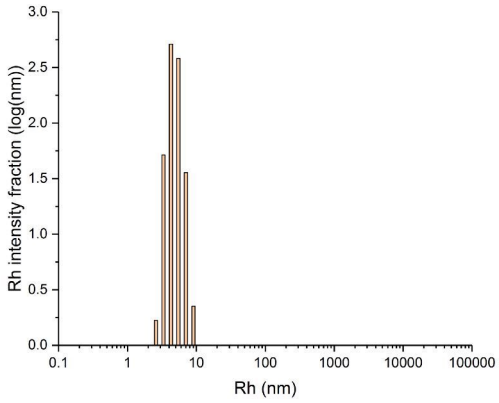

(e) Native mab1

Figure 6.8: Plots of DLS data presenting the size distribution of control (quiescent conditions) and aggregated mAb1 under the presence of a wait time. Wait time corresponds to a total time of 10 minutes before (6.8a), 30 s in between each cycle (2 passes)(6.8b) and 10 minutes after exposure to the extensional flow (6.8c). Samples have been stressed for the normal experimental time in the absence of a wait time (6.8d) and samples in quiescent conditions presenting the native state of mAb1 (6.8e) (absence of extensional flow).

are not stressed immediately, but after or before a wait time, there is a temperature shift in the system as the sample equilibrated with its surrounding which induces aggregation and dis-aggregation.

The experiment induces changes in the complex mechanism of mAb1 aggregation. The wait time seems to disturb the rate of formation or refolding of the aggregation-prone state, causing disruption between the states "ii" and "iii" before the final stage of the aggregation mechanism which corresponds to irreversible insoluble aggregates as it is shown in figure 6.7. However, due to the complexity of the mechanism, it is difficult to determine the exact effect of wait time along the aggregation pathway. The position and duration of a wait time has been found to affect the size distribution of the aggregated samples. This, does highlight the importance of controlling the conditions within the experiment.

6.2 Surface's role in extensional flow induced aggregation

To investigate the interaction of protein molecules that could correlate to their interaction with equipment surfaces during manufacturing, flow experiments have been conducted with the variation of the surface properties of the extensional flow device. Surface modification on the syringe parts, capillary and syringe plungers correspond to the set of surfaces that the molecules interact with during the conduction of the experiments.

Model proteins for the particular experiments were three monoclonal antibodies (mAbs) STT, WFL and mAb1 which are provided by AstraZeneca, and they have been previously characterised in terms of their aggregation propensity when exposed to flow environments using the extensional flow device [1, 2]. However, their previous aggregation profiles have been investigated in a range of parameters such as buffer, strain rate range, timescale in flow environment controlled by the pass number. All of these experiments have been conducted at the standard surfaces which are untreated and used as they arrive from the manufacturer. The effect of these equipment parts is investigated by their surface modification, and flow experiments are conducted to evaluate whether the surface parameter can affect their previously characterised aggregation profile on standard untreated glass surface. This set of experiments will give insights into the effects of surface as the molecules are interacting with the equipment surfaces under flow. As the current proposed flow induced aggregation mechanism involves the bulk mediated aggregation pathway (figure 6.7), the question this section addressees, is how this particular aggregation pathway can be modified or affected by introducing an additional surface pathway alongside aggregation within the bulk.

To investigate this, a library of surface treatment agents was constructed and characterised by contact angle measurements, indicating the degree of hydrophobicity. The selection of the particular agents, alongside with the procedure followed to conduct the surface

treatment of the device component parts, has been previously described in section 5.2. The final surface library consists of five different surfaces with increased hydrophobicity: mPEGMA (23°), untreated glass (47°), APTES (58°), HTS (80°) and FDTS (94°) as summarised in table 6.1 alongside with their contact angle profiles of water on glass, as shown in figure 6.9.

Table 6.1: Water contact angle measurements on treated float glass slides at pH=7.

Surface	Contact angle (°)
Poly(ethylene glycol) methyl ether methacrylate, mPEGMA	23
Untreated glass	47
Silane A: 3-Aminopropyltriethoxysilane, APTES	58
Silane B: n-Hexyltrimethoxysilane, HTS	80
Silane C: Perfluorodecyltrichlorosilane, FDTS	94

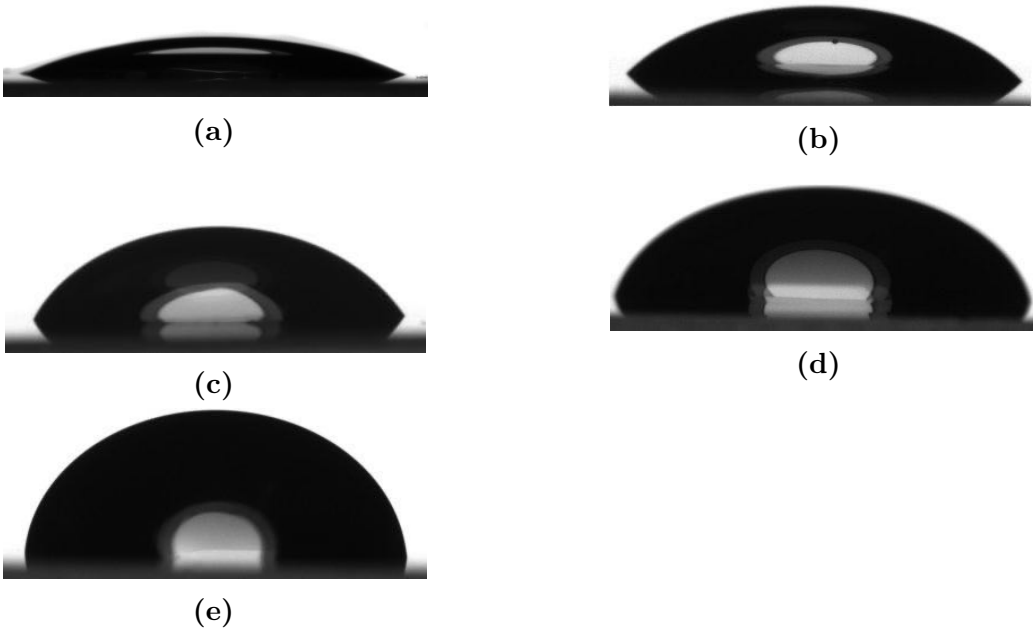

Figure 6.9: Water contact angle image profiles on the surface library constructed for the investigation of surface effect on aggregation including: mPEGMA (6.9a), glass (6.9b), APTES (6.9c), HTS (6.9d) and FDTS (6.9e).

6.2.1 Protein affinity for the surface

Firstly, to investigate the affinity of protein molecules to the modified surfaces, QCMD experiments have been conducted investigating the adsorbed mass as well as protein thickness adsorbed on each surface, as fully described in the previous chapter, chapter 5, section 5.3.1. The experiments are conducted in quiescent conditions to allow the distinct effect of surface to be explored in the absence of flow contribution. The extent to which WFL, mAb1 and STT proteins adsorb onto this surface library under quiescent conditions, was then assessed using Quartz Crystal Microbalance with dissipation (QCMD). By

measuring changes in the crystal's oscillation, this method quantifies protein adsorption in terms of aerial mass (ng/cm^2) as well as protein layer thickness (nm), calculated assuming the protein solution density to be 1000 kg/m^3. The oscillation of the crystal is indicated in the raw data, by shifts in frequency (Δf) while mass adsorbs on the surface and shifts in energy dissipation (ΔD).

The average protein layer thickness and mass adsorption was interpreted as an average protein layer thickness and aerial mass, as shown in figure 6.10. The average layer thickness is found to be unaffected by the surface treatment ∼15-17 nm, as shown in figure 6.10a. As the radius of hydration (Rh) of WFL, obtained by dynamic light scattering, is 6 nm [1], these data suggest the formation of a monolayer, considering the protein diameter of 12 nm (2×6 nm), although water can contribute to additional mass [195, 261] via direct hydration, viscous drag, or entrapment of cavities in the adsorbed film [262]. Overall, it can be also observed that the there is a slightly higher tendency for WFL (filled circles) to interact with the surface compared to mAb1 (open squares) as higher aerial mass and respective layer thickness is recorded. This observation can be linked with the previously characterised aggregation profile of WFL to aggregate. On the other hand, STT which has been previously shown to be aggregation resistant molecule, shows to have the minimum absorption on the surface corresponding to ∼1500 ng/cm^2 compared to the maximum aerial mass recorded for WFL ∼2500 ng/cm^2 on the mPEGMA, where the bigger variation on the protein adsorption is recorded for the particular surface, with a contact angle of 23°.

6.2.2 Synergistic effects of surface and flow

As the surface modification presented to have a small effect on the protein interaction with the surfaces in the absence of shear and extensional flows, flow experiments have been conducted to investigate whether the aggregation can be affected in the presence of a range of surfaces, as shown in figure 6.11. As previously mentioned mAb1, STT and WFL proteins have been exposed to the same number of passes (100), at constant plunger speed of 8 mm/s, to ensure the molecules are exposed to the same strain rate magnitude. The aggregation profiles are compared to their respective control samples, where the samples were left in the device equipment surfaces (syringe body and capillary) for the longest experimental time, corresponding to 10 minutes (10 passes=1 minute). As shown in figure 6.11a, intermediate levels of aggregation can be observed with the maximum aggregation to be reached at ∼50% for mPEGMA, untreated glass and FDTS surfaces. Interestingly, the suppression of aggregation to ∼18% was shown for the HTS, (Hexyl.) and ∼20% for APTES surface, highlighting the protective effect of the particular surfaces against aggregation. Similar protective effects from the particular surfaces can be also seen for the most aggregation-prone molecule WFL in figure 6.11b, where it is shown to be highly aggregated when exposed to mPEGMA, untreated glass and FDTS, inducing full damage

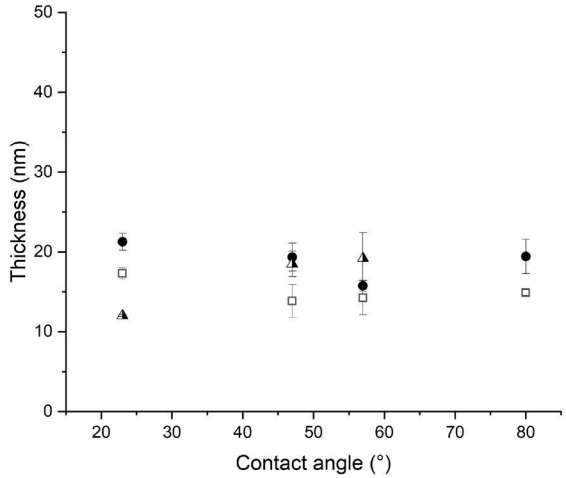

(a)

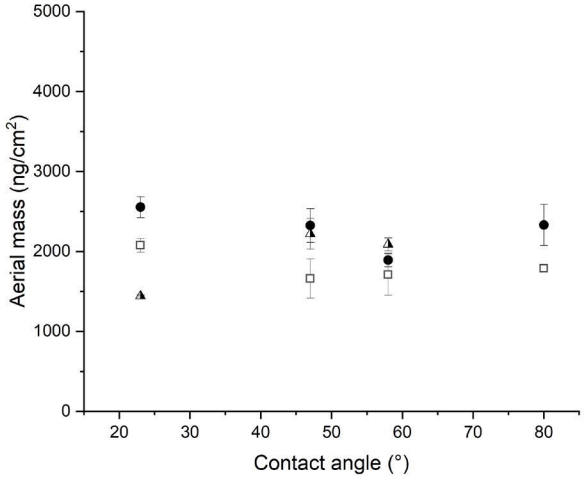

(b)

Figure 6.10: Thickness and aerial mass of adsorbed WFL (filled circles), mAb1 (open squares) and STT (semi-filled triangles) protein layers under quiescent conditions (i.e. absence of extensional flow). Sample concentration=0.5 mg/mL in 150 mM Ammonium acetate buffer on QCM sensors (5 MHz 14 mm Cr/Au/SiO_2) with multiple contact angles at a flow rate of 0.21 mL/min. N=2, error bars=standard deviation. Surfaces (in increasing contact angle): mPEGMA, bare glass, APTES-Silane A, HTS-Silane B (Hexyl.) 6.10a: Average layer thickness of adsorbed WFL, mAb1 and STT protein layers. The average layer thickness range of the three proteins corresponds to a minimum layer thickness of ∼11 nm to a maximum of ∼20 nm. 6.10b: Average aerial mass of adsorbed WFL, mAb1 and STT protein layers. The average aerial mass range of the three proteins corresponds to a minimum aerial mass of ∼1500 ng/cm^2 to a maximum of ∼2500 ng/cm^2.

to protein reaching to ∼90%. On the other hand, the protection of the particular molecule is obtained when the molecule is exposed to HTS and APTES surfaces, obtaining ∼38% and ∼50% protein in pellet (i.e., aggregation) respectively, implying into aggregation suppression by 60% and 40% respectively.

These results highlight the significant effects of surface acting synergistically under the effects of flow, providing enhancement of protein stability in the extreme case of highly aggregation-prone molecules, including WFL. For the most aggregation resistant molecule, STT, the aggregation levels of these molecules as expected are decreased, with a maximum aggregation to be obtained at ∼40% across the surfaces of APTES, HTS and FDTS as shown in figure 6.11c. Surprisingly, enhanced aggregation levels were obtained when STT is exposed to mPEGMA surface, suggesting the protein instability as the molecule interacts with the particular surface under exposure to flow events. The most protective surface is shown to correspond to APTES, with minimum levels of aggregation. These results suggest that the surface parameter acts synergistically along the flow parameter, affecting the aggregation profiles of the molecules. In the absence of flow events, the surface parameter has no effect into the aggregation of samples left within the device's surface components. It is also worth mentioning that a general aggregation level of ∼10-15% is observed in the absence of flow across the surface library as the samples are incubated within the syringe and capillary bodies. This observation can be explained from the data shown in the previous section (section 6.2.1), where a protein monolayer is formed in the absence of flow events. Combining the aggregation level and aerial mass data for samples in quiescent conditions (absence of flow), it is shown that there is an interaction between the protein molecules and the surface of the device, which is indicated by the low aggregation levels and the monolayer formed. Therefore, the formation of the monolayer can explain the aggregation levels of ∼10-15% obtained in the absence of flow events. The aggregation of quiescent samples was quantified previously using the pelleting assay in the absence of the surface interaction, indicating ∼2-3% of aggregation when the samples were incubated within tubes stored on ice for the longest experimental time [1, 2]. This indicates the contribution of surface and flow to the aggregation propensity of samples exposed to either surface and flow.

The formulation pH of the experiments is an additional parameter which can affect the water contact angle, particularly with the Silane A treated surface, APTES. APTES performs a bifunctional nature where in the presence of hydrolysing agents such as water, the alkoxy groups of APTES are readily hydrolysed to silanols (Si-OH), promoting the reactivity of the newly formed species toward other functionalities which corresponds to the formation of protonated amine ($-NH_3^+$) [263]. In this work, the contact angle measurements have been performed in water at pH=7, whereas the protein adsorption and flow experiments have been performed in ammonium acetate buffer (among others) at pH=6. The water contact angle has a maximum value at the point of zero charge (pzc)

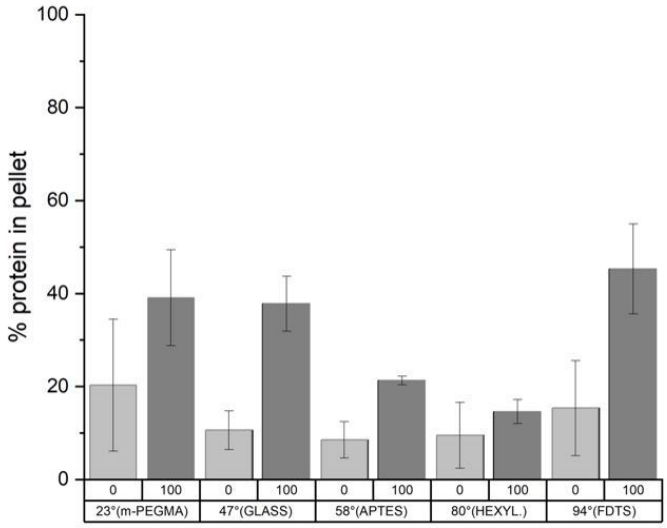

(a)

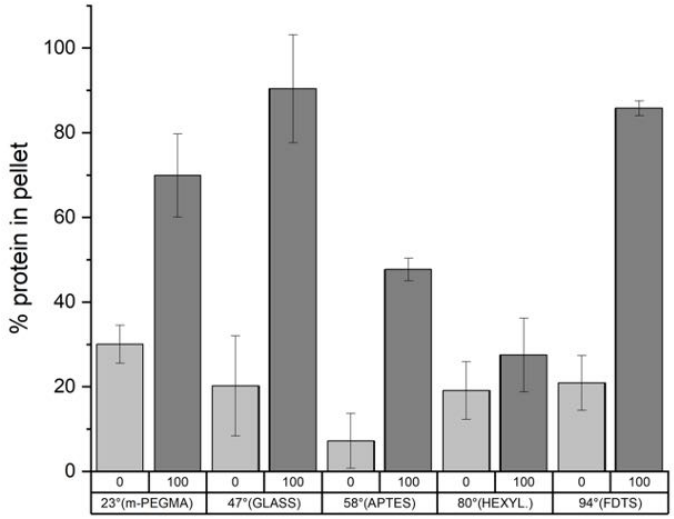

(b)

Figure 6.11: Effect of interface contact angle on percentage of aggregated mAb1 (6.11a), WFL (6.11b) and STT (6.11c) following quiescent incubation in the EFD (0 passes) or after 100 passes at a plunger speed of 8 mm/s. The contact angle of surfaces in the device ranged from 23° to 94°. Sample concentration = 0.5 mg/mL, buffer=150 mM ammonium acetate, pH = 6. Surfaces (in increasing contact angle): m-PEGMA, bare borosilicate glass, Silane A, Silane B, Silane C. N=3, error bars = standard deviation

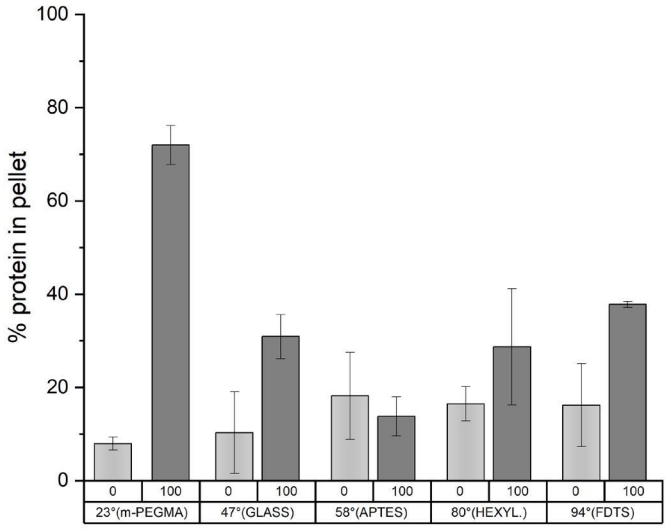

(c)

Figure 6.11: Effect of interface contact angle on percentage of aggregated mAb1 (6.11a), WFL (6.11b) and STT (6.11c) following quiescent incubation in the EFD (0 passes) or after 100 passes at a plunger speed of 8 mm/s. The contact angle of surfaces in the device ranged from 23° to 94°. Sample concentration = 0.5 mg/mL, buffer=150 mM ammonium acetate, pH = 6. Surfaces (in increasing contact angle): m-PEGMA, bare borosilicate glass, Silane A, Silane B, Silane C. N=3, error bars = standard deviation. (cont.)

where the solid surface is uncharged, and the pzc can be determined by contact angle measurements at various pH values [264]. As reported in [264], the pzc of APTES surface corresponds to ∼7.3, indicating that 90% of silanol groups are negatively charged and 100% of amine functions are positively charged. At pH=6, it was shown that the water contact angle on APTES is similar to that at pH=7, as it is close to pzc. Alternative to pzc, the determination of surface pK_a is commonly described as it is an important parameter for controlling the interaction between silicon modified surfaces with charged biomacromolecules such as proteins. The experimental determination of pK_a in various literature studies has been described via means of contact angle titrations, fluorescent nanoparticle and chemical force titration assays for APTES modified surfaces. The amount of protonated amine groups can be correlated with the pK_a. Based on the studies in [265, 266] the pK_a has been reported within a range of ∼6-10. However, the exact amount between silanol and protonated amine groups is difficult to be defined for the case of the APTES treated surface (silane A) in this work, as the pK_a is reported in literature with multiple values depending on the experimental method for pK_a determination, surface treatment protocol used in each study and the resulting density of APTES deposited on surface. As the particular surface exhibits surface charge properties depending on the pK_a, it is expected that the pH in which the surface adsorption and flow experiments are conducted (pH=6) can contribute to potential charge interactions between the surface and

protein molecules affecting the protein adsorption and flow experiments for the particular surface.

Statistical analysis

Conduction of statistical analysis performing ANOVA tests was used to investigate whether there is a significant difference between surfaces in the absence and presence of flow for mAb1, WFL and STT as shown in figures 6.12, 6.13 and 6.14 respectively. For all the molecules it is shown that the surface has no effect at 0 passes (absence of flow), suggested by non-significant difference as shown for mAb1 in figures 6.12a, 6.12b, for WFL in figures 6.13a, 6.13b and STT in figures 6.14a, 6.14b. At 100 passes, (presence of flow), the surface significantly affects the aggregation propensity. Particularly for mAb1, as shown in figures 6.12c and 6.12d, significant difference in the aggregation induced between silane C (FDTS) and silane B (HTS) surface, silane C (FDTS) and silane A (APTES), silane B (HTS) and glass and silane B (HTS) and mPEGMA. The particular surface sets which indicated significant difference in the mAb1 aggregation propensity can be found in table 6.2.

For WFL as shown in figures 6.13c and 6.13d, significant aggregation differences are obtained between the surface sets of silane C (FDTS) and silane B (HTS, Hexyl.), silane C (FDTS) and silane A (APTES), silane B (HTS, Hexyl.) and glass, silane B (HTS, Hexyl.) and mPEGMA, silane A (APTES) and mPEGMA (see also table 6.3). Finally, for STT, as shown in figures 6.14c and 6.14d, significant effects of surface sets corresponding to silane C (FDTS) and silane B (HTS, Hexyl.), silane C (FDTS) and silane A (APTES), silane C (FDTS) and mPEGMA, silane B (HTS, Hexyl.) and mPEGMA, silane A (APTES) and mPEGMA, glass and mPEGMA are indicated, which are also highlighted in table 6.4.

By comparing the analysis between the three molecules, it can be observed that there are two common surface combinations in which they show to have significant effects in aggregation between the three model proteins. By comparing the surface sets between the three molecules as shown in tables 6.2, 6.3 and 6.4, the particular surface combinations correspond: to silane C (FDTS) and silane A (APTES) and the surface set: silane B (HTS, Hexyl.) and mPEGMA. The particular analysis indicates that all the three model proteins (mAb1, WFL, STT), exhibited distinct aggregation profiles when exposed to silane C and silane A surfaces. Distinct aggregation profiles were also exhibited between silane B and mPEGMA surfaces.

Effects of surface interaction under higher strain rate conditions

At plunger speed of 8 mm/s and exposure time of molecules to flow events for 10 minutes, (corresponding to 100 passes), the particular flow conditions are observed to induce aggregation for all three molecules. The particular flow conditions of plunger speed at 8

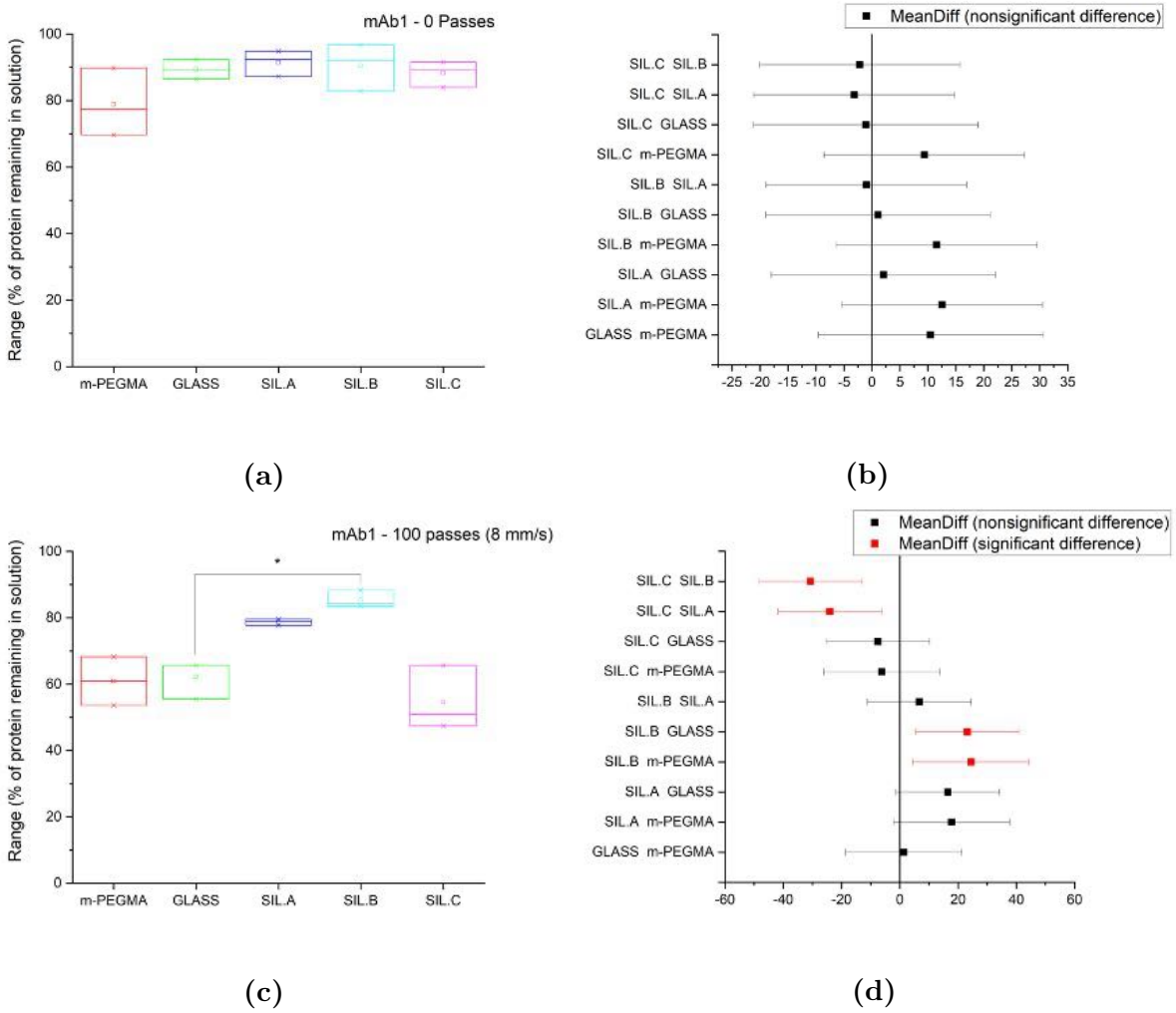

Figure 6.12: Statistical analysis of % protein remaining in solution for mAb1 following quiescent incubation in the EFD in the presence of different surfaces. Box plots showing median and interquartile ranges across the different samples. Data obtained from samples in figure 6.11a. One-way ANOVA analysis of means comparison plots of samples, performed in Origin 2017. Error bars indicate standard deviation.

Table 6.2: Summary of statistical analysis data, indicating the surface sets which presented significant difference in mAb1 aggregation levels under flow (8 mm/s, 100 passes). Surface sets with significant difference in aggregation are highlighted for comparison reasons with a checkmark, building from the ANOVA analysis, taken from figure 6.12d (mean difference plot, MeanDiff).

Model protein, mAb1	Untreated glass	Silane A	Silane B	Silane C	mPEGMA
Untreated glass					
Silane A (APTES)					
Silane B (HTS-Hexyl.)	✓				✓
Silane C (FDTS)		✓	✓		
mPEGMA					

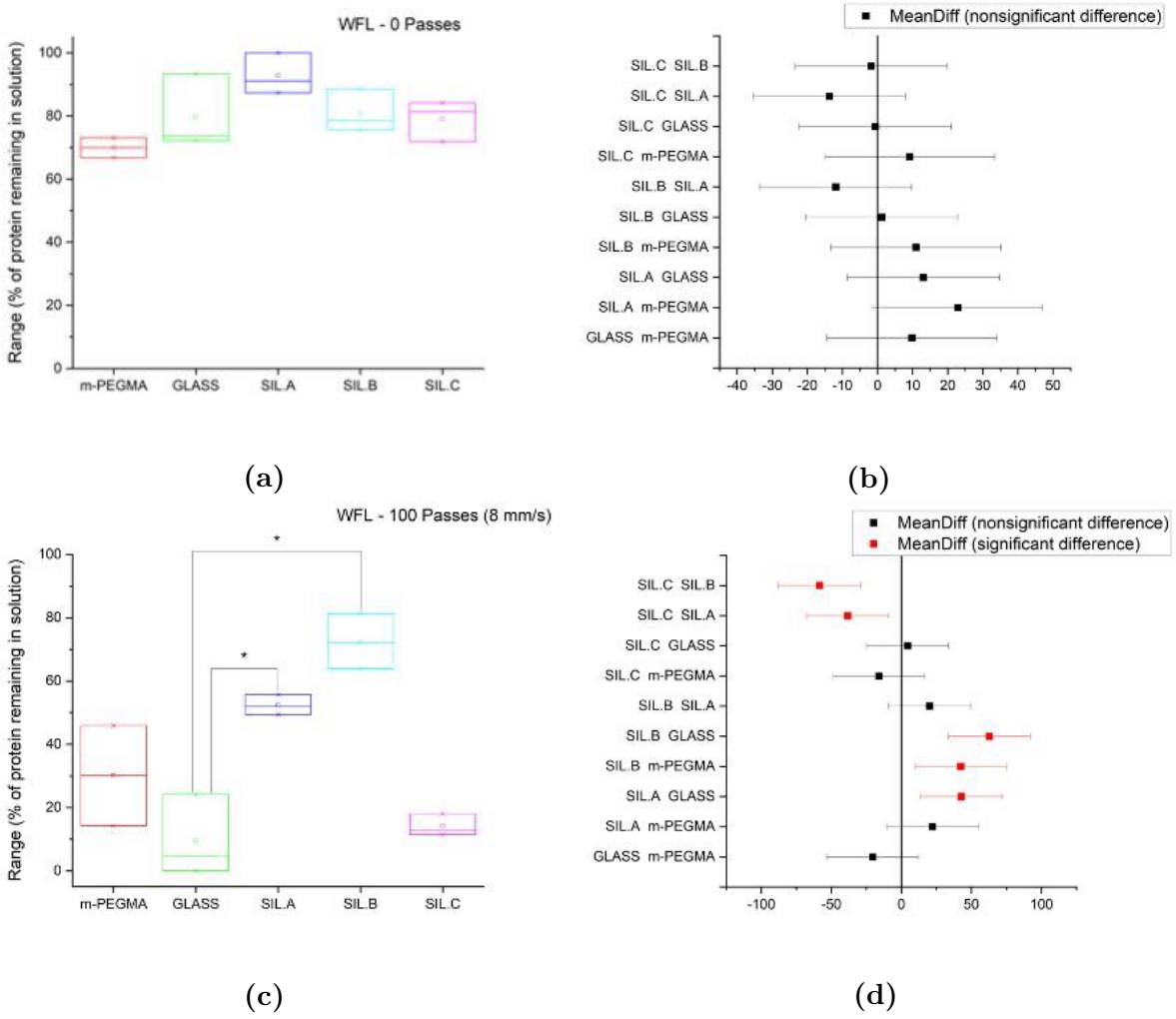

Figure 6.13: Statistical analysis of % protein remaining in solution for WFL stressed for 100 passes at a plunger velocity of 8 mm/s in the presence of different EFD surfaces. Box plots showing median and interquartile ranges across the different samples. Data obtained from samples in figure 6.11b. One-way ANOVA analysis of means comparison plots of samples, performed in Origin 2017. Error bars indicate standard deviation, *P <0.05.

Table 6.3: Summary of statistical analysis data, indicating the surface sets which presented significant difference in WFL aggregation levels under flow (8 mm/s, 100 passes). Surface sets with significant difference in aggregation are highlighted for comparison reasons with a checkmark, building from the ANOVA analysis, taken from figure 6.13d (mean difference plot, MeanDiff).

Model protein, WFL	Untreated glass	Silane A	Silane B	Silane C	mPEGMA
Untreated glass					
Silane A (APTES)	✓				
Silane B (HTS-Hexyl.)	✓				✓
Silane C (FDTS)		✓	✓		
mPEGMA					

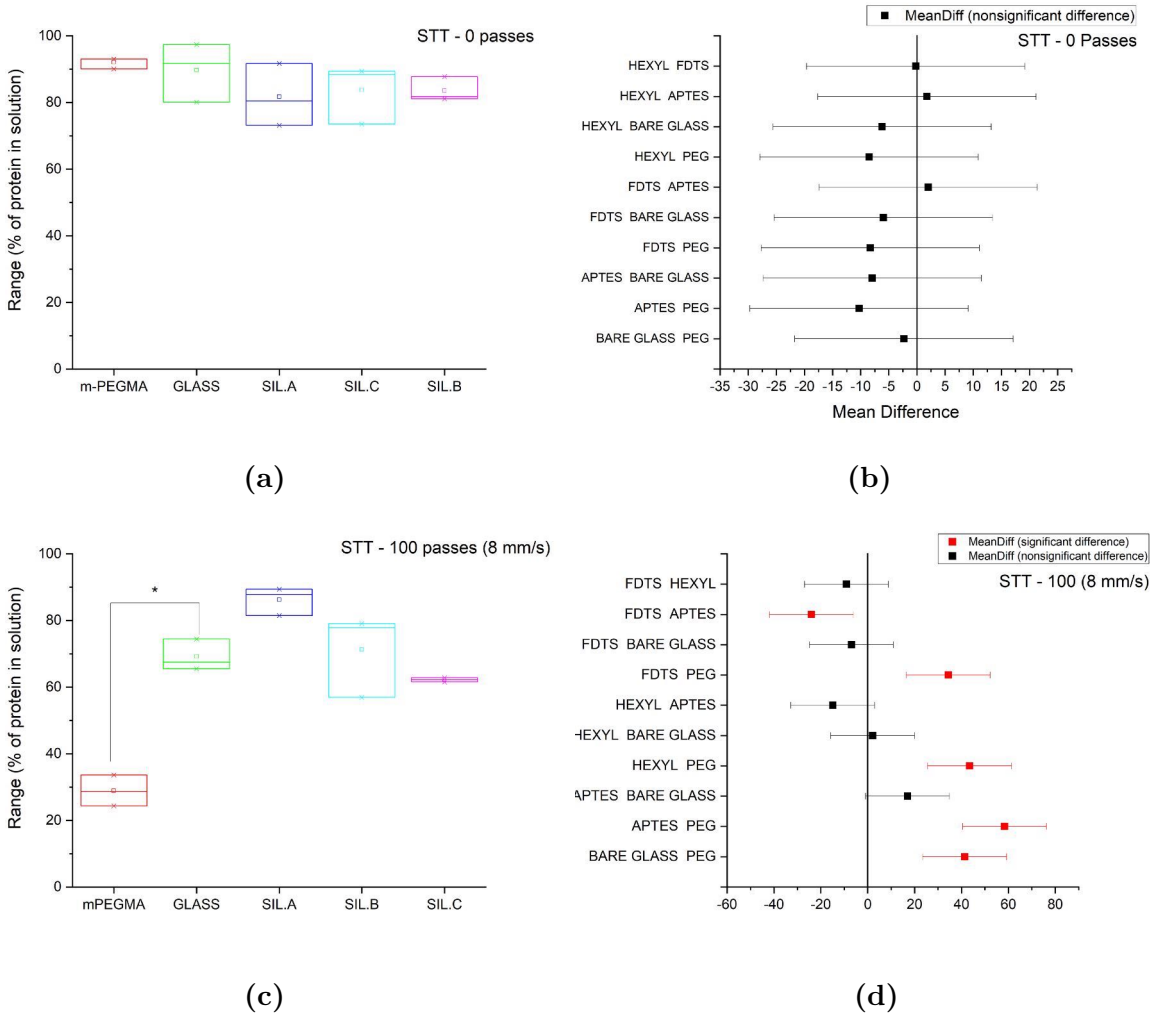

Figure 6.14: Statistical analysis of % protein remaining in solution for STT stressed for 100 passes at a plunger velocity of 8 mm/s in the presence of different EFD surfaces. Box plots showing median and interquartile ranges across the different samples. Data obtained from samples in figure 6.11c. One-way ANOVA analysis of means comparison plots of samples, performed in Origin 2017. Error bars indicate standard deviation, *P <0.05.

Table 6.4: Summary of statistical analysis data, indicating the surface sets which presented significant difference in STT aggregation levels under flow (8 mm/s, 100 passes). Surface sets with significant difference in aggregation are highlighted for comparison reasons with a checkmark, building from the ANOVA analysis, taken from figure 6.14d (mean difference plot, MeanDiff).

Model protein, STT	Untreated glass	Silane A	Silane B	Silane C	mPEGMA
Untreated glass					✓
Silane A (APTES)					✓
Silane B (HTS-Hexyl.)					✓
Silane C (FDTS)			✓		✓
mPEGMA					

mm/s, subjected to flow for 100 passes (experimental time of 10 minutes), have been set for the investigation of the surface effect as they have been previously shown to induce protein aggregation [1–3]. For all the molecules investigated, the surface modification was shown to affect their aggregation propensity to different extents depending on the hydrodynamic stability of each molecule. As we have seen earlier, WFL, described as a highly aggregation-prone molecule, reached aggregation of ∼90 % under these benchmark flow conditions, when exposed to the untreated glass surface and FDTS (figure 6.11b); therefore, the particular molecule is shown to have an enhanced aggregation propensity profile. On the other hand, mAb1 and STT molecules, with better hydrodynamic stability characteristics, can be used as model proteins investigating how the surface can affect their aggregation at higher flow conditions.

The aim of the particular set of experiments is to determine whether the surface parameter can still offer further aggregation stability to the molecules even under "higher" flow conditions. Doubling of the plunger speed at 16 mm/s exposes the molecules to double amount of strain rate of ∼25 $\times 10^3$ s^{-1} [1]. As mAb1 is an intermediate aggregation prone molecule, 100 passes as the duration time of the experiment is selected and for STT as the aggregation resistant molecule, 200 passes have been selected as shown in figures 6.15 and 6.16. As mentioned earlier, the aggregation landscapes of these molecules give an overview guide of the flow conditions and combinations for each molecule to observe significant aggregation levels, as shown in [2, 260].

Interestingly, the surface is shown to enhance the stability of the molecules compared to their aggregation induced when exposed to untreated glass surface, suggesting that the surface modification can act as a highly protective strategy against aggregation at these high flow conditions. Particularly, as shown in figure 6.15, mAb1 aggregation from ∼65% is suppressed to ∼20% when the equipment surface is treated with APTES (Silane A), suggesting an aggregation reduction by ∼45%. The same surface APTES, alongside with HTS (Hexyl., Silane B) suppressed the aggregation levels of STT from the aggregation state of ∼85% when exposed to the untreated glass surface, to ∼55% for APTES and ∼65% for HTS (Hexyl., Silane B) as shown in figure 6.16. The interaction of STT molecules with the particular surfaces offered aggregation suppression with reduction levels of ∼40% and ∼25% for APTES and HTS (Hexyl., Silane B) surfaces respectively.

Comparing these aggregation profiles with the aggregation profiles of the molecules when exposed to the standard flow conditions (8 mm/s, 100 passes) a common pattern in terms of the protective surfaces is observed. More specifically, for mAb1, APTES and HTS (Hexyl., Silane B) surfaces showed to enhance stability to aggregation, which was also observed for the APTES surface when exposed to higher flow conditions. Interestingly, the protective effect of HTS (Hexyl., Silane B) surface observed at the standard flow conditions (figure 6.11a) is not protective for the higher flow conditions. This observation can inform

us about the flow and surface complexity that the molecules encountered during the aggregation pathway. This could correspond to various stages of protein interactions with the surface and potential release of these into the bulk of the solution. These interactions and the degree in which they are encountered might be strain rate-dependent between the different flow conditions investigated. On the other hand, for STT, APTES was shown to correspond to the most protective surface among the surface library, for both standard flow conditions and higher flow conditions (figures 6.11c and 6.16). This could also suggest that the aggregation is highly protein-dependent, as the aggregation profiles and surface interactions are shown to be different between molecules under flow.

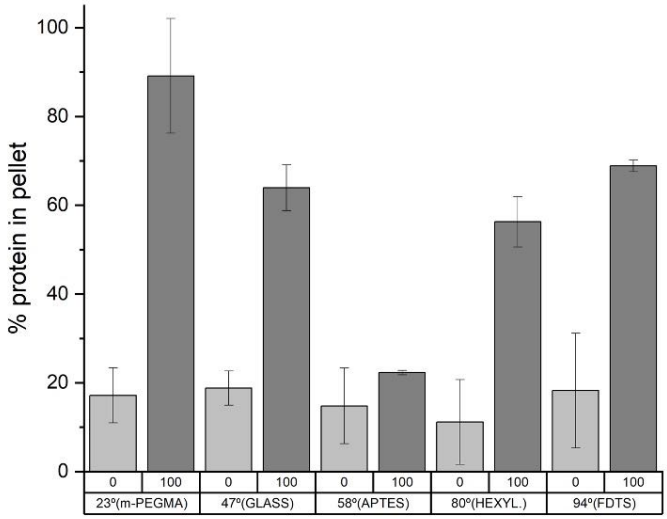

Figure 6.15: Percentage of mAb1 aggregation remaining in pellet at a concentration of 0.5 mg/mL in 150 mM Ammonium Acetate pH=6, stressed within the EFD in the absence (0 Passes) and presence (100 Passes) of extensional flow at a plunger speed of 16 mm/s for a range of contact angles between 23° to 94°, N=2, error bars=standard deviation. Significant aggregation suppression is observed for silane A treated surface.

Effect of surface on the size distribution

As the effect of surface under flow has now been demonstrated, the effect of surface on the size distribution of the protein aggregates was then investigated. The experiments have been performed at the standard flow conditions of 100 passes at 8 mm/s. mAb1 and WFL proteins have been used as the protein models of interest as they have shown intermediate and highly aggregation prone profiles and their size distribution profiles are shown in figures 6.17 and 6.18 respectively. To allow the detailed investigation of surface effects, molecules inducing reasonable levels of aggregation have been selected. The data in figures 6.17a, 6.17c, 6.17e, 6.17g and 6.17i present the size distribution profiles of mAb1 exposed to mPEGMA, untreated glass, APTES, HTS, and FDTS surfaces in conditions in

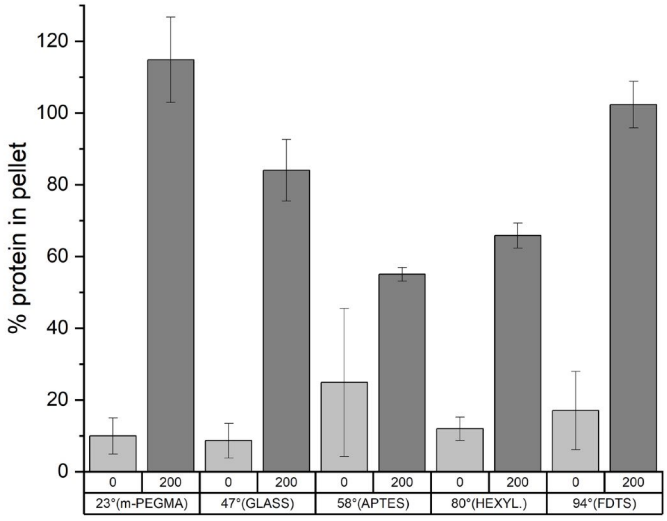

Figure 6.16: Percentage of STT aggregation remaining in pellet at a concentration of 0.5 mg/mL in 150 mM Ammonium Acetate pH=6, stressed within the EFD in the absence (0 Passes) and presence 200 Passes) of extensional flow at a plunger speed of 16 mm/s for a range of contact angles between 23° to 94°, N=2, error bars=standard deviation. Significant aggregation suppression is observed for silane A treated surface.

which the molecules were not exposed to flow (quiescent). For all the surfaces investigated, the size distribution shows a common profile of three distinct peaks corresponding to a monomeric peak, (where for a quiescent IgG molecule a hydrodynamic radius is measured at 6 nm). The formation of the two additional peaks could correspond to populations of bigger size molecules, and potential unfolded species, as it has been previously shown that there is a generic aggregation range in the order of ∼10-15 % for control samples left within the device surfaces. Appeared peaks of size bigger than 5 μm, cannot be considered as reliable information as they exceed the detectable size range of the DLS instrument. The monomeric peaks of mAb1 can be seen to be more distinct for the HTS (Hexyl.) and FDTS surfaces as shown in figures 6.17g and 6.17i respectively. In the presence of flow as shown in figures 6.17b, 6.17d, 6.17f, 6.17h and 6.17j, the size distribution corresponds to mainly three distinct peaks as shown for the control case, except the case of FDTS surface, presenting a broader size distribution as shown in figure 6.17j. As the molecules are introduced into partially unfolding events inducing aggregation, the intensity of monomeric peak can be seen to be decreased compared to the monomeric peak seen in the control samples, confirming the aggregation of the molecules with the transition of the monomeric species into partially unfolded state with the increase in size species comparing the populations of the second peaks.

For WFL control samples, the size distribution varies depending on the surface of interaction. Broader range of size populations appear for the untreated glass surface with four distinct

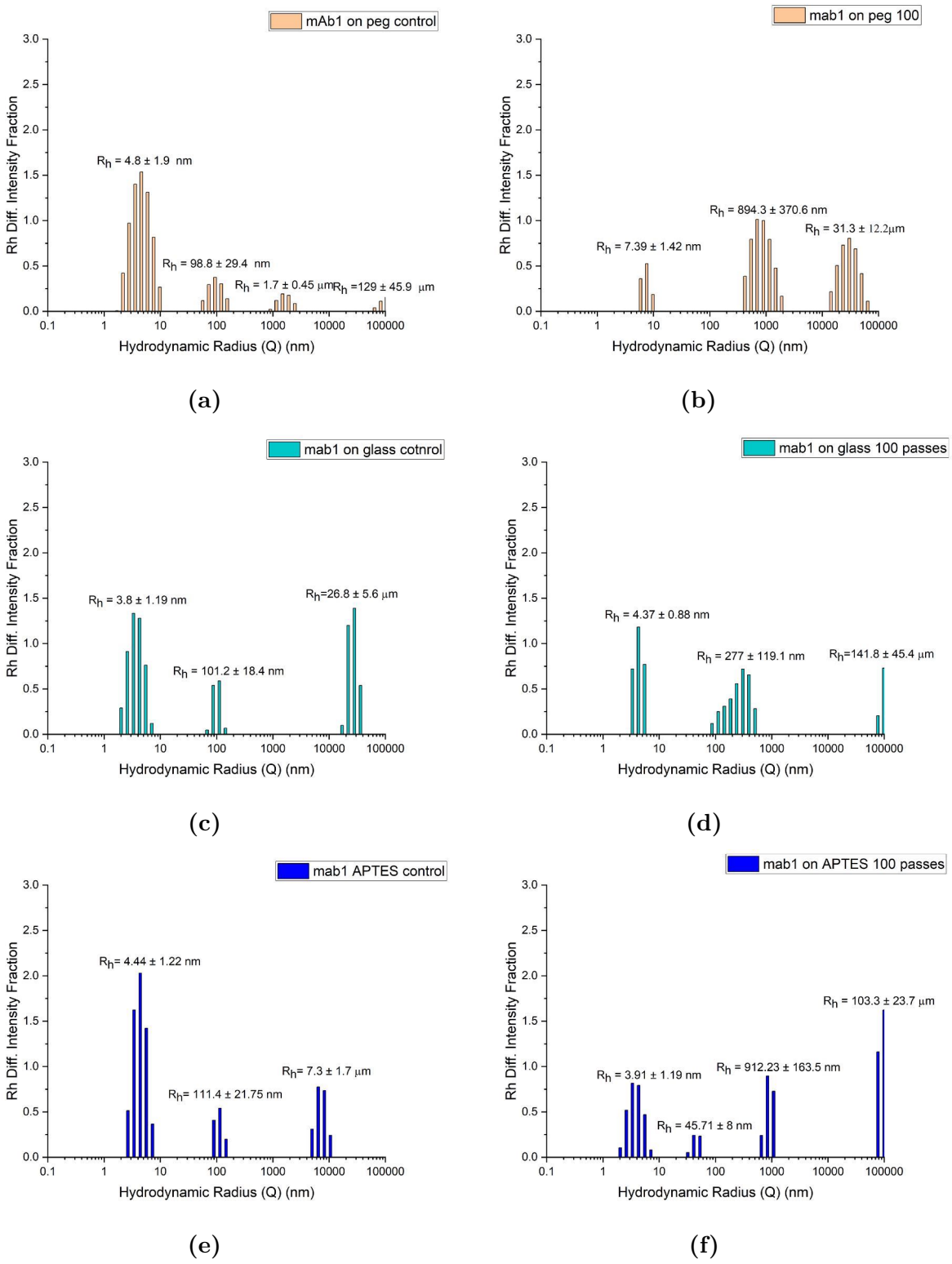

Figure 6.17: Plots of DLS data presenting the size distribution of control (samples left within the device surface bodies; syringe and capillary) and aggregated mAb1 in the presence of surfaces: mPEGMA(6.17a & 6.17b), bare borosilicate glass (6.17c & 6.17d), APTES (6.17e & 6.17f), HTS-Hexyl. (6.17g & 6.17h) and FDTS (6.17i & 6.17j). Samples have been stressed at 8 mm/s for 100 passes in 150 mM Ammonium Acetate buffer, pH=6.

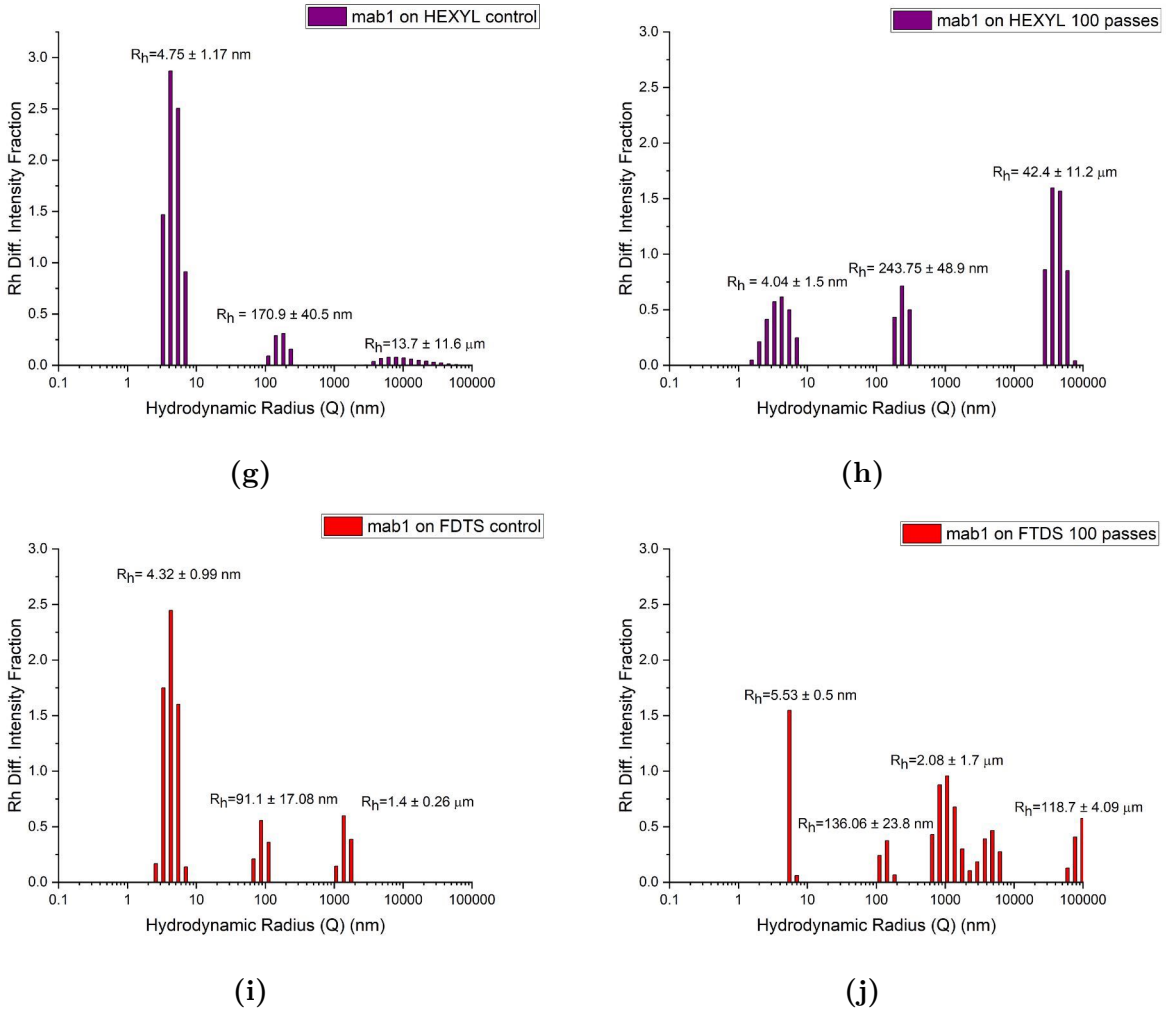

Figure 6.17: Plots of DLS data presenting the size distribution of control (samples left within the device surface bodies; syringe and capillary) and aggregated mAb1 in the presence of surfaces: mPEGMA (6.17a & 6.17b), bare borosilicate glass (6.17c & 6.17d), APTES (6.17e & 6.17f), HTS-Hexyl. (6.17g & 6.17h) and FDTS (6.17i & 6.17j). Samples have been stressed at 8 mm/s for 100 passes in 150 mM Ammonium Acetate buffer, pH=6. (cont.)

peaks as shown in figure 6.18a, three peaks for APTES as shown in figure 6.18c and FDTS shown in figure 6.18g and finally the less variation in size range is observed on the HTS (Hexyl.) surface as shown in figure 6.18e. A more distinct monomeric peak is observed for the HTS (Hexyl.) surface, as shown in figure 6.18e. In the presence of flow, the intensity of monomeric peaks is significantly suppressed suggesting the unfolding of the monomeric species and this is observed for the untreated glass surface in figure 6.18b, APTES in figure 6.18d and FDTS surface as shown in figure 6.18h. Interestingly, the monomeric peak is conserved in the presence of flow for the HTS (Hexyl.) surface as shown in figure 6.18f with the size distribution to present a similar profile to the one in the absence of flow (figure 6.18e). This observation can be correlated with the protective effects of the particular surface against the WFL aggregation, as shown previously in figure 6.11b.

6.3 The surface effect in high and low shear flow regions

The EFD used for the conduction of the flow experiments, comprises two syringes connected by a borosilicate capillary. Consequently, proteins are exposed to a variety of flow conditions as the solution is passed between syringes, as previously shown in figure 6.2. To understand the relationship between the flow regions and surface properties, mAb1 and WFL proteins were stressed using hybrid EFDs consisting of differing syringe and capillary surfaces. The syringe corresponds to the low shear surface where the proteins are exposed to minimal hydrodynamic forces (∼5 s between subsequent passes), whilst the capillary region corresponds to high shear as proteins are initially accelerated due to the sudden contraction [1, 2], followed by exposure to high shear rates for times of ∼40 ms per pass (figure 6.2).

Consequently, the role of surface wettability in the high shear region was determined by modifying the surface of the capillary in the EFD while keeping the syringe surface constant, as schematically shown in figures 6.19 and 6.20. Two sets of experiments were performed using non-derivatised syringes (i.e., bare glass that gives poor protection against aggregation), shown in figure 6.19a and syringes derivatised with silane B (the most protective surface) as shown in figure 6.20a. Both hybrid devices were used to subject mAb1 to 100 passes at 8 mm/s. Quantification of the resulting aggregation using these hybrid devices clearly shows that the surface wettability of the syringe barrels has a marked effect on aggregation (compare right-hand bars in figures 6.19b and 6.20). By contrast to figure 6.11, in these hybrid devices, aggregation is unaffected by the alteration of capillary surface. The same observation is made for WFL when it is stressed in the presence of various capillary modified surfaces (figure 6.19c).

The differential effect of surface modification within the low shear (syringe) and high shear

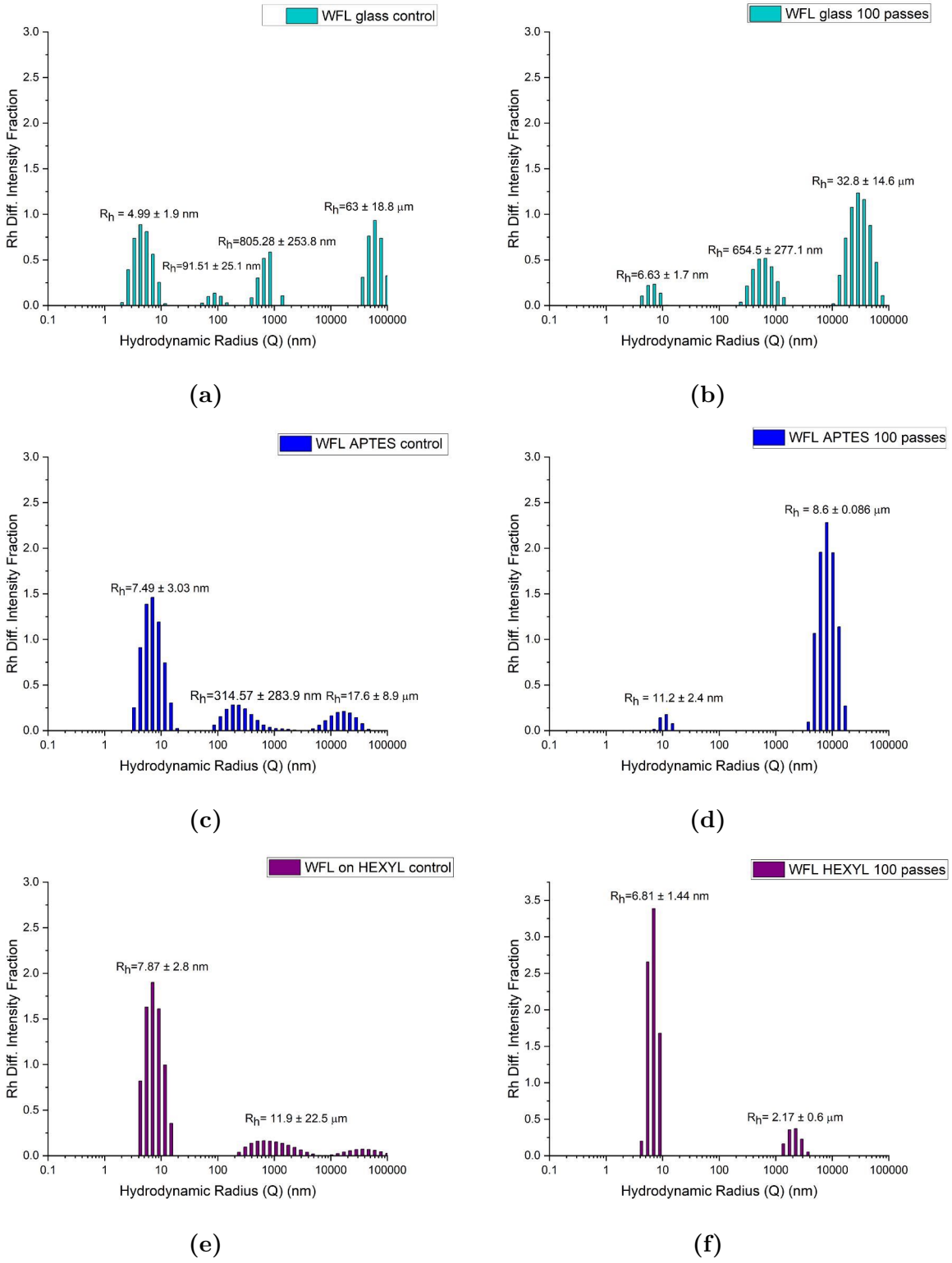

Figure 6.18: Plots of DLS data presenting the size distribution of control (samples left within the device surface bodies; syringe and capillary) and aggregated WFL in the presence of surfaces: bare borosilicate glass (6.18a & 6.18b), APTES (6.18c & 6.18d), HTS-Hexyl. (6.18e & 6.18f) and FDTS (6.18g & 6.18h). Samples have been stressed at 8 mm/s for 100 passes in 150 mM Ammonium Acetate buffer, pH=6.

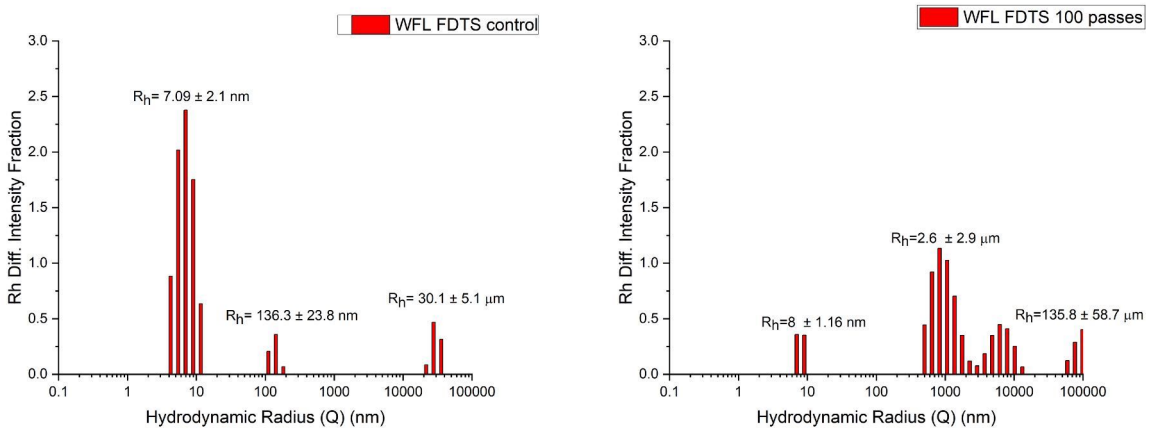

(g) **(h)**

Figure 6.18: Plots of DLS data presenting the size distribution of control (samples left within the device surface bodies; syringe and capillary) and aggregated WFL in the presence of surfaces: bare borosilicate glass (6.18a & 6.18b), APTES (6.18c & 6.18d), HTS-Hexyl. (6.18e & 6.18f) and FDTS (6.18g & 6.18h). Samples have been stressed at 8 mm/s for 100 passes in 150 mM Ammonium Acetate buffer, pH=6. (cont.)

(capillary) regions are clearly illustrated by comparing the fold-change in aggregation between mAb1 solutions subjected to 0 and 100 passes at 8 mm/s through EFDs with distinct surface characteristics. Table 6.5 summarises the fold-change in aggregation induced by EFDs with (i) no surface treatment: (ii) full surface treatment in silane B, (iii) both syringes treated in silane B with untreated capillary and (iv) both syringes in untreated glass with a silane B treated capillary. The greatest fold-increase in aggregation levels is observed when the surface arrangement of the device corresponds to bare glass on the low shear surface (syringe) with a silane B treated capillary. Conversely, the relative change in aggregation is smallest when the surface treatments are switched (low shear surface treated in silane B and untreated glass capillary). These data thus suggest that the surfaces experiencing low shear (the syringe barrel surface) dominate surface-induced protein aggregation under the flow conditions found within these experiments. This can be attributed to either the short time which the protein spends within the high shear region or the relatively low surface area of the high shear region, or a combination of the two (0.04 s and 71 mm^2) when compared to the low shear region (5 s and 461 mm^2).

6.4 Suppressing flow induced aggregation through formulation

The data above demonstrates the importance of interface wettability in modulating flow-induced protein aggregation. As many interfaces are encountered during manufacture and that the magnitude of these effects are protein-dependent, mitigating these effects on a platform manufacturing pipeline would be challenging to implement. An alternative

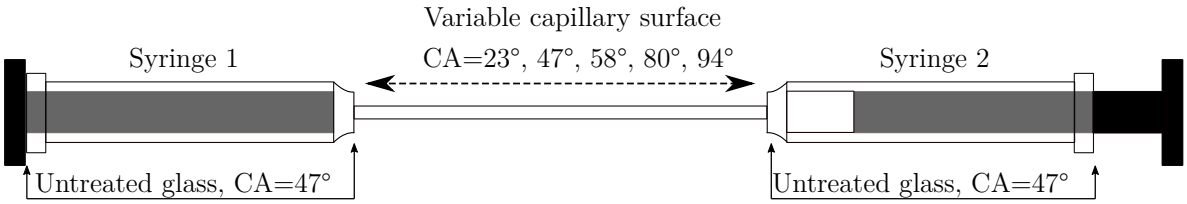

(a)

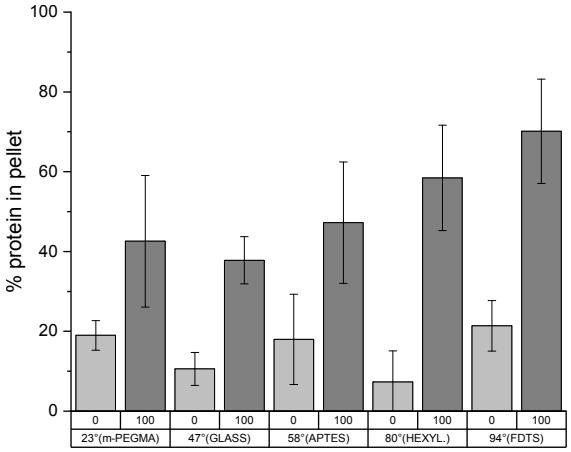

(b)

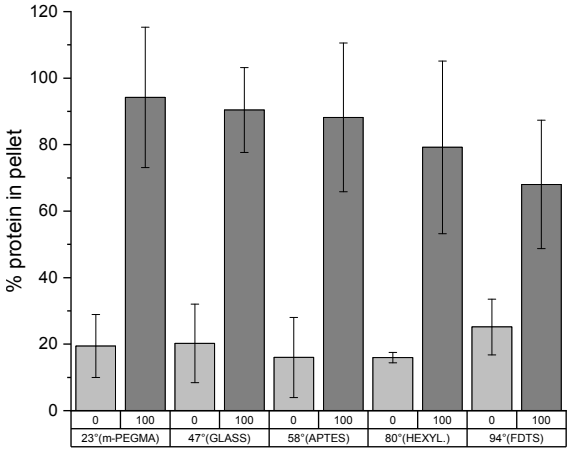

(c)

Figure 6.19: Investigating the effect of surface wettability in the high and low shear regions of the EFD under capillary surface variation for syringe surfaces remained untreated (bare borosilicate glass) (6.19a). Percentage of aggregated mAb1 (6.19b) and WFL (6.19c) following quiescent incubation in the EFD (0 passes) or stress in the device for 100 passes at a plunger speed of 8 mm/s. The contact angle of surfaces in the device ranged from 23° to 94°. Sample concentration = 0.5 mg/mL, buffer = 150 mM ammonium acetate, pH=6. N=3, error bars = standard deviation.

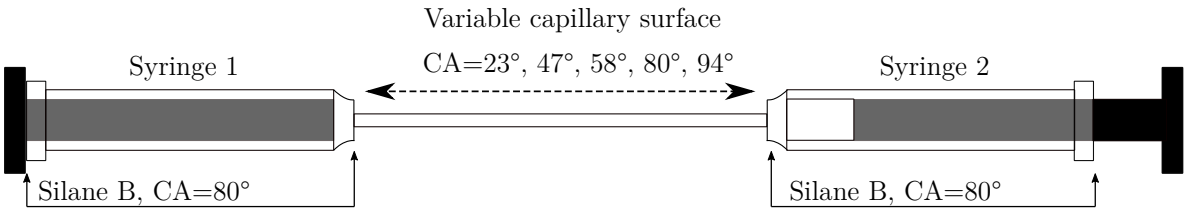

(a)

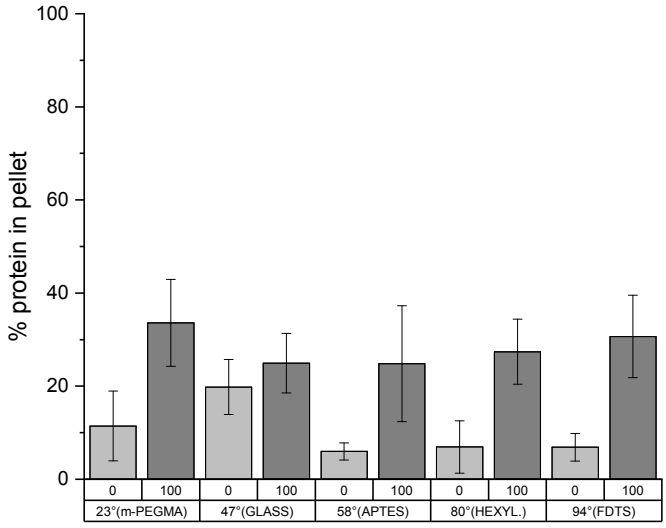

(b)

Figure 6.20: Investigating the effect of surface wettability in the high and low shear regions of the EFD under capillary surface variation for syringe surfaces silane B treated (6.20a). Percentage of aggregated mAb1 following quiescent incubation in the EFD (0 passes) or stress in the device for 100 passes at a plunger speed of 8 mm/s. The contact angle of surfaces in the device ranged from 23° to 94° (6.20b). Sample concentration=0.5 mg/mL, buffer = 150 mM ammonium acetate, pH=6. N=3, error bars = standard deviation.

Table 6.5: Summary of surface variation experiments. Experimental sets correspond to four surface combinations. Syringes and capillary remained untreated in bare glass surface (i), syringes and capillary treated with silane B (ii), syringes treated in silane B whereas the capillaries were untreated (iii), syringes remained untreated whereas capillary is treated with silane B (iv).

Surface set	Syringe	Capillary	Aggregation at 0 passes (%)	Fold change
(i)	Untreated glass	Untreated glass	10.6	3.6
(ii)	Hexyl. (HTS), Silane B	Hexyl. (HTS), Silane B	6.9	3.9
(iii)	Hexyl. (HTS), Silane B	Untreated glass	19.8	1.3
(iv)	Untreated glass	Hexyl. (HTS), Silane B	9.5	8

approach is to use additives within the solution to change the nature of the protein-surface interaction. The novelty found in the particular set of experiments is the simultaneous investigation of solid (surface) and liquid (surfactant) interfaces under the exposure to flow. Building from the previous section, it was suggested that the solid interface has a significant impact on the aggregation. Accordingly, the next step was to investigate whether the presence of a surfactant (Tween 20) or arginine, excipients previously shown to reduce protein aggregation [267–269], could mitigate the effects of surface wettability on flow-induced mAb aggregation, with the results shown in figure 6.21. As both additives have previously been shown to minimise protein aggregation, their effectiveness in preventing aggregation when exposed to the five distinct surface wettability values within the derivatised EFDs (bare glass, mPEGMA and silane A, B and C) was assessed using WFL, owing to its high aggregation propensity.

Tween 20, PS20

The addition of 0.1% v/v Tween 20 under extensional flow shows the suppression of aggregation, resulted in similar levels of aggregation observed for all of the surfaces examined here as shown in figure 6.21a. Comparison of the effects of the surface wettability in the absence and presence of surfactant (Figures 6.11b and 6.21a), shows that Tween 20 (PS20) affords the same level of aggregation reduction as the presence of silane B surfaces alone (CA=80°) which corresponds to the surface that gave the largest aggregation suppression. Tween 20 thus appears to suppress the effects of surface wettability. For example, flow in the presence of the two most hydrophilic surfaces (mPEGMA with a CA=23° and bare glass (CA=47°) causes a 2.3 and 4.5-fold increase in aggregation, in the absence of Tween 20. By contrast, in the presence of Tween 20, these surfaces only induce a 3.15- and 1-fold increase. This observation could be attributed to the proposed mechanisms of Tween, which correspond to surface blocking preventing protein surface interactions or the surfactant-protein interaction creating complexes preventing the protein-protein and protein-surface interactions [15]. A long-term stability study, under quiescent conditions using silane B, could be implemented to validate the potentially suppressive effect of this surface on protein aggregation as an alternative strategy to traditional formulation approaches. This may be advantageous, as Tween 20 degradation can lead to aberrant modification of biopharmaceuticals [268, 270].

Arginine

The effects of changing the buffer composition to 125 mM arginine and 20 mM succinate, pH=6) can be seen in figure 6.21b. In agreement with previously published data, arginine suppresses aggregation [267] including WFL when under flow [2]. For example, for bare glass, the presence of arginine reduced the observed aggregation by 62% (Figures 6.11b and 6.21b). Similar to the effects of Tween 20, arginine succinate buffer largely negated

the effects of the modified surfaces on flow-induced aggregation (a maximum difference of 2.15-fold and 4.5-fold between the surfaces in the presence and absence of arginine, respectively).

Despite this similarity between excipients, Tween 20 was observed to suppress aggregation to a greater extent (mean values of 29 and 46% for protein aggregation across surfaces for stress experiments performed in the presence of Tween 20 and arginine-succinate buffer, respectively). Both Tween 20 and arginine, suppressed WFL aggregation in a surface-independent manner, suggesting that both minimise the interaction of protein with the surface. To further investigate this possibility, the effect of Tween 20 and arginine on protein adsorption under quiescent conditions was investigated using QCMD. These data show that these excipients have distinct effects, as shown in figure 6.22. Tween 20 (0.1% v/v) suppressed protein adsorption to such an extent that only ∼3 nm layer was detected as shown in figure 6.22a (filled triangles), corresponding to a monolayer of detergent (the average diameter of a Tween 20 micelle is ∼8 nm [271, 272]).

These results suggest that the suppressive effect of Tween 20 is dominated by its surface activity properties, preventing protein adsorption at the surface which has been blocked by a monolayer of Tween. It should be noted that the molecular surfactant-to-protein ratio is 27, which might account for the preferential adsorption of the surfactant on the surface. Also, the protein adsorption kinetics are slower compared to the surfactant adsorption, as studied in [114], where the adsorption of a polysorbate (PS80) at increased concentrations was faster compared to the adsorption of mAbs at the air-water interface as indicated by surface tension measurements. By contrast to Tween 20, arginine did not affect protein surface adsorption as both the aerial mass and thickness as shown in figure 6.22, were similar to that in ammonium acetate buffer (figure 6.10) suggesting that a mAb monolayer forms in both cases (average thicknesses of 21.2 nm and 18.9 nm in arginine-succinate and ammonium acetate, respectively). This suggests that arginine's protective effects arise in the bulk solution, driven by antibody-arginine interactions [268]. However, the exact mechanistic pathway for the suppressive effects of arginine on aggregation has not been clarified in the literature. There are multiple hypotheses around arginine's action, which include its effect on surface tension, preferential hydration and preferential interaction [4]. Among the multiple effects of arginine, it is reported that arginine increases the surface tension of water molecules, with the authors stating that this observation cannot explain the suppressive effects of arginine on aggregation [273]. As concluded by the authors in [273], arginine interacts favourably with a majority of amino acid side chains, whereas, binding of arginine to the protein surface is limited, which plays a major role in its ability to suppress aggregation. On the other hand, regarding the effects of surfactants, it is widely reported that surfactants reduce the surface tension, reducing protein-protein interactions, and protein-surface interactions [4].

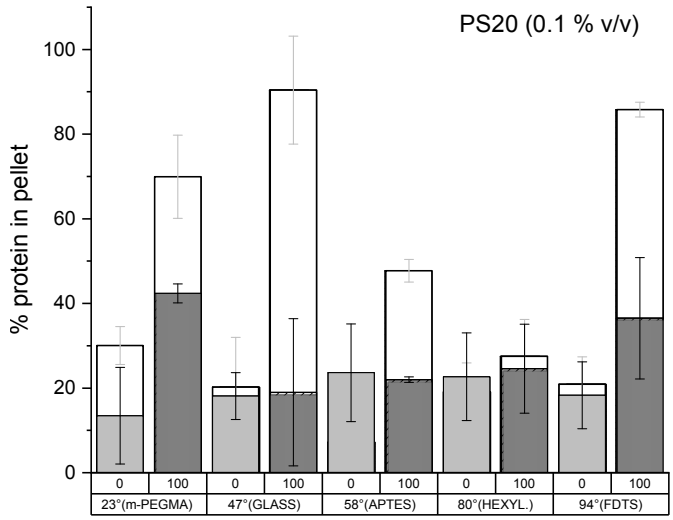

(a)

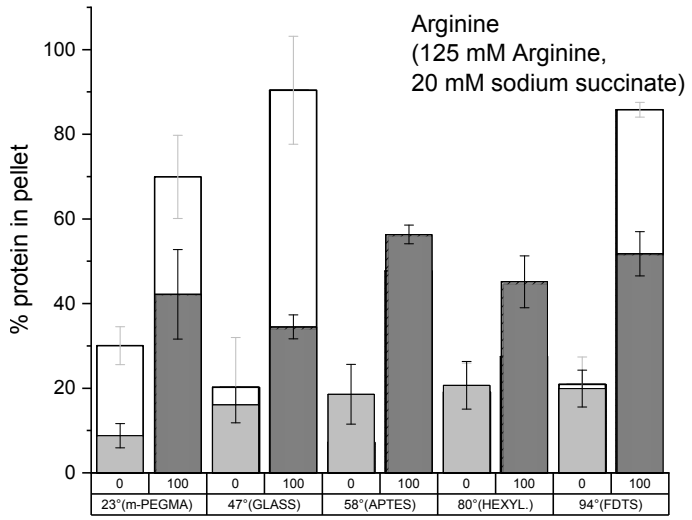

(b)

Figure 6.21: Percentage protein in pellet of WFL following quiescent incubation in the EFD (0 passes) or stress in the device for 100 passes at a plunger speed of 8 mm/s. The contact angle of surfaces in the device ranged from 23° to 94°. Sample concentration = 0.5 mg/ml, pH=6. 6.21a: Combined effect of surfactant and extensional flow indicating the aggregation profile of WFL in 150 mM Ammonium Acetate buffer with 0.1% v/v Tween 20 (PS20), pH=6. 6.21b: WFL aggregation stressed for 100 passes at 8 mm/s in 125 mM Arginine, 20 mM Sodium Succinate, N=3, error bars = standard deviation. For comparison purposes, white bars represent the WFL stressed in the standard formulation (150 mM Ammonium Acetate in the absence of formulation excipients) as taken from figure 6.11b.

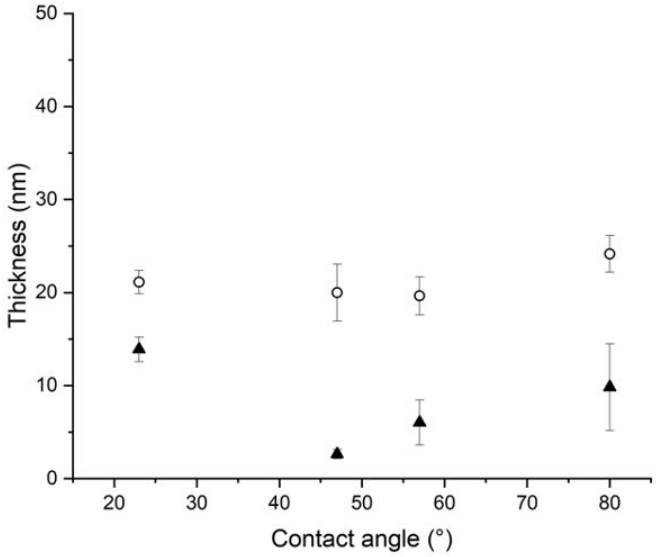

(a)

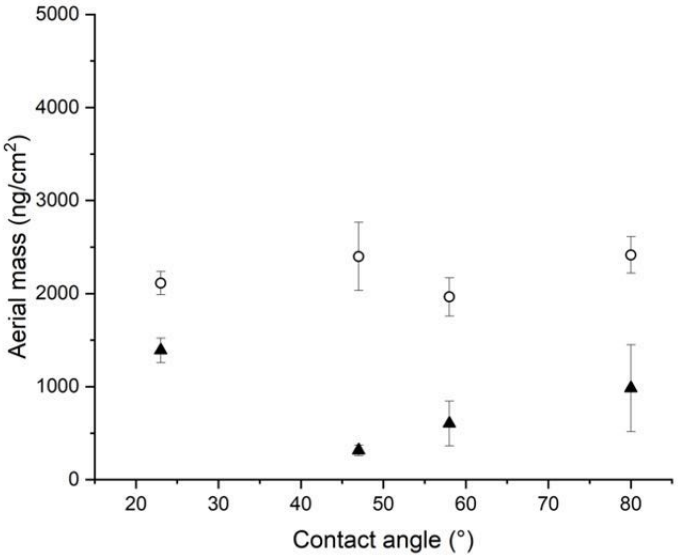

(b)

Figure 6.22: Average layer thickness (6.22a) and aerial mass (6.22b) of quiescent (absence of extensional flow) WFL (0.5 mg/ml) in 125 mM Arginine, 20 mM Sodium Succinate buffer (open circles) and 150 mM Ammonium Acetate + 0.1% v/v Tween 20 (filled triangles) on QCM sensors (5MHz 14 mm $Cr/Au/SiO_2$) with multiple contact angles at a flow rate of 0.21 ml/min. The average aerial mass of WFL in Arginine Succ. is similar to WFL in 150 mM Ammonium Acetate corresponding to 2000-2500 ng/cm^2, and average layer thickness of 15-20 nm, N=2. Significant drop in adsorption is recorded for WFL + 0.1% v/v Tween 20 corresponding to ∼315 ng/cm^2 and average layer thickness of ∼3 nm, N=2, error bars=standard deviation.

The particular data reveal distinct mechanisms of aggregation protection for Tween 20 and arginine (interface and bulk mediated, respectively) and begin to reveal the mechanism underlying EFD-induced protein aggregation. Together, these data show that the surface plays a vital role in flow-induced aggregation and that surface passivation together with formulation offers promising methods for aggregation reduction.

6.5 Aggregation induced by protein-protein interactions

As the chemical modification of the surface was shown to affect the aggregation pathway, the investigation of aggregation by developing a surface with protein adsorption on the surface is investigated here. The purpose of the experiment is to address whether a chemical modification or a protein conformational state already adsorbed on the surface is responsible for affecting the aggregation propensity as molecules are exposed to flow. BSA and STT proteins have been covalently labelled on the surface of glass syringes, and plungers, which were firstly treated with APTES and then cross-linked using BS3 linker which were performed by Dr Leon Willis as fully described previously in chapter 5 (subsection 5.2.2).

To demonstrate the success of the protein labelling on the surface, surface images presenting the topographical profile of the surfaces have been collected as shown in figure 6.23. Bare untreated glass (fig. 6.23a), APTES (fig. 6.23b), APTES-STT (fig. 6.23c) and APTES-BSA (fig. 6.23d) surfaces are characterised, demonstrating the surface modification. The protein-coated surfaces show higher features than the uncoated and APTES treated surfaces shown in figures 6.23c and 6.23d clearly due to the deposition of STT and BSA proteins respectively. The maximum topographical height recorded for the surfaces is shown to correspond to 15 nm. As expected for an untreated glass surface, the topographical image is relative flat, corresponding to a smoother surface as shown in figure 6.23a compared to a chemically treated surface using APTES as shown in figure 6.23b. Topographical heights also show a more populated protein surface on BSA cross-linked surface (figure 6.23d) compared to STT cross-linked surface (figure 6.23c). The average surface roughness of the surfaces (root-mean-square, R_q), as extracted from Nanoscope software, indicates increase in surface roughness with the surface modification corresponding to 0.602 nm for glass, 0.892 for APTES, 0.958 nm for STT and 2.11 nm for BSA. The maximum surface height, along with the average surface roughness, reflect the non-uniformity of STT and BSA deposition on the surface.

Alongside the topographical characterisation of the surfaces, contact angle measurements have been also performed as shown in figure 6.24, characterising the surface hydrophobicity. For the surface comparison between the modified surfaces, APTES is also plotted, as the

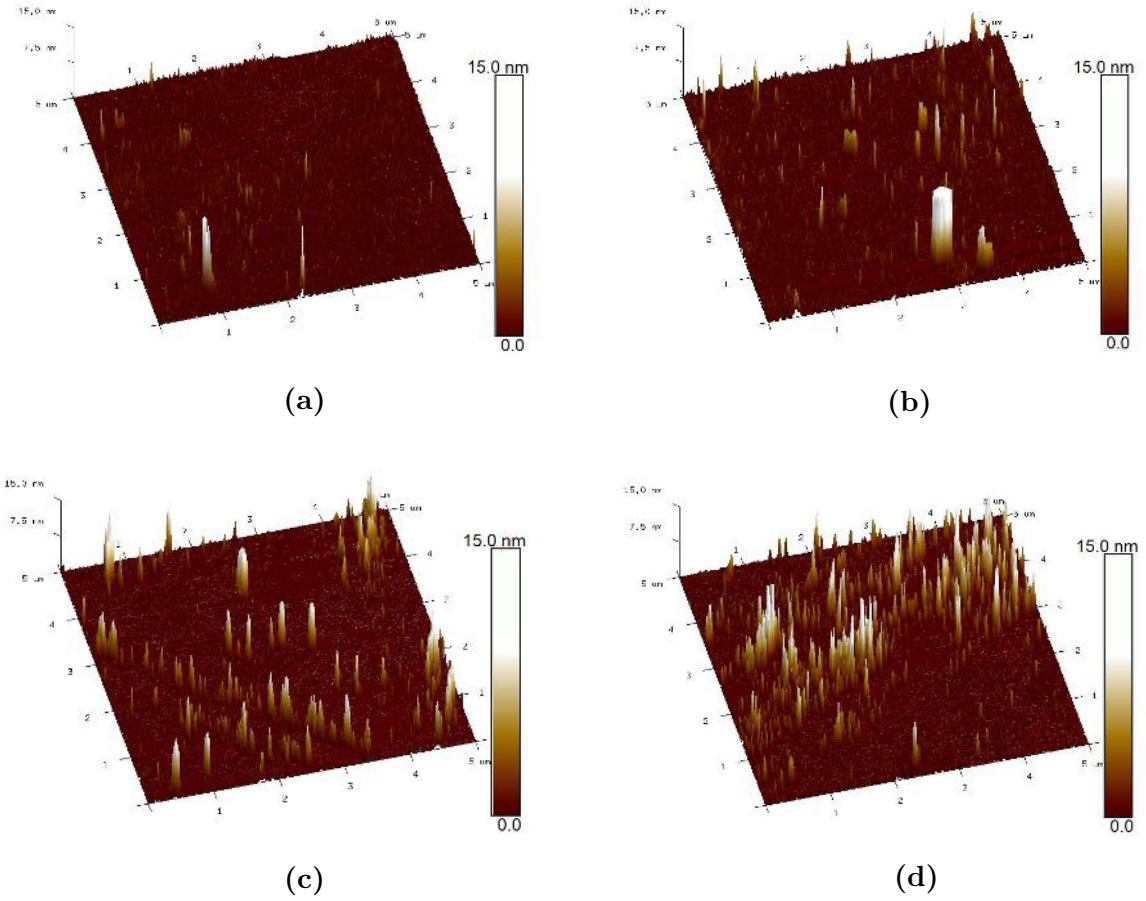

Figure 6.23: AFM images of the float glass slide surfaces before (6.23a) and after modification with APTES (6.23b), after immobilisation with STT antibody APTES-STT (6.23c), BSA APTES-BSA (6.23d). Scan size = 5×5 μm.

primary surface on which the protein cross-linking procedure is conducted. From the results it is shown that protein cross-linking enhanced the hydrophobicity of the surface with the contact angle (CA) increased from ∼58° for APTES to ∼75°.

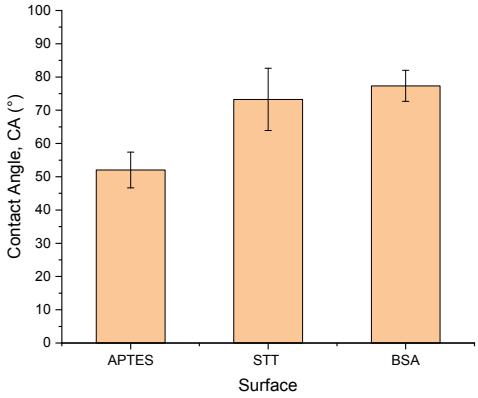

Figure 6.24: Water contact angle measurements for APTES (Silane A), STT cross-linked, and BSA cross-linked, error bar=sd.

As for the previous study, the effect of surface modification was firstly investigated in the absence of flow. STT adsorption experiments were then conducted to investigate whether the adsorption of the protein is enhanced in the presence of already adsorbed protein layer as shown in figure 6.25, followed by the raw data as shown in figure 6.26. The mass adsorption of STT molecules, on STT and BSA cross-linked surfaces, alongside their respective STT protein thickness on each surface, is quantified by QCMD experiments. As shown in figure 6.25, there is a similar propensity of STT to interact with the molecules of its family, i.e., STT cross-linked surface and similar tendency to interact with different molecules, i.e., BSA cross-linked surface within error of magnitude. The adsorption of STT on cross-linked surface is similar compared to its adsorption on APTES (58°) treated surface only, as shown previously in figure 6.10. This also implies the formation of monolayer with the recorded layer thickness at ∼20 nm.

The type of the adsorption of the molecule can be extracted by studying the raw data of the QCMD experiment, during the washing step. The washing or rinsing step, is the last step during the experiment, and depending on the profile of the raw parameters during the particular step, the type of the molecule's adsorption on the surface can be determined. As shown in figures 6.26a, 6.26b and 6.26c, there are shifts in frequency, Δf (shown in blue shades) and dissipation Δf (red shades) upon mass adsorption on the untreated glass, STT cross-linked and BSA cross-linked surfaces respectively, which are then followed by a buffer rinse as the last step in the experimental procedure.

As mentioned in chapter 2, section 2.8.1, the mass information about the protein adsorbed on the surface, can be detected by monitoring the oscillation frequency (Δf). A generic overview of the profile of the experimental data corresponding to mass adsorption events

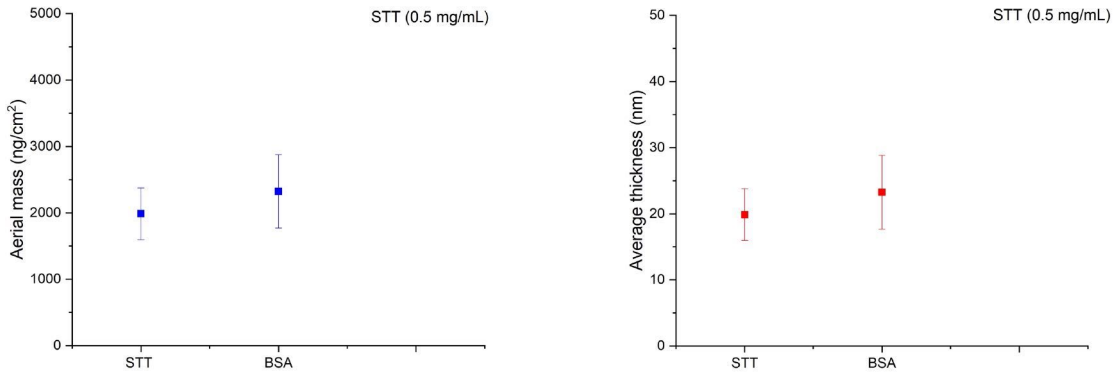

(a) **(b)**

Figure 6.25: QCM data for STT in the absence of extensional flow showing the aerial mass (6.25a) and average layer thickness (6.25b) for STT repeated experiment, N=2, error bars=standard deviation.

is previously presented in figure 2.21. A frequency shift by a decrease in frequency will indicate that mass is added to the QCMD sensor, whereas an increase in the frequency will indicate the mass removal from the surface. For fully adsorbed molecules on the surface, which are irreversibly adsorbed, the frequency and dissipation profiles will remain constant (flat), over time during the washing step with buffer (see right-hand side in figure 2.21b). Irreversible adsorption of molecules on the surface will imply that the molecule remains on the surface after rinsing or washing step. On the other hand, reversible adsorption of the molecule will imply that the molecules are rinsed off along with the buffer during the rinsing step, which is observed for all the experimental conditions investigated. Therefore, by isolating the buffer rinsing steps for the STT molecules on the untreated glass, STT cross-linked and BSA cross-linked surfaces, after the sudden shifts in frequency and dissipation, it can be observed that the frequency still increases as shown in figure 6.26 (right-hand side). This indicates a mass removal from the surface during the buffer rinsing step, implying that the type of protein adsorption observed is reversible. This reversible type of adsorption indicates that the molecules can interact with the surface and "travel" within the bulk of the solution. Molecule reversible adsorption, combined with the exposure to shear and extensional flow regions, implies the potential complexity encountered when flow is introduced in the system. The molecule can follow multiple potential reversible adsorption events with the device's surface along the conduction of the experiment.

Additional to the type of adsorption process of molecules, QCMD raw data can be used to determine the rate in which the molecules dissociate from the surface. The raw data of frequency shift allows the experimental determination of the desorption/off rate of molecules from the surface. This will give insights into whether the modification of the

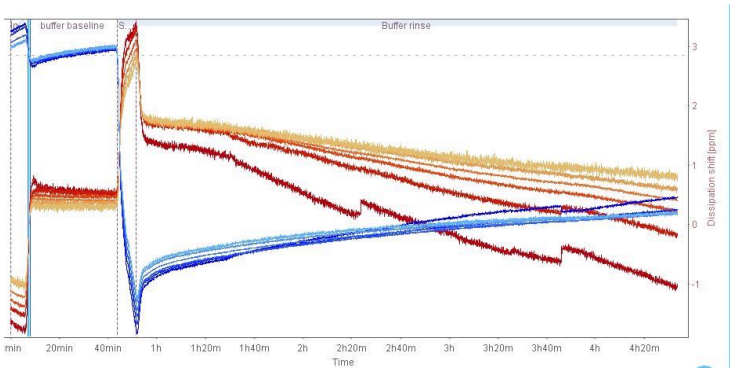

(a)

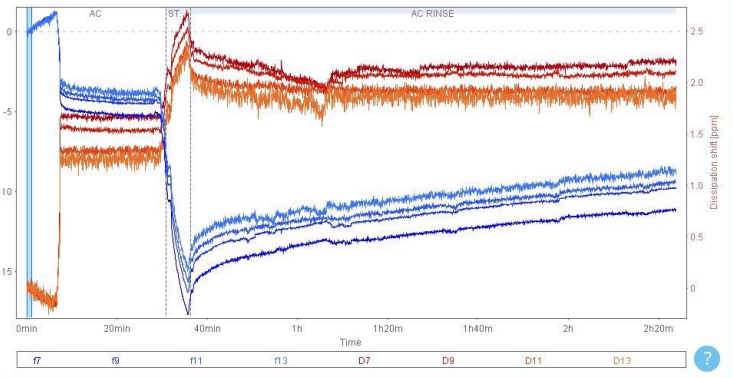

(b)

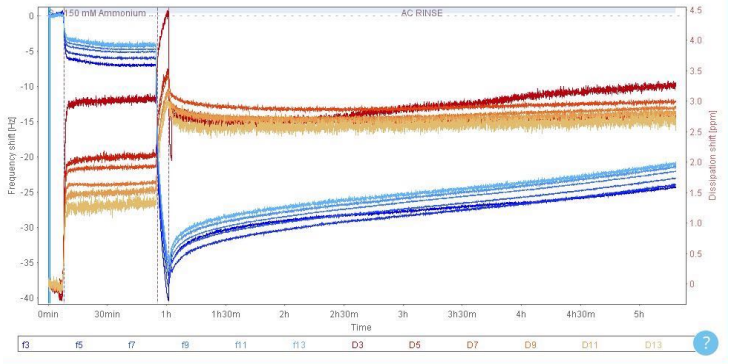

(c)

Figure 6.26: QCMD raw data showing frequency (shown in blue shades) and dissipation (shown in red shades) shifts when molecules start to adsorb on the surface for a range of frequency overtones. Data show STT adsorption on glass surface 6.26a, STT cross-linked surface 6.26b, and BSA cross-linked surfaces 6.26c.

surface with cross-linked protein molecules can affect the desorption rate of STT when it is exposed to an untreated surface such as that of glass (untreated) compared to STT and BSA cross-linked surfaces. To obtain the desorption rates on the various surfaces, the slope of the frequency increase step is automatically obtained, and the parameter τ is determined in seconds (s). Then the off rate C, is determined as the inverse of the slope (C=$1/\tau$) as shown for bare glass, STT and BSA surfaces with the final desorption/off rates to be calculated based on the slopes as C_{glass}=1/112= 8.9×10^{-3} s^{-1}, C_{STT}=1/19919657= 5.02×10^{-8} s^{-1}, and C_{BSA}=1/2589391= 3.86×10^{-7} s^{-1}, from the slopes taken from the frequency data as shown in figures 6.27a, 6.27b and 6.27c respectively.

Interestingly, the data show that STT protein desorbs slower with protein molecules already adsorbed on the surfaces, compared to the untreated glass surface with the higher desorption rate. This implies that the interaction between protein molecules is significant compared to a surface with no protein molecules, with the rate to be slower in the order of 10^5 for STT and 10^4 for BSA compared to the glass surface. The slower desorption rate is shown to correspond to the STT-cross linked surface, implying that molecules from the same population interact highly with one another compared to molecules from different populations. This will also imply to the scenario where a protein is already adsorbed on the equipment surface of the device under flow. In this case, a potential interaction of molecules from the bulk state with the molecules landed on the surface state can have slower desorption rates. This could imply that there is more time for the interaction between the molecules already landed on the surface with the molecules within the bulk state.

Flow experiments on the surfaces with covalently attached proteins were then followed, to examine the effect of protein-protein interactions, as shown in figure 6.28. The particular set of experiments, investigates the effect of the interaction between same and different protein populations to determine whether the interaction between same molecules is more aggregation-prone, inducing further aggregation by exposing STT molecules on STT cross-linked surfaces as shown in figure 6.28a. The effect of interaction between different protein molecules was also investigated by examining the flow behaviour of BSA molecules on STT cross-linked surfaces, as shown in figure 6.28b. The experiments were kindly performed by Dr Leon Willis.

Multiple hypotheses scenarios can determine the type of interaction under flow conditions. Suppressed aggregation can be expected in the situation where surface adsorbed molecules catalyse refolding of the native protein state in the presence of a protein attached on the surface. Alternatively, suppressed aggregation can be induced by the full passivation of STT cross-linked molecules on the surface, where it will be no molecular space for aggregation to be induced on the surface. The next hypothesis corresponds to the case where aggregation is enhanced, where protein adsorbed molecules catalyse aggregation.

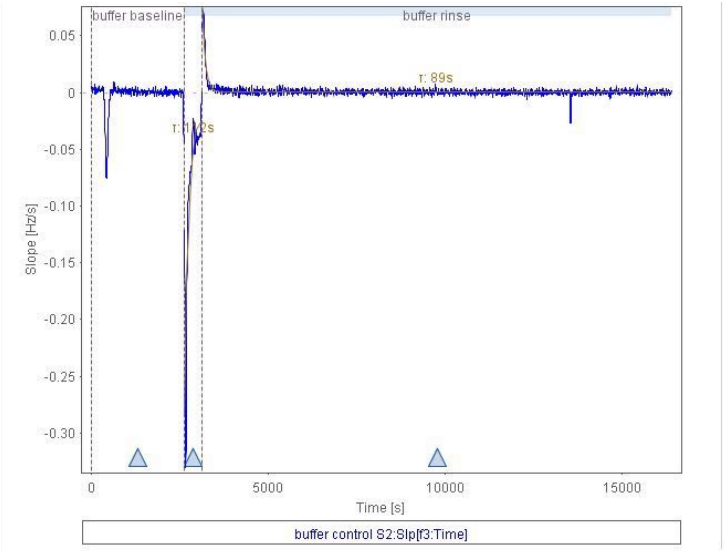

(a)

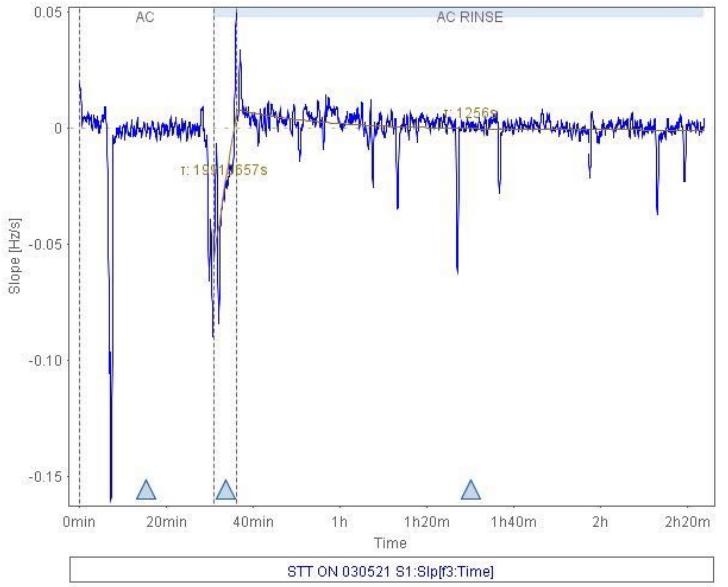

(b)

Figure 6.27: Frequency slope data indicating potential desorption rates as extracted from DFind software. Data correspond to STT (0.5 mg/mL, in 150 mM Ammonium Acetate, pH=6) loaded to untreated glass (6.27a), STT cross-linked surface (6.27b) and BSA cross-linked surface (6.27c). Exponential fit determines constant τ, which can be used to determine the desorption/off rate which is C=1/τ.

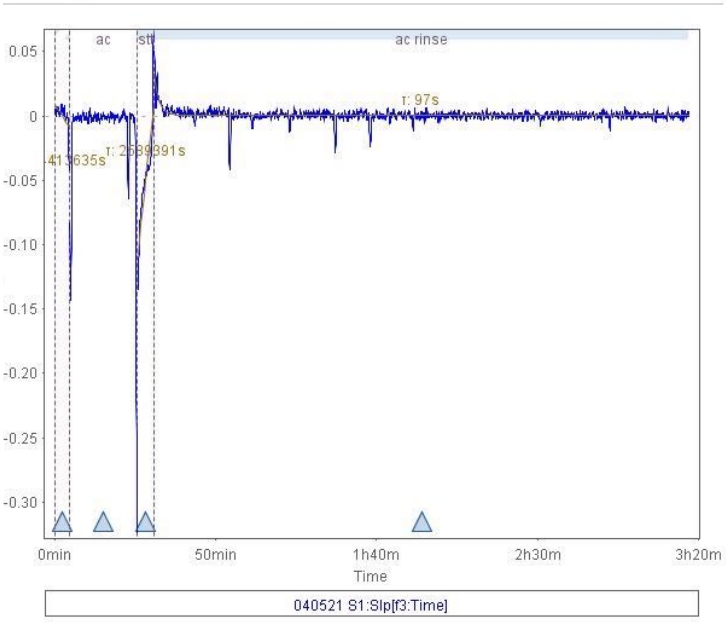

(c)

Figure 6.27: Frequency slope data indicating potential desorption rates as extracted from DFind software. Data correspond to STT (0.5 mg/mL, in 150 mM Ammonium Acetate, pH=6) loaded to untreated glass (6.27a), STT cross-linked surface (6.27b) and BSA cross-linked surface (6.27c). Exponential fit determines constant τ, which can be used to determine the desorption/off rate which is C=1/τ. (cont.)

Flow induced aggregation of the molecules on the STT cross-linked surface indicated that the aggregation between same molecules is suppressed compared to the aggregation between different molecule populations. From the data, it is also shown that the STT XL surface has a protective effect, with slower aggregation and non-complete aggregation observed at 0.25 mg/mL. This observation can also be linked with the desorption rates obtained in the absence of interaction of flow from the QCMD experiments, as shown above. The STT desorption from the STT cross-linked surface was shown to be slower compared to BSA cross-linked surfaces, implying that the STT-cross linked surface is more protective as the molecules desorb slower from the particular surface and the aggregation induced under flow for the particular surface is less compared to BSA cross-linked surface.

6.6 Summary

This chapter considered three main sections, including the effects of (i) solid interfaces, (ii) liquid interfaces through formulation strategies and lastly (iii) protein-protein interactions in the flow induced aggregation. The investigation of solid interface effects was achieved via the surface modification of the extensional flow device components (syringes, capillary) highlighting that the solid interface can impact the aggregation propensity under flow conditions. This suggested that there is a synergy between flow and the solid interface parameter, which both contribute in affecting the aggregation of the molecules. This

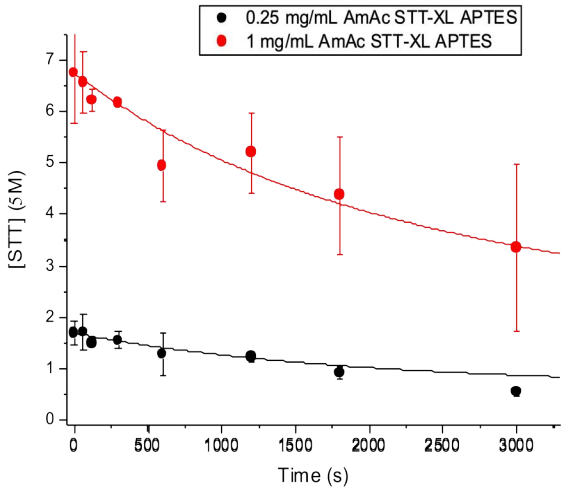

(a)

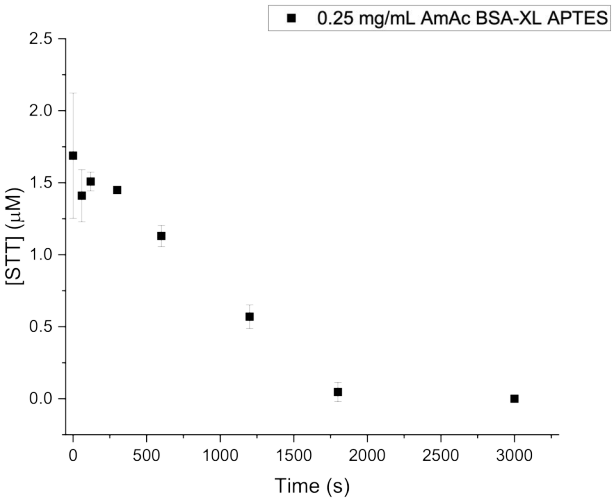

(b)

Figure 6.28: Effect of cross-linked surfaces on the STT concentration as a function of time (pass number, 1 pass = 6 s). 6.28a: STT initial concentration at 0.25 mg/mL (shown in black), and 1 mg/mL (red) stressed in syringes coated with STT-XL-APTES. 6.28b: STT initial concentration at 0.25 mg/mL stressed in syringes coated with BSA-XL-APTES. Experiments were conducted by Dr Leon Willis at a plunger velocity of 8 mm/s in 150 mM Ammonium Acetate (AmAc), pH=6.

finding is important, as it suggests the complexity of the flow-induced aggregation, and sheds light into the redesign of the currently proposed aggregation pathway, which it was based on the flow-induced aggregation via the bulk pathway. Therefore, there is a need to integrate and further investigate the solid interface parameter into the previously proposed aggregation pathway, as presented in [2]. From the results, it was also shown that specific surface sets have been found to enhance the stability of the molecules when exposed to shear and extensional flow conditions by suppressing the aggregation levels compared to the standard equipment surface (bare glass). From a practical perspective, accessible equipment components including filters, syringes, pistons, plungers etc, could be treated with the particular surfaces, which can enhance the stability of the molecules during their manufacturing.

The second aspect of the chapter, expanded on the investigation of a broader parameter space by including the liquid interface effects such as excipients including arginine and surfactant (PS20). From the particular section it was shown that using suitable protein formulation conditions, the stability of the molecules can be enhanced. This can be applicable to conditions where the components part of the manufacturing process are not accessible or difficult to be surface treated. Therefore, formulation strategies can be applied accordingly.

The third part of the chapter investigated the covalent attachment of proteins on the equipment surfaces, and investigating whether the conformational state of protein which is already landed on a surface can impact the aggregation. The data, accompanied by experimentally determined off-rates, suggested that the interaction between protein-protein molecules from the same population is slower compared to protein-protein from different populations, and even slower from surface-protein interactions. It was also shown that the adsorption of proteins on surfaces is a reversible process, which also highlights the complexity of the aggregation pathway mechanism with the potential involvement of multiple steps throughout the aggregation pathway.

Chapter 7

Effect of surfactants on flow induced aggregation

In the previous chapter, the suppression of flow induced aggregation was shown to be achieved via surface modification strategies. The use of a surfactant was also investigated using tween 20 (PS20), where it was shown to offer enhanced stability to the molecules when exposed to extensional flow. This chapter builds on the work conducted previously, investigating the aggregation suppression from the formulation perspective with the application of a surfactant library. Model proteins for the conduction of the formulation studies are: MEDI8852 (an IgG1), and MEDI3549 (a bispecific molecule), both provided by AstraZeneca, where their aggregation propensity under extensional flow conditions is not known. MEDI3549, which is a bispecific molecule, corresponds to an interesting candidate to study its aggregation performance due to its relatively high molecular weight (∼200 kDa) compared to the standard molecular weight of ∼150 kDa for IgGs. Different experimental studies conducted for each molecule are presented, to investigate how their stability can be enhanced under flow conditions which have been previously defined to induce aggregation.

An overview of the main sections covered in the current chapter is shown in figure 7.1. Initially, the chapter explores the rheological characterisation of these molecules at low and high concentrations by the conduction of viscosity measurements which will be discussed in section 7.1, followed by the investigation of the effect of high concentration on their aggregation propensity in section 7.2. The formulation of these molecules is then modified, and their respective aggregation is then characterised by various analytical methods by the introduction of a surfactant library, which will be described in section 7.3. Next, the further characterisation of the surfactant library effect is explored by the surfactant screening using the extensional flow device, followed by the overall chapter summary in sections 7.4 and 7.5 respectively.

7.1 Rheological characterisation

7.1.1 Experimental viscosity characterisation

Firstly, the rheological characterisation of these model proteins was conducted to investigate their viscosity profiles. Their rheological characterisation was conducted at the standard

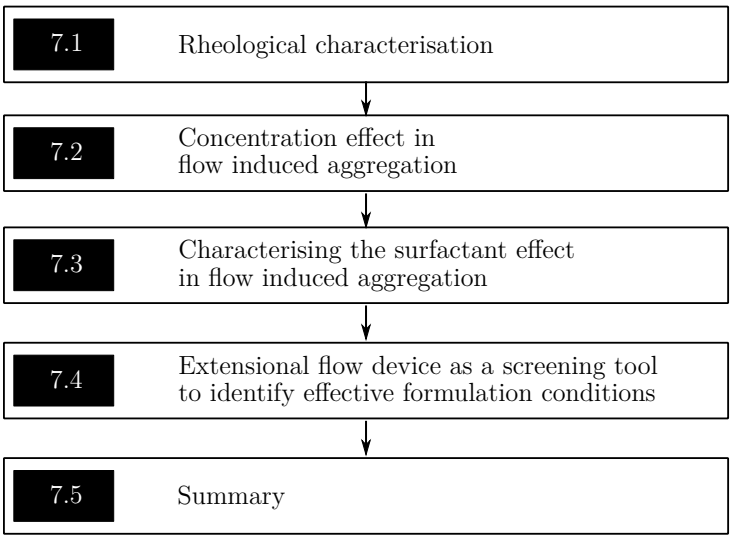

Figure 7.1: Overview of the main sections covered in the effect of surfactants in flow induced aggregation chapter.

concentration used in the previous chapter of 0.5 mg/mL and also at higher concentrations including 5, 10, 20 and 40 mg/mL. The development of proteins in high concentration is commonly encountered due to the high dose requirements and delivery convenience to patients, reducing the injection frequency [274]. Therefore, concentration of >50 mg/mL corresponds to the concentration in which many monoclonal antibodies are marketed [275]. Specifically, as reviewed in [276], a list of commercial mAb-based products, indicates that commercialised products can be found with active concentration range from 0.15 mg/mL with maximum active concentration of 200 mg/mL. The development of these biopharmaceuticals at high concentrations can encounter various challenges including solubility limitations, phase separation, increased viscosity, and aggregation propensity that may restrict the manufacturability, deliverability, stability, and shelf life of the product [274, 275].

The aim of the particular experiment was to investigate whether the molecules experience molecular structural rearrangements, especially at higher concentrations, when exposed to shear flow. This will allow determining an initial overview of any molecular rearrangement when these molecules are exposed to shear flow conditions. As mentioned earlier, the use of excipients is a commonly found strategy to enhance molecular stability. Sucrose corresponds to one of these excipients which can be included in protein formulations. The formulation buffer for these particular proteins is 235 mM Sucrose, 25 mM Histidine at pH=6. Therefore, to investigate the viscosity profile of these molecules, the viscosity of their formulation buffer is firstly collected as shown in figure 7.2, presenting a Newtonian profile as the shear viscosity is constant along the increase in shear rate. At the particular sucrose concentration, the corresponding measured viscosity is recorded at 0.001 Pas. The recorded viscosity agrees with previously published sucrose viscosity data, where for a sucrose at a concentration of 10% w/w, the viscosity is measured as 1.13 mPas (0.0013

Pas) as shown in [277]. The rheological characterisation of sucrose corresponds to the relative control, as it corresponds to the formulation buffer of the model proteins.

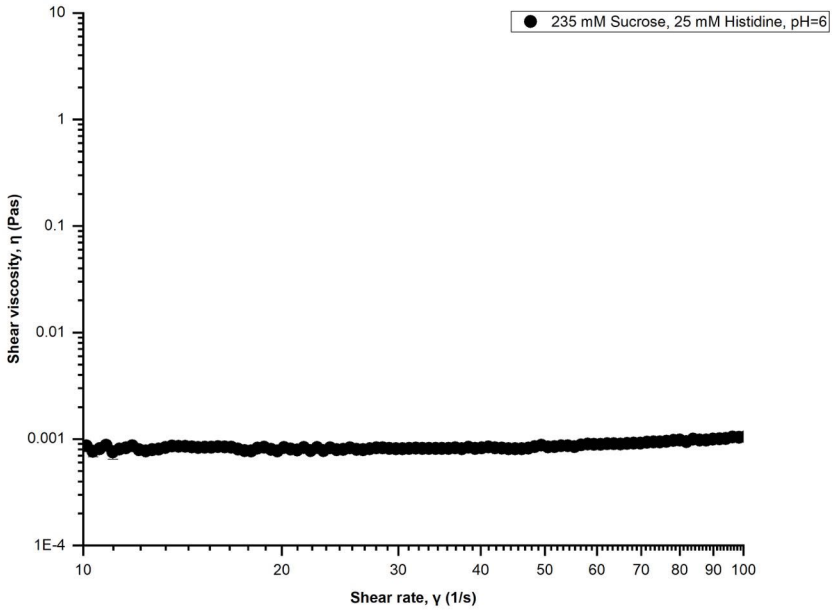

Figure 7.2: Viscosity profile for 235 mM Sucrose, 25 mM Histidine, pH=6 at 25 ℃. Errors indicate the standard deviation between 3 samples, N=3.

The viscosity profiles of MEDI3549 and MEDI8852 are then determined as shown in figures 7.3 and 7.4 respectively. Interestingly, the viscosity profiles of both molecules shows a shear-thinning profile, with the viscosity values to decrease at increase shear rates. The shear thinning effect is largely confined to shear rates of less than the order of 100 s^{-1}.

This shear thinning effect of high concentrated antibodies is also reported in literature studies [218, 221, 278]. The shear thinning flow behaviour of both molecules, is shown to be affected by the bulk effects encountered by the increase in the formulation concentration. The shear thinning flow behaviour can be affected by excipients, such as the effect of surface-active agents (Tween). This has shown that such interactions can significantly affect the shear thinning profile, diminishing the shear thinning effect [278]. This suggests the surfactant can reduce intra-protein interactions.

7.1.2 Computational characterisation

Due to sample volume and concentration limitations, the rheological characterisation was described with maximum protein concentration at 40 mg/mL. Computationally, the effects of shear thinning behaviour of protein samples can be investigated using a theoretical shear thinning model coupled with experimental data, as shown in the study conducted in

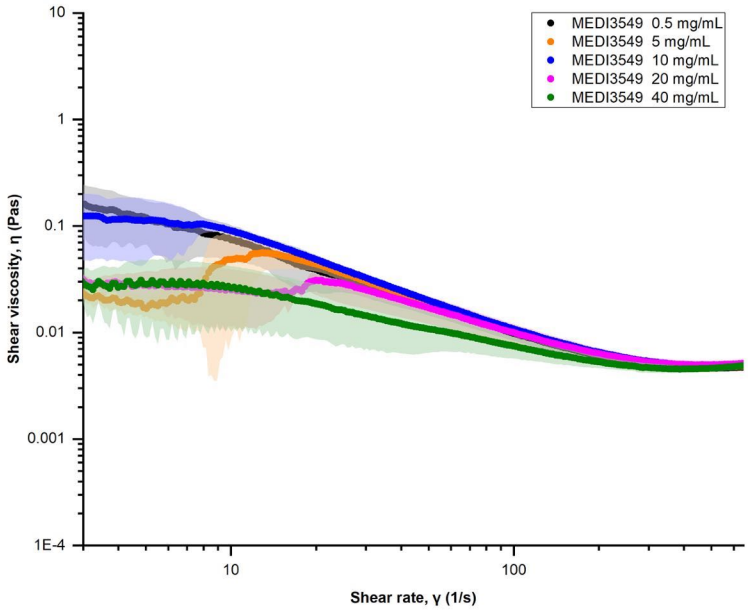

Figure 7.3: Viscosity profile for 0.5 mg/mL (shown in black), 5 mg/mL (orange), 10 mg/mL (blue), 20 mg/mL (magenta) and 40 mg/mL (olive) MEDI3549 in 235 mM Sucrose, 25 mM Histidine, pH=6 at 25 ℃. Errors indicate the standard deviation between 2, (5 mg/mL, 20 mg/mL), n=2 and 3 sample repeats, (0.5 mg/mL, 10 mg/mL, 40 mg/mL), n=3.

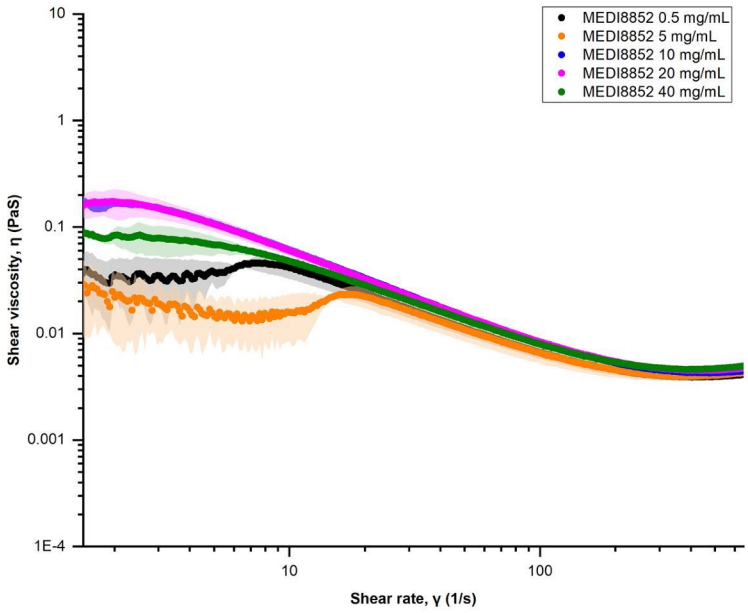

Figure 7.4: Viscosity profile for 0.5 mg/mL (shown in black), 5 mg/mL (orange), 10 mg/mL (blue), 20 mg/mL (magenta) and 40 mg/mL (olive) MEDI8852 in 235 mM Sucrose, 25 mM Histidine, pH=6 at 25 ℃. Errors indicate the standard deviation between 2 sample repeats.

[8]. Therefore, the effects of a non-Newtonian protein sample can be correlated with the flow environment within the extensional flow device. The aim is to assess whether the shear thinning profile of these high concentrated samples can impact the flow distribution developed within the extensional flow device. The model was introduced into COMSOL software at a concentration series of 120, 170, 210 and 225 mg/mL and the simulation results are presented in figure 7.5. The effects of shear-thinning high concentrated protein samples were investigated by focusing on the flow profiles of viscosity, velocity magnitude and strain rate, alongside with the respective flow profiles in the scenario of a Newtonian fluid. Flow profiles of viscosity velocity magnitude and strain rate for a Newtonian fluid are shown in figures 7.5a, 7.5c and 7.5e, whereas the respective profiles of Carreau model describing the shear thinning flow profiles are shown in figures 7.5b, 7.5d and 7.5f. As shown in figure 7.5a, the viscosity profile of a Newtonian fluid, where in the simulation the flow properties of water are used, and it is as expected constant across increased shear rate. On the other hand, for a shear thinning fluid, the viscosity profile shows to decrease with the increase in shear rate as shown in figure 7.5b. Moreover, the decrease in viscosity is most significant at increased protein concentrations, as shown for the maximum concentration used in the simulations of 225 mg/mL (turquoise). The initial viscosity at the particular concentration corresponds to ∼0.045 Pas compared to ∼0.005 Pas calculated for the lowest concentration of 120 mg/mL.

Regarding the velocity profile, it was previously shown that for the Newtonian case, the velocity accelerates through the sudden contraction and remains constant along the post-acceleration flow event as shown in figure 7.5c. Interestingly, the increased protein concentrations, affect the velocity profile developed immediately after the extensional flow event, suggesting disruptions of flow profile, as it is shown in figure 7.5e that the peak velocity decelerates after the extensional point. This observation could imply to the fact that these particular high concentrated protein solutions, which are shown as quite viscous, extend the time for the flow development as the protein solutions travel into the high shear region of the device. The high concentrated solutions are linked with this increase in viscosity, as it was shown in multiple studies in literature [218, 275, 279, 280]. To further investigate whether these flow rearrangements affect the development of extensional flow, the development of strain rate for the Newtonian case as means for comparison, along the range of protein concentrations was then characterised as shown in figures 7.5e and 7.5f. As previously shown, the expected strain rate developed within the extensional flow device for the standard flow conditions (8 mm/s, 100 passes) corresponds to a maximum strain rate of ∼10,000 s^{-1}. The shear thinning model predicts enhancement to the development of strain rate, suggesting that its correlation with the enhancement of protein aggregation, which is already shown to be directly correlated with flow induced aggregation. Specifically, for the concentration range investigated of 120, 170, 210 and 225 mg/mL, the respective maximum strain rates predicted from the simulations, correspond to ∼12,000 s^{-1}, ∼14,000 s^{-1}, ∼15,000 s^{-1} and ∼15,000 s^{-1} respectively.

7.2 Concentration effect in flow induced aggregation

In the previous chapter, all the flow experiments were conducted at a protein concentration of 0.5 mg/mL. Higher concentrated protein formulations have been investigated using the extensional flow device, using $\beta_2 m$ and BSA proteins [1]. Previously, the highest concentration, investigated using the extensional flow device, was 10 mg/mL, where it was shown that the number of aggregates was increased with increasing BSA concentration [1]. The effects of high-protein concentrations have not been investigated previously using antibody or bispecific molecules, therefore in this section a concentration range was investigated examining the flow induced aggregation of MEDI8852 and MEDI3549. Therefore, to explore the effects of high concentrated molecules, concentration in the range of 0.5, 5, 20 and 40 mg/mL has been investigated for the flow induced aggregation of MEDI3549. Alongside the effect of high concentration, the effect of the duration of the molecules exposed to the extensional flow was examined for 2 and 10 minutes corresponding to 20 and 100 passes respectively as shown in figure 7.6. Initially, the flow induced aggregation of the molecule at 20 passes indicated aggregation levels of ∼30% at 0.5 mg/mL. This reduces to ∼5% at 5 mg/mL, and aggregation levels are then increasing to ∼25% at 20 mg/mL. The suppressive effect of higher concentration is more pronounced for

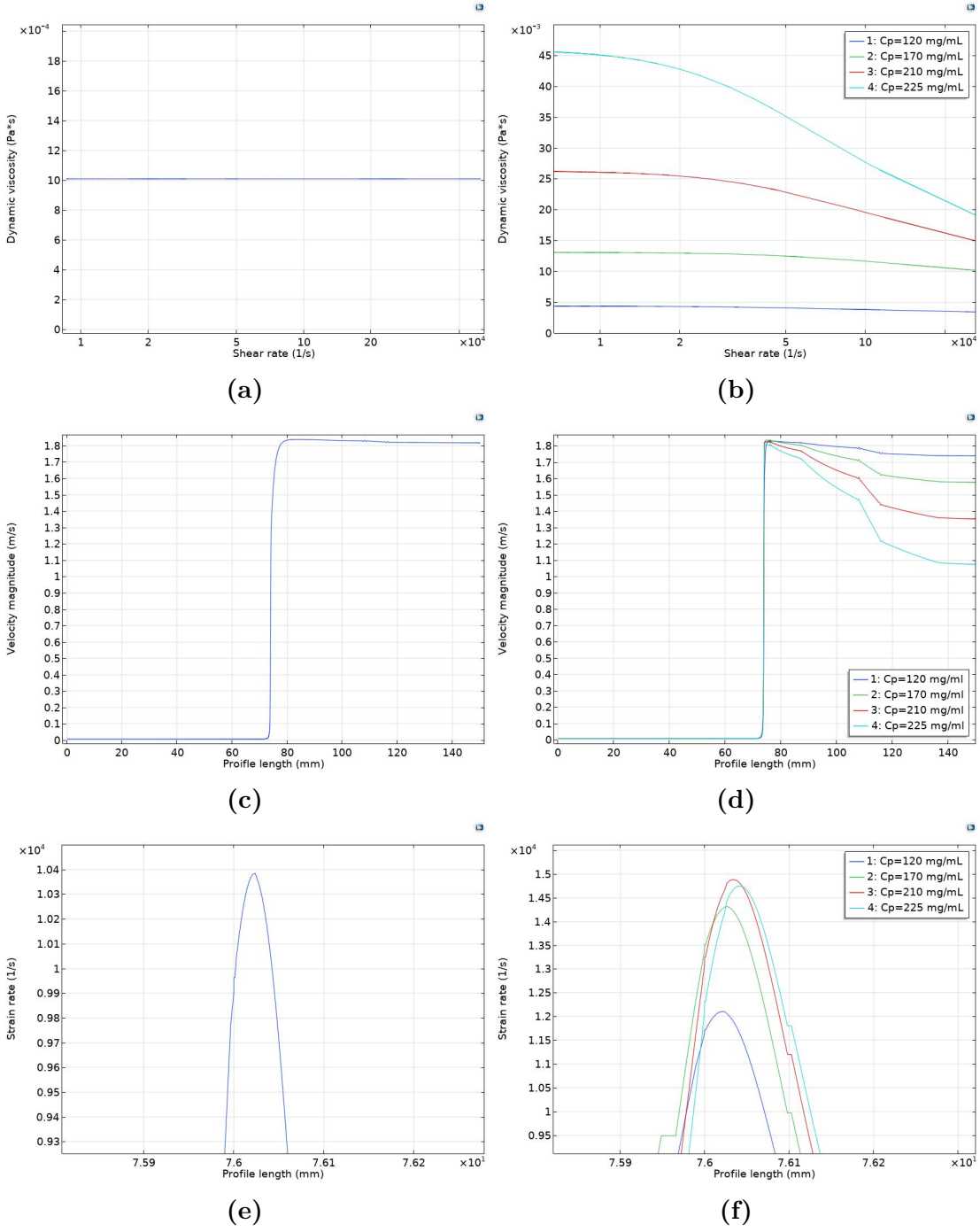

Figure 7.5: Viscosity (7.5a), velocity magnitude (7.5c) and strain rate (7.5e) profiles of Newtonian fluid simulated within EFD. Effect of higher concentrations representing Non-Newtonian fluids of viscosity (7.5b), velocity magnitude (7.5d) and strain rate (7.5f) profiles with different concentrations (c_p) of mAb1, 120 mg/mL (blue line), 170 mg/mL (green), 210 mg/mL (red) and 225 mg/mL (turquoise) as a function of the effective shear rate (25 °C), measured using a plate/cone rheometer as reported in [8]. Data taken from the study were inputted in COMSOL for CFD characterisation. The viscosity, velocity and strain rate profiles in figs. 7.5b, 7.5d and 7.5f were modelled by the Carreau model based on eq.4.4 and the corresponding fitting parameters are summarised in table 4.1.

the longest experimental time of 10 minutes (100 passes). Here, the aggregation propensity of the molecule at 0.5 mg/mL is shown to correspond to ∼60% which is significantly suppressed to ∼15% (a percentage decrease of ∼80%) at 5 mg/mL. The aggregation is further suppressed to ∼5% at 20 mg/mL and rises to ∼10% at 40 mg/mL.

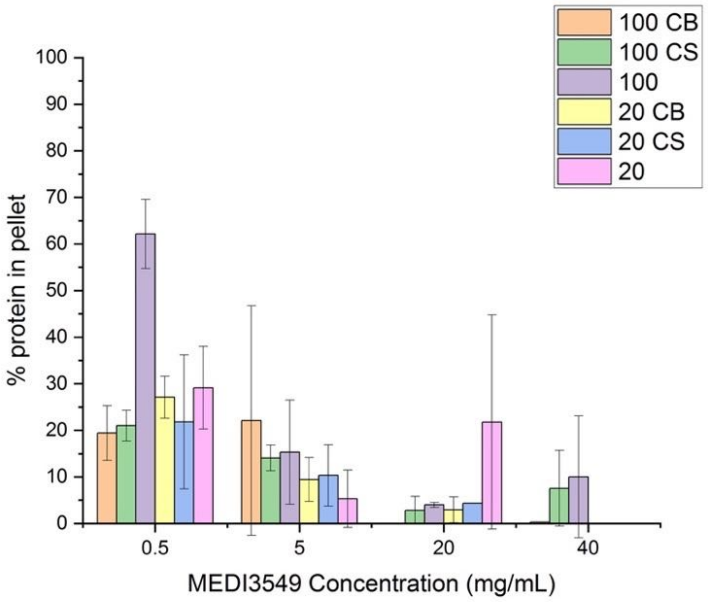

Figure 7.6: Effect of concentration range of 0.5, 5, 20 and 40 mg/mL on MEDI8852 aggregation. All experiments have been conducted at 8 mm/s for 20 and 100 passes. 100 CB and 100 CS - control sample incubated on bench and within borosilicate syringe and capillary bodies for 100 passes experiment (10 minutes), 20 CB and 20 CS - control sample incubated on bench and within borosilicate syringe and capillary bodies for 20 passes experiment (2 minutes). N=2 for 0.5 mg/mL at 20 and 100 passes, N=2 for 20 mg/mL and 5 mg/mL at 20 passes, N=2 for 40 mg/mL at 20 passes, error bars=sd.

To further investigate whether the suppressive effect of higher concentration is a molecule-dependent effect, the higher protein formulations of MEDI8852 at 0.5, 5, 10 and 20 mg/mL concentrations were investigated at the standard flow conditions (100 passes, 8 mm/s plunger speed) as shown in figure 7.7. Interestingly, the same suppressive effect is also shown when this specific antibody is exposed to flow induced aggregation at higher concentrations. Initially, the molecule presents an aggregation profile of ∼58%. The aggregation is further suppressed to ∼25% at 5 mg/mL, ∼10% at 10 mg/mL and ∼15% at 20 mg/mL. The data suggests that the bulk effects of aggregation are present alongside with surface effects which have been presented in the previous chapter. The observed aggregation profile, where aggregation is suppressed at increased protein concentrations, does not align with previous results [1, 59]. However, this inverse concentration dependence effect agrees with the findings reported in [24, 66, 281], suggesting that the suppressed aggregation, which is observed at higher protein concentrations (under their exposure to shear flow fields), can be related with interface saturation effects. This could imply that the surface contribution along the aggregation pathway by the potential protein interaction

of proteins at increased concentrations, populating on the surface compartments of the device.

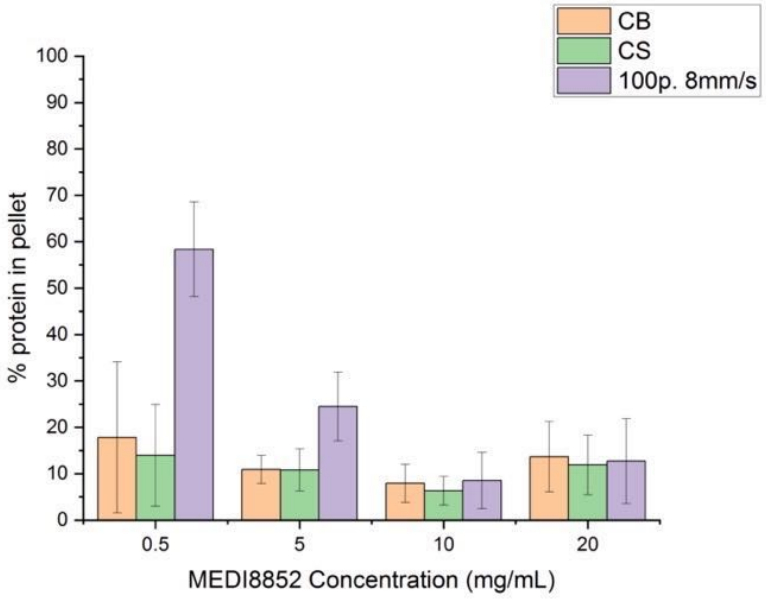

Figure 7.7: Effect of concentration range of 0.5, 5, 10 and 20 mg/mL on MEDI8852 aggregation. All experiments have been conducted at the standard flow conditions (8 mm/s, 100 passes). CB - control sample incubated on bench, CS - control sample incubated within borosilicate syringe and capillary bodies (10 minutes). N=4 for 20 mg/mL, N=2 for 0.5 mg/ml, N=4 for 5 mg/mL, N=2 for 10 mg/mL, error bars=sd

7.3 Characterising the surfactant effect in flow induced aggregation

As the aggregation has been previously shown to be induced by a synergy between flow and interface, this section explores the interface aspect, using surfactants, and their effects on flow induced aggregation. As shown previously in section 7.2, MEDI3549 and MEDI8852 are the model molecules, where a range of experiment analysis is conducted. An overview of the experimental analysis followed for MEDI3549 is shown in figure 7.8. To investigate the simultaneous effects of interfaces and flow, the particular molecule is formulated using the surfactant library previously described at a constant concentration of 0.02% w/v. Alongside the effect of liquid interfaces which correspond to the liquid state, using the surfactants in the formulation of the protein, the effect of solid interface is also investigated. Based on the findings presented in the previous chapter, silane B surface (corresponding to contact angle of 80°) is shown to offer a significant protective effect, enhancing molecule stability under flow. Therefore, the particular solid interface is selected for its protective effect, in combination with the presence of surfactants, alongside the untreated glass surface as a reference. The flow induced aggregation is also explored based on the type of

flow environment developed during manufacturing which is mimicked using the extensional flow as a flow tool and also from the aspect of shipping, using a shipping simulator. As the name suggests, the shipping simulator is used to expose the molecules to the shear flow conditions in which the molecules are encountered throughout their shipping, via truck and plane transportations. Specifically, the mimicking of transportation stress environments using lab-based equipment including a rotator, orbital shaker, vortexer and shipping simulator (corresponding to a vibration table) have been used and correlated with real-time shipment data for a number of antibodies as shown in [282]. Among the stress tests examined, the shipping simulator was shown to predict the formation of aggregated particles in a correlation of about ∼90% compared with real-time shipment samples [282]. The analysis and characterisation of the flow induced aggregation under the simultaneous exposure of solid and liquid interfaces on the aggregation of the molecule is then conducted by employing a range of techniques including monomer fraction, visual inspection and particle concentration.

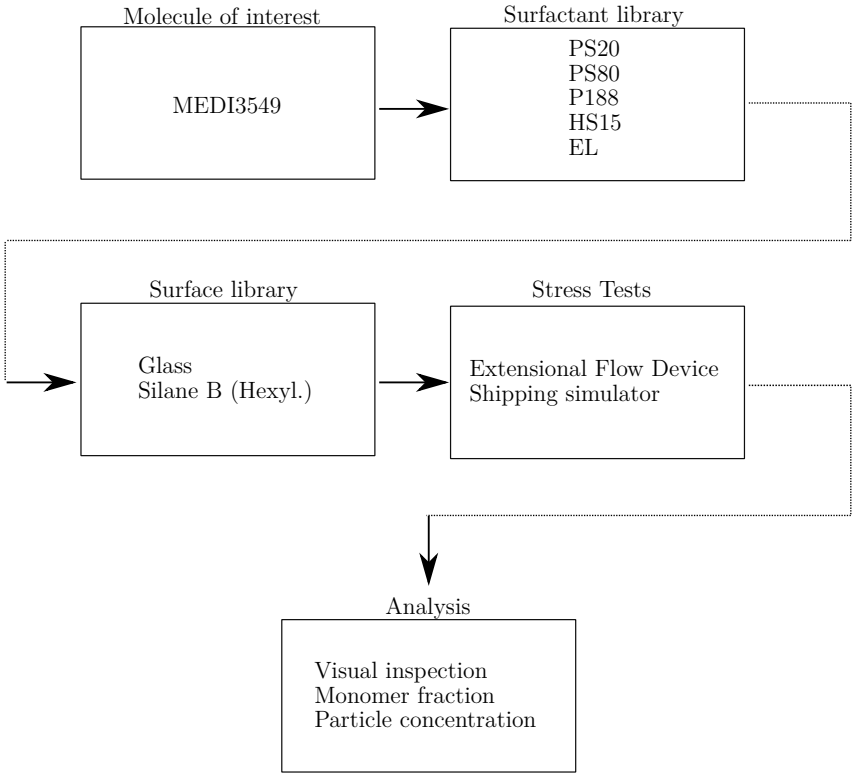

Figure 7.8: Experimental analysis framework followed for characterising the flow induced aggregation of 0.5 mg/mL MEDI3549 in the presence of interfaces.

7.3.1 Surfactant library

The construction of the surfactant library was based on well characterised and applied formulation agents in biopharmaceutical studies, as well as the introduction of novel molecules which have not currently been well characterised in literature. Therefore, the efficiency of novel surfactants is explored alongside well characterised molecules so as to

allow their comparison under the same flow conditions. Additional to this novelty, the surfactant library involves molecules with a broad molecular weight range. This will allow the analysis to be conducted in a range of molecules with various molecular weights so as to investigate whether the particular property can influence their protective properties against aggregation. The molecules consisting of the surfactant library present also different critical micelle concentration (CMC) in which they form micelles. This corresponds to another parameter that can be linked and correlated with their protective properties. The surfactant library consists of five molecules including polysorbate 20 (PS20), polysorbate 80 (PS80), poloxamer 188 (P188), HS15 and EL which are all non-ionic, as non-ionic surfactants are favoured for their use with biotherapeutics due to their proven safety profile [6, 283]. On the contrary, ionic surfactants are reported for their action as denaturing agents of proteins [6].

The surfactant library was constructed based on well-studied surfactants in biopharmaceutical industry, and particularly polysorbates (PS) including PS20 and PS80 alongside poloxamers including P188. The presence of polysorbates is commonly found in biopharmaceutical drug formulations, with a concentration range from 0.0003% (w/v) to 0.3% (w/v) [111], or 0.001 to 0.1% (w/v) [6]. These particular surfactants have previously shown their protective effects against aggregation after protein exposure to flow conditions [284]. The suppressive effect of polysorbate 20 against aggregation induced by mechanical stress, is reported in multiple studies investigating several model proteins including porcine growth hormone, recombinant human growth hormone (rHGH) recombinant human factor XIII [6]. Polysorbate 80 is also reported offering stability to molecules exposed to various stress conditions involving vortexing and freeze-thaw [6]. The effect of non-ionic surfactants, including polysorbates 20, 80 and poloxamer 188 (among others), was also studied in [95] indicating desirable aggregation-prevention during agitation stress test. Apart from the well-studied polysorbate and poloxamer surfactants, the library involves the addition of two novel surfactants, EL and HS15. EL, is a nonhydrogenated hydrophilic surfactant, which is produced by the reaction of castor oil with ethylene oxide at a molar ratio of 1:35 [285]. Its application is known in parenteral formulations of hydrophobic drugs such as cyclosporine A and paclitaxel (Taxol), with its application expanding for the solubilisation of poorly water-soluble drugs in lipid-based formulations (LBFs), and cosmetics because of its water solubility and attractive safety profile after oral administration [285]. Its application in pharmaceutical industries has been reported due to its ability to solubilise, protect and encapsulate the lipophilic bioactive compounds, with its application to be correlated with the enhancement of permeability and bioavailability of drugs [286]. HS15 is a commercially available amphiphilic copolymer, and its application is reported as a parenteral excipient in aqueous formulations [287]. Its current use can be found on the enhancement of aqueous solubility of poorly aqueous soluble drugs [287].

7.3.2 Monomer fraction

The flow induced aggregation of MEDI3549 is characterised by performing HPSEC, with the amount of monomer presented as a fraction with respect to the control samples (control bench and control syringe) and flow (EFD and shipping simulator) samples as shown in figure 7.9. The range of surfactant molecules is screened at a constant surfactant concentration of 0.02% w/v. Interestingly, for all surfactant molecules investigated, it can be observed that the shipping simulator shows no effect on the aggregation. The monomer fraction for shipping simulator corresponds to ∼1 suggesting negligible effects of the shipping simulator on flow induced aggregation, with the monomer fraction to agree with the samples corresponding to control bench, control syringe glass and control syringe silane B surfaces. Additionally, as the samples are fully monomeric during shipping simulator conditions, in the formulation with no surfactant (n/a), the addition of surfactant molecules to the molecule formulation, has no further effects. This observation suggests that the sample does not aggregate during shipping conditions, which mimic the stress applied to the samples during their shipping via truck and plane transportations. On the other hand, the molecule in the absence of any surfactant in its formulation (n/a), is shown to be highly prone to aggregation when exposed to the extensional flow device, with the monomer fraction (i.e., the protein remaining in solution) suppressed to ∼0.45 when exposed to the extensional flow device with untreated glass surface, corresponding to a decrease in monomer molecules in a percentage of ∼55%. When the molecule is then exposed to the silane B surface, the monomer fraction corresponds to ∼0.52 suggesting the enhancement of the flow stability of the molecule.

Overall, the silane B surface (green bars) offers protective effects of the molecule against aggregation, shown by the increased levels of monomer fraction compared to the untreated glass surface (orange bars) for all the surfactant formulations. This observation agrees with the data presented in the previous chapter, highlighting the protective properties of the particular surface when the molecules are exposed to the extensional flow device. However, the flow stability of the molecule is fully enhanced with the addition of the surfactant molecules in the formulation buffer, suggesting the role of the simultaneous presence of solid and liquid interface during flow induced aggregation. Particularly, the maximum monomer fraction detected under extensional flow device, is achieved with the interface combination of the following sets: silane B&PS20, silane B &PS80, silane B&HS15 and silane B&EL, corresponding to monomer fraction of ∼0.7 compared to the highest aggregation condition of ∼0.45 with no surfactant (n/a) and exposed to untreated glass surface.

These data suggested the protective effects of silane B surface and a range of surfactant molecules highlighting the role of interfaces in flow induced aggregation, and it acknowledges the dynamic of extensional flow device to be used as a formulation tool for screening

the best formulation candidates enhancing the stability of the molecules during their manufacture. Additionally, by comparing the flow conditions to which the molecules are exposed during the shipping simulator and extensional flow device, it can be seen that the more damage to molecules is occurred during their exposure to the extensional flow device.

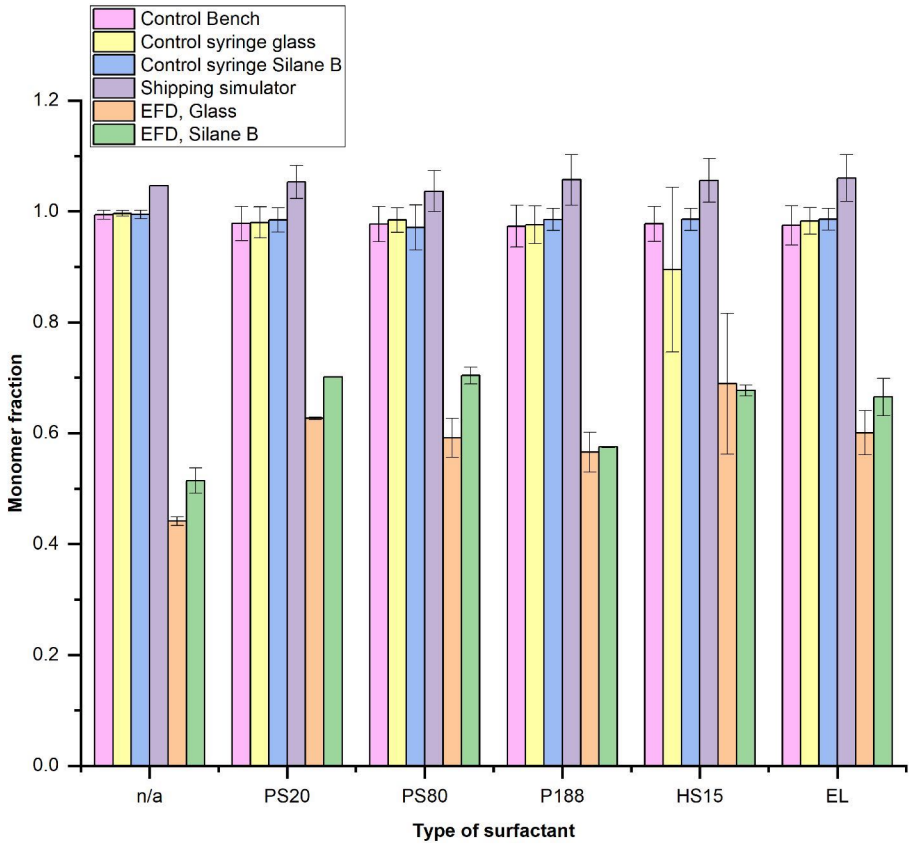

Figure 7.9: Monomer fraction of 0.5 mg/mL MEDI3549 as determined from HPSEC. Samples have been exposed to shipping simulator (purple bars), extensional flow device (EFD) (100 passes, 8 mm/s) in glass (orange bars) and Silane B treated surfaces (green bars) in the absence, n/a and in presence of surfactant formulations 0.02% w/v PS20, PS80, P188, HS15, EL in 235 mM Sucrose, 25 mM Histidine, pH=6. Samples have been incubated in tubes left on the bench (pink bars) and in equipment surface (syringe and capillary bodies) corresponding to bare borosilicate glass (yellow bars) and silane B treated surfaces (blue bars) for the longest experimental time (10 minutes). Errors indicate the standard deviation between 2 samples loaded for each condition.

7.3.3 Visualisation of protein aggregates

The identification of soluble and insoluble protein aggregates is conducted firstly by visual inspection. The need to ensure minimum introduction of unintended particulate matter to patients during the delivery of injectable medication, requires the conduction of visual inspection of parenteral products [288]. The assessment of visible particles, which is

conducted by human visual inspection, is critically dependent by the performance of the human vision, where it has been reported that the threshold for human vision is generally accepted to be 50 μm [288]. The source of the development of particulate matter in injectable drugs is reported to be induced by several parameters including the environment, packaging materials, solution and formulation components, product packaging interactions and process-generated particles [289]. The detailed report of potential particle contaminants, their sources and intrinsic/extrinsic natures are defined by United States Pharmacopeia (USP), Methods for the Determination of Particulate Matter in Injections and Ophthalmic Solutions-Chapter <1788> [289]. The particular chapter also specifies the classification of particulate matter as intrinsic and extrinsic. The former corresponds to particulate matter which is associated with the package, formulation and/or assembly process and capable of change upon aging, whereas the latter refers to particulate matter as additive, foreign, unchanging, and not part of the formulation, package or assembly process [289]. The visual inspection conducted in the current work is focused on the intrinsic particulate matter driven by solution and formulation conditions which correspond to a range of particulate materials including precipitates, oligomers, degradants, agglomerates and undissolved material [289].

Aggregation visualisation pre and post extensional flow

As described previously, the effect of the equipment surface is also investigated with samples exposed to untreated glass and a previously characterised protective surface corresponding to silane B surface. Firstly, samples in quiescent conditions have been inspected on a black background, as shown in figures 7.10 and 7.11 which corresponds to untreated glass surface. The aim of the visual inspection is to quickly detect and assess the formulation state of the sample in quiescent and flow conditions. To investigate the effects of flow on aggregation, two respective controls are firstly obtained to allow their comparison with the flow exposed samples. Quiescent samples, correspond to samples incubated in eppendorf tubes for the longest experimental time, as well as samples incubated within the syringe and capillary bodies of the extensional flow device also incubated for the longest experimental time. The flow conditions applied to the samples correspond to the standard flow conditions which have been previously shown (among others) to induce the aggregation of previously studied antibodies [1–3], and correspond to a pass number of 100 and plunger speed of 8 mm/s. As shown in figure 7.10, there is no apparent detection of particles for all the surfactant formulations investigated and shown by the visual inspection images presented analytically in figures 7.10a, 7.10b, 7.10c, 7.10d and 7.10e which agrees with the monomer fraction data, presented above (figure 7.9) indicating that the sample incubated in the bench is fully monomeric.

The second set of control samples in quiescent conditions, was then inspected with the samples incubated within the syringe and capillary bodies, corresponding to untreated

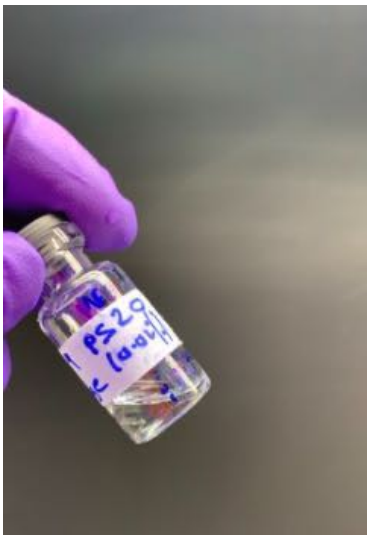

(a) PS20

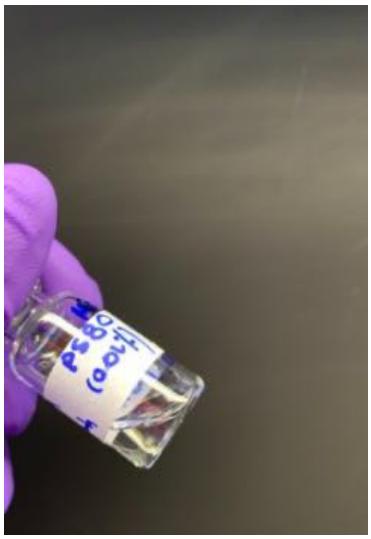

(b) PS80

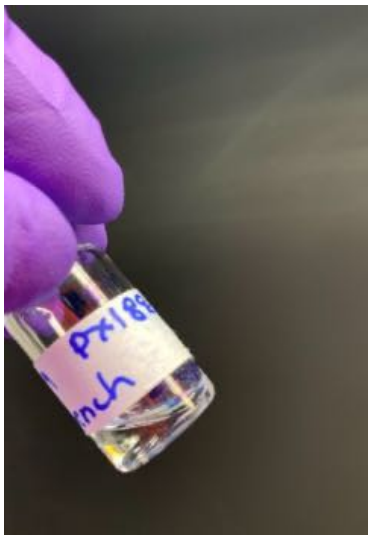

(c) P188

(d) HS15

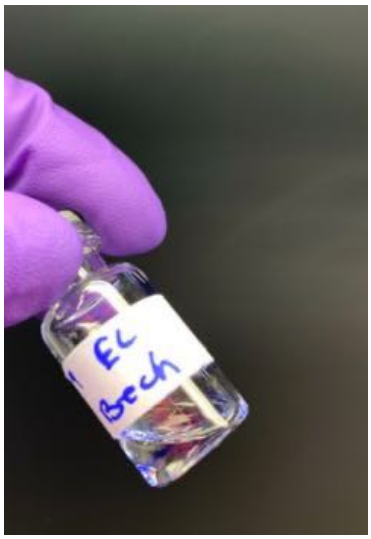

(e) EL

Figure 7.10: Visual inspection images of 0.5 mg/mL MEDI3549 under quiescent conditions (absence of extensional flow) in presence of surfactant formulations 0.02% w/v PS20, PS80, P188, HS15, EL (figs. 7.10a to 7.10e) in 235 mM Sucrose, 25 mM Histidine, pH=6. Samples have been incubated in tubes left on the bench, for the longest experimental time (10 minutes).

glass surfaces. As shown in figure 7.11, no apparent formation of particles is detected visually, suggesting the monomeric state of the sample for all the formulations.

(a) PS20

(b) PS80

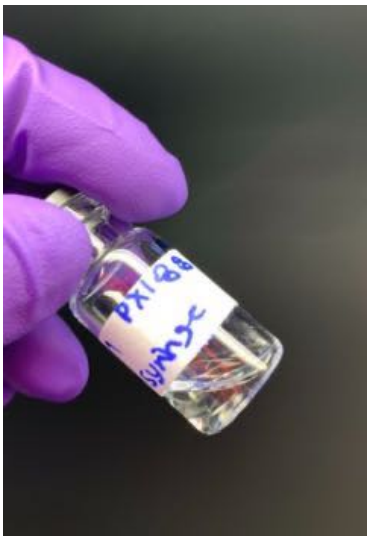

(c) P188

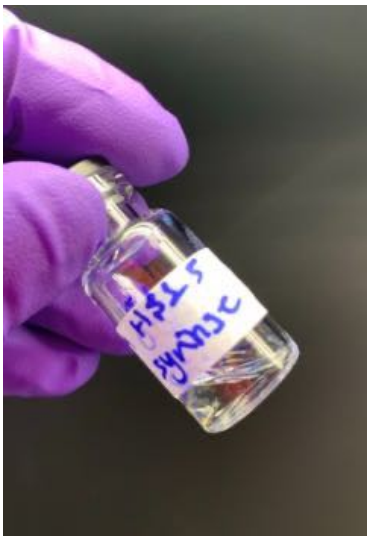

(d) HS15

(e) EL

Figure 7.11: Visual inspection images of 0.5 mg/mL MEDI3549 under quiescent conditions (absence of extensional flow) in presence of surfactant formulations 0.02% w/v PS20, PS80, P188, HS15, EL (figs. 7.11a to 7.11e) in 235 mM Sucrose, 25 mM Histidine, pH=6. Samples have been incubated in equipment surface (syringe and capillary bodies), corresponding to bare borosilicate surfaces, for the longest experimental time (10 minutes).

Next, the samples have been then inspected after their exposure to extensional flow on the untreated glass surface. As expected from the previous data, extensional flow induces the aggregation of the particular molecule for all the formulations investigated. This is also determined by the visual inspection of the samples which indicate the severe aggregation of the molecule, resulted in cloudy solutions as shown in figure 7.12. Less particle formation is also observed for the formulations of PS80 and EL, as shown in figures 7.12b and 7.12e with lower sample cloudiness and particles can be detected corresponding to suppressed aggregation levels. Linking this observation with the monomer fraction data, presented

above (figure 7.9) the aggregation profile of the molecule is also detected to be suppressed for the particular surfactant molecules with the corresponding monomer fraction data to be ∼0.58 compared to ∼0.45 for the surfactant-free formulation.

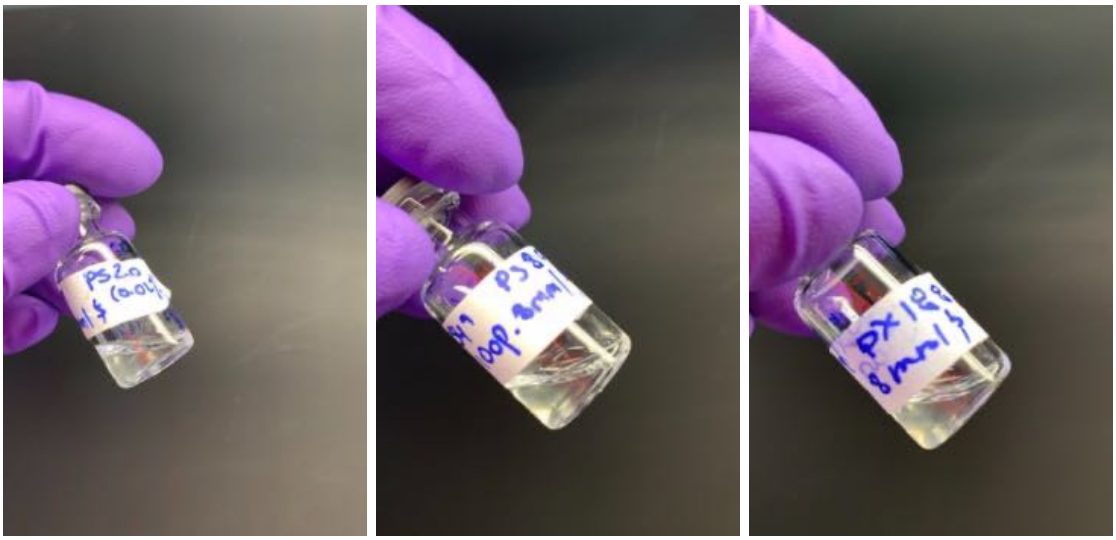

(a) PS20 **(b)** PS80 **(c)** P188

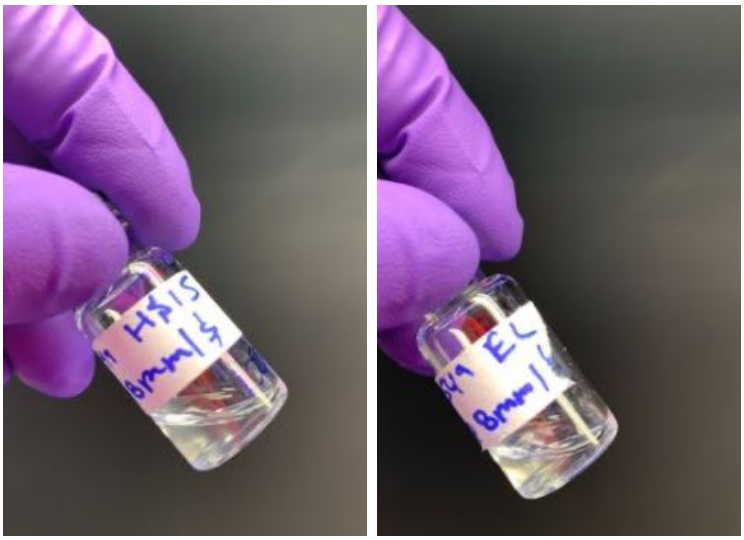

(d) HS15 **(e)** EL

Figure 7.12: Visual inspection images of 0.5 mg/mL MEDI3549 under extensional flow conditions (100 passes, 8 mm/s) in presence of surfactant formulations 0.02% w/v PS20, PS80, P188, HS15, EL (figs. 7.12a to 7.12e) in 235 mM Sucrose, 25 mM Histidine, pH=6. Samples have been exposed to flow in equipment surface (syringe and capillary bodies), corresponding to bare borosilicate surfaces, for the longest experimental time (10 minutes).

The sample is then exposed to silane B treated surface, with firstly the quiescent samples which were incubated within the syringe and capillary bodies and inspected as shown in figure 7.13. For all the formulations examined, no apparent sample turbidity of the samples is observed, suggesting that the samples have not aggregated so as no particles can be detected via the visual inspection.

When the sample is then exposed to the extensional flow device on the silane B treated

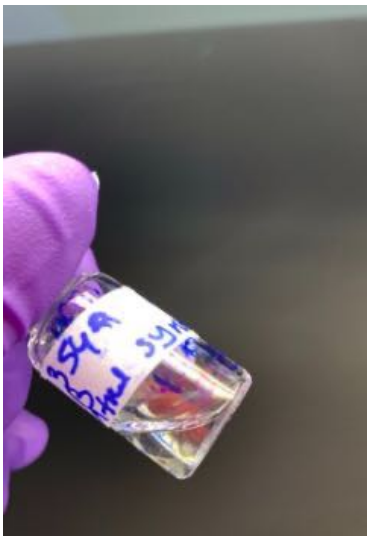

(a) PS20

(b) PS80

(c) P188

(d) HS15

(e) EL

Figure 7.13: Visual inspection images of 0.5 mg/mL MEDI3549 under quiescent conditions (absence of extensional flow) in presence of surfactant formulations 0.02% w/v PS20, PS80, P188, HS15, EL (figs. 7.13a to 7.13e) in 235 mM Sucrose, 25 mM Histidine, pH=6. Samples have been incubated in equipment surface (syringe and capillary bodies), corresponding to Silane B surfaces, for the longest experimental time (10 minutes).

surface, a sample turbidity is observed for all the protein formulations as shown in figure 7.14. Interestingly, lower sample turbidity is observed for PS20 and PS80 formulations, as shown in figures 7.14a and 7.14b. This agrees with previous data suggesting the suppressed aggregation levels detected for the particular formulations corresponding to monomer fraction of ∼0.7. Therefore, visual inspection can be used as a visualisation tool to qualitatively assess the particle formation, which is also linked with the results obtained from HPSEC. However, the detection of aggregated and visible particle can be quite challenging and from a practical perspective, it is a method which depends highly on the individual operator, inspection device, inspection time, as well as the morphology, number and refractive index of the particles [91]. Therefore, to overcome these limitations and asses the particle formation both qualitatively and quantitively, the background membrane imaging technique is then conducted to accurately detect the particle concentration as well as the particle sizing for each experimental condition and protein formulation.

7.3.4 Particle concentration

The quantification of subvisible particulate (SVP) is then assessed using a novel membrane-based, optical microscopy particle-counting method based on the technology of high-throughput background membrane imaging (BMI) [290]. The HORIZON device, which was used to conduct the aggregation characterisation, is a recently developed device which was introduced in 2017 for the analysis of subvisible particle by BMI, in the size range staring from ∼2 μm [102]. The dynamic of the BMI method in the process of particle characterisation has been investigated in recently published studies, focusing on the characterisation of subvisible particulate from several model proteins including enzymes and monoclonal antibodies as well as antibodies with surfactant formulations [99, 102, 290–292]. The technique, which allows the visualisation and quantification of the particles, it is used to characterise the aggregation tendency of the molecule during its exposure to shipping simulator and extensional flow device. As indicated from the previous data, HPSEC, the sample is highly aggregation prone when exposed to the extensional flow device, particularly when exposed to the untreated glass surface. The enhancement of its flow stability against aggregation was shown to be achieved by the presence of surfactants and silane B equipment surface. To visually determine the protective effect of the particular surface, BMI images are presented below indicating the particle formation during the surface transition from the untreated glass to the silane B treated surface.

Effect of low surfactant concentration

Initially, the effect of extensional flow was investigated at low concentrations of surfactant formulation and particularly P188 which was shown to offer the minimum protection compared to the other surfactant molecules as shown previously in figure 7.9. As expected, the contribution of extensional flow is significant in inducing the particle formation as

(a) PS20

(b) PS80

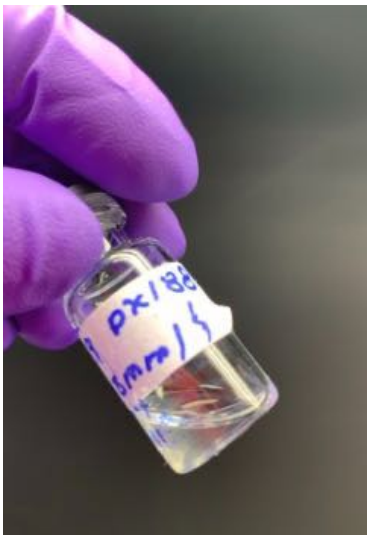

(c) P188

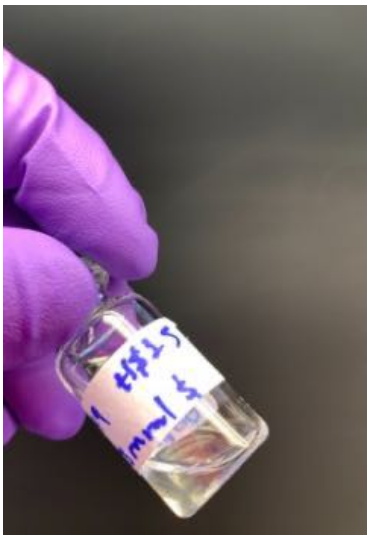

(d) HS15

(e) EL

Figure 7.14: Visual inspection images of 0.5 mg/mL MEDI3549 under extensional flow conditions (100 passes, 8 mm/s) in presence of surfactant formulations 0.02% w/v PS20, PS80, P188, HS15, EL (figs. 7.14a to 7.14e) in 235 mM Sucrose, 25 mM Histidine, pH=6. Samples have been exposed to flow in equipment surface (syringe and capillary bodies), corresponding to Silane B surfaces, for the longest experimental time (10 minutes).

shown in figure 7.15c compared to the absence of flow in bench and syringe body surfaces shown in figures 7.15a and 7.15b respectively. No visible particles were detected for the quiescent conditions where the sample is incubated in the bench and interestingly for the control as shown in figure 7.15a whereas when the sample is incubated within the syringe and capillary bodies the formation of few particles is observed as shown in figure 7.15b, indicating the affinity of proteins to interact with interfaces. In the previous chapter, it was also shown that in the absence of extensional flow, it was shown that the protein can form a monolayer on the surface, indicating its interaction with the surface. The surface effect was then investigated by exposing the samples to the extensional flow device to the untreated glass surface (figure 7.15) and silane B surfaces (figure 7.16), along with their respective controls, where the samples were incubated in eppendorf tubes in the absence of flow, on the bench (figure 7.16a) and within the syringe bodies (figure 7.16b) for the longest experimental time. Interestingly, the formation of few particles is observed when the sample is incubated within the silane B treated syringe and capillary bodies similar to the formation of few particles observed when the sample is incubated within the syringe and capillary bodies, untreated surfaces as shown in figures 7.16b and 7.15b. The protective effect of the particular surface is clearly shown in figure 7.16c when the population of aggregated particles is significantly suppressed compared to the particles generated during their exposure to the untreated glass surface as shown in figure 7.15c. This observation indicates that the protective effect of the particular surface is not molecule-specific, as its suppressive aggregation effects have been previously shown on antibodies (as indicated in the previous chapter) and here on a bispecific molecule.

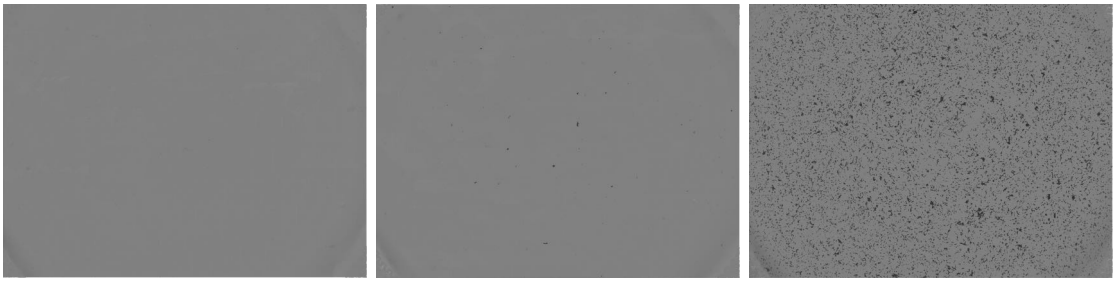

(a) **(b)** **(c)**

Figure 7.15: BMI images of 0.5 mg/mL MEDI3549 under quiescent conditions (absence of extensional flow) figs. 7.15a and 7.15b and flow conditions (100 passes, 8 mm/s) 7.15c in the presence of P188 formulations 0.002% w/v in 235 mM Sucrose, 25 mM Histidine, pH=6. Samples have been incubated in tubes left on the bench (7.15a), in equipment surface (syringe and capillary bodies) (7.15b), and exposed to flow in equipment surface corresponding to bare borosilicate glass surfaces for the longest experimental time (10 minutes).

Effect of surfactant library on untreated extensional flow device surface

Next, to investigate the effect of formulation in the aggregation, the surfactant library including PS20, PS80, P188, HS15 and EL molecules was studied both in quiescent

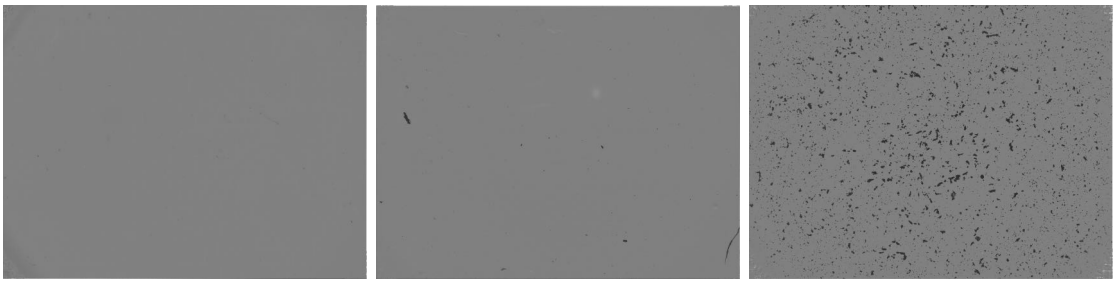

(a) **(b)** **(c)**

Figure 7.16: BMI images of 0.5 mg/mL MEDI3549 under quiescent conditions (absence of extensional flow) figs. 7.16a and 7.16b and flow conditions (100 passes, 8 mm/s) 7.16c in the presence of P188 formulations 0.002% w/v in 235 mM Sucrose, 25 mM Histidine, pH=6. Samples have been incubated in tubes left on the bench (7.16a), in equipment surface (syringe and capillary bodies) (7.16b), and exposed to flow in equipment surface corresponding to Silane B surfaces for the longest experimental time (10 minutes).

conditions, with samples incubated in bench, and device equipment surface (syringe body and capillary) and flow conditions. Firstly, the effect of surfactant molecules was investigated by exposing the molecules to the untreated glass surface of the extensional flow device, which is previously shown to correspond to the surface in which the molecule is highly aggregation prone. As shown in figure 7.15, there is an absence of significant particle formation when the samples are incubated on the bench, with few particles observed for the cases where no surfactant (figure 7.17a) is present in the formulations, and few particles observed for PS20 (figure 7.17b), PS80 (figure 7.17c) and HS15 (figure 7.17e) formulations. Formulations including P188 and EL indicated the absence of any particle formation, as shown in figures 7.17d and 7.17f.

The control samples which represent the sample incubation within the equipment surface, syringe and capillary surfaces, are then presented as shown in figure 7.18 indicating similar effects with the samples incubated in tubes on the bench. Similar to the samples incubated in bench, it is shown that there are few particles generated for particular protein formulations including surfactant-free formulation (figure 7.18a), PS20 (figure 7.18b), HS15 (figure 7.18e), whereas no particles were detected for the formulations including P188 and EL, as shown in figures 7.18d and 7.18f respectively.

The effect of the surfactant formulation, can be then investigated when the sample is exposed to the extensional flow device as shown in figure 7.19. When the sample is exposed to extensional flow conditions, it is shown that it is highly aggregated, with significant particle formation observed for all the formulations investigated. From the previous data, it was shown that the sample in surfactant-free formulation, is highly aggregated when exposed to the untreated glass surface (figure 7.9), which can be also correlated with the BMI images indicating significant particle generation as shown in figure 7.19a indicating the formation of aggregated protein molecules. The addition of surfactant to the protein's formulation is shown to significantly affect the particle formation, with the

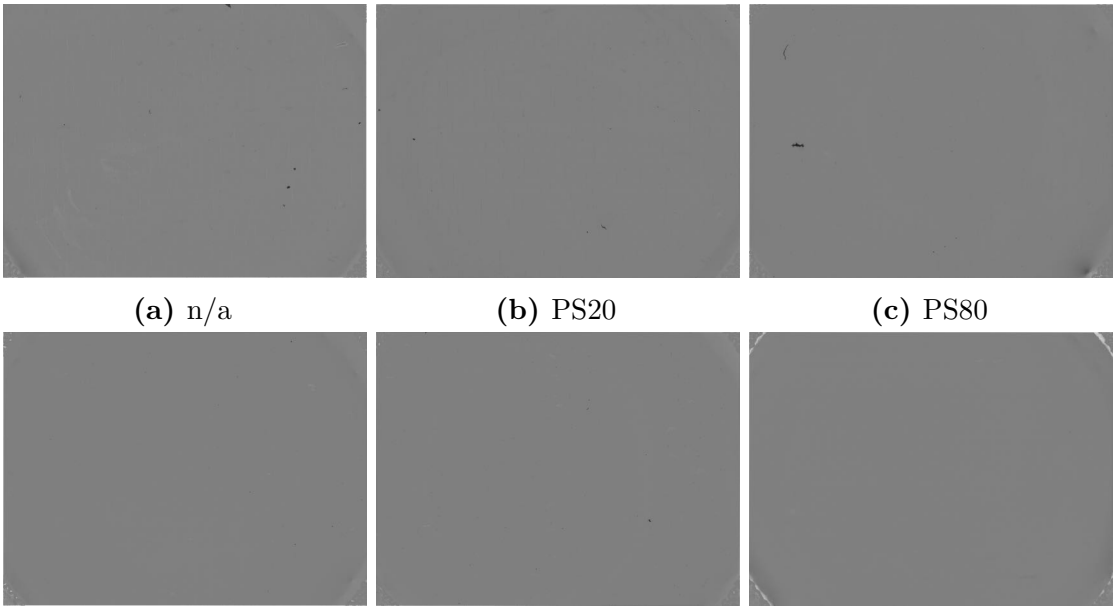

(a) n/a **(b)** PS20 **(c)** PS80

(d) P188 **(e)** HS15 **(f)** EL

Figure 7.17: BMI images of 0.5 mg/mL MEDI3549 under quiescent conditions (absence of extensional flow) in the absence, n/a (7.17a) and presence of surfactant formulations 0.02% w/v PS20, PS80, P188, HS15, EL (figs. 7.17b to 7.17f) in 235 mM Sucrose, 25 mM Histidine, pH=6. Samples have been incubated in tubes left on the bench, for the longest experimental time (10 minutes).

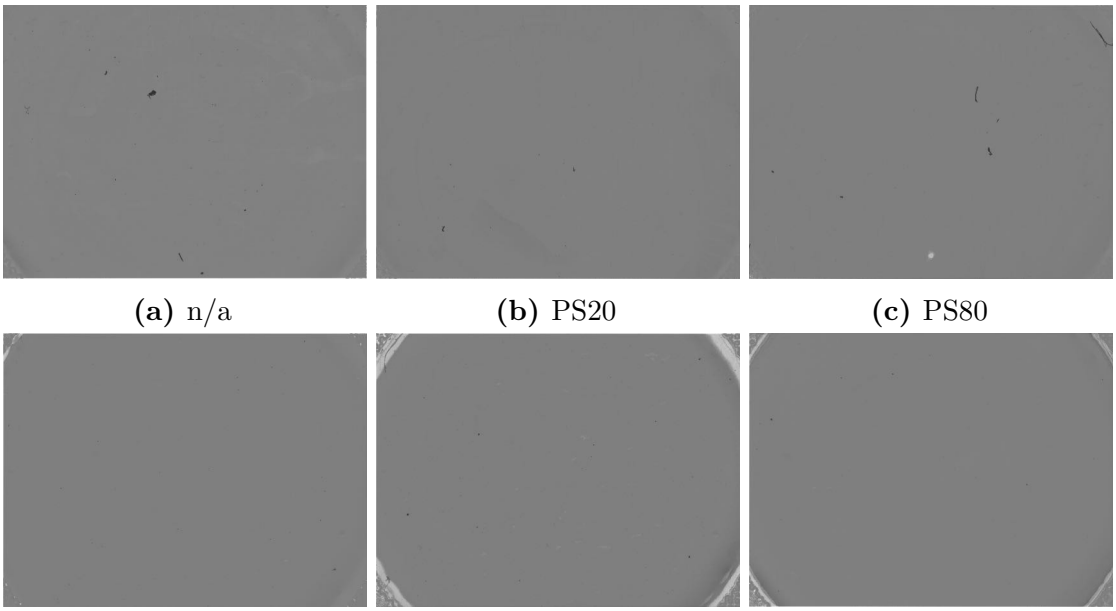

(a) n/a **(b)** PS20 **(c)** PS80

(d) P188 **(e)** HS15 **(f)** EL

Figure 7.18: BMI images of 0.5 mg/mL MEDI3549 under quiescent conditions (absence of extensional flow) in the absence, n/a (7.18a) and presence of surfactant formulations 0.02% w/v PS20, PS80, P188, HS15, EL (figs. 7.18b to 7.18f) in 235 mM Sucrose, 25 mM Histidine, pH=6. Samples have been incubated in equipment surface (syringe and capillary bodies), corresponding to bare borosilicate glass surfaces, for the longest experimental time (10 minutes).

particle population shown to be suppressed for all the surfactants investigated, as shown in figures 7.19b, 7.19c, 7.19d, 7.19e and 7.19f. Visually, it can be also observed that the formulation consisting of P188 shows to correspond to the formulation containing relatively large particles among the surfactant molecules investigated, as shown in figure 7.19d. This observation can be correlated with the results presented previously in figure 7.9, indicating that the particular surfactant was shown as the weakest among the library when exposed to the untreated glass surface, based on the minimum monomer fraction corresponding to ∼0.58 compared to ∼0.7 obtained for formulations including HS15.

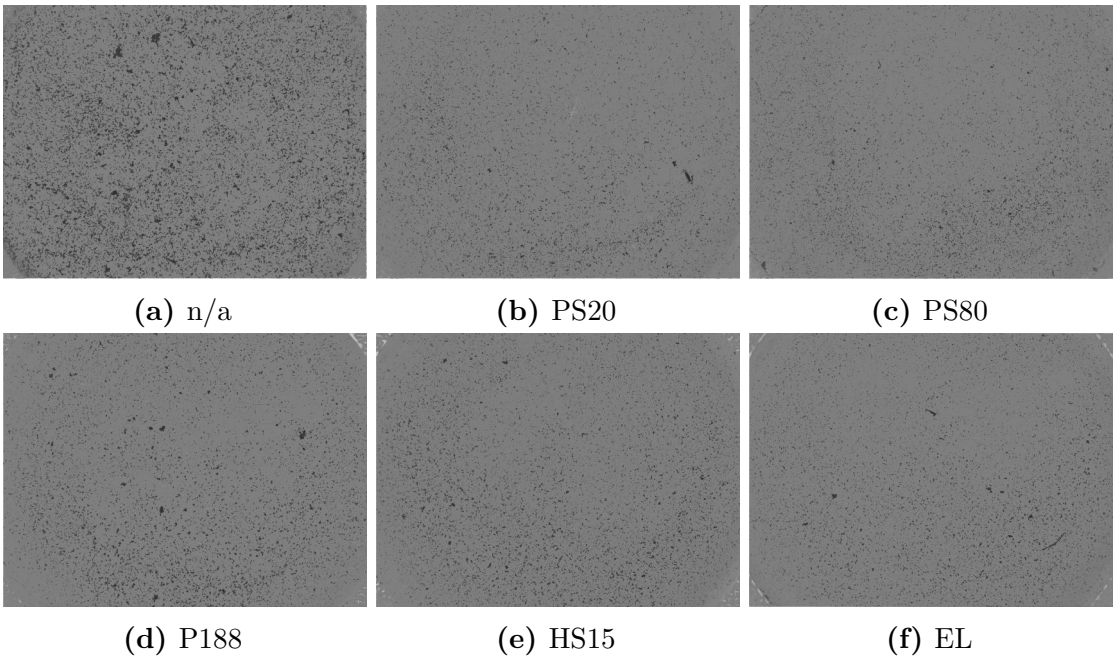

(a) n/a **(b)** PS20 **(c)** PS80

(d) P188 **(e)** HS15 **(f)** EL

Figure 7.19: BMI images of 0.5 mg/mL MEDI3549 under extensional flow conditions (100 passes, 8 mm/s) in the absence, n/a (7.19a) and presence of surfactant formulations 0.02% w/v PS20, PS80, P188, HS15, EL (figs. 7.19b to 7.19f) in 235 mM Sucrose, 25 mM Histidine, pH=6. Samples have been exposed to flow in equipment surface (syringe and capillary bodies), corresponding to bare borosilicate glass surfaces, for the longest experimental time (10 minutes).

Effect of surfactant library on silane B treated extensional flow device surface

As the liquid interface was investigated by the variation of surfactant formulation, the experimental procedure was then conducted by exposing the molecules to surfaces where the component parts of the extensional flow device have been previously treated with silane B. The aim of this set of experiments is to identify and predict the best formulation and surface combination that will allow the enhancement of the molecule stability against aggregation. Firstly, the control samples are presented as shown in figure 7.20 indicating the formation of few particles specifically for the surfactant-free formulation, and P188 formulation as shown in figures 7.20a and 7.20d respectively. The formation of few particles in quiescent conditions, in which the sample is incubated and left to interact with the

equipment surface. This implies to the fact that the protein is expected to interact with the interface, where the formation of a monolayer was shown in previous experiments, presented in the previous chapter.

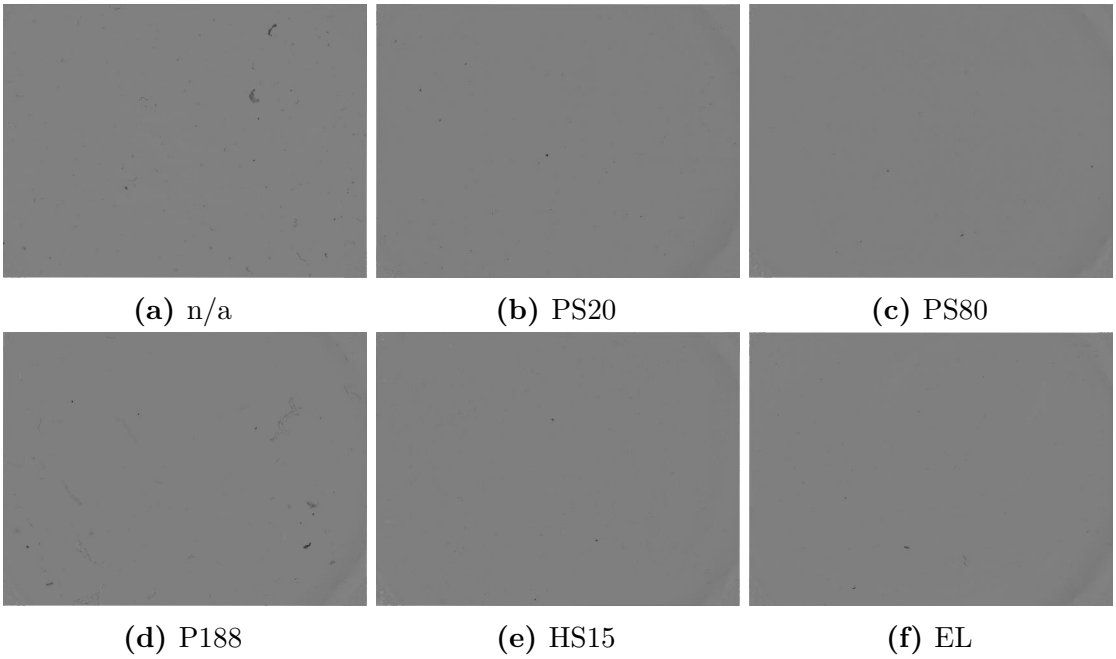

(a) n/a **(b)** PS20 **(c)** PS80

(d) P188 **(e)** HS15 **(f)** EL

Figure 7.20: BMI images of 0.5 mg/mL MEDI3549 under quiescent conditions (absence of extensional flow) in the absence, n/a (7.20a) and presence of surfactant formulations 0.02% w/v PS20, PS80, P188, HS15, EL (figs. 7.20b to 7.20f) in 235 mM Sucrose, 25 mM Histidine, pH=6. Samples have been incubated in equipment surface (syringe and capillary bodies), corresponding to Silane B surfaces, for the longest experimental time (10 minutes).

The effect of surfactant formulation is then investigated by the exposure of the molecule to the treated extensional flow device. Interestingly, in surfactant-free formulation conditions, the particles are smaller and sparsely distributed along the wall plate of the instrument as it is shown in figure 7.21a compared to the populated particles detected when the molecule is exposed to the untreated glass surface 7.19a. The particular surface is shown to offer protective properties during the exposure of the molecule to the extensional flow, highlighting the significance of the solid interface in which the molecule is interacting with during its exposure to flow environments. This also acknowledges the synergy of flow and surface in affecting the aggregation propensity of the molecule. The presence of surfactant molecules in the formulation, is shown to enhance further the stability of the molecule, as the size of the particles generated is smaller for all the surfactant formulations (figs. 7.21b to 7.21f) compared to the surfactant-free formulation (fig. 7.21a). These results shed light into the simultaneous effects of flow and interfaces on the aggregation propensity of the molecule, in which the effects of the particular interfaces can be detected visually.

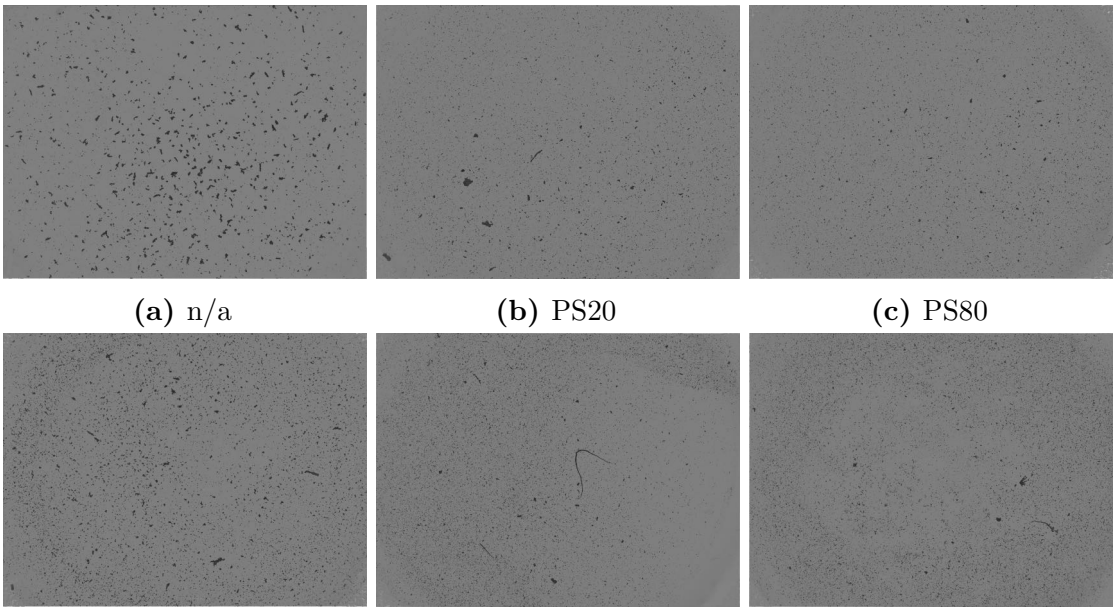

(a) n/a **(b)** PS20 **(c)** PS80

(d) P188 **(e)** HS15 **(f)** EL

Figure 7.21: BMI images of 0.5 mg/mL MEDI3549 under extensional flow conditions (100 passes, 8 mm/s) in the absence, n/a (7.21a) and presence of surfactant formulations 0.02% w/v PS20, PS80, P188, HS15, EL (figs. 7.21b to 7.21f) in 235 mM Sucrose, 25 mM Histidine, pH=6. Samples have been exposed to flow in equipment surface (syringe and capillary bodies), corresponding to Silane B surfaces, for the longest experimental time (10 minutes).

Shipping simulator

Alongside the exposure of the molecule to the extensional flow device representing the fluid forces in which the molecule is expected to be encountered during its manufacture, shipping simulator studies have been also conducted. Based on the monomer fraction data, the sample is fully monomeric for all the conditions investigated, for both quiescent and flow conditions. This observation is also verified by the particle concentration obtained based on the BMI images as shown in figure 7.22. As expected from the monomer fraction data, the sample is not aggregated with the absence of severe particle formation. This implies that the flow developed within the shipping simulator is different and not comparable with the flow fields developed within the extensional flow device. Moreover, the temperature in which the two different stress experiments performed was different. Extensional flow experiments were performed at a room temperature of ∼25 ℃ compared to the ∼4 ℃ of samples stressed within the shipping simulator. Additionally, the two stress experiments involve the presence of different interfaces. Particularly, the extensional flow experiments are conducted in the presence of solid-liquid interface, whereas the shipping simulator experiments consist of solid-liquid-air interfaces. Therefore, as the parameter space involved in two of these setups is not the same, they cannot be directly compared. From the shipping simulator data presented, it can be concluded that the molecule is not expected to further unfold or aggregate during its shipping.

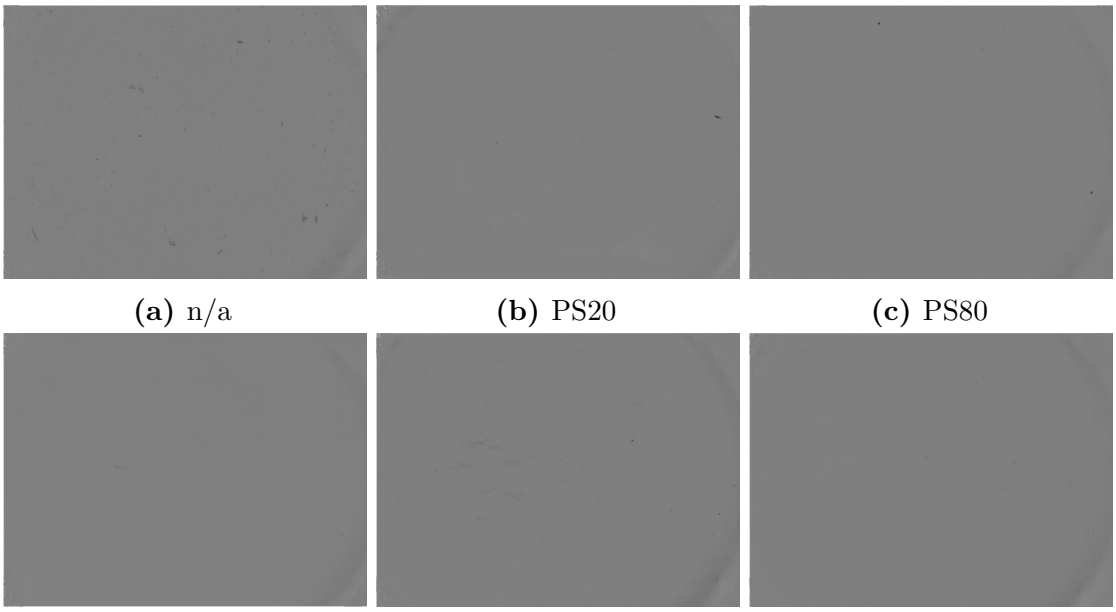

(a) n/a **(b)** PS20 **(c)** PS80

(d) P188 **(e)** HS15 **(f)** EL

Figure 7.22: BMI images of 0.5 mg/mL MEDI3549 under shear flow conditions in shipping simulator in the absence, n/a (7.22a) and presence of surfactant formulations 0.02% w/v PS20, PS80, P188, HS15, EL (figs. 7.22b to 7.22f) in 235 mM Sucrose, 25 mM Histidine, pH=6.

7.3.5 Aggregation size

As the aggregation was firstly characterised qualitatively by visual inspection and particle visualisation using BMI, the quantitive characterisation is then investigated. The BMI method has also the flexibility to provide information about the quantity of the particle concentration, as well as providing detailed size range of the aggregated particles. To determine the effect of the various surfactant molecules on the aggregation propensity of the molecule, the total number of particles detected for each flow condition representing extensional flow device (for untreated and silane B treated glass surface) and shipping simulator is shown in figure 7.23. According to the previous results obtained from HPSEC, visual inspection and BMI images, the samples in quiescent conditions represent monomeric samples with monomer fraction corresponding to ∼1, with no apparent particles being detected from visual inspection, as well as from BMI images. Apart from the quiescent conditions, no aggregation was detected when the samples were exposed to the shipping simulator, for all the surfactant formulations investigated. Linking to the previous observations, the total number of particles detected for the samples exposed to the shipping simulator is significantly lower compared to the number of particles detected when the samples were exposed to the extensional flow device. Specifically, for surfactant-free formulations (n/a), the total number of particles detected during the molecule exposure to shipping simulator corresponds to $\sim 7 \times 10^3$ particles/mL compared to $\sim 4.5 \times 10^5$ when exposed to extensional flow device on the untreated glass surface.

The presence of surfactants in the formulation shows to suppress the particle formation when the sample was exposed to the shipping simulator (purple bars) for the whole surfactant library. On the other hand, the opposite effect is shown, leading to increase in the total number of particles detected when the sample was exposed to the extensional flow device (orange and green bars). This suggests that the particle formation of aggregates is critically dependent on the type of flow they encountered, with the extensional flow to induce severe aggregation of particles inducing an increase in the particle concentration of 2 orders of magnitude compared to the shipping simulator. Regarding the quiescent samples, the minimum number of particles was detected for the control samples which were incubated in bench for the longest experimental time (pink bars), which was lower or similar compared to the shipping simulator induced particle for surfactant-free formulations, PS20, PS80, P188 and EL formulations. Quiescent samples which were incubated within the device's components (syringe body and capillary) incubated within the glass untreated surface (yellow bars), are shown to induce similar number of particles with the samples incubated in bench for the surfactant-free formulation, and higher number of particles for the whole surfactant library, suggesting the surface activity of the surfactants. On the other hand, quiescent samples which were incubated within the silane B treated surface (blue bars) corresponding to surfactant-free formulations, induce the formation of a high number of particles corresponding to 2 orders of magnitude compared to quiescent samples incubated in bench and untreated glass surface for surfactant-free formulation. The distinct effect of the solid interface under extensional flow conditions and specifically of silane B surface is significant as shown for the surfactant-free formulations. The total number of particles is shown to significantly suppressed by $\sim 2\times10^5$ particles/mL when the samples are exposed to the extensional flow device which is treated with the silane B. However, with the addition of surfactants into the protein formation, the suppressive effect of the silane B surface, on the particle concentration is no longer observed. The total number of particles is increased with surfactant formulations corresponding to P188, HS15 and EL compared to the respective formulation exposed to the untreated glass surface. The maximum number of particles is detected for the surfactant formulations of HS15 and EL when exposed to the extensional flow device treated with silane B surface, reaching a total number of particles corresponding to $\sim 8\times10^5$ and $\sim 1\times10^6$ particles/mL respectively.

The instrument provides the size distribution for various size groups which are analytically shown, in figures 7.24, 7.25 and 7.26 corresponding to size groups for control samples, samples exposed to the shipping simulator as well as for samples exposed to the extensional flow device for untreated and silane B treated surfaces. Particles were detected in size groups, with the detectable size beginning from 2 μm up to >25 μm, with size groups categorised within a range of 1 μm (i.e., 2-3 μm, 3-4 μm, 4-5 μm, etc). As shown in figure 7.24a, for surfactant-free formulations, the particle concentration detected for quiescent samples which were incubated on the bench (pink bars) and within the extensional flow

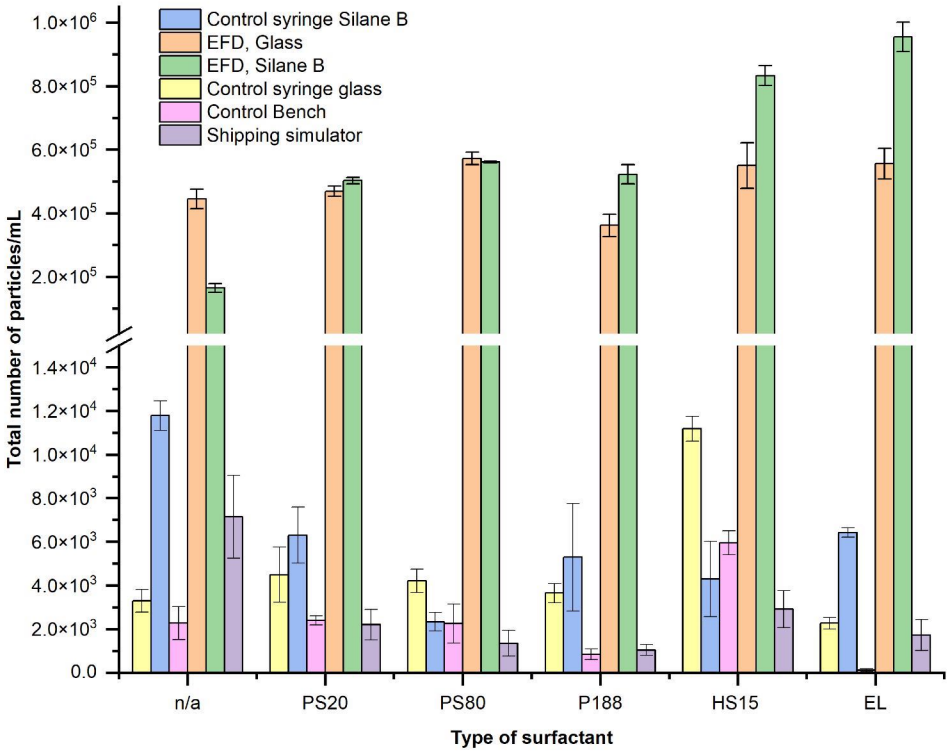

Figure 7.23: Total number of particles/mL of 0.5 mg/mL MEDI3549 as determined from HORIZON. Samples have been exposed to shipping simulator (purple bars), extensional flow device (EFD) (100 passes, 8 mm/s) in glass (orange bars) and Silane B treated surfaces (green bars) in the absence, n/a and in presence of surfactant formulations 0.02% w/v PS20, PS80, P188, HS15, EL in 235 mM Sucrose, 25 mM Histidine, pH=6. Control samples have been incubated in tubes left on the bench (pink bars), in equipment surface (syringe and capillary bodies) corresponding to bare borosilicate glass surfaces (yellow bars) and silane B treated surfaces (blue bars). Errors indicate the standard deviation between 3 samples loaded for each condition.

device components in untreated glass (yellow bars) present similar size distribution to the similar extent. The maximum number of particles correspond to particles with a size range of 2-3 μm which is detected to correspond to ~1,000 particles/mL. On the other hand, for the quiescent samples which were incubated in extensional flow device components treated with silane B, particle concentration was detected to a much higher extent corresponding to a maximum particle concentration of ~4,000 particles/mL. For PS20 formulations, the size distribution is shown in figure 7.24b, exhibiting similar profile between the three control samples, with the maximum particle concentration corresponding to silane B control with particle concentration reaching $\sim 2.5\times10^3$ particles/mL compared to $\sim 0.8\times10^3$ particles/mL for control samples incubated in bench for the size group of 2-3 μm. The same group, with particle size of 2-3 μm, is shown in figure 7.24c to correspond to the most particles detected for the particular size group, for PS80 formulations with a maximum number detected at $\sim 2.5\times10^3$ particles/mL for samples incubated within the untreated glass surface components of the extensional flow device (yellow bars). The same maximum number of $\sim 2.5\times10^3$ particles/mL is detected for P188 formulation for control samples incubated within silane B treated surfaces (blue bars), as shown in figure 7.24d. Interestingly, for HS15 formulations the particles detected correspond to the maximum among all the formulation conditions examined for the quiescent samples, reaching an average particle concentration of $\sim 6\times10^3$ particles/mL, as shown in figure 7.24e. For EL formulations, minimum particles were detected for samples incubated in the bench, and the maximum number of particles was detected for $\sim 2.5\times10^3$ particles/mL for samples incubated within silane B treated syringes as shown in figure 7.24f. From the size distribution analysis of quiescent samples, it can be observed that the interaction between the surfactant molecules investigated, and the surface aspect have distinct effects on the particle formation detected. Overall from quiescent samples the maximum particles detected had a size range of 2-3 μm, and the size distribution of the molecules was similar throughout the formulation conditions examined, with different extents between the control samples and surfactant formulations.

Firstly, the size distribution of particles was investigated for the samples exposed to flow effects within the shipping simulator, as shown in figure 7.25. From previous data, it was shown that the protein state of the molecules during their exposure to the shipping simulator remained as monomeric. Compared to the control samples, the shipping simulator data were similar to the control samples, suggesting that the samples are expected to have no aggregation tendency during their shipping based on the shipping simulator data. To investigate the size profile of the samples and how these correlate with their respective controls, the detailed size distribution for all the formulation conditions is then investigated. As an overall observation, the profile of the size distribution is shown to be the same between the quiescent and shipping simulator samples, where the majority of the samples have a size of 2-3 μm. This suggests that the molecules have not been aggregated,

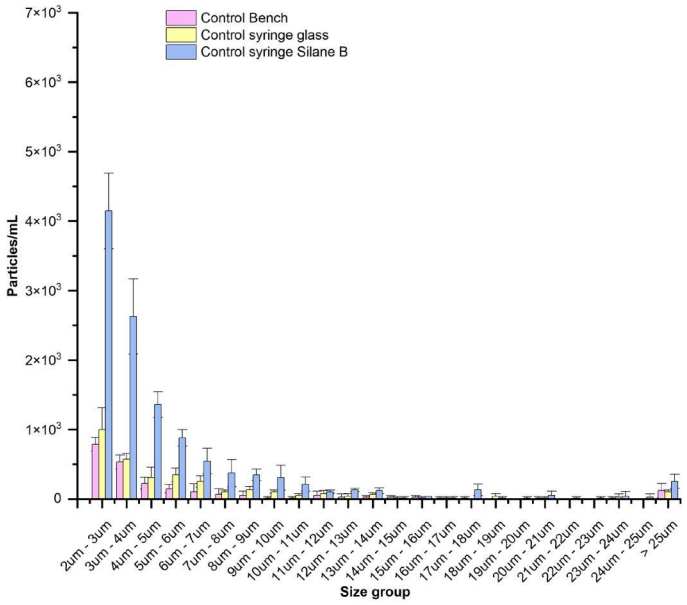

(a) n/a

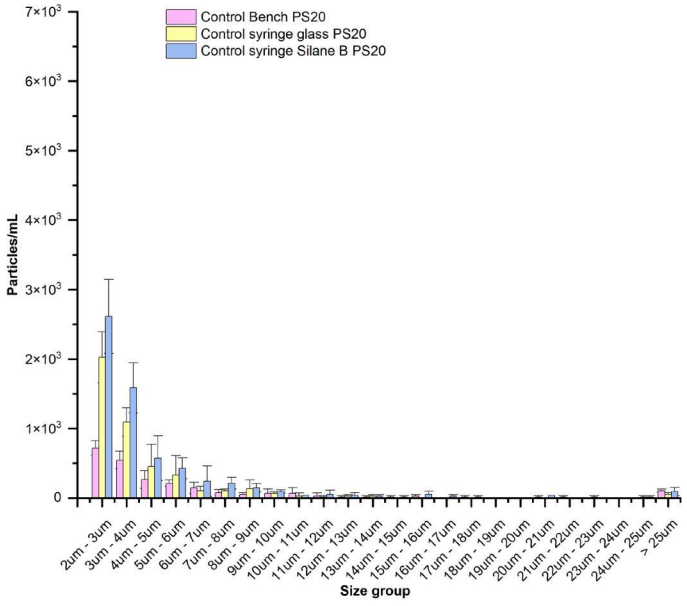

(b) PS20

Figure 7.24: Average number of particles/mL of 0.5 mg/mL MEDI3549 as determined from HORIZON. Quiescent samples have been incubated to bench in tube (control bench, pink bars) and in device's surface, syringe and capillary bodies for untreated glass (control syringe glass, yellow bars) and silane B treated surfaces (control syringe silane B, blue bars), in the absence, n/a (7.24a) and in presence of surfactant formulations 0.02% w/v PS20, PS80, P188, HS15, EL (figs. 7.24b to 7.24f) in 235 mM Sucrose, 25 mM Histidine, pH=6. Control samples have been incubated in tubes left on the bench (pink bars), in equipment surface (syringe and capillary bodies) corresponding to bare borosilicate glass surfaces (yellow bars) and silane B treated surfaces (blue bars). Errors indicate the standard deviation between 3 samples loaded for each condition.

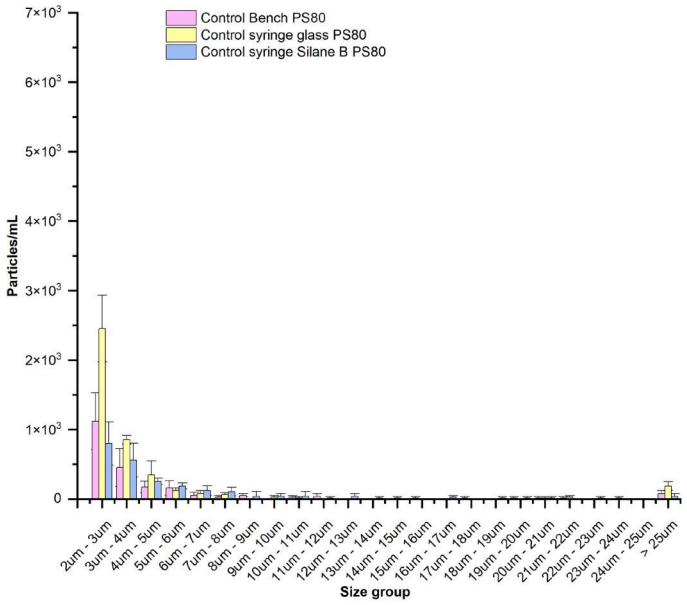

(c) PS80

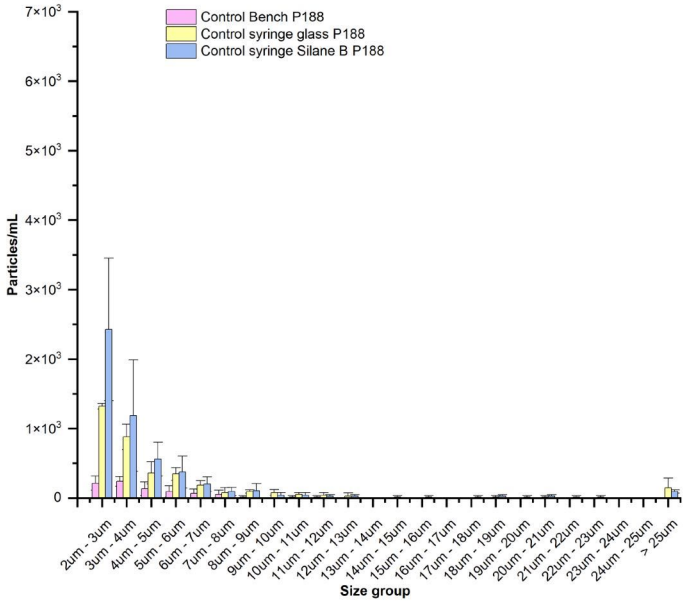

(d) P188

Figure 7.24: Average number of particles/mL of 0.5 mg/mL MEDI3549 as determined from HORIZON. Quiescent samples have been incubated to bench in tube (control bench, pink bars) and in device's surface, syringe and capillary bodies for untreated glass (control syringe glass, yellow bars) and silane B treated surfaces (control syringe silane B, blue bars), in the absence, n/a (7.24a) and in presence of surfactant formulations 0.02% w/v PS20, PS80, P188, HS15, EL (figs. 7.24b to 7.24f) in 235 mM Sucrose, 25 mM Histidine, pH=6. Control samples have been incubated in tubes left on the bench (pink bars), in equipment surface (syringe and capillary bodies) corresponding to bare borosilicate glass surfaces (yellow bars) and silane B treated surfaces (blue bars). Errors indicate the standard deviation between 3 samples loaded for each condition. (cont.)

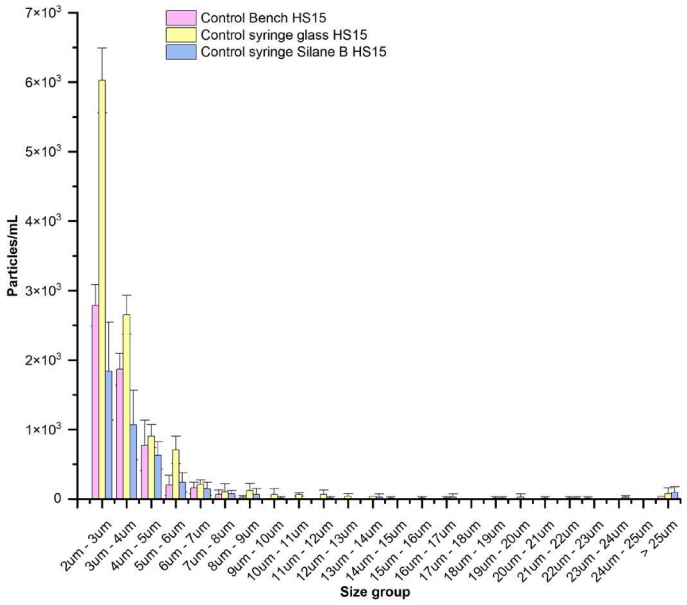

(e) HS15

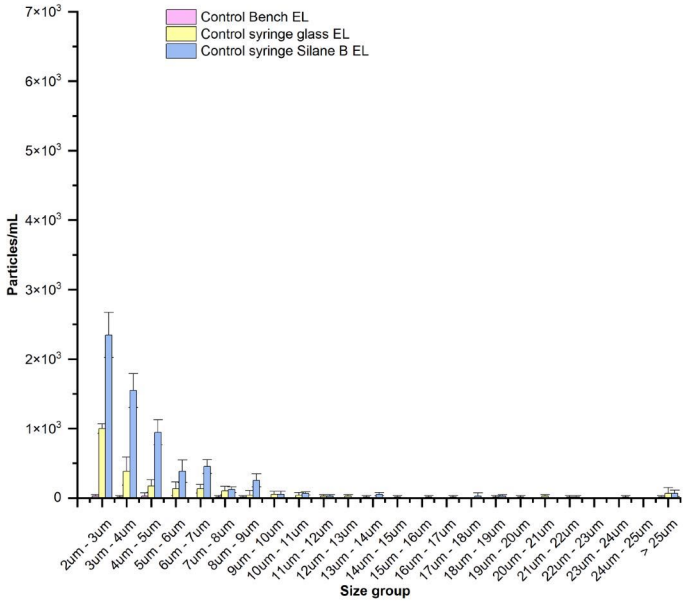

(f) EL

Figure 7.24: Average number of particles/mL of 0.5 mg/mL MEDI3549 as determined from HORIZON. Quiescent samples have been incubated to bench in tube (control bench, pink bars) and in device's surface, syringe and capillary bodies for untreated glass (control syringe glass, yellow bars) and silane B treated surfaces (control syringe silane B, blue bars), in the absence, n/a (7.24a) and in presence of surfactant formulations 0.02% w/v PS20, PS80, P188, HS15, EL (figs. 7.24b to 7.24f) in 235 mM Sucrose, 25 mM Histidine, pH=6. Control samples have been incubated in tubes left on the bench (pink bars), in equipment surface (syringe and capillary bodies) corresponding to bare borosilicate glass surfaces (yellow bars) and silane B treated surfaces (blue bars). Errors indicate the standard deviation between 3 samples loaded for each condition. (cont.)

where in the case of aggregation and potential protein unfolding the samples would be expected to have a bigger size, confirming the further unfolding and aggregation. The maximum number of particle concentration is detected for the surfactant-free formulation sample, as it is shown in figure 7.25a, and the maximum number of particles detected corresponds to $\sim 3.2\times10^3$ particles/mL for the size group of 2-3 μm. For samples with surfactant formulations, the size distribution is similar, however with suppressive effect on the overall size distribution of the particles, with the effect being more pronounced for the particles with the size 2-3 μm. Particle concentration corresponding to $\sim 1.25\times10^3$, $\sim 0.7\times10^3$, $\sim 0.5\times10^3$, $\sim 1.5\times10^3$ and $\sim 0.9\times10^3$ particles/mL is detected for formulations with PS20, PS80, P188, HS15 and EL as shown in figures 7.25b, 7.25c, 7.25d, 7.25e and 7.25f respectively. Overall, the minimum number of particles is detected for P188 formulation, indicating its suppressive effect on the particle concentration for size group 2-3 μm, with the particle concentration decrease by $\sim$80% compared to surfactant-free formulation.

The effect of extensional flow on the size and quantity of particles induced during their exposure to extensional flows is shown in figure 7.26. From previously presented data, it was shown that the molecule is highly aggregation prone during its exposure to extensional flow, whereas its stability against aggregation is enhanced by the presence of surfactants within its formulation buffer. To further investigate how this observation can be linked with the quantity and size distribution of particles alongside the monomer fraction data obtained from HPSEC data, the size distribution of particles is presented for each experimental setup. For each formulation condition, the molecule has been exposed to two solid surfaces of interest, corresponding to the untreated glass surface (orange bars) and the surface treated with silane B agent (green bars).

Initially, for the surfactant-free formulations as shown in figure 7.26a, the type of solid surface is shown to strongly influence the quantity of particles detected as well as their relative size. Specifically, when the molecule is exposed to the untreated glass surface, the maximum particle concentration detected corresponds to $\sim 4.9\times10^4$ particles/mL for particles with size of 5-6 μm. Interestingly, when the molecule is exposed to the silane B surface, the size of the particles induced, is reduced to 2-3 μm which corresponds to the size of particles with the maximum concentration $\sim 3.4\times10^3$ particles/mL. This implies that the silane B exhibits protective effects to the molecule as it is exposed to extensional flow. The majority of the molecules have a size of 2-3 μm which agrees with the size of the particles detected during quiescent conditions (figure 7.24). The size distribution profile for the silane B treated surface is similar to the profile detected for the quiescent and shipping simulator flow conditions, with the maximum particle size detected for size groups of 2-3 μm, in contrast with the size distribution of particles detected after the exposure to the extensional flow device on glass untreated surface. Moreover, the aggregation prone profile of the molecule to the extensional flow is also shown based on the formation of

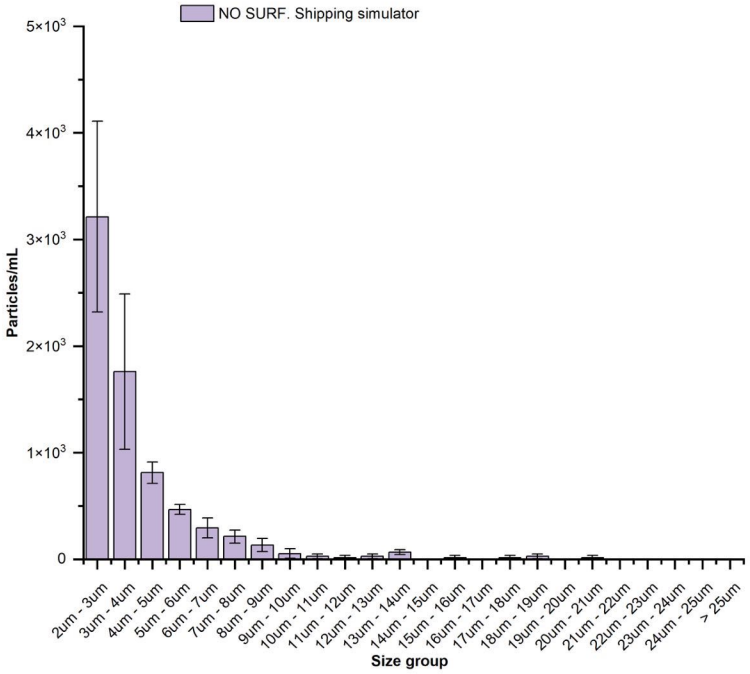

(a) n/a

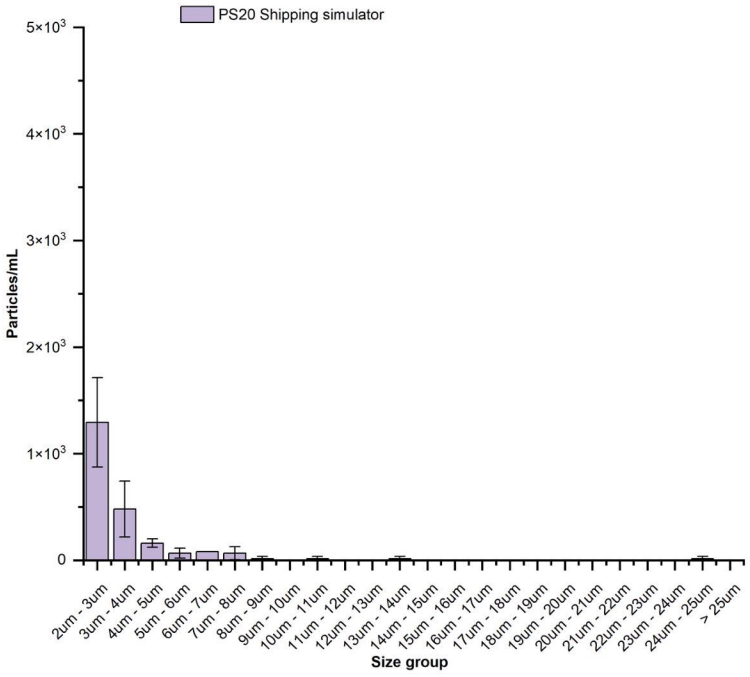

(b) PS20

Figure 7.25: Size distribution of particles/mL of 0.5 mg/mL MEDI3549 as determined from HORIZON. Samples have been exposed to the shipping simulator, in the absence, n/a (7.25a) and in presence of surfactant formulations 0.02% w/v PS20, PS80, P188, HS15, EL (figs. 7.25b to 7.25f) in 235 mM Sucrose, 25 mM Histidine, pH=6. Errors indicate the standard deviation between 3 samples loaded for each condition.

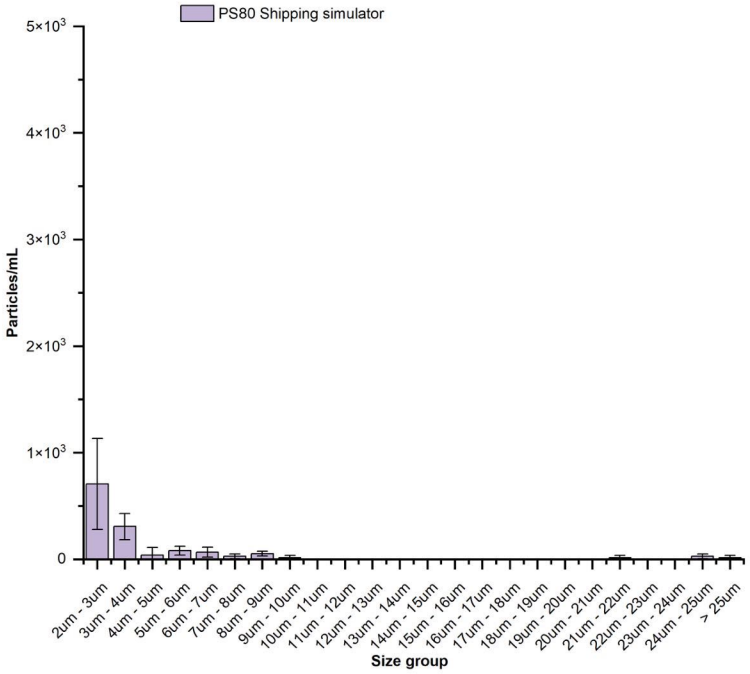

(c) PS80

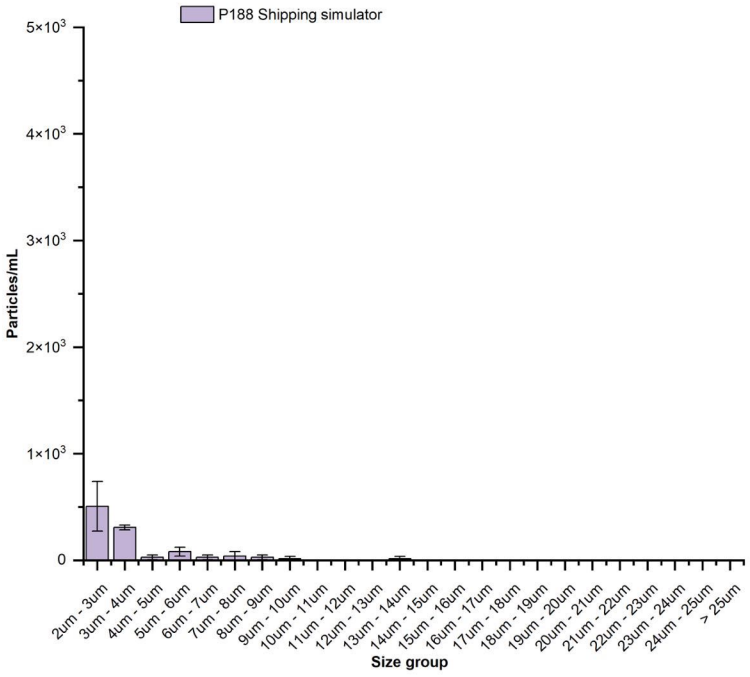

(d) P188

Figure 7.25: Size distribution of particles/mL of 0.5 mg/mL MEDI3549 as determined from HORIZON. Samples have been exposed to the shipping simulator, in the absence, n/a (7.25a) and in presence of surfactant formulations 0.02% w/v PS20, PS80, P188, HS15, EL (figs. 7.25b to 7.25f) in 235 mM Sucrose, 25 mM Histidine, pH=6. Errors indicate the standard deviation between 3 samples loaded for each condition. (cont.)

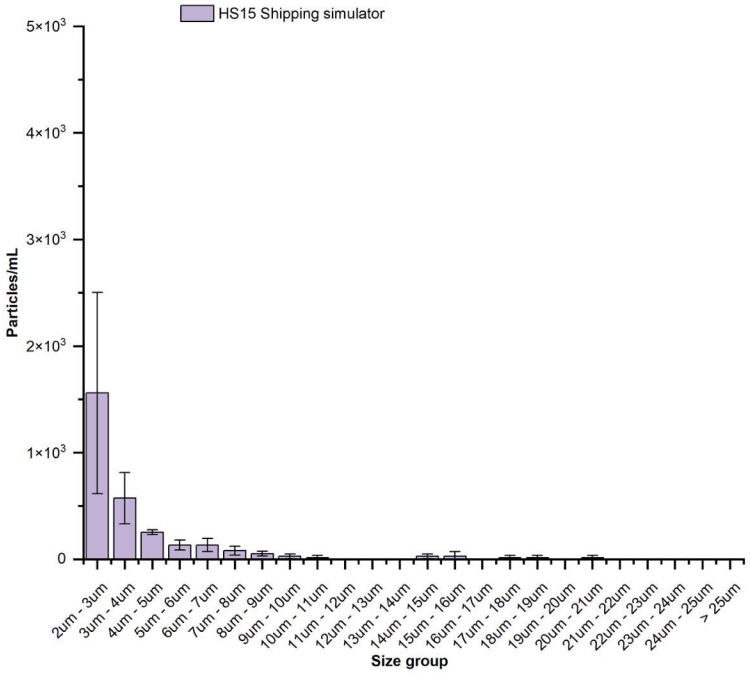

(e) HS15

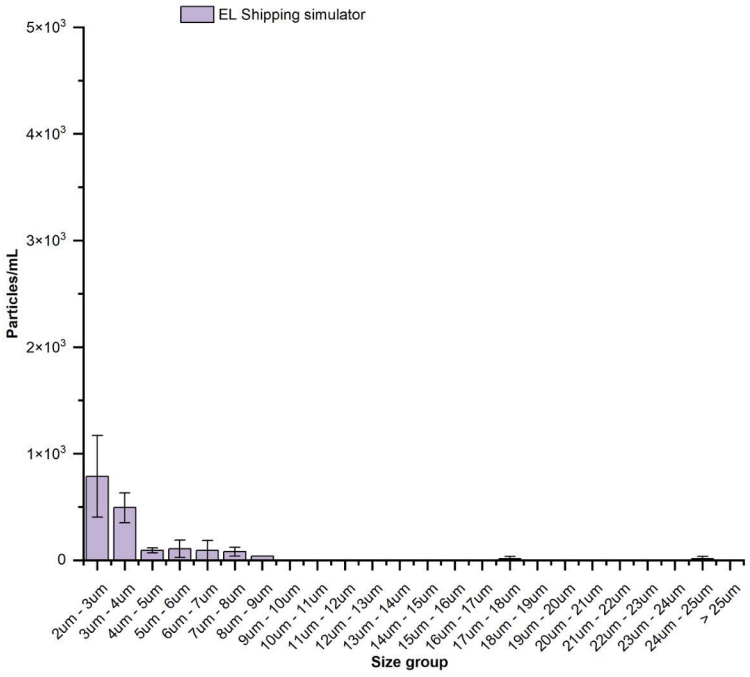

(f) EL

Figure 7.25: Size distribution of particles/mL of 0.5 mg/mL MEDI3549 as determined from HORIZON. Samples have been exposed to the shipping simulator, in the absence, n/a (7.25a) and in presence of surfactant formulations 0.02% w/v PS20, PS80, P188, HS15, EL (figs. 7.25b to 7.25f) in 235 mM Sucrose, 25 mM Histidine, pH=6. Errors indicate the standard deviation between 3 samples loaded for each condition. (cont.)

bigger particles, which can correspond to aggregated particles having a size of >25 μm. The suppressive effect of silane B surface is also pronounced on the formation of bigger particles, that can be detected from the instrument. Particularly, silane B suppressed the formation of bigger particles by ∼40% compared to particles detected after the exposure to the untreated glass surface within the extensional flow device. These results further highlight the previously observed effect of synergy between flow and interface in affecting the aggregation propensity of several molecules.

Moving to surfactant formulation conditions, it can be observed that the profile distribution of particles is similar for the two (solid) surfaces of glass and silane B, however with different extents for all the surfactant molecules investigated, as shown in figures 7.26b, 7.26c, 7.26d, 7.26e and 7.26f, with increased particles detected for silane B treated surface. The different extent in particle concentration between the two solid surfaces, clearly indicates that the solid-liquid aspect is important in affecting the aggregation pathway of the molecule. With the addition of surfactants in the protein formulation, the maximum number of particles detected is higher compared to the surfactant-free formulations. Additionally, as observed previously from quiescent and shipping simulator samples, the most common size of particles corresponds to 2-3μm. From the shipping simulator data, it was shown that the minimum number of particles was detected for P188 formulation (figure 7.25d). From the extensional flow experiments, minimum particles were also detected for the same formulation with P188, when exposed to untreated glass and silane B treated surfaces (figure 7.26d).

To summarise the effects of the parameters involved in the conduction of the particular experiments, including solid and liquid interfaces alongside with the type of flow distribution, the particles have been grouped in larger size bins. Particularly, particles are presented in three group sizes, such as particles are grouped in 2-10 μm, 10-25 μm and >25 μm. Particles have been grouped in quiescent conditions (absence of flow) and in flow conditions after their exposure to shipping simulator and extensional flow device as shown in tables 7.1 and 7.2 respectively. As the size distribution is automatically obtained in the size groups with 1 μm range from HORIZON instrument, to summarise the data in bigger size groups is obtained by the total sum of the particles in each size group. The categorisation of particles in bigger range groups allows their comparison with literature findings, where the particle concentration is typically presented as groups of >2 μm, >10 μm and >25 μm. Moreover, limits for subvisible particles of sizes ≥10 μm and ≥25 μm have been defined by the United States of Pharmacopeia chapter <788> [102].

Firstly, a summary of the control samples in quiescent conditions is presented in table 7.1. For all the formulation conditions explored, the majority of particles detected correspond to the size group of 2-10 μm. For control samples incubated in the bench during the conduction of the experiment, the maximum number of particles is shown to correspond

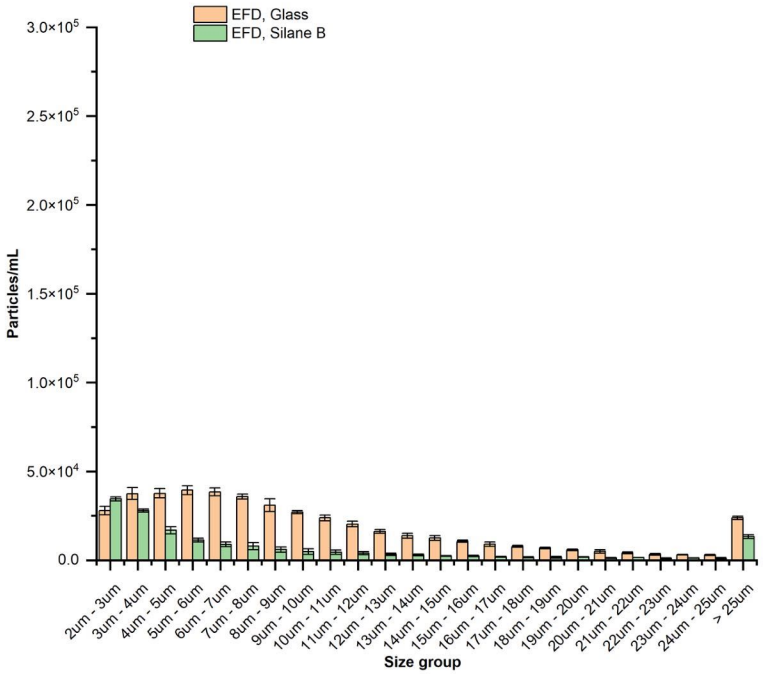

(a) n/a

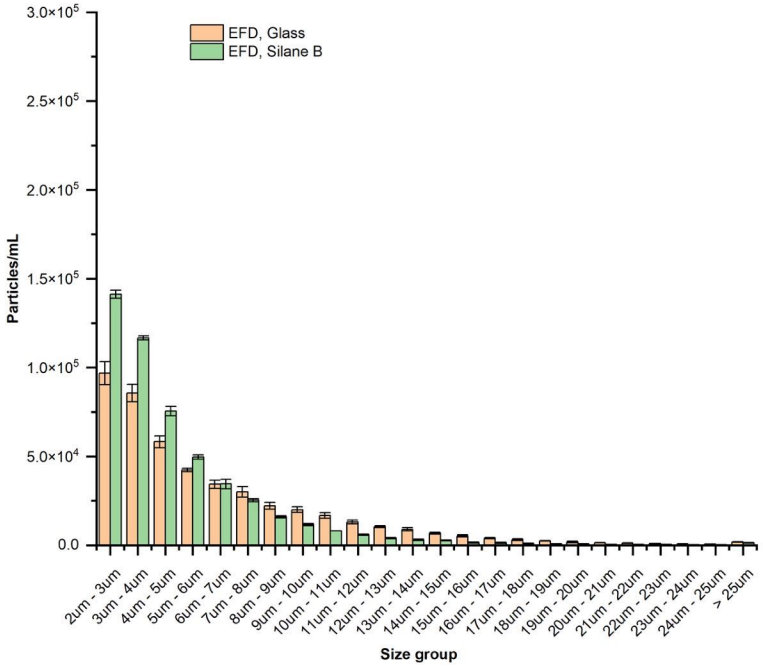

(b) PS20

Figure 7.26: Size distribution of particles/mL of 0.5 mg/mL MEDI3549 as determined from HORIZON. Samples have been exposed to extensional flow device (EFD) (100 passes, 8 mm/s) in glass (orange bars) and Silane B treated surfaces (green bars) in the absence, n/a (7.26a) and in presence of surfactant formulations 0.02% w/v PS20, PS80, P188, HS15, EL (figs. 7.26b to 7.26f) in 235 mM Sucrose, 25 mM Histidine, pH=6. Errors indicate the standard deviation between 3 samples loaded for each condition.

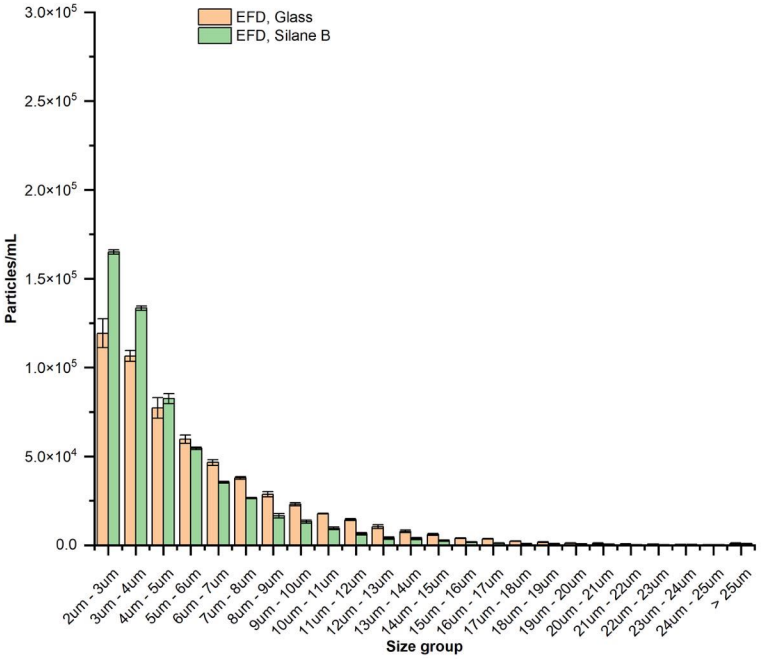

(c) PS80

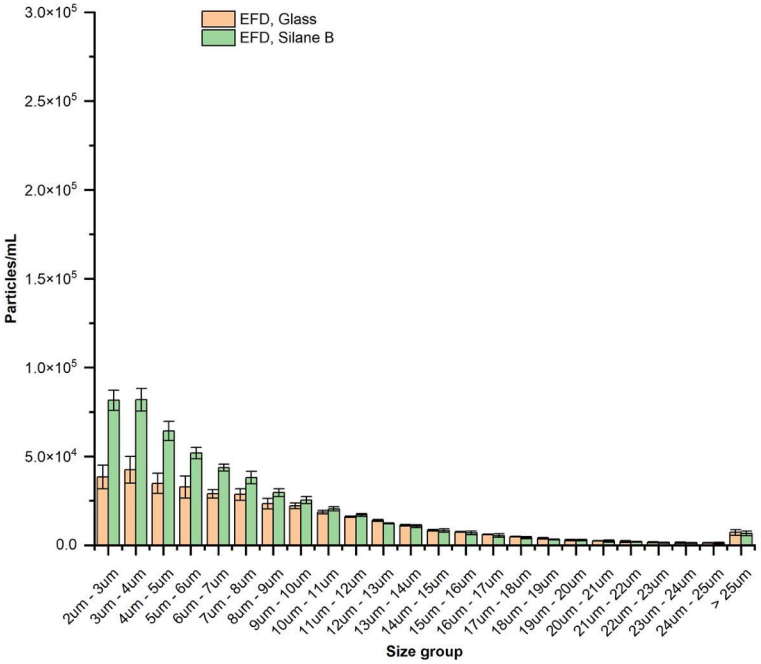

(d) P188

Figure 7.26: Size distribution of particles/mL of 0.5 mg/mL MEDI3549 as determined from HORIZON. Samples have been exposed to extensional flow device (EFD) (100 passes, 8 mm/s) in glass (orange bars) and Silane B treated surfaces (green bars) in the absence, n/a (7.26a) and in presence of surfactant formulations 0.02% w/v PS20, PS80, P188, HS15, EL (figs. 7.26b to 7.26f) in 235 mM Sucrose, 25 mM Histidine, pH=6. Errors indicate the standard deviation between 3 samples loaded for each condition. (cont.)

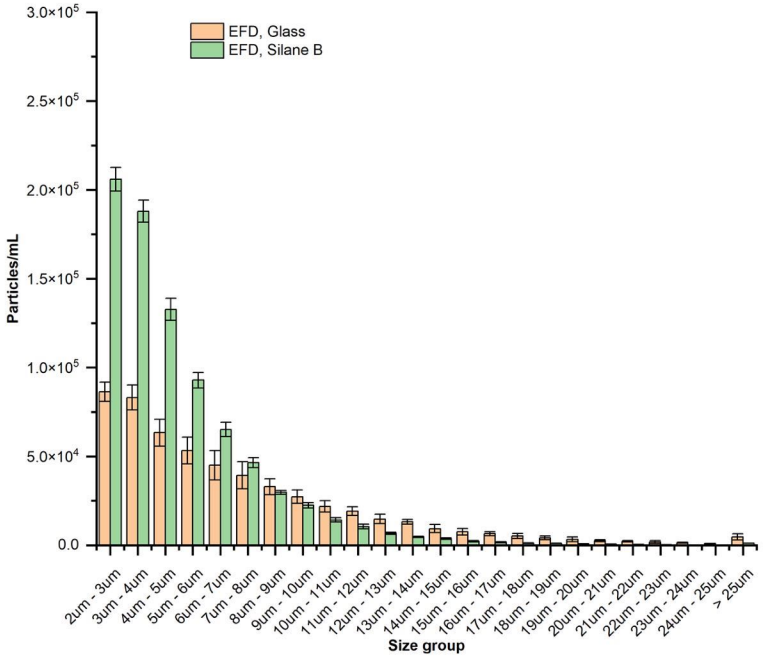

(e) HS15

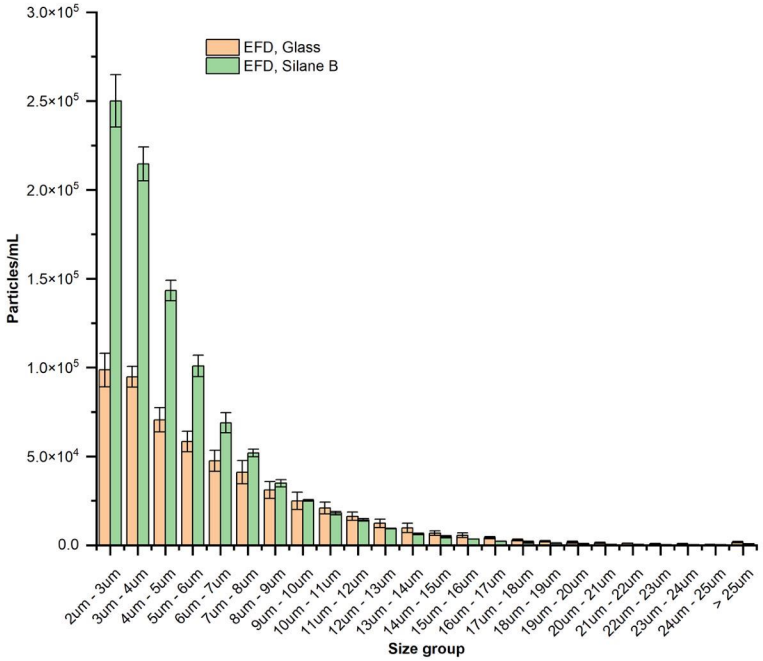

(f) EL

Figure 7.26: Size distribution of particles/mL of 0.5 mg/mL MEDI3549 as determined from HORIZON. Samples have been exposed to extensional flow device (EFD) (100 passes, 8 mm/s) in glass (orange bars) and Silane B treated surfaces (green bars) in the absence, n/a (7.26a) and in presence of surfactant formulations 0.02% w/v PS20, PS80, P188, HS15, EL (figs. 7.26b to 7.26f) in 235 mM Sucrose, 25 mM Histidine, pH=6. Errors indicate the standard deviation between 3 samples loaded for each condition. (cont.)

to HS15 formulation with a total number of particles detected to 5,880 particles/mL for particles sided within the range of 2-10 μm. No particles were detected for the bigger size group of >25 μm in the P188 formulation. For samples incubated within the device components of glass untreated surface, the maximum particle concentration is detected for HS15 formulations for the size group of 2-10 μm similar with the control bench incubation samples. On the other hand, for these control samples, the minimum number of particles was detected for PS20 formulation, corresponding to 53 particles/mL. For samples incubated within the silane B treated surface, the maximum number of particles was detected for surfactant-free formulations corresponding to a total number of 10,587 particles/mL (2-10 μm) whereas minimum particles were detected for PS80 formulation corresponding to 40 particles/mL (>25 μm).

Table 7.1: Data summary of MEDI3549 (0.5 mg/mL) indicating the total number of particle concentration for the size groups of 2-10 um, 10-25 um and >25 um in the absence (n/a) and presence of surfactants (PS20, PS80, P188, Kolliphor HS15 & Kolliphor EL) under quiescent conditions. Samples have been incubated in bench, extensional flow device on glass, SiO_2 and Silane B treated surfaces. All surfactant samples have been formulated at the same surfactant concentration = 0.02% w/v in 235 mM Sucrose, 25 mM Histidine, pH=6.

Surfactant	Size group	Control bench (Particles/mL)	Control syringe glass (Particles/mL)	Control syringe silane B (Particles/mL)
n/a	2-10 um	1,933	2,827	10,587
n/a	10-25 um	227	360	945
n/a	>25 um	120	107	253
PS20	2-10 um	2,093	4,320	5,893
PS20	10-25 um	200	120	320
PS20	>25 um	107	53	93
PS80	2-10 um	2,040	3,947	2,107
PS80	10-25 um	133	80	187
PS80	>25 um	80	187	40
P188	2-10 um	813	3,347	4,987
P188	10-25 um	27	160	213
P188	>25 um	-	147	93
HS15	2-10um	5,880	10,800	4,080
HS15	10-25 um	27	307	120
HS15	>25 um	40	80	93
EL	2-10 um	93	2,027	6,107
EL	10-25 um	13	173	253
EL	>25 um	13	67	67

A summary of particle concentration of the samples exposed to shipping simulator, extensional flow device with untreated and silane B treated surfaces is shown in table 7.2. Among the three flow conditions examined, minimum particles have been detected when the particles were exposed to shipping simulator. Based on the previous data presenting the monomer fraction, it was shown that the particles were fully monomeric, which can be linked to the low particle concentration detected for the shipping simulator. Between the samples exposed to the shipping simulator, maximum number of particles was detected for surfactant-free formulations with size group of 2-10 μm corresponding to a total number of 6,947 particles/mL, whereas no particles with size of >25 μm have been detected for surfactant free, P188, HS15 and EL formulations. When the sample is then exposed to the extensional flow device, the number of particles is increased by two orders of magnitude for

particles with size group of 2-10 μm for both solid surfaces including untreated glass and silane B treated surface. For samples exposed to the untreated glass surface, the maximum number of particles detected corresponds to a total number of 499,027 corresponding to particles with size group of 2-10 μm for PS80 formulation. The minimum number of particles for the upper detectable size range of >25 μm corresponds to a total number of 1,053 also for PS80 formulation. For samples exposed to the silane B treated surface of the extensional flow device, the maximum number of particles was detected for the size group of 2-10 μm corresponding to a total particle concentration of 889,960 particles/mL for EL formulation. Minimum particles have been detected for the size group of >25 μm with a total particle concentration of 800 particles/mL also for EL formulation.

Comparing the effects of surfactant molecules between the three different flow conditions, it can be observed that the suppressive effect of surfactants in particle concentration is both flow and surface dependent. The impact of the extensional flow on the particle concentration, is significant when compared to the samples exposed to shear flow during their exposure to the shipping simulator. This suggests that the molecule is more prone to potential unfolding and aggregation during its manufacture compared to its shipping, however with formulation strategies and silane B protective surface, their stability is improved.

The particle concentration detected for the samples exposed to the shipping simulator can be compared with the study conducted in [282] where the aggregation of samples in a range of formulation and concentration conditions was investigated using various agitation methods, including a shipping simulator. Based on the results presented in [282], the authors showed that the concentration of the particles with size of 2-10 μm correspond to a concentration of ∼1,000 particles/mL. For particles with size of 10-25 μm a particle concentration of ∼10 particles/mL was observed, and for bigger particles with size of >25 μm, ∼2 particles/mL. The data corresponds to the antibody investigated with the lower concentration considered in [282], (6 mg/mL with the antibody formulated within sugar excipient). Their data correlates and agree with the particles detected in the current study within the same order of magnitude for particles with size of 2-10 μm and similar concentration for particles with size of >25 μm. However, for particles with size of 10-25 μm the particles detected in the current study compared with the study in [282] have a difference of two orders of magnitude. Particularly, for the surfactant-free formulation, particle concentrations for size groups of 2-10 μm, 10-25 μm were ∼6,947 particles/mL and ∼200 particles/mL whereas no particles with size of >25 μm were detected as shown in table 7.2. The disparity in the actual particles detected between the current study and literature study in [282] is expected due to the difference in the parameter space involved between the two studies including protein molecule, concentration, formulation and volume.

Table 7.2: Data summary of MEDI3549 (0.5 mg/mL) indicating the total number of particle concentration for the size groups of 2-10 um, 10-25 um and > 25 um in the absence (n/a) and presence of surfactants (PS20, PS80, P188, Kolliphor HS15 & Kolliphor EL) under the exposure to the shipping simulator, and extensional flow for 100 passes at 8 mm/s. Samples have been exposed to extensional flow device on glass, SiO_2 and Silane B treated surfaces. All surfactant samples have been formulated at the same surfactant concentration = 0.02% w/v in 235 mM Sucrose, 25 mM Histidine, pH=6.

Surfactant	Size group	Shipping simulator (Particles/mL)	EFD, Glass (Particles/mL)	EFD, Silane B (Particles/mL)
n/a	2-10 um	6,947	274,973	118,533
n/a	10-25 um	200	145,840	32,880
n/a	>25 um	-	23,867	13,307
PS20	2-10 um	2,160	389,693	470,613
PS20	10-25 um	27	77,480	30,627
PS20	>25 um	13	1,840	1,293
PS80	2-10 um	1,293	499,027	527,467
PS80	10-25 um	40	72,160	32,840
PS80	>25 um	13	1,053	880
P188	2-10 um	1,027	251,667	416,160
P188	10-25 um	13	102,733	99,587
P188	>25 um	-	7,200	6,627
HS15	2-10 um	2,813	430,867	783,587
HS15	10-25 um	107	114,413	48,080
HS15	>25 um	-	4,747	1,147
EL	2-10 um	1,693	467,093	889,960
EL	10-25 um	27	87,093	63,747
EL	>25 um	-	1,720	800

To allow an overview of the results, the link between the monomer fraction data along with the particle concentration data will permit the comparison between the formulation surfactants, for each experimental setup. The parallel correlation between the monomer fraction and particle concentration in groups of particles of 2-10 μm, 10-25 μm and $\geq$25 μm will shed light into selecting the suitable formulation conditions and candidates that enhance molecule stability against unfolding and aggregation. The surfactant molecules in a range of flow conditions including shipping simulator and extensional flow device in untreated and silane B treated surfaces are presented in figures 7.27, 7.28 and 7.29. As shown in figure 7.27, the effect of surfactant formulation is pronounced mostly for the small and intermediate size range groups of 2-10 μm and 10-25 μm. The shipping simulator has no effect on the monomer fraction of the molecule, however, concentration-wise, there is slight difference between some of the formulations (within one order of magnitude). Based on figures, it can be proposed that all the surfactant molecules can be good formulation candidates. However, the HS15 formulation induced the maximum particle concentration observed across the surfactant library (figs. 7.27b and 7.27c). Therefore, formulations including PS20, PS80, P188 and EL can be considered as the best candidates during shipping conditions.

For extensional flow conditions on untreated glass surface, it was shown that the maximum average monomer fraction was detected for HS15 formulation, however within error the monomer fraction is similar to the rest of the formulation molecules. Therefore, the comparison between formulations can be based on the surfactant formulation that

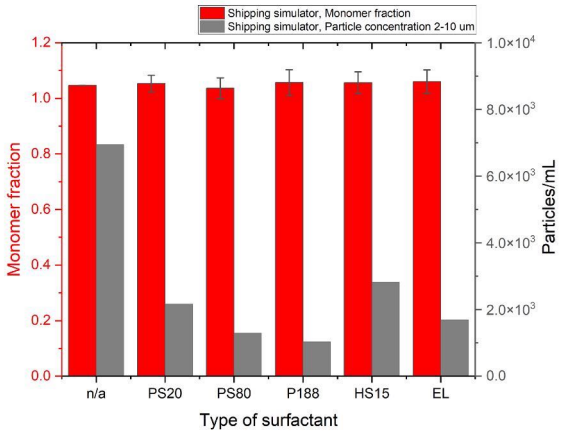

(a)

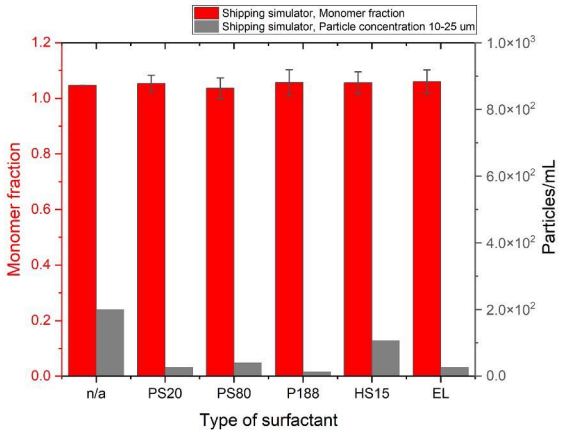

(b)

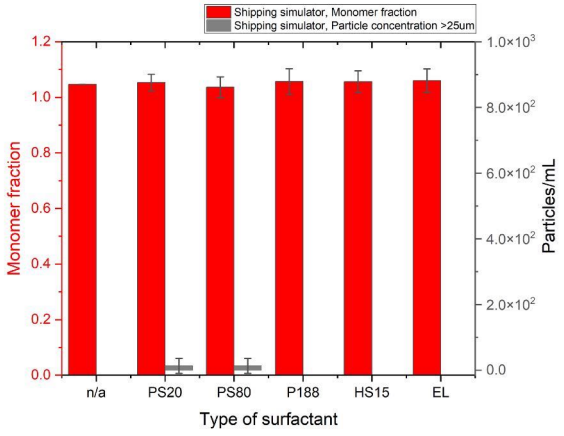

(c)

Figure 7.27: Correlation between monomer fraction and particle concentration data for a range of surfactant formulations including n/a, PS20, PS80, P188, HS15 and EL of MEDI3549 (0.5 mg/mL) in 235 mM Sucrose, 25 mM Histidine, pH=6, after exposure to shipping simulator. Particle concentration is presented for sized groups of 2-10 μm (7.27a), 10-25 μm (7.27b), and $>$ 25 μm (7.27c).

contributed the least particle concentration across the size groups of interest. As it is shown in figure 7.28 the particle concentration between the surfactant molecules lies within the same order of magnitude between the molecules for sized groups of 2-10 μm and $>$ 25 μm. Particle concentration for size group of 2-10 μm lies within the order of 10^5 and for particles with size of $>$ 25 μm, concentration lies within the order of 10^3. The significant difference between induced particle concentration corresponds to a difference of one order of magnitude, ranging from 10^4 to 10^5 for particles of 10-25 μm as shown in figure 7.28b. Based on the particle concentration for the specific size group, minimum particles were detected for PS20, PS80 and EL formulations.

For extensional flow conditions within silane B treated surface (figure 7.29), it was shown that the surfactant formulations have significant effects with difference of one order of magnitude on particle concentration for particle size groups of 10-25 μm, and $>$ 25 μm. Particle concentration has been detected to lie within the same order of magnitude for particles with size of 2-10 μm as shown in figure 7.29a. Specifically, for particles with size of 10-25 μm, the range of particle concentration between the surfactant formulations lies in the order of magnitudes between 10^4 and 10^5 (figure 7.29b), whereas for particles with size group of $>$ 25 μm particle size group ranges between 10^2 and 10^3 (figure 7.29c). Based on the monomer fraction data, the maximum surfactant monomer was detected for the formulations of PS20 and PS80 formulations. Combining the monomer fraction and particle concentration data, PS20 and PS80 formulations can be proposed as suitable formulation candidates.

7.4 Extensional flow device as a screening tool to identify effective formulation conditions

Following the work presented in the previous section, extensional flow device can contribute into an effective formulation tool. Extensional flow device, as shown in the previous section, allows the differentiation between surfactant molecules on the aggregation propensity and monomer fraction. However, their effects were investigated at the same surfactant concentration (0.02% w/v) which corresponds relative to the critical concentration CMC, in which they form micelles as previously summarised in table 5.6. Therefore, to get a better understanding about the association state in which surfactants can offer molecule stability against aggregation, the association state of surfactants will be explored in the current section. The effect of the association state can be investigated by the variation of proportionality between surfactant and protein molecule concentrations. Specifically, a schematic summarising the analysis framework followed for the conduction of the surfactant screening experiments is shown in figure 7.30. The analysis is based on MEDI8852 as the protein molecule, using the same surfactant library previously constructed (PS20, PS80, P188, HS15 and EL) for the analysis of flow induced aggregation of MEDI3549.

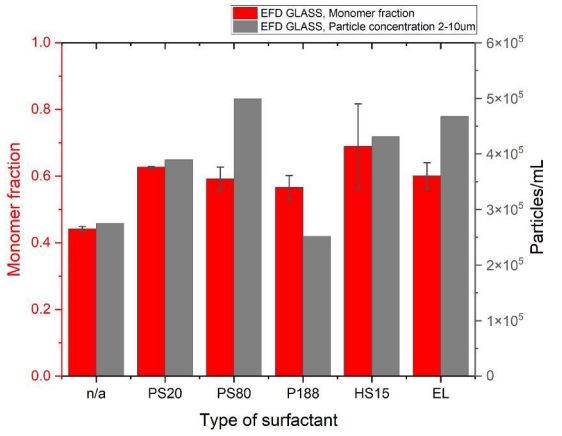

(a)

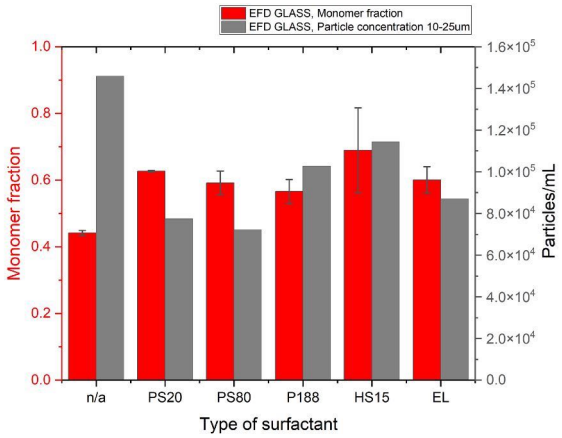

(b)

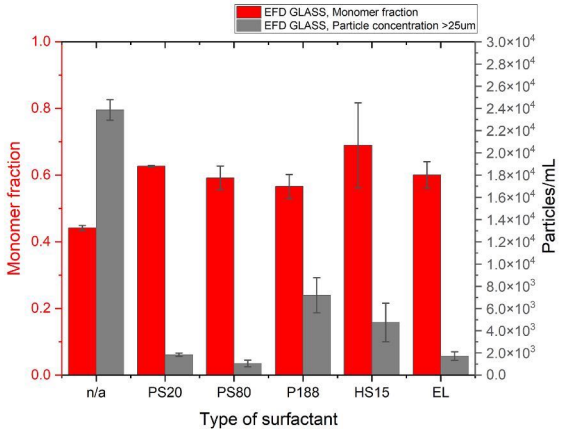

(c)

Figure 7.28: Correlation between monomer fraction and particle concentration data for a range of surfactant formulations including n/a, PS20, PS80, P188, HS15 and EL of MEDI3549 (0.5 mg/mL) in 235 mM Sucrose, 25 mM Histidine, pH=6, after exposure to extensional flow device for bare borosilicate glass surface. Particle concentration is presented for size groups of 2-10 μm (7.28a), 10-25 μm (7.28b) and $>$ 25 μm (7.28c).

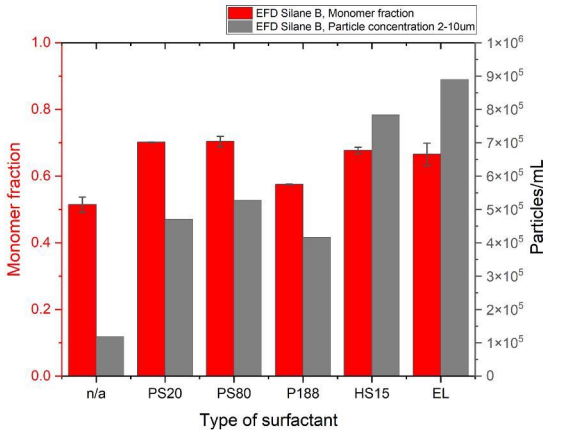

(a)

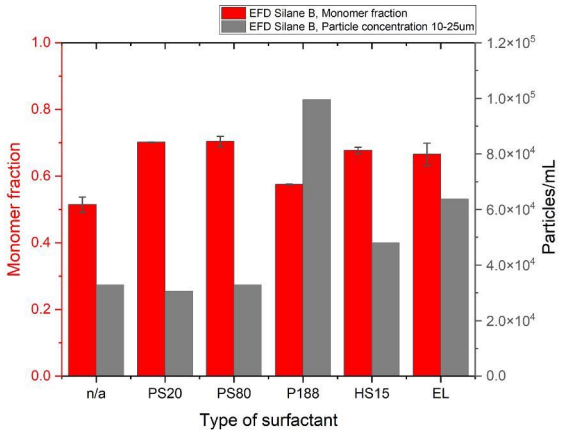

(b)

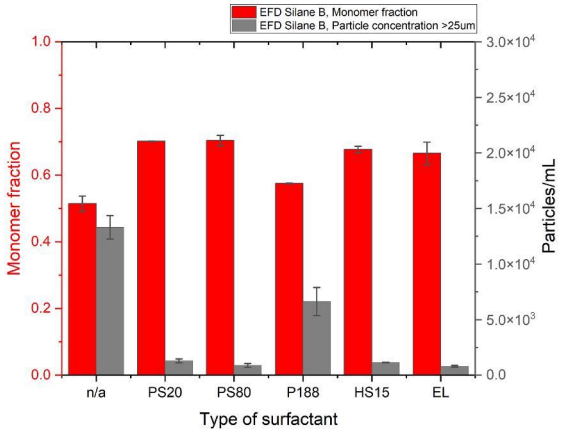

(c)

Figure 7.29: Correlation between monomer fraction and particle concentration data for a range of surfactant formulations including n/a, PS20, PS80, P188, HS15 and EL of MEDI3549 (0.5 mg/mL) in 235 mM Sucrose, 25 mM Histidine, pH=6, after exposure to extensional flow device for silane B treated surface. Particle concentration is presented for size groups of 2-10 μm (7.29a), 10-25 μm (7.29b) and $>$ 25 μm (7.29c).

The variation of surfactant concentration is then expressed as a ratio between and surfactant (S) and protein (P) molecules, at a constant protein concentration. The ratios of interest, correspond to various association states of surfactants including an excess state of protein molecules represented by 0.2:1 (S:P). This is followed by an equilibrium state corresponding to the equal proportion between surfactant and protein molecules, represented by a ratio of 1:1 (S:P). The last concentration of interest corresponds to the condition where the surfactant molecules are in excess compared to proteins, and the concentration is such that the surfactants are above their critical micelle concentration, represented by a ratio of >CMC:1 (S:P). As the focus of this set of experiments is the association state of surfactants, the surfaces of interaction (syringes, plungers, capillary) remained chemically unmodified using the standard glass surface (as received from the manufacturer) of the extensional flow device. Finally, the analysis of the stability of the molecule will be followed by the techniques of fluorescence spectroscopy, optical density and the pelleting assay. The overall aim of the current set of studies, is to investigate the surface activity of surfactants and extensional flow stability on MEDI8852 which is an IgG. Comparison between a range of surfactant molecules will be investigated mainly on the influence of surfactant concentrations (below and above CMC) at a constant protein concentration which is found to induce high aggregation levels (e.g. 0.5 mg/mL).

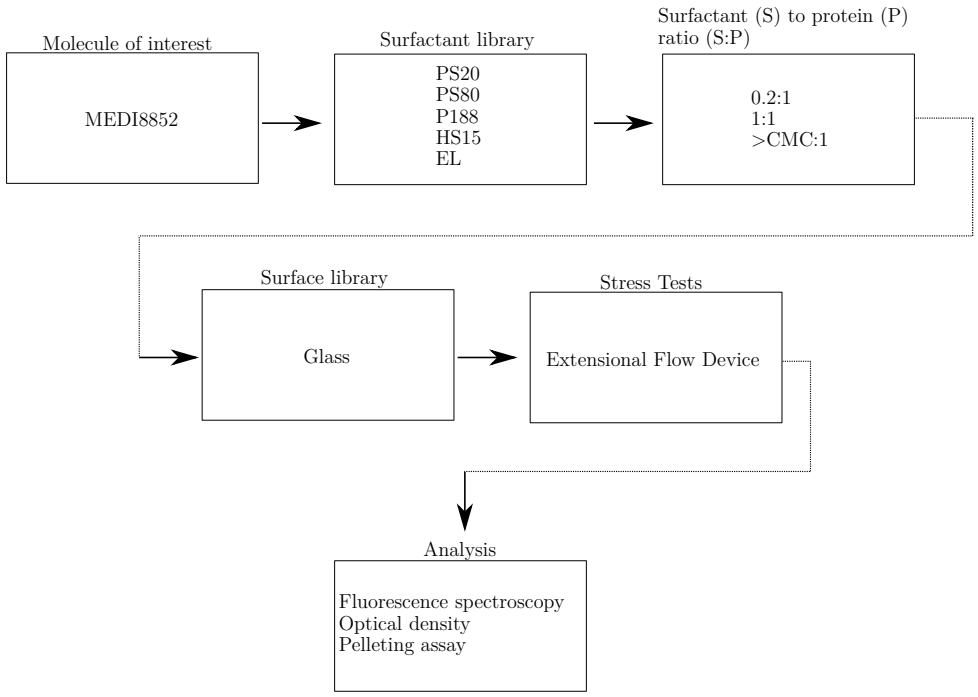

Figure 7.30: Experimental analysis framework followed for characterising the surfactant effect in flow induced aggregation of 0.5 mg/mL MEDI8852.

7.4.1 Experimental determination of critical micelle concentration, CMC

As the effect of the association state of surfactants is based on their tendency to form micelles, the experimental determination of the concentration in which they form micelles, is firstly investigated. Several techniques have been reported in literature as means to experimentally determine CMC, including surface tension, osmotic pressure, fluorescence, electrokinetic chromatography, calorimetry, light scattering, electron paramagnetic resonance and analytical ultracentrifugation [111]. Among these techniques, fluorescence was selected due to its higher sensitivity in detecting and quantifying analytes compared to most other techniques [293]. Therefore, fluorescence spectroscopy is conducted for the determination of CMC. Particularly, the indirect approach is followed, which involves the emission spectra of an added reporter, where its relative change is correlated with the surfactant concentration. The added reporter corresponds to a turn on probe, where turn on probes show weak emission in solutions before CMC but strong emission in micelles [293]. This will be translated into the increment of the fluorescence intensity of the probe, as the concentration of the added surfactant within the sample formulation also increases.

Fluorescence probe selection

ANS probe has been employed as the selected probe among several fluorescence probes that have been reported in literature including Pyrene, Fluorescein, Coumarin, Hoechst 33342, Curcumin, Acridine Orange, poly [2,5-di (propyloxysulfonate)-1,4-phenylene-ethynylene-9,10-anthrylene], 3-(benzoxazol-2-yl)-7-(N,N-diethylamino)chromen-2-one, and 4- [2- [6-(dioctylamino)-2-naphthalenyl]ethenyl]-1-(3-sulfopropyl)-pyridinium (di-8-ANEPPS) [293]. The use of ANS corresponds to a suitable fluorescence probe, and as it is described in [294] the CMC values determined with the particular probe, agree with the data reported in literature from other methods.

The selection of the suitable probe is critical for the possibility of the CMC evaluation based on the charge of the selected probe and surfactant molecule. Specifically, in the study conduced in [295], the authors proposed the use of the non-ionic ANS to be used with non-ionic surfactants. Based on their experiments, the authors showed that when the probe and surfactant carry the same charge, the fluorimetric titrations curves showed two straight lines. On the other hand, when the probe and surfactant have opposite charges, the titration curves present complex titration curves, not readily amendable for estimating the CMC. Therefore, the selection of the ANS probe is suitable, as all the surfactant molecules are non-ionic. ANS at a concentration of 40 μm has been used to experimentally determine the CMC of the surfactant library, allowing the comparison of the experimentally obtained critical concentrations with the critical concentrations reported

in literature. The ANS experiments will offer the determination of CMC experimentally, so as the effect of surfactant association state experiments can be conducted ensuring that the critical concentration is included to represent their association state where they can form micelles.

Fluorimentric titrations

Fluorimetric titrations of the surfactant molecules have been conducted at a concentration range of 0.001-0.1 mM as shown in figure 7.31. The critical concentration in which the surfactants form micelles is determined by the breakpoint in which the fluorescence intensity suddenly increases. It has been reported that the break point can be exhibited by the environmentally sensitive fluorescent probes, when the surfactant concentration reaches the CMC [296]. Below CMC, fluorescent probes exist mainly in an aqueous medium [296]. The CMC for each molecule is then determined by a linear fitting of the fluorescence emission spectra, upon excitation at 389 nm against the surfactant concentration. As it is shown in figure 7.31, two straight lines have been fitted through the experimental points for PS20, PS80, P188, HS15 and EL (figs. 7.31a to 7.31e), and their intersection is taken as the CMC, as also described in [296]. The highest CMC is shown to correspond to HS15, as shown in figure 7.31d, whereas the lowest corresponds to PS20 and PS80 as shown in figures 7.31a and 7.31b respectively.

Analytically, to allow the comparison between the CMCs in exact terms, the point of intersection of each surfactant is reported in table 7.3, alongside with their respective CMCs as reported in literature. Comparing the CMC as determined in the current work, with the work conducted in literature studies, it can be observed that there is a disparity between the values reported here and literature. This is expected, as the CMC experiments conducted in this work, have been performed in the desired formulation conditions required for the following up extensional flow experiments. In particular, the desired formulation buffer is 235 mM Sucrose, 25 mM Histidine, pH=6, whereas the conditions in which CMCs are reported in literature, are usually conducted in standard systems such as deionised water or PBS buffer. Moreover, the studies employed different strategies to determine the CMC; therefore this is another parameter that can explain the difference observed between the current work and literature. Additionally, for the case where the same technique is followed (fluorescence spectroscopy) the fluorescence probe used was different (Pyrene) than the probe used in the current work (ANS). This comparison highlights the importance and effect of the formulation buffer in which the surfactant micelles can be formed, as well the strategy selected for determining the CMC.

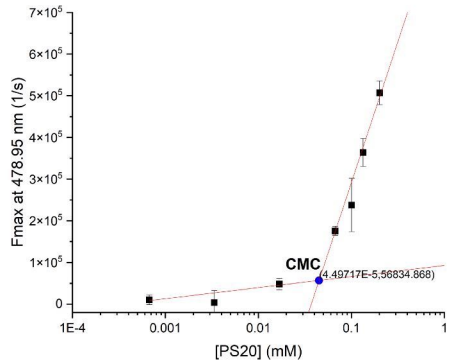

(a) PS20

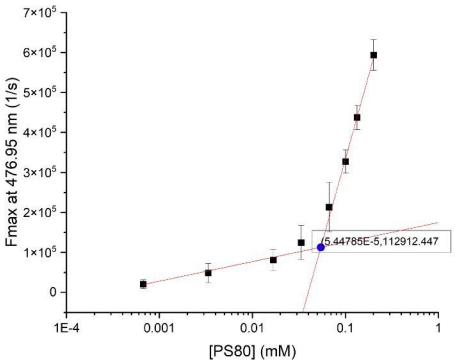

(b) PS80

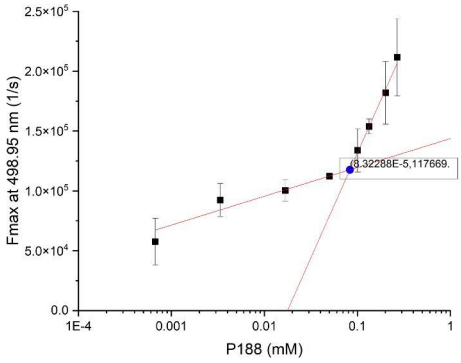

(c) P188

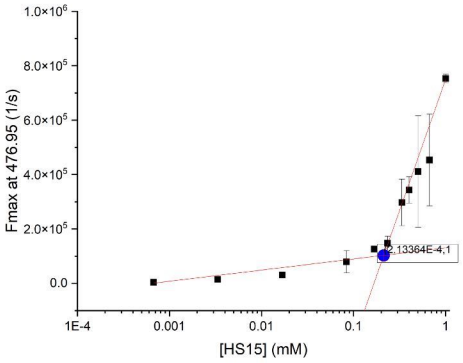

(d) HS15

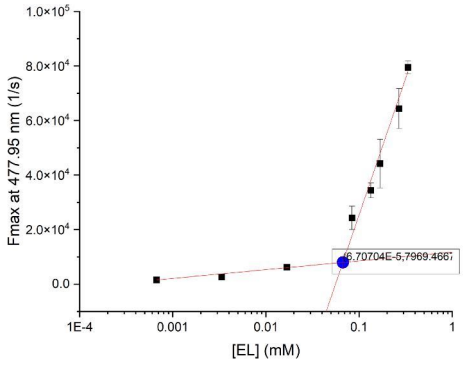

(e) EL

Figure 7.31: Fluorimetric titrations of 40 μM ANS with PS20 (7.31a), PS80 (7.31b), P188 (7.31c), HS15 (7.31d) and EL (7.31e). Different concentrations of PS20, PS80, P188, HS15 and EL (0.001 - 1 mM) were prepared in 235 mM Sucrose, 25 mM Histidine, pH=6, by dilution of a 10% w/v stock solution of PS20, PS80, P188, HS15 and EL respectively. The point of intersection between the fitted straight lines on the experimental data indicate the critical micelle concentration (CMC) of each surfactant molecule. Errors indicate the standard deviation between 3 sample repeats.

Table 7.3: CMC determined from the point of intersection between the fitted straight lines from the experimental data as taken from fluorimetric titrations of 40 μm ANS (figure 7.31), along with their respective CMCs as reported in literature. Point of intersection is determined using the Intersection Gadget in OriginPro.

Surfactant	CMC determined in the current work (mM)	CMC reported in literature (mM)
PS20	0.045	0.049 [296]
PS80	0.054	0.015 [111]
P188	0.083	0.04 [297]
HS15	0.213	0.06-0.1 [298]
EL	0.067	0.04 [299]

7.4.2 Effect of surfactant association state

As the CMCs have been determined, the association state of surfactants can be then explored in surfactant-protein ratio terms, so as to investigate the parameter of proportionality of surfactant molecules compared to the protein molecules. The aim of the current set of studies is to address various states between the molecules such as there is an excess in protein molecules, equivalence between protein and surfactant molecules and a state where there is an excess of surfactant molecules which is close or above its CMC. Analytically, the conversion of molarity to the desired surfactant to protein ratios was previously summarised in table 5.6. Specifically, the proportion ratios of 0.2:1 and 1:1 representing protein excess and equivalence, correspond to the same converted molar concentration for all the surfactant molecules. However, for the surfactant excess state, the experimentally determined CMC was taken into consideration for each surfactant molecule. This is required to include the state in which the surfactant molecules, which are in excess compared to the protein molecules, are also in their micelle formation state. Based on these requirements, surfactant, (S) to protein, (P) ratios (S:P) correspond to 0.2:1, 1:1 and >CMC:1 respectively.

Fluorescence spectroscopy, single peptide system - NATA

To understand the exclusive effect of surfactant binding in the presence and absence of extensional flow, NATA (N-Acetyl-L-tryptophanamide) is used as a simplified system. The experiments have been performed in the same formulation condition buffer as the one used for the conduction of the CMC experiments with the addition of 40 μM NATA in 235mM Sucrose, 25mM His, pH=6 which is the formulation buffer. Figure 7.32 shows the emission scans of NATA in the various surfactant to protein ratios as previously described. Based on the values summarised in the table 5.6, these ratios correspond to the molar concentrations of 0.67 and 3.35 μM for 0.2:1 (S:P) and 1:1 (S:P) ratios respectively. For the association state in which the surfactant molecule form micelles, the respective S:P ratio is accordingly determined and corresponds to molar concentrations of 67 μM - 20:1 (S:P) for PS20, 67 μM - 20:1 (S:P) for PS80, 134 μM - 40:1 (S:P) for P188, 335 μM - 100:1

(S:P) for HS15 and 83.8 μM - 25:1 (S:P) for EL (figs. 7.32b to 7.32f) and can be found analytically in table 5.6.

To firstly investigate the effect of different surfactant association states, in the absence of flow contributions, NATA was selected as the model system as it is providing a simplified protein structure and realistic model for Tryptophan (Trp) peptide which is found in proteins [93]. The use of NATA as a model system, applies to its single Trp as it is a single peptide. Therefore, its molecular weight is relative small ∼245 Da compared to the average molecule weight of antibody proteins ∼150 kDa. This simplified protein system will allow firstly to investigate whether the various association states of surfactants can affect the stability of the protein under quiescent conditions in the absence of extensional flow.

As shown in figure 7.32, all surfactant molecules, irrespective their association state, show an emission maximum at 350 nm which is the emission maximum that Trp exhibits. When Trp exhibits an emission maximum (λ_{max}) at 350 nm, this corresponds to the condition where it is completely exposed to water, i.e., a polar environment [93]. This will suggest that for the condition of a non-polar environment where micelles form, there is no interaction between the surfactant with the protein affecting the protein's conformational state as the emission maximum remains at 350 nm. It has been reported that the conformational changes in which the protein can be encountered are accompanied by changes in the local environment of the Trp residue [93]. The changes in the microenvironment of Trp which can consequently be encountered upon unfolding, can be reflected as a change in the intensity or the transition of the emission wavelength [93]. From the results presented here, it can be observed that the surfactant molecules investigated in their various association states can slightly affect the average Trp intensity for specific formulation conditions, including PS80, HS15 (with the least variation), and EL as seen from the variation in the Trp intensity, within the magnitude of error (figs. 7.32c, 7.32e and 7.32f). At increased surfactant concentrations, the intensity is decreased for PS80 and EL formulations (within error) (figs. 7.32c and 7.32f), whereas for PS20 and P188 formulation conditions, the Trp intensity remains stable at increased surfactant concentrations (figs. 7.32b and 7.32d). The data could suggest that under quiescent conditions (absence of flow), the conformational state of NATA can be conserved as the emission of Trp for all the surfactant formulations remains at 350 nm and the intensity remains constant within error, which is also comparable with the Trp emission wavelength in the absence of surfactant formulation (figure 7.32a).

Fluorescence spectroscopy, antibody system - MEDI8852

To further investigate the effect of the various association state of surfactants during the contribution of flow, extensional flow experiments were then conducted using MEDI8852 as model protein. As previously mentioned, the emission wavelength of Trp will shed light into possible conformation changes of the proteins under flow. From the fluorescence

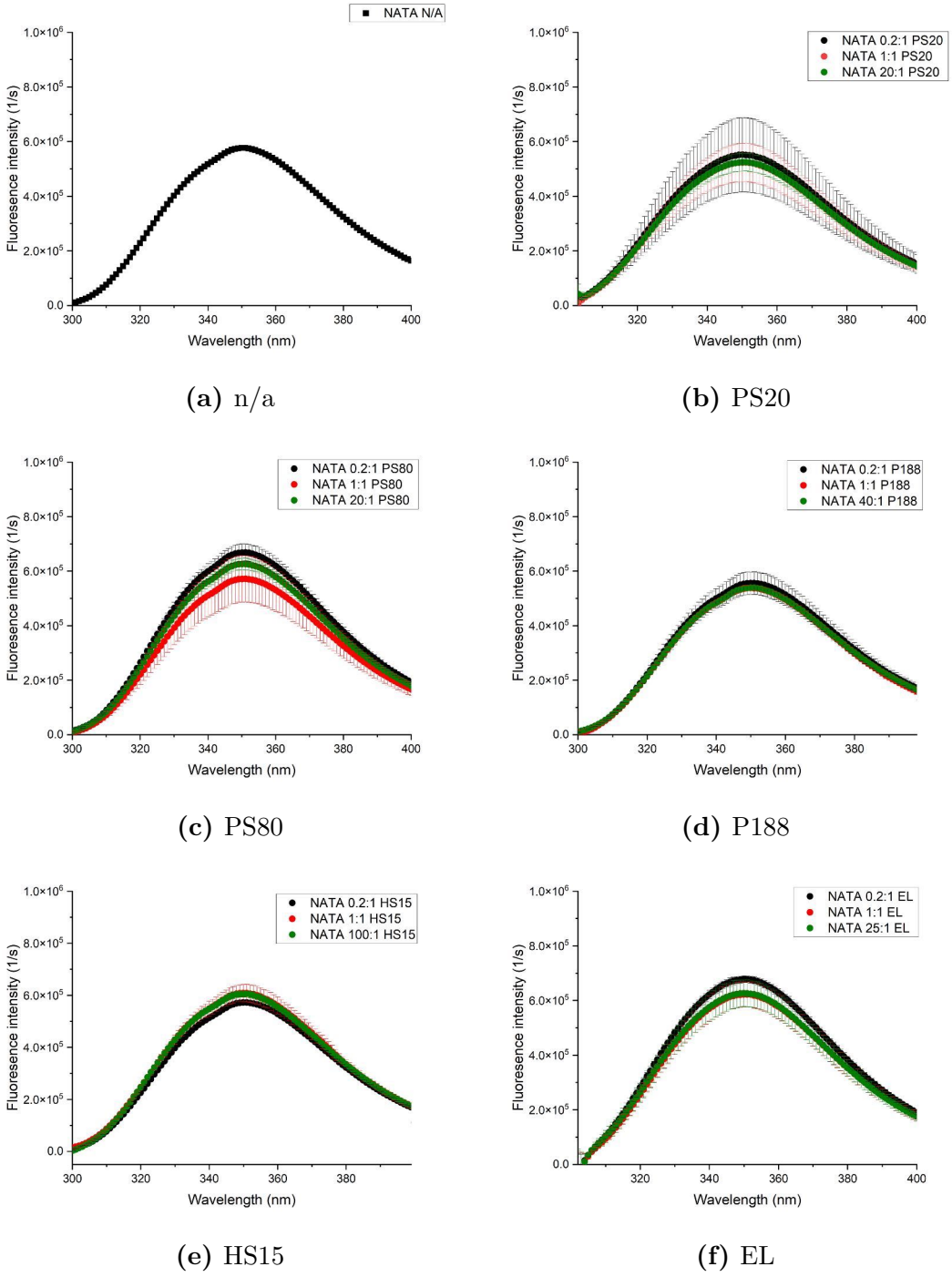

(a) n/a **(b)** PS20

(c) PS80 **(d)** P188

(e) HS15 **(f)** EL

Figure 7.32: Representative intrinsic tryptophan (Trp) fluorescence spectra of 40 μM NATA in formulations with the absence n/a (7.32a), and presence of surfactants PS20 (7.32b), PS80 (7.32c), P188 (7.32d), HS15 (7.32e) and EL (7.32f). The concentration series of surfactants were expressed as a surfactant (S) to protein (P) ratio (S:P), up to the ratio representing >CMC (0.2:1->CMC:1). The concentration series of surfactants were 0.2:1 (S:P), 1:1 (S:P) and >CMC:1 (S:P) ratios. The formulations were in the primary buffer of 235 mM Sucrose, 25 mM His at pH 6.0 under quiescent conditions (absence of extensional flow). The excitation wavelength is 295 nm. All spectra were measured in triplicates from formulations subtracted by the corresponding buffer blank. Errors indicate the standard deviation between two sample repeats.

experiments, the effect of surfactant molecules on the protein stability allows to be investigated based on the emission of Trp. Other techniques previously conducted such as pelleting assay, DLS, HPSEC and Horizon, all quantify the propensity for aggregation either qualitatively or quantitively; however, they do not provide any information about the effect of the desired parameters on the conformational state of the protein. As the project addresses the encounter of flow into the biological manufacture of protein-based pharmaceuticals, the parameter of protein stability is desired. From a formulation perspective of view, the surfactant screening, examining their effect on the protein stability will allow the selection of suitable formulation candidates that will offer the desired molecule stability.

Based on the results presented above, the range of surfactant association states did not contribute to the instability of NATA based on the expected emission of NATA at ∼350 nm. However, when a more complicated system is considered; represented by that of a protein, the emission spectra of Trp vary compared to that of NATA as shown in figure 7.33. Firstly, it can be observed that the Trp emission occurs at shorter wavelengths such as ∼323-326 nm compared to the ∼350 nm of NATA. The blue-shifted emission of Trp which corresponds to the emission at shorter wavelength, emitted when MEDI8852 is considered, agrees with data reported in literature. In particular, in the study conducted in [300], the maximum emission of Ovalbumin Trp was reported at ∼330 nm and the maximum emission of two IgG1 monoclonal antibodies was reported at ∼328 and ∼330 nm as shown in [95]. This blue-shifted emission of Trp indicates that the tryptophan residue is buried in a hydrophobic environment within the protein [300]. As reported in [93], the maximum emission wavelength at 330 nm corresponds to spectral class I of Trp which is observed when it lies in a relatively polar but a rigid environment. This contradicts with the red-shifted emission at longer wavelengths of that of NATA with longer emission maximum at ∼350 nm corresponding to spectral class III indicating the protein contact with free water molecules. The particular spectral class also represents a typical condition for the unfolded state of proteins [93]. Additional to spectral classes I and III, spectral class II corresponds to Trp which lies on the protein surface and is exposed to water (bound water) and other polar groups, exhibiting a maximum wavelength around 340 nm [93]. Apart from the emission maximum observed, the emission spectra of MEDI8852 show to differ when the molecule is exposed to flow. When the sample is exposed to extensional flow, a red-shift is shown from ∼323 nm (control incubated in bench) and ∼324 nm (control incubated in syringe and capillary bodies) to ∼326 nm, corresponding to 3 nm wavelength range.

Additionally, at the extensional flow condition, the appearance of a shoulder at 300 nm is observed, compared to the quiescent condition samples, corresponding to sample incubation in bench and device equipment surface bodies, for a surfactant-free formulation condition as shown in figure 7.33. The analysis of a surfactant-free formulation allows to firstly build

an understanding of the unfolded state of the protein compared to its respective controls, enabling the incorporation of surfactant into the protein formulation to be investigated and compared. Additional to the variation in the emission wavelength, variation in the intensity of fluorescence emitted is observed, indicating higher fluorescence intensity for the sample incubated in the bench compared to the respective control sample incubated within syringe bodies and sample exposed to the extensional flow. In particular, a decrease in fluorescence intensity can be observed for the samples incubated within the syringe bodies as shown in red and for samples exposed to flow as shown in blue (figure 7.33). The decrease in fluorescence intensity in spectral class I, is correlated with the unfolding event of protein, as proposed in [93]. Therefore, this will suggest that the conformation state of the protein is also affected during its incubation within the equipment surface bodies, indicating the contribution of the surface on protein's structure. This phenomenon has been observed from previous experiments, indicating low levels of aggregation ∼10-20 % for the condition in which the protein is incubated in syringe and capillary bodies (CS). This highlights the sensitivity of protein's structure during its contact with surfaces, which can vary to several such as glass to aluminium to plastic to name a few, throughout the production line.

Additionally, the exposure of the protein to flow induces its structure perturbation, as indicated by a decrease in fluorescence. However, the link between fluorescence intensity and unfolding is reported to be protein-dependent. Specifically, as reported in [301], the emission of tryptophan is highly quenched suggesting fluorescence decrease in the native state of protein (e.g., heme proteins) with the protein unfolding inducing increase in the fluorescence intensity. However, the opposite observation is reported for other proteins including staphylococcal nuclease, where the tryptophan has a relatively high quantum yield, emitting strong fluorescence in the native state, whereas its fluorescence is efficiently quenched, inducing fluorescence decrease in the unfolded state [301].

As the unfolding of the particular protein is firstly characterised in a surfactant-free formulation condition, the surfactant screening using the extensional flow device as a tool is followed. The aim of the particular set of experiments was firstly to identify the role of the different association states of surfactants and secondly identify which surfactant molecules preserve the conformational state of the model protein (MEDI8852) when exposed to flow. As previously described, the variation of surfactant association states is conducted by varying the surfactant (S) to protein (P) ratio (S:P). Three surfactant association states are investigated, with the first corresponding to conditions in which the protein molecules are in excess compared to protein, with the corresponding surfactant to protein ratio of 0.2:1 (S:P). The second corresponds to the condition where there is an equal amount of surfactant and protein molecules corresponding to a ratio of 1:1, whereas the third association state corresponds to the condition where surfactants form micelles based on their CMC, such as the surfactant to protein ratio corresponds to >CMC:1

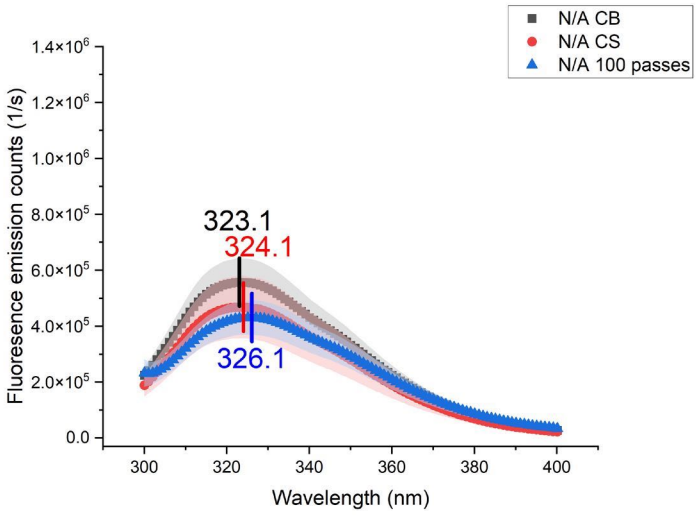

Figure 7.33: Representative intrinsic tryptophan (Trp) fluorescence spectra of 0.5 mg/mL MEDI8852 quiescent, sample incubated in bench CB (shown in black), control left in syringe, sample incubated in untreated glass syringe and capillary bodies (CS) (red), under flow for 100 passes at 8 mm/s (100P) (blue) in the absence of surfactant formulation n/a.) The formulation was in the primary buffer of 235 mM Sucrose, 25 mM His at pH 6.0. The excitation wavelength is 295 nm. All spectra were measured in triplicates from formulations subtracted by the corresponding buffer blank. N=3, area under curve=sd. The wavelength at the maximum peak of the emission spectra for each sample is indicated using the Peak Analyzer in OriginPro.

(S:P). The emission scans of tryptophan for each association state for the surfactant library molecules is shown in figure 7.34. A big variation between the samples can be observed at particular concentrations, which are indicated by the areas under the curves. This variation in results can be explained due to the manual setting of slit widths in the instrument, which is required for the conduction of the experiments. Therefore, the results are compared and analysed based on their average fluorescence intensity and emission wavelength values. As shown in figures 7.34a, 7.34b and 7.34c the different association states of surfactants are shown to affect the fluorescence intensity of the tryptophan to different extents depending on the association state of the surfactant. Based on the previous observation for the surfactant-free formulation condition, the intensity is shown to decrease for samples incubated within the syringe and capillary bodies and samples exposed to the extensional flow device.

The same effect is shown for all PS20 ratios explored, indicating higher fluorescence intensity for quiescent control samples. Interestingly, among the three association states explored, in the protein excess state (figure 7.34a) the variation between fluorescence intensity between the control and flow samples is less when compared to the surfactant to protein ratios (S:P) of 1:1 and >CMC:1 (figures 7.34b and 7.34c). This will suggest that the least variation between the emission of the fluorescence of tryptophan induces the least conformational perturbation on the protein, suggesting that the association state

of surfactants is important for preserving the protein structure. This also suggests that the surfactant concentration can be more effective at a lower concentration than the CMC of PS20, based on the least variation of the tryptophan emission (figure 7.34a).

On the other hand, it is shown that the structural conformation of the protein can be conserved for the condition where the surfactant molecules form micelles as shown in figure 7.34f using PS80 as a formulation agent compared to the lower concentrations (figures 7.34d and 7.34e), suggesting that the effectiveness of the particular surfactant is defined by the condition in which there is micelle formation. The enhanced stability of the molecule at the condition where there is a micelle formation, is indicated by the overlapping of the fluorescence spectra between the three samples. This is also indicated by the minimum wavelength shift between quiescent and samples exposed to the extensional flow, with wavelength shift in a range of 1 nm (7.34f) compared to 3 nm for the surfactant-free formulation condition (7.33).

For formulations using P188 as the surfactant agent, it is also shown that the association state of the surfactant matters on maintaining protein's conformational state. Higher tryptophan fluorescence variations are observed for surfactant to protein ratios corresponding to 0.2:1 and 40:1 (S:P) as shown in figures 7.34g and 7.34i respectively. Interestingly, minimum variation in the tryptophan intensity is observed for the condition where there is an equal proportionality between surfactant and protein molecules 1:1 (S:P) as shown in figure 7.34h.

For HS15 formulations, the condition in which the particular surfactant forms micelles with a surfactant to protein ratio of 100:1 (S:P), corresponds to the condition where the protein conformation is conserved. This is shown from the overlapping of fluorescence intensity of tryptophan between the samples incubated in the bench and within the syringe and capillary bodies, as shown in figure 7.34l, compared to surfactant to protein ratios of 0.2:1 and 1:1 HS15 as shown in figures 7.34j and 7.34k respectively. Additionally, the enhancement of the protein structure at the particular concentration of HS15 (figure 7.34l), is shown by the fact that the wavelength of the maximum fluorescence intensity is shifted only to 1 nm compared to 3 nm for the condition of surfactant free formulation (figure 7.33).

Lastly, for EL formulations the variation between the tryptophan intensity is shown for all the surfactant to protein ratios as shown in figures 7.34m, 7.34n and 7.34o respectively, following the same observation shown previously. The control sample incubated in the bench inducing higher fluorescence intensity with respect to samples incubated in syringe and samples exposed to extensional flow. Particularly, for the lowest surfactant to protein ratio, the biggest variation between tryptophan intensity is shown (figure 7.34m) indicating compared to the remaining ratios investigated.

Overall, the results suggest that the proportionality between surfactant and protein

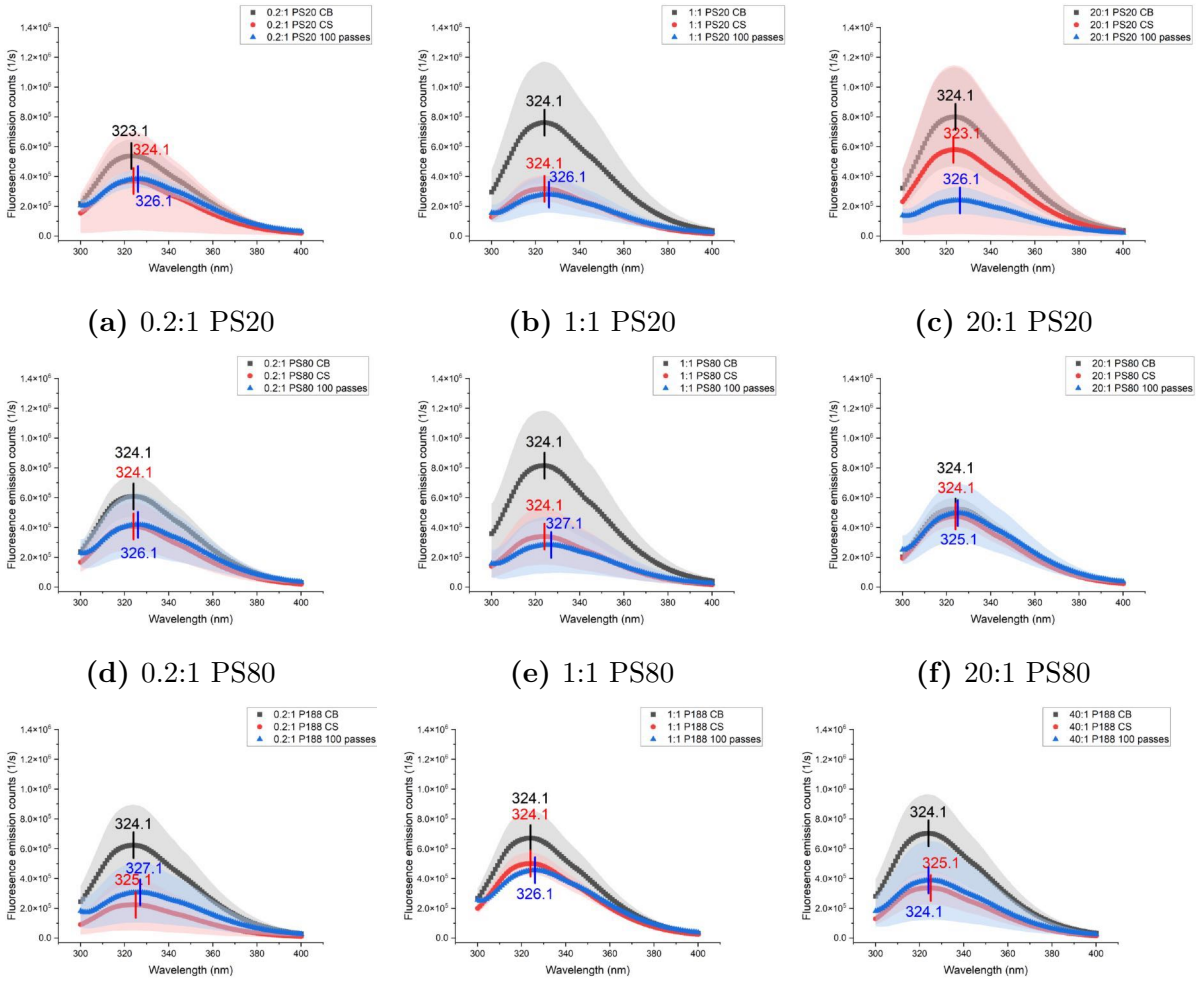

(a) 0.2:1 PS20 **(b)** 1:1 PS20 **(c)** 20:1 PS20

(d) 0.2:1 PS80 **(e)** 1:1 PS80 **(f)** 20:1 PS80

(g) 0.2:1 P188 **(h)** 1:1 P188 **(i)** 40:1 P188

Figure 7.34: Representative intrinsic tryptophan (Trp) fluorescence spectra of 0.5 mg/mL MEDI8852 quiescent, sample incubated in bench (CB shown in black), control left in syringe, sample incubated in untreated glass syringe and capillary bodies (CS, red), under flow for 100 passes at 8 mm/s (100P, blue) in the presence of surfactant formulations with PS20 (7.34a, 7.34b, 7.34c), PS80 (7.34d, 7.34e, 7.34f), P188 (7.34g, 7.34h, 7.34i), HS15 (7.34j, 7.34k, 7.34l) and EL (7.34m, 7.34n, 7.34o). The concentration series of surfactants, were expressed as a surfactant (S) to protein (P) ratio (S:P), up to the ratio representing CMC (0.2:1->CMC:1). The concentration series of surfactants were 0.2:1 (S:P), 1:1 (S:P) and >CMC:1 (S:P) ratios. The formulations were in the primary buffer of 235 mM Sucrose, 25 mM His at pH 6.0. The excitation wavelength is 295 nm. All spectra were measured in triplicates from formulations subtracted by the corresponding buffer blank. N=3, area under curve=sd. The wavelength at the maximum peak of the emission spectra for each sample is indicated using the Peak Analyzer in OriginPro.

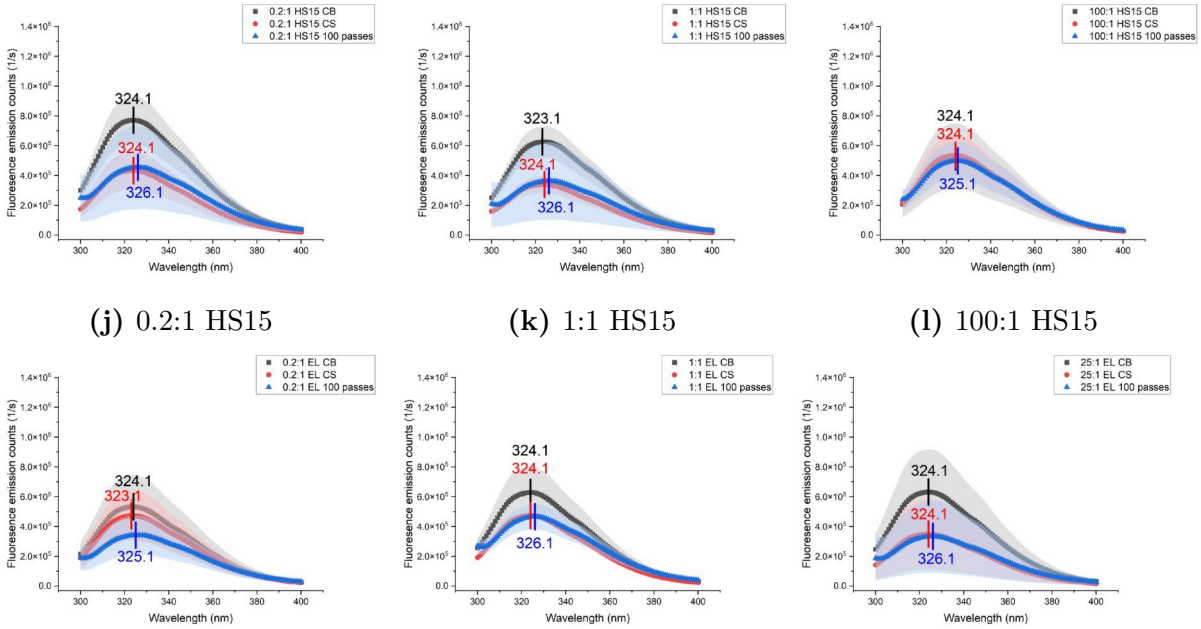

(j) 0.2:1 HS15 **(k)** 1:1 HS15 **(l)** 100:1 HS15

(m) 0.2:1 EL **(n)** 1:1 EL **(o)** 25:1 EL

Figure 7.34: Representative intrinsic tryptophan (Trp) fluorescence spectra of 0.5 mg/mL MEDI8852 quiescent, sample incubated in bench (CB shown in black), control left in syringe, sample incubated in untreated glass syringe and capillary bodies (CS, red), under flow for 100 passes at 8 mm/s (100P, blue) in the presence of surfactant formulations with PS20 (7.34a, 7.34b, 7.34c), PS80 (7.34d, 7.34e, 7.34f), P188 (7.34g, 7.34h, 7.34i), HS15 (7.34j, 7.34k, 7.34l) and EL (7.34m, 7.34n, 7.34o). The concentration series of surfactants were expressed as a surfactant (S) to protein (P) ratio (S:P), up to the ratio representing >CMC (0.2:1->CMC:1). The concentration series of surfactants were 0.2:1 (S:P), 1:1 (S:P) and >CMC:1 (S:P) ratios. The formulations were in the primary buffer of 235 mM Sucrose, 25 mM His at pH 6.0. The excitation wavelength is 295 nm. All spectra were measured in triplicates from formulations subtracted by the corresponding buffer blank. N=3, area under curve=sd. The wavelength at the maximum peak of the emission spectra for each sample is indicated using the Peak Analyzer in OriginPro. (cont.)

molecules, has a significant effect on the conformational stability of the protein, in quiescent and flow conditions. It was also shown that potential perturbation on protein's structure can be observed when the sample is incubated within the syringe and capillary surface bodies, suggesting the effect of protein-surface interactions is present in the absence of flow (at least to some extent). The enhancement and conservation of protein's conformational state is shown to be reached by the application of particular surfactant formulations in the concentration in which they form micelles. Particularly, among the surfactant library investigated, PS80 and HS15 surfactants, indicated the maximum molecule stability based on the emission of the protein's tryptophan by conserving the intensity of the tryptophan among the quiescent and flow conditions. Interestingly, the desired effect of the protein molecule is reached when the surfactant molecules associate into micelles, by the respective surfactant to protein ratios corresponding to 20:1 (S:P) for PS80 and 100:1 (S:P) for HS15 formulations as shown in figures 7.34f and 7.34l respectively.

Overall, the data indicates the importance of surfactant to protein ratio into the enhancement of protein stability under extensional flow. The criteria for determining the suitable formulation candidates were based on the fluorescence intensity changes as well as on the emission wavelength. Based on this set of requirements, the suitable candidates enhancing molecule stability, correspond to PS80 and HS15 formulations, at the condition where they are in excess in proportionality compared to the protein molecules, forming micelles. As shown in figures 7.34f and 7.34l, PS80 and HS15 formulations with a surfactant to protein ratio of 20:1 (S:P) and 100:1 (S:P) respectively, minimum changes in fluorescence intensity and wavelength shifts are observed, indicating the maximum stability among the concentrations investigated.

The enhancement of molecule stability at increased surfactant concentrations is also shown in the study conducted in [95], highlighting that the protein stability depends on the type and concentration of both surfactants and protein molecules. However, the authors concluded that the stabilising effects of the surfactant library investigated, relied on their absolute concentrations, and the concentration does not have to be above their CMC. This contradicts with the findings of the current study, indicating that specific surfactant formulations provided the enhancement of the molecule stability at concentrations close or above their CMC. The conflict between the current study and literature findings can be relied on the CMC values which were taken as a reference for the conduction of the surfactant screening experiments. Particularly, the authors based their findings relative to the CMC values as reported in other literature studies conducted in water, whereas their experiments were performed in 20 mM HisHCl at pH 6.0. The majority of the CMC values, as reported in literature, corresponds to data determined in pure water; however, it is known that the presence of protein in the formulation can affect the corresponding CMC. This highlights the need to confirm the CMC at the desired formulation conditions of the experiment. In the current study, the CMC values have been determined experimentally

under the same formulation buffer as the flow experiments, in 235 mM Sucrose, 25 mM Histidine, pH=6, confirming that CMC. Therefore, the findings conducted in the current study are objective and based on the desired buffer formulation.

Optical density

To determine the effect of the surfactant library on the overall aggregation profile of the molecule, additional techniques can be combined to allow a conclusive overview of the surfactant formulation. Optical density experiments were performed investigating the aggregation propensity of the molecule through wavelength excitation at 350 nm, indicating the turbidity of the samples as shown in figure 7.35. Turbidity technique is commonly applied (among others) for the investigation of mAbs stability studies, as reviewed in [9]. The report of opalescence solutions is conducted based on the European Pharmacopeia reference suspensions measured photometrically in the wavelength range of 340-360 and 350 nm [13]. Generally, the analysis of turbidity measurements, is performed at 350 nm as the desired wavelength, as the sensitivity required for turbidity detection is higher at lower wavelengths [13]. Optical density, which is also called turbidity or opalescence, can be described as a cloudy-white translucent appearance for opalescence and a cloudiness of fluids as turbidity caused by individual particles consisting of various sizes [13]. The analysis of samples through turbidity measurements is also reported in the European Pharmacopeia as a complementary method required for the overview characterisation of uniform opalescent solutions [13]. Protein aggregation is correlated with the turbidity, as it has been reported that increase in turbidity is induced by aggregation over storage or stress conditions [13]. Optical density can also be investigated through visual inspection strategies, as previously presented, comparing the aggregation induced by the shipping simulator and extensional flow device. However, visual inspection can be also conducted based on arithmetic values indicating the optical density of the samples, allowing the comparison between quiescent (control) and stressed samples with various surfactant formulations, based on actual numerical values. As a complementary analysis along with visual inspection, turbidity measurements present the visual information, which indicate that higher absorbance values at 350 nm correspond to solutions that appear more opalescent to the eye [48].

As it is shown in figure 7.35, the optical density values of quiescent samples correspond to $\sim$0 indicating the absence of particles. However, when the samples are exposed to the extensional flow device the optical density values are increased, indicating protein aggregation. Analytically, PS20 formulations as it is shown in figure 7.35a, indicated maximum average value of optical density corresponding to surfactant to protein ratios (S:P) of 1:1 and 20:1 respectively, reaching an average optical density value of $\sim$0.20 compared to surfactant-free and 0.2:1 formulations reaching $\sim$0.15. The range of the detected optical density data lie within the turbidity data analysis detected from samples

during the filtration process of the biopharmaceutical production and particularly during diafiltration in the presence of excipient, reaching a turbidity value of 0.166 and during ultrafiltration in the absence of excipient reaching a turbidity value of 0.2 as shown in [48] which is close to the maximum value detected from the extensional flow experiments. This suggests that the molecule quality as characterised in the current study can be correlated and compared with the quality of products throughout the purification process of the biopharmaceutical production.

The slight increase in the optical density of higher surfactant concentrations can be linked with the previous observation of MEDI3549, where the particle concentration of the samples was increased with the addition of surfactants in the formulation. For the remaining surfactant formulations of PS80, P188, HS15 and EL (figs. 7.35b to 7.35e) similar levels of optical density values were detected among the various association states of surfactant molecules. This indicates that the optical density experiments do not bring additional quantitative information about the effects of each surfactant on the aggregation propensity. However, the aggregation propensity of all the formulation conditions was determined between control and samples exposed to the extensional flow, indicating that the aggregation propensity is linked with the increase in optical density.

The optical density results qualitatively show the significance of the extensional flow, they could not provide any further insights into the specific effects of surfactants and their corresponding association states (S:P ratios) on the overall aggregation propensity.

Pelleting assay

To investigate the effect quantitatively, pelleting assay experiments were performed to investigate the aggregation propensity of the molecule. As the addition of surfactant into the solution formulation induced the increment of particles (size group of 2-10 μm) when exposed to the extensional flow device, final results obtained from the pelleting assay have been modified accordingly. The increase in particle concentration for the particular size group of 2-10 μm as seen in table 7.2, correlates with the addition of surfactants into the protein formulation when samples were exposed to the extensional flow device. Therefore, potential increase in particles can accumulate in the pellet of the sample after completing ultracentrifugation, with the results to include the addition of surfactant particles and not protein aggregated particles. The modification of the results correspond to a final ratio of supernatant, which has been determined by normalising the amount of supernatant of each sample by its corresponding control incubated in the bench. The increase in supernatant ratio corresponds to the minimum aggregation propensity of the sample and vice versa.

The overall supernatant ratio results are shown in figure 7.36 corresponding to the range of the surfactant library molecules along with the respective surfactant-free formulation.

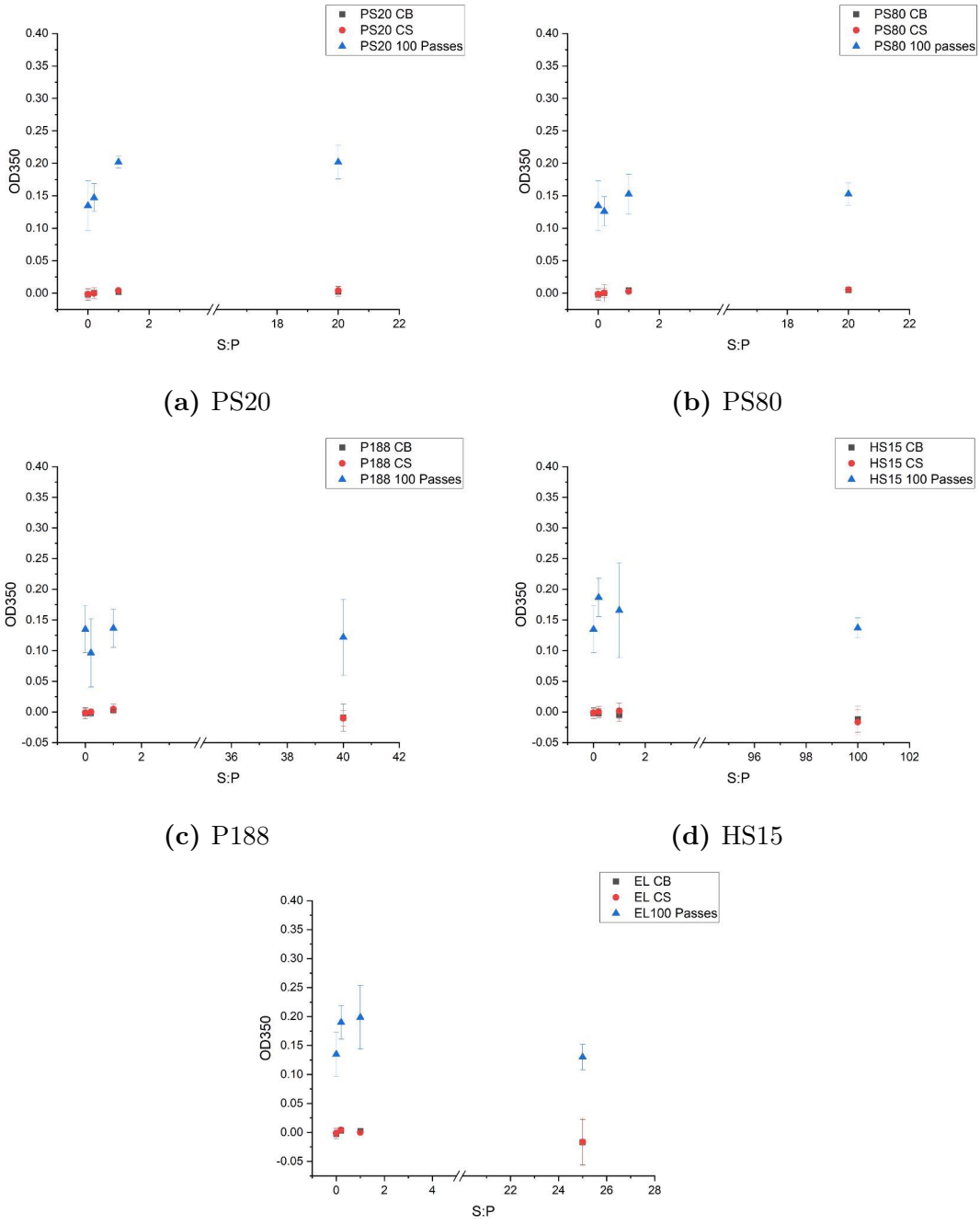

(a) PS20 **(b)** PS80

(c) P188 **(d)** HS15

(e) EL

Figure 7.35: Optical density data, excited at 350 nm (OD350) of 0.5 mg/mL MEDI8852 quiescent, sample incubated in bench (CB shown in black), control left in syringe, sample incubated in untreated glass syringe and capillary bodies (CS, red), under flow for 100 passes at 8 mm/s (100P, blue) in the absence (0), and presence of surfactant formulations with PS20 (7.35a), PS80 (7.35b), P188 (7.35c), HS15 (7.35d) and EL (7.35e). The concentration series of surfactants, (S) were expressed as a surfactant to protein ratio (S:P) up to the ratio representing >CMC (0.2:1->CMC). The formulations were in the primary buffer of 235 mM Sucrose, 25 mM His at pH 6.0 under quiescent conditions (absence of extensional flow). All optical density data were measured in duplicates from formulations subtracted by the corresponding buffer blank. Errors indicate the standard deviation between three sample repeats.

As it is shown in figure 7.36a, the supernatant ratio is shown to increase with increased surfactant to protein ratios specifically for 1:1 and to the state of micelles formation 20:1 indicating the suppression of protein aggregation, reaching an average supernatant ratio of ∼0.8 compared to ∼0.6 for surfactant-free formations and protein excess formulation conditions (0.2:1).

A similar observation is shown for PS80 formulation, indicating the enhancement of molecule stability at the state in which micelles are formed, as shown in figure 7.36b, reaching an average supernatant ratio of ∼0.75. Interestingly, for P188 formulations as shown in figure 7.36c, the maximum supernatant ratio of ∼0.8 is shown to be reached for the condition where surfactant and protein molecules are in equilibrium state (1:1), highlighting the effect of the association state of surfactants into the overall aggregation propensity of the molecule.

On the other hand, for HS15 formulations, as shown in figure 7.36d, the maximum average supernatant ratio corresponds to ∼0.85 at the micelle formation state for surfactant to protein ratio corresponding to 100:1 which is shown to correspond with the maximum average supernatant ratio among all the surfactant candidates investigated.

Lastly, for EL formulations as shown in figure 7.36e, the maximum supernatant ratio is determined at the condition where there is an equilibrium between surfactant and protein molecules (1:1) reaching a maximum supernatant ratio of ∼0.8, whereas no significant effect on the suppression of aggregation was shown for 0.2:1 and 25:1 surfactant to protein ratios.

Overall, it was shown that the association state of the surfactant in which offers the maximum suppression in protein aggregation significantly depends on the choice of surfactant. The maximum supernatant ratio was shown to correspond for PS20 (20:1), PS80 (20:1), and HS15 (100:1) formulations (micelle state). On the other hand, maximum supernatant ratios were determined at the equilibrium state for P188 and EL formulations between surfactant and protein molecules (1:1). This set of data highlights the significance of the ratio between surfactant and protein molecules, on enhancing the molecule stability under flow. Depending on the surfactant molecule, the association state in which the aggregation of the protein is suppressed, varies accordingly.

Combining the data obtained from the pelleting assay and fluorescence experiments (investigated in untreated surfaces of the extensional flow device), specific surfactant formulations can be suggested as protective in terms of enhanced stability in protein structure and aggregation suppression under flow. The conformational state of MEDI8852 is conserved under flow for PS80 (20:1) and HS15 (100:1) formulations which also suppress the aggregation under flow as seen by the increased supernatant ratio values, at the condition in which they form micelles.

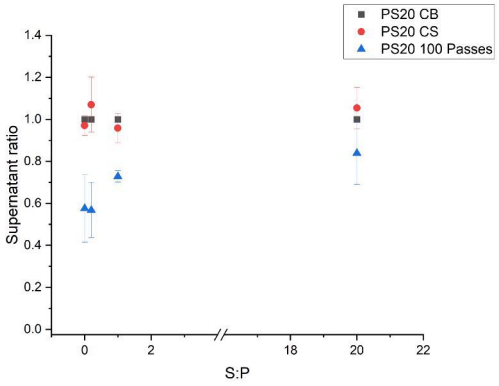

(a) PS20

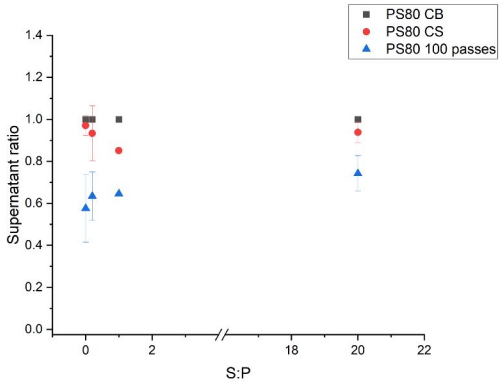

(b) PS80

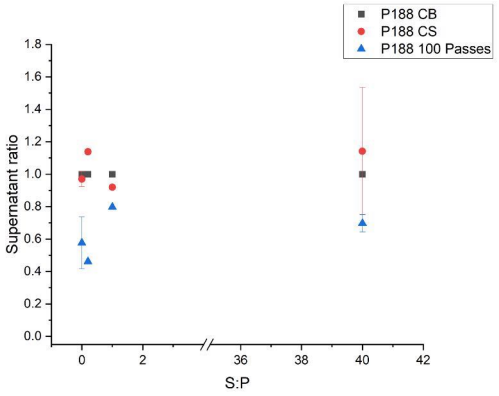

(c) P188

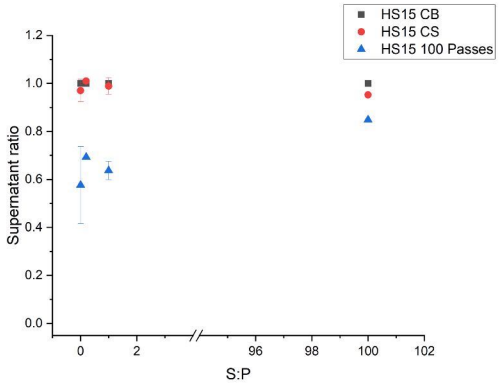

(d) HS15

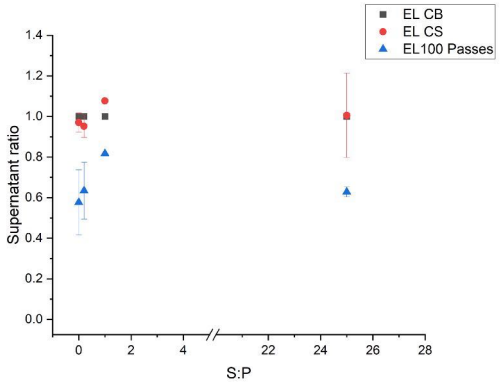

(e) EL

Figure 7.36: Supernatant ratio of 0.5 mg/mL MEDI8852 quiescent, sample incubated in bench (CB shown in black), control left in syringe, sample incubated in untreated glass syringe and capillary bodies (CS, red), under flow for 100 passes at 8 mm/s (100P, blue) in the absence (0) presence of surfactant formulations with PS20 (7.36a), PS80 (7.36b), P188 (7.36c), HS15 (7.36d) and EL (7.36e). The concentration series of surfactants, (S) were expressed as a surfactant to protein ratio (S:P) up to the ratio representing >CMC (0.2:1->CMC). The formulations were in the primary buffer of 235 mM Sucrose, 25 mM His at pH 6.0 under quiescent conditions (absence of extensional flow). All optical density data were measured in duplicates from formulations subtracted by the corresponding buffer blank. Errors indicate the standard deviation between two or three sample repeats. Samples with no error bar indicate the data from one sample, taken as the average from three repetitive repeats of the same sample population.

7.5 Summary

The particular chapter investigated the formulation properties of two molecules of interest and their characterisation in the absence and presence of flow conditions. Initially, the molecules have been characterised rheologically at higher protein formulations, which lie within the reported range of dose requirements of biopharmaceuticals. From the computational characterisation, it was shown that these highly concentrated molecules exhibit structural rearrangements (shear thinning effect) under shear flow. Additionally, with the application of a theoretical method, highly concentrated molecules affected the development of flow, affecting the shear rate, velocity and strain rate profiles of the molecules during their exposure to the extensional flow. The work conducted in the current chapter was expanded from the findings reported in chapter 6, where silane B surface was found to enhance the stability of the molecules at various flow conditions. The extensional flow device corresponds to a powerful technique for surfactant screening studies and identifying the suitable formulation candidates, depending on the flow conditions. The surfactant library involved the investigation of novel surfactant molecules (HS15, EL), where their application has not been well characterised in biopharmaceuticals. The application of these molecules was investigated in the context of shipping and manufacturing conditions, involving several studies at shipping conditions in air and truck levels (with the use of a shipping simulator) as well as during manufacturing (with the use of the extensional flow device).

The combined effects of solid and liquid interfaces were investigated, to determine the conditions where the maximum stability of the molecules can be achieved. This involved the synergistic effects of silane B surface and surfactant molecules. Moreover, the aggregation analysis involved several analytical techniques including the particle concentration, monomer fraction, visual inspection, turbidity, fluorescence spectroscopy and pelleting assay. The overall characterisation of the aggregation and the selection of suitable formulation conditions was evaluated by this plethora of techniques. From the results it was also shown that the suitable formulation candidates depend on a range of parameters including the type of flow, model protein as well as the surface of interaction.

Based on the overall characterisation and the combined results, specific formulation candidates have been identified for offering the maximum molecule stability under flow. PS80 and HS15 molecules at the state where they form micelles, are shown to enhance molecule stability for the IgG1 molecule, MEDI8852. On the other hand, PS20 and PS80 correspond to the best formulation candidates for the bispecific molecule, MEDI3549, based on the combined monomer fraction and particle concentration data. Therefore, the application of surfactants, correspond to alternative formulation strategies to enhance the stability of the molecules during their manufacturing where the surface modification equipment surfaces is not accessible.

Chapter 8

Proof-of-concept studies

Chapter structure

This section contains information on two shorter sub-studies that can be considered as proof-of-concept data for future work, where initial experimentation or computational data provides information that requires building on from the current work into further studies. Particularly, the first study investigated the effects of flow in a system in the absence of an extensional flow event, which is a variation of the extensional flow device. This involved the previously characterised protein molecules (aggregation prone-WFL, and aggregation-resistant, STT) as investigated in chapter 6 within the extensional flow device. In section 8.1, the particular molecules were exposed in to a sliding interface system and compare how the aggregation of the molecules induced within the particular system correlates with the aggregation induced within the extensional flow device. The second sub-study investigated the transition of the molecules into microfluidic platforms which is described as Flow stability system, FloSSy which will be described in section 8.2 and finally an overview of the work carried in the particular chapter is then summarised in section 8.3.

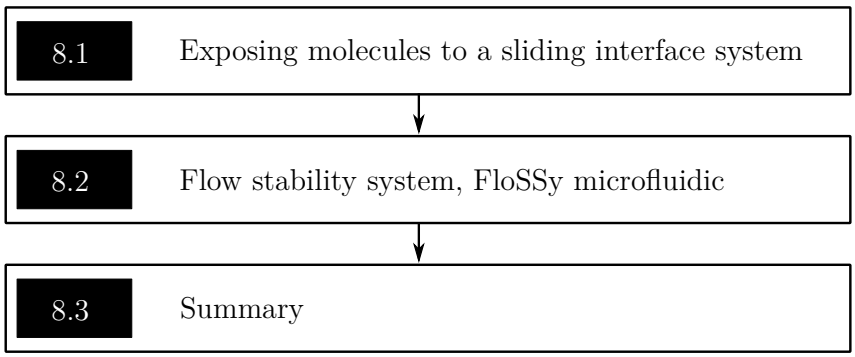

Figure 8.1: Overview of the main sections covered in the proof-of-concept chapter.

8.1 Exposing molecules to a sliding interface system

Since the previous study described in chapter 6, section 6.2 shows that the influence of surfaces is important, this work starts to identify a new design of experimentation to study the sliding interface region of the flow cell, without influence of extensional flow. A variation of the extensional flow device, by eliminating the contraction event inducing the extensional flow event, allows the investigation of the shear flow events by ensuring the

extensional flow event is removed from the system. The system investigated the subjection of samples into the development of shear flow events by subjecting the molecules into multiple passes with the movement of two plungers as indicated in figure 8.2.

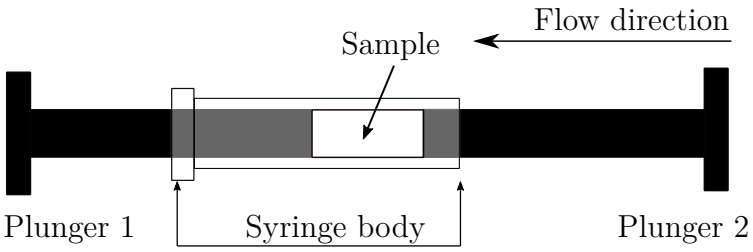

Figure 8.2: Schematic illustration of the sliding interface device. Sample is loaded in a single syringe body, which is then subjected to shear flow events with the movement of two plungers with the flow direction as indicated.

To investigate the shear flow effects in the absence of the extensional flow, two antibodies which were previously characterised under flow have been selected as the two extreme cases. STT which is an aggregation resistant molecule and WFL as an aggregation prone molecule have been selected as the model proteins for the particular experiment. Their distinct aggregation profiles, will allow the determination of shear flow effects as developed within the sliding interface system. Based on previous work investigating the relation of parameters with aggregation, presented as landscapes in the study conducted in [2], the aggregation of the two molecules can be controlled to be induced in similar profiles by adjusting the pass number. WFL as an aggregation prone molecule, its aggregation propensity is enhanced when exposed to less number of passes such as 50 passes which have previously shown to induce the aggregation. As STT is an aggregation resistant molecule, its aggregation propensity is enhanced at increased number of passes, i.e., 100 passes.

The role of extensional flow has also been highlighted, indicating its importance into the aggregation pathway via constriction angle experiments. Previously, in [302], it was shown that the aggregation depends on the constriction angle of the geometry, indicating enhanced aggregation for increasing constriction angles, suggesting the role of pure extensional flow. In these [1–3] and other studies, [24, 303] the damaging hydrodynamic flow fields are generated using syringes and the protein subjected to multiple cycles. Consequently, in addition to the direct hydrodynamic force, protein aggregation is also strongly affected by the surface of the syringe barrel [56, 304] and components including stoppers [305] and silicone oil [56, 116, 306] suggesting the complication of aggregation induced phenomena under bulk-interface interactions [23, 201, 307]. The plunger effect on the aggregation using a sliding interface system (figure 8.2), was investigated, using previously characterised WFL and STT proteins. Their aggregation propensity exposed to the sliding interface is shown in figures 8.3a and 8.3b for WFL and STT respectively. For comparison reasons, the experiments performed using the extensional flow device are also plotted as shown in the

right-hand side of the figures. Their aggregation propensities have been characterised as supernatant ratios along with the corresponding control sample. Interestingly, the sliding interface, induces similar levels of protein aggregation for both proteins, suggesting the importance of shear flow events encountered within the sliding interface setup. However, there is still a relatively complex flow field developed within the device, which will be discussed later, and it is shown in figure 8.5. The findings suggest that these effects are contributing to protein damage, however, their extensive effects on aggregation are beyond the scope of this work. As these protein fouled surfaces are themselves subjected to high friction by the action of the plungers (which may release aggregation seeds into the solution [304]), the relative importance of hydrodynamic flow and surface wettability to the ability of the EFD to induce protein aggregation remained unclear.

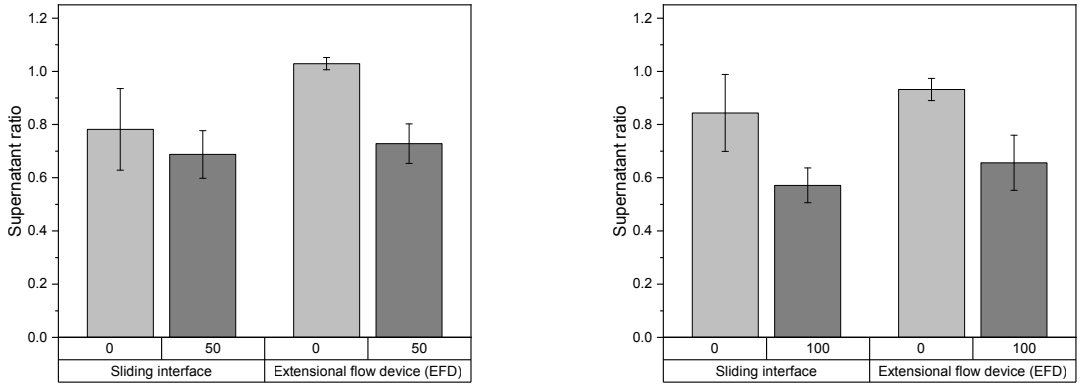

(a) **(b)**

Figure 8.3: Supernatant ratio of WFL (8.3a) and STT (8.3b) following quiescent incubation in the sliding interface and extensional flow device (0 passes) or stress in the devices for 50 (WFL) and 100 passes (STT) at a plunger speed of 8 mm/s. Sample concentration=0.5 mg/mL, buffer=150 mM ammonium acetate, pH=6. N=2, error bars= standard deviation.

To investigate whether the aggregation within the sliding interface system is mostly dominated by the effect of plunger, the addition of a formulation agent, polysorbate 20 (PS20), was investigated as shown in figure 8.4. The hypothesis behind the experiment is that if the action of the plunger is dominant, the addition of PS20 will have no effect on the aggregation. The addition of PS20 enhances the stability of STT against aggregation compared to the formulation with no PS20 (figure 8.3b). This suggests that the aggregation induced within the sliding interface systems is not dominated by the exclusive effect of plungers.

To further investigate the flow environment developed within the sliding interface, flow simulations were conducted. Computational fluid dynamics simulations, show the complexity of the flow fields generated within the sliding interface setup, as shown in figure 8.5. The development of extensional flow events within regions of the geometry, includ-

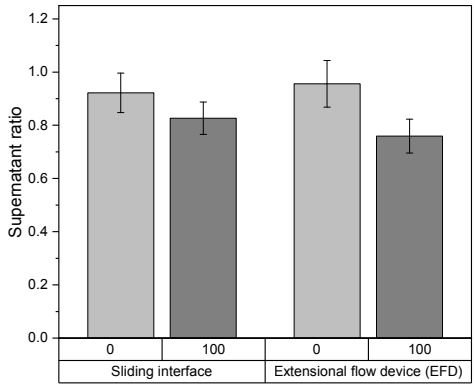

Figure 8.4: Supernatant ratio of STT following quiescent incubation in the sliding interface and extensional flow device (0 passes) or stress in the devices for 100 passes (STT) at a plunger speed of 8 mm/s. Sample concentration=0.5 mg/mL, buffer = 0.1% v/v PS20, 150 mM ammonium acetate, pH=6. N=2, error bars= standard deviation. Experiments were kindly conducted by Dr Leon Willis and Mr Alex Page.

ing corners, can be correlated with the protein damage observed. Timescale is also an important parameter, referring to the time the molecules are exposed into flow-interface environments.

To investigate whether these effects are dominated by diffusion mediated pathways, diffusion time calculations have been performed to allow comparison with the experimental time. Assuming the diffusion coefficients (D) for WFL and STT taken from [308], as 3.8 $\times 10^{-7}$ cm^2/s and 4.8 $\times 10^{-7}$ cm^2/s respectively, the calculated diffusion times for the molecules to diffuse within the syringe diameter are $\sim$19 (19.4) hours for WFL and $\sim$15 (15.4) hours for STT. The experimental time for the standard flow conditions undertaken for the conduction of the experiments presented, corresponds to a total time of 10 minutes, which is significantly faster compared to the diffusion time of the molecules. This suggests the dominance of flow-interface interactions compared to diffusion-driven effects.

8.2 Flow stability system, FloSSy microfluidic

The work on the EFD device has also been extended previously into a smaller scale microfluidics device, by Dr Kumar (A. Kumar, personal communication, 2019). A computational fluid dynamic study of the flow chips has been carried out to retrospectively support the experimental data of Dr Kumar and this will be reported elsewhere. The effect of shear and extensional flow events can be investigated by the use of microfluidic platforms, allowing the exposure of molecules to multiple flow events based on the configuration of the flow channels. As shown in figure 8.6, samples are exposed into multiple cycle of passes by the sample exposure to flow channel from syringe to syringe 2, and the flow rate in which the sample is introduced to the multiple flow arrangements is controlled by the plunger

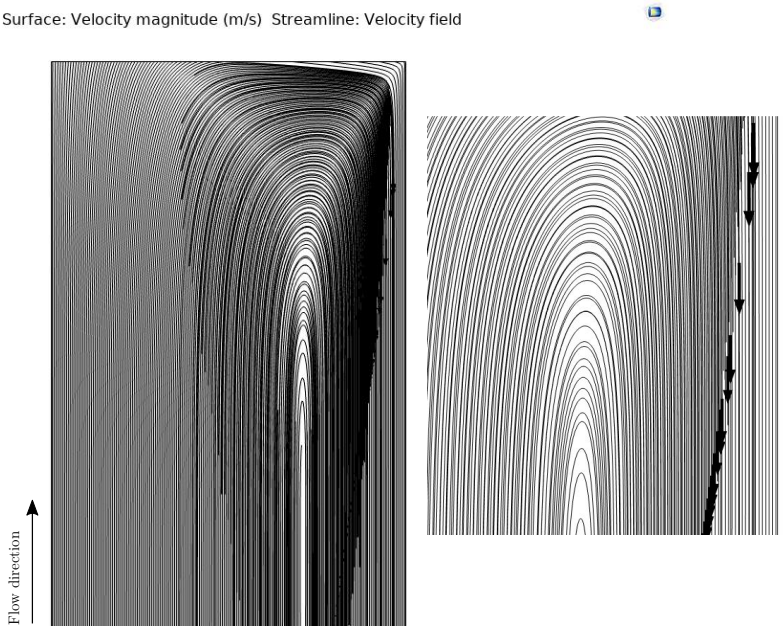

Figure 8.5: Characterisation of the flow field developed within the sliding interface device using CFD. Velocity field streamlines show the direction of flow, indicating areas with flow recirculation inducing extensional flow events.

speed. FloSSy microfluidic platforms consist of channels with multiple extensional flow events by the channel geometry consisting of either one (N1-1), two (N1-2), four (N1-4), 10 (R1-10 & S1-10) or 21 (O1-21 & P1-21) constriction in series. As described previously, the experiments have been conducted by Dr Amit Kumar using mAb1 protein sample. The new results reported here are the characterisation of the flow fields. The detailed flow channel dimensions are presented in appendix B, indicating the engineering drawings for each design as presented in figure B.1.

8.2.1 Flow characterisation

The channel consisting of a single constriction is selected for the flow characterisation as to allow the capture of key flow events in the simpler flow configuration. Flow regions of interest corresponds into regions before flow acceleration-low shear, sudden acceleration-extensional region and region after flow acceleration-high shear, with the protein unfolding event expected to be occurred at the sudden contraction event as illustrated in figure 8.7. The effect of these particular flow regions will give insights into the contribution of each region to protein aggregation of the molecules. A summary of the simulation parameters along the geometrical features for the conduction of simulation studies is summarised in table 8.1.

As shown previously, the extensional flow event within the extensional flow device (EFD) was shown to be developed at the sudden point of contraction. To capture the event at the microfluidic platform, computational simulations were performed indicating the extensional flow event, corresponding to the sudden flow acceleration along the channel

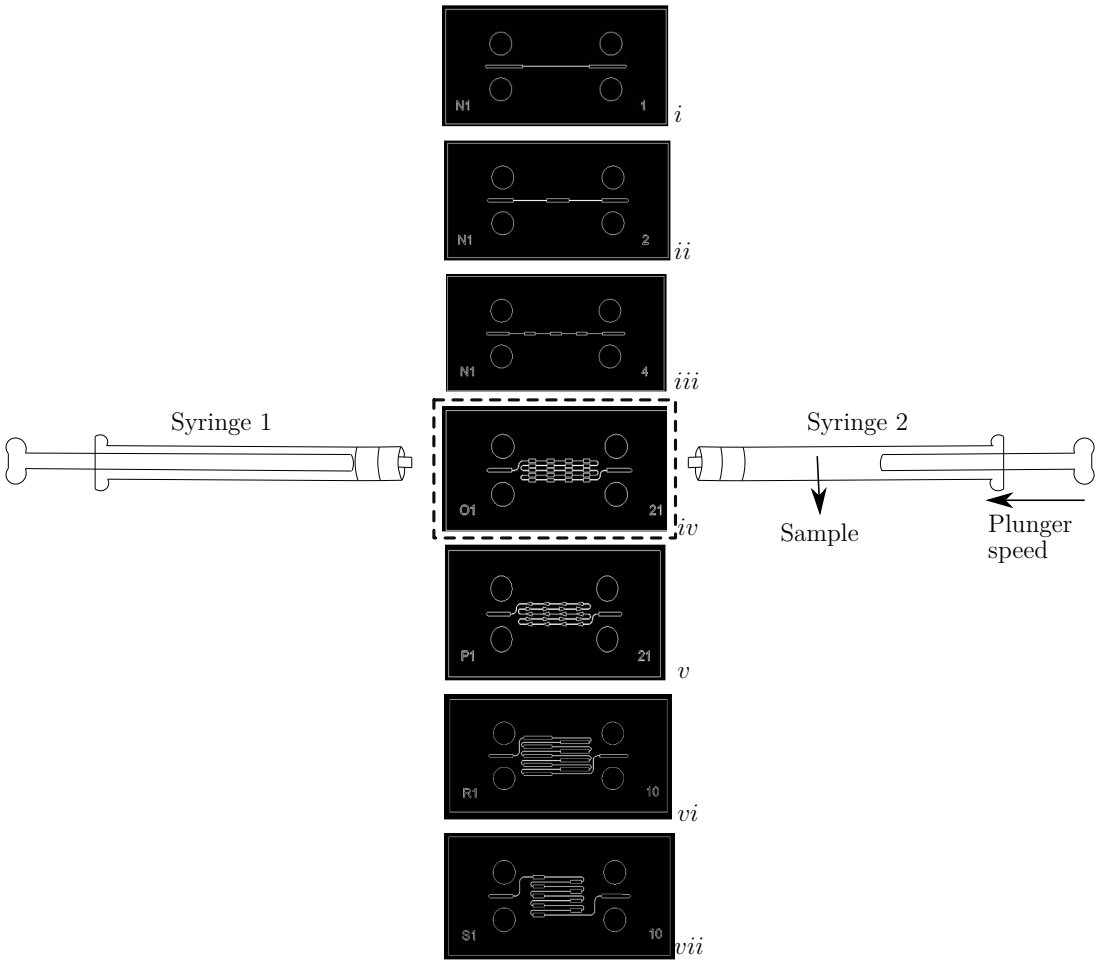

Figure 8.6: Schematic illustration of the Flow Stability System (FloSSy) experimental setup. Samples are introduced into multiple flow channel designs consisting of contractions in series such as one N1-1 (i), two N1-2 (ii) and four N1-4 (iii) contractions, channels consisting of 21 contractions with rectangular O1-21 (iv), triangular P1-21 (v) shapes and channels with 10 contractions in series, R1-10 (vi) and S1-10 (vii). Sample flow rate is controlled by the plunger speed, where the sample is introduced into shear and extensional flows in multiple cycles of passes between syringe 1 and syringe 2.

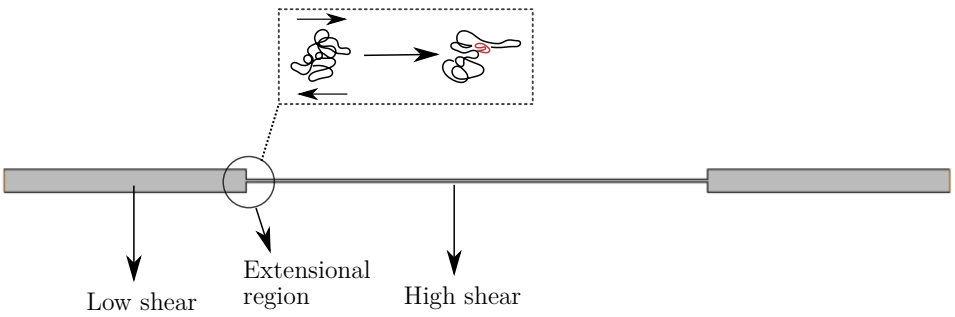

Figure 8.7: Schematic illustration of shear and extensional regions where the protein is exposed to within the N1-1 microfluidic device.

Table 8.1: Simulation parameters involving geometrical features and flow parameters for the N1-1 flow channel.

Entity	Value
Contraction ratio (W_1/W_2)	7.5
Channel thickness, t	250 μm
Plunger speed	8 mm/s
Average velocity at the contraction	5.34 m/s
Volumetric flow rate (syringe)	0.134 mL/s
Calculated Reynolds number (syringe)	34
Calculated Reynolds number (W_1)	266
Calculated Reynolds number (contraction)	761
Centre line strain rate	1.417 $\times 10^5$ s^{-1}
Maximum wall shear rate (high shear region)	2.33 $\times 10^5$ s^{-1}

length as show in figure 8.8 along the flow visualisation in contour plots shown in figure 8.9.

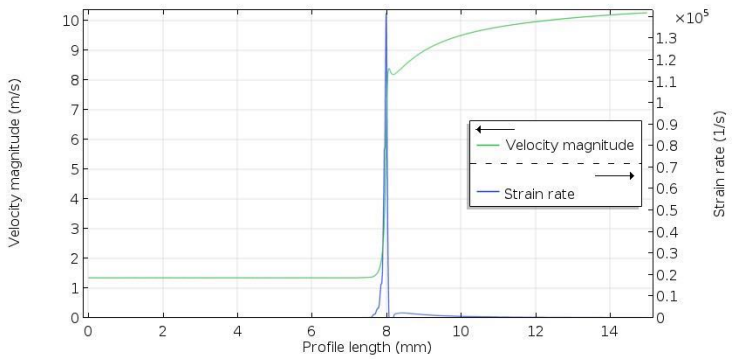

Figure 8.8: Development of velocity (green line) and strain rate (blue line) profiles along the channel length within N1-1 device flow channel. Flow is accelerated, inducing the strain rate development as it passes through the sudden contraction. Plunger speed=8 mm/s.

Compared to the extensional flow device, the strain rate developed within the N1-1 flow channel corresponds to an increase in one order of magnitude, achieving the development of a strain rate at $\sim$1.4 $\times 10^5$ s^{-1} compared to $\sim$0.1$\times 10^5$ s^{-1} in the extensional flow device at the same plunger speed (8 mm/s). The increased strain rate magnitudes can be also compared with studies found in literature, using microfluidic platforms to investigate protein aggregation. Particularly, in the study conducted in [150], the effect of constriction angle on development of strain rate was investigated on platelet aggregation, where the authors showed a maximum strain rate to be achieved at $\sim$1.2 $\times 10^5$ s^{-1}, which corresponds to similar strain rate obtained into N1-1 microfluidic platform. Similar strain rate magnitudes have been achieved in the study conducted in [151]. The effect of constriction stenosis, using a microfluidic platform investigating platelet aggregation, showed maximum strain rate to be achieved at 1.9 $\times 10^5$ s^{-1}. Lower strain rate magnitudes, are determined, in [132], subjecting blood samples to a maximum peak strain rate of >0.2 $\times 10^5$ s^{-1}. The authors hypothesised that, the elevated strain rate magnitude developed

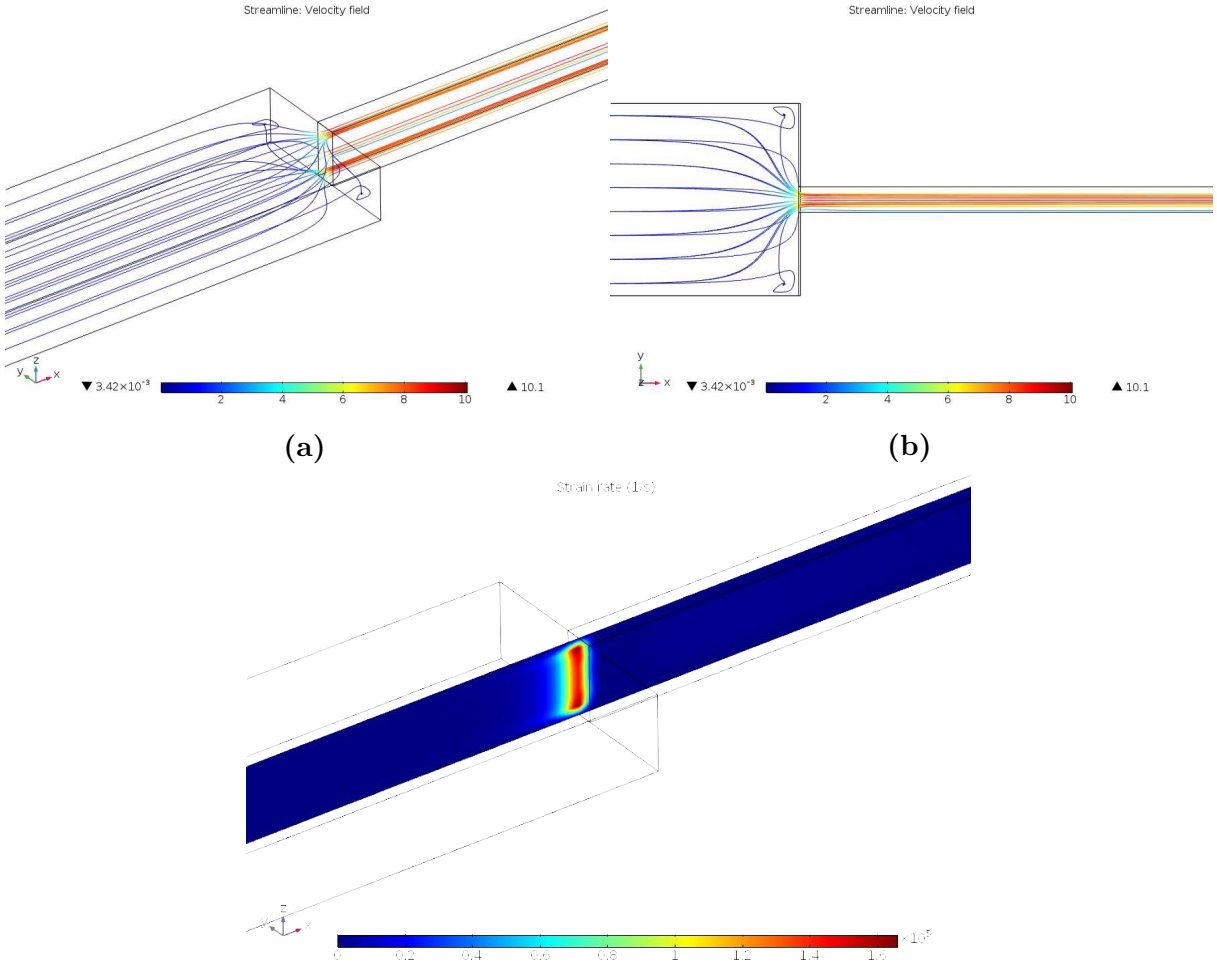

Figure 8.9: Contour plots of velocity and strain rate development of flow within N1-1 device flow channel. 8.9a & 8.9b: Velocity streamlines indicating the direction of flow within the flow channel in isometric and top views respectively. 8.9c: Development of strain rate through the sudden geometry contraction. Plunger speed=8 mm/s.

within their microfluidic device, induced platelet aggregation. In the study conducted in [309], a maximum shear rate of 0.3 $\times 10^5$ s^{-1} was obtained computationally at platelets within a microfluidic channel consisting of a block.

8.2.2 Determining the relation between constriction and aggregation

The effects of flow parameters, including plunger speed, strain rate and time in which the molecules spend within the region of extensional flow, will give insights into their distinct effects on aggregation. This is achieved by conducting simulations for various chip designs, as previously described (subsection 4.4.4). The simulations have been based on the set of the previously experimental work conducted, by organising the set of experiments according to the number of extensional events depending on the chip design and experimental parameters such as plunger speed as shown previously in table 4.2. Specifically, the following results presented, correspond to group A where the protein samples have been stressed within the EFD for various plunger speeds. This set of experiment is crucial for understanding how the proteins behave when they are exposed to increased hydrodynamic forces as the plunger speed increases. The significance of the particular experiments is the representation of hydrodynamic forces present during the production and formulation process of biopharmaceuticals, where they are exposed into different strain rates. The effect of plunger speed is shown to be dramatically affect the velocity developed at the sudden geometry contraction as shown in figure 8.10.

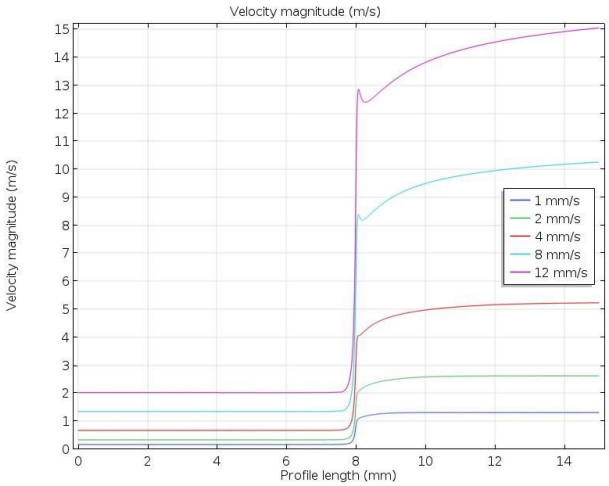

Figure 8.10: Effect of a range of plunger speeds: 1 mm/s (shown in blue), 2 mm/s (green), 4 mm/s (red), 8 mm/s (turquoise) and 12 mm/s (pink) on the development of flow velocity profile showing flow acceleration through the sudden contraction, N1-1 flow design.

Coupled simulation and experimental results, for the microfluidic chips, give insights into what happens into a protein as long as it is exposed into the extensional flow, as they are shown in figure 8.11. In particular, the correlation between plunger speed and strain rate

is shown to be directly proportional, as indicated in figure 8.11a. This is attributed to the fact that the strain rate is described as the velocity gradient, parallel to the direction of flow, the linear relationship between the plunger speed is expected. As the strain rate has been previously linked to induce protein aggregation [1–3], coupled simulation and experimental results have been combined to investigate the relation between the simulated strain rate with the aggregation observed experimentally. The aggregation propensity of mAb1 has been characterised experimentally by Dr Amit Kumar and the computational work presented in this chapter, is provided to Dr Kumar to allow him to complete his experimental study which will be reported elsewhere (A. Kumar, personal communication, 2019). As shown in figure 8.11b, the aggregation of mAb1 protein, which has been previously characterised presenting intermediate resistance to aggregation, is shown to be correlated linearly with aggregation using N1-1 flow channel as the geometry of reference. Additionally, an important parameter of consideration is to examine the relation of the time in which the molecule spends in the extensional flow region. Interestingly, the relation between time in extensional region and strain rate, follows an exponential trend as shown in figure 8.11c, suggesting that the more damage to the molecules is obtained as they spend the minimum time in the extensional region. This can be explained by the fact that for increased strain rates, the acceleration of flow is higher corresponding to smaller time scales of molecules within the regions of extensional flow. Therefore, this implies that the protein can be more damaged under high strain rate for short exposure time. On the other hand, the protein is found to be less damaged when it is exposed longer under a lower strain rate, quantified experimentally with lower aggregation percentage.

Alongside the simulation results presented for the N1-1 flow channel, simulation studies have been performed across the range of microfluidic flow configurations, characterising the key flow regions of interest. An overview of the parameters, varied for the conduction of the simulations, is shown on table 8.2. Table 8.2 summarises the plunger speed combination along with the flow configuration. The simulations were performed for the particular set of parameters based on previous experimental work conducted by Dr Amit Kumar. The scope of the particular section is the flow characterisation in the multiple flow channels; therefore, the results presented are focused into the computational aspect. The input parameters for the simulations was the plunger speed for each flow channel design, with the time in extensional region, shear rate obtained in low and high shear regions as well as the strain rate developed for each design is reported. Comparing the different experimental parameters, more damage is expected at the maximum plunger speed of 12 mm/s, achieving a maximum strain rate of 2.184 $\times 10^5$ s^{-1} within the N1-1 flow design. On the other hand, at the lower speed investigated (1 mm/s), the corresponding strain rate developed at 0.18×10^5 s^{-1}, suggesting the least protein damage. The corresponding times in extensional flow region is minimum for the maximum strain rate, 4.34 $\times 10^{-5}$ s and maximum for the minimum strain rate, 0.00051 s. It is also important to note that the

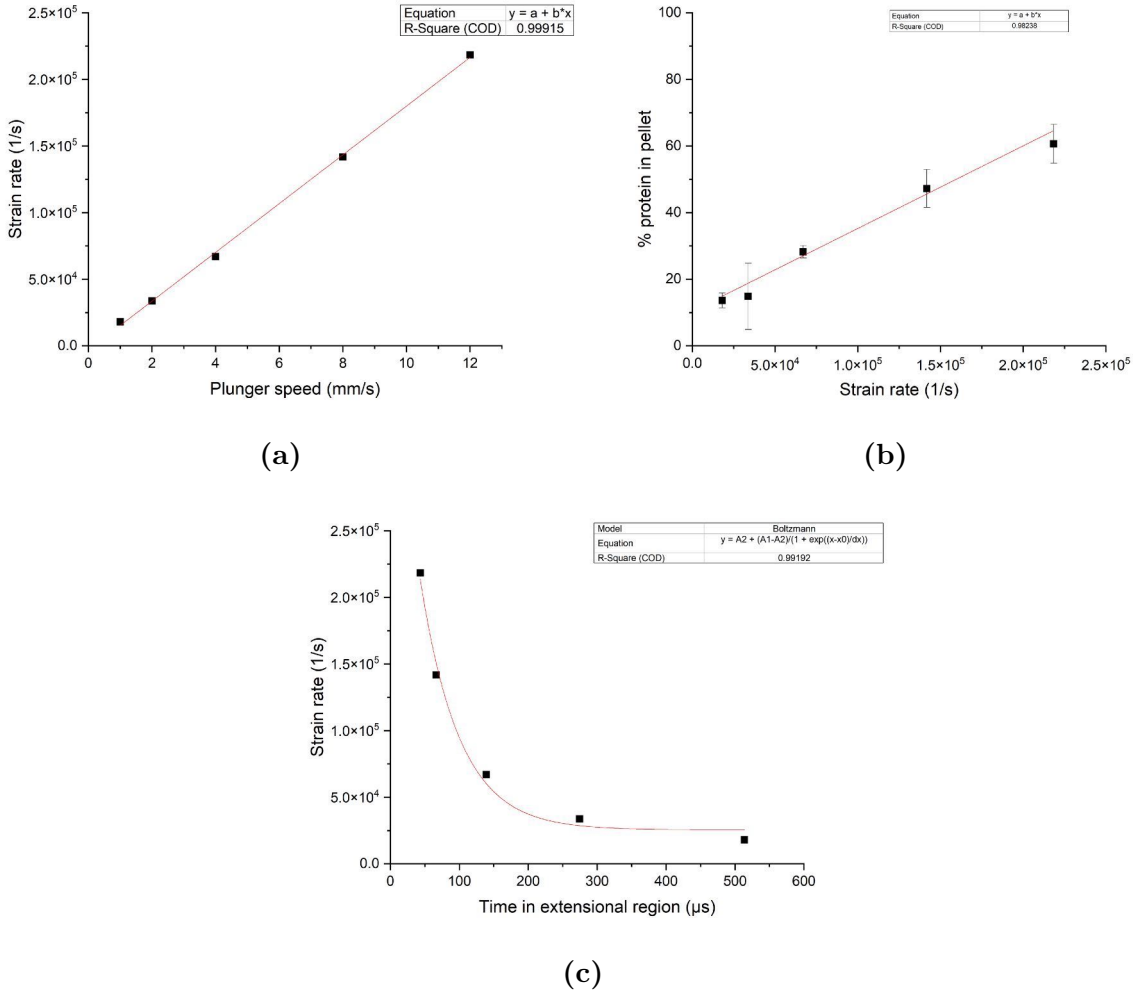

Figure 8.11: Coupled experimental and computational results for the N1-1 microfluidic chip device. The sample used for the conduction of experiments was 700 μL of mAb1 at 0.5 mg/mL, stressed for 100 passes. 8.11a: Effect of plunger speed on the development of strain rate through the sudden geometry contraction. 8.11b: Effect of plunger speed on the aggregation of mAb1. Experimental data (% protein in pellet) was collected by Dr Amit Kumar, Astbury Centre (A. Kumar, personal communication, 2019). 8.11c: Relation between time in which the molecules spend within the extensional flow region and strain rate.

strain rate magnitudes developed within the FloSSy designs are much higher compared to the ones previously explored using the EFD, extensional flow device. This will imply that the use of these microfluidic platforms will be useful for studying molecules that are highly resistant when exposed to flow and the investigation of their aggregation propensity under the standard flow conditions, using the extensional flow device, can be challenging.

Table 8.2: Simulation flow parameters for the FloSSy flow designs along with the plunger speed, time molecules spend within the extensional flow region (T-E), shear rate developed within the low shear region (LS), strain rate developed within the extensional flow region (E), and shear rate developed within the high shear region (HS).

FloSSy Design	Plunger speed (mm/s)	T-E (μs)	Shear rate LS (s^{-1})	Strain rate, E (s^{-1})	Shear rate HS (s^{-1})
N1-1	1	514	0.0236×10^5	0.18×10^5	0.273×10^5
N1-1	2	274	0.0473×10^5	0.337×10^5	0.547×10^5
N1-1	4	139	0.095×10^5	0.67×10^5	1.112×10^5
N1-1	8	67	0.189×10^5	1.417×10^5	2.33×10^5
N1-1	12	43	0.284×10^5	2.184×10^5	3.62×10^5
O1-21	4	187	0.14×10^5	0.798×10^5	1.875×10^5
P1-21	4	185	0.53×10^5	0.613×10^5	1.75×10^5
P1-21	8	90	1.35×10^5	1.18×10^5	3.58×10^5
R1-10	4	117	0.125×10^5	0.61×10^5	1.1×10^5
S1-10	4	140	0.145×10^5	0.815×10^5	1.04×10^5

To allow design comparison, flow characterisation within the flow channels at constant plunger speed of 4 mm/s presenting strain rate and shear rates corresponding to the flow channel designs of N1-1, O-21, P1-21, R1-10 and S1-10 as shown in figure 8.12a. For a fair comparison between the range of the flow designs, strain rate at a constant plunger speed of 4 mm/s, investigating the strain rate development and shear rate in low and high shear regions as shown in figures 8.12b and 8.12c. The maximum strain rate is shown to be developed in O1-21 and S1-10 designs, whereas maximum shear rates at the high shear region is shown to be developed at O1-21 and P1-21 flow channels.

8.3 Summary

The work covered in the current section presented the foundation for the conduction of further studies, which can contribute into the development of better understanding of these proof-of-concept studies. As presented in section 8.1, preliminary studies indicated that using a variation of the extensional flow device, using the sliding interface system, the aggregation induced in the absence of the extensional flow point (geometry contraction) is also significant and is comparable with the aggregation induced using the standard extensional flow device. The particular experiments conducted in the sliding interface system, identify a new design of experimentation to study the sliding interface region of the flow cell, without influence of extensional flow. It is also shown that the complexity of the flow field developed in the system induces the generation of further extensional flow events, which may explain the aggregation propensity induced in the particular system. The second aspect of the chapter in section 8.2, presented the transition to

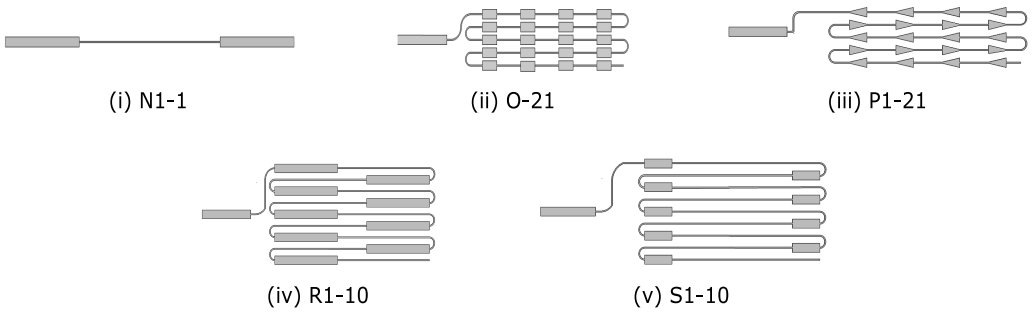

(a)

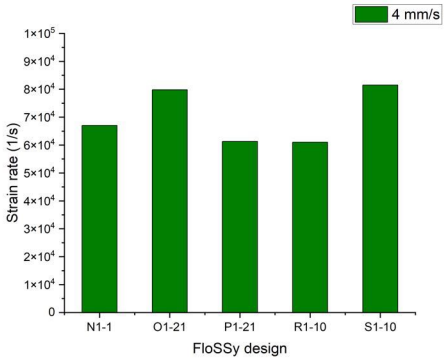

(b)

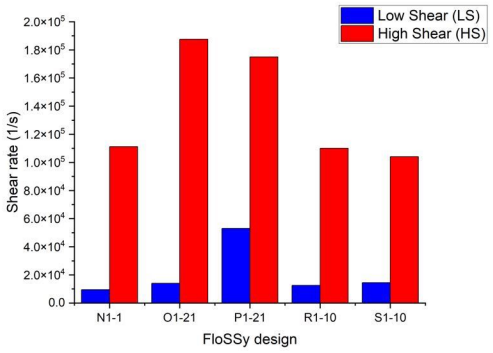

(c)

Figure 8.12: Flow characterisation within the range of Flow Stability System (FloSSy) designs as shown in 8.12a including N1-1 (i), O-21 (ii), P1-21 (iii), R1-10 (iv) and S1-10 (v) at inlet plunger speed of 4 mm/s. 8.12b: Development of strain rate at the point of sudden geometry contraction, found in the range of the flow designs investigated. 8.12c: Development of shear rate at the low and high shear regions of flow.

microfluidic scale systems, to investigate the aggregation propensity of molecules alongside their flow characterisation within a range of microfluidic flow channel designs. From the computational simulations, it was shown that the magnitude of the strain rate developed in these microfluidic platforms is significantly higher compared to the strain rate developed within the extensional flow device (at the same flow conditions, plunger speed=8 mm/s). This suggests the ability of microfluidics to expose molecules into high orders of strain rate magnitudes, suggesting their prospective application in the study of potentially more aggregation resistant molecules. The studies presented in the particular section, support the designing of a wider variety of flow profiles, including wait times, delays, times within various regions of the flow. In overall, the results presented in this chapter are not conclusive, however these studies can extend the possible understanding of the contribution of flow and interfaces in systems in the absence of extensional flow point events, and the design of a wider variety of flow profiles within various microfluidic flow channels.

Chapter 9

Conclusions

The current work investigated several strategies which can enhance the stability of biopharmaceutical molecules under characterised flow conditions, which are industrially relevant. Particularly, the flow conditions found during cross-flow filtration process, as reported in [58], correspond to shear rates of 1,000 up to 10,000 s^{-1}, with the maximum shear rates expected during normal processing operations reach to 20,000 s^{-1}. The use of the extensional flow device as a flow tool has been used for building a better understanding of how biopharmaceuticals behave under flow, and how this links with their propensity to aggregate. The significance and contribution of the extensional flow to induce protein aggregation has been previously shown in [3], highlighting the uniqueness of the extensional flow among other developability assays, indicating that the extensional flow device has a distinct branch on the family tree of assays assessed in a clinical dataset. The data indicate the distinct aggregation or association mechanisms induced by the extensional flow device compared to other assays employed in exposing molecules to aggregation.

Flow characterisation was firstly conducted by determining the flow conditions in which the experimental conditions are relevant to the conditions found in industrial processes. Computational fluid dynamic simulations indicated that the desired range of the strain rate to which the molecules are exposed within the extensional flow device, corresponds to $\sim$10,000 s^{-1} for a plunger velocity of 8 mm/s, and for aggregation resistant molecules such as STT, the flow conditions were adjusted such as the maximum strain rate examined in the current work reached $\sim$20,000 s^{-1} for a plunger speed of 16 mm/s [1]. The development of the extensional flow is found to be directly proportional to plunger speed, as extensional flow corresponds to the flow developed parallel to the direction of flow.

Additionally, as part of this work, the application of the extensional flow within a microscale device was also characterised with several geometrical features including multiple number of contractions and contraction shapes. Flow characterisation in these microfluidic channels indicated that the flow developed is mainly dependent on the time in which the molecules spend during the extensional flow event. It was also shown that by selecting particular flow channel designs, molecules are exposed to extremely high flow conditions compared to those found in the larger scale extensional flow device with maximum strain rate values in the order of $\sim 10^5$ s^{-1} within the microfluidic flow channels, compared to $\sim 10^4$ s^{-1} using the extensional flow device. The one-fold increment in the development of the extensional flow using the microfluidic channels, can be advantageous in investigating the aggregation of molecules with high stability. This can be reflected in studies using

the STT molecule which corresponds to an aggregation resistant molecule, where its aggregation characterisation was conducted at higher flow conditions compared to the aggregation prone WFL molecule. The flow characterisation of the microfluidic showed that the geometrical features, including the thickness of the flow channel as well as the contraction ratio responsible for the flow acceleration, are critical for the development of the extensional flow.

Building on the flow characterisation and the identification of parameters that are important in developing the extensional flow, the main focus of the project was to investigate additional parameters that can influence the aggregation propensity of the molecules. Particularly, from the perspective of equipment surfaces, the interaction of pharmaceuticals with different surface materials, is inescapable during manufacturing. Therefore, the work was focused into the characterisation of the aggregation profile of various molecules under several surfaces during their exposure to extensional flow. Alongside the contribution of solid interfaces, the effect of "liquid" interfaces in particular is also addressed from the protein formulation perspective. Therefore, the critical questions that the current work aims to address are followed in the next sections 9.1 and 9.2.

9.1 What is the role of surface in flow induced aggregation?

The effect of the surface contribution into the aggregation propensity of the molecules was firstly investigated via surface modification and surface characterisation. A surface library was constructed based on the degree of hydrophobicity. The effect of surface and the protein interaction was firstly investigated in a system where the molecules sit under quiescent conditions (in the absence of extensional flow). Interestingly, the molecules exhibit similar tendency in adsorption on the various surfaces, with the most aggregation prone molecule (WFL) shown to be as the most surface-active molecule among the ones investigated.

With the introduction of extensional flow, the molecules exhibit complex aggregation profiles, which depend on the hydrophobicity of the surface. The results indicated the significance of extensional flow and its ability to unfold protein molecules at defined flow conditions, where mainly the focus of previous literature studies is the investigation of protein aggregation under shear flow. It is shown that particular surfaces, with increased hydrophobicity compared to the untreated glass surface, offer protective effects against aggregation under flow. The effects of two interrelated sources inducing protein aggregation, corresponding to surface wettability of the protein solution container and mechanical shock, were investigated in [206]. In contrast to the results observed in the current study, the authors there proposed that the most hydrophilic surface (PEG) among the library

investigated, offered protective effects in terms of the reduced formation of larger aggregates caused by low protein adsorption. The contribution of an air interface was also present in the particular study inducing cavitation events, that could not be defined in a controlled method. Therefore, this suggests that the protective effects of surfaces can be attributed to the type of flow in which the molecules are encountered as well as the type of interfaces in which they interact.

This work shows that where the molecules were incubated on the bench and syringe bodies, the surface was found to have no effect in inducing aggregation compared to the case where they were exposed to the extensional flow. From the results, it can be concluded that in order for the surface to affect the aggregation, flow must be simultaneously applied. This finding indicates the phenomenon of synergy between surface and flow, which has been recently acknowledged in literature [23, 24]. The surface contribution in the aggregation pathway, will suggest that the previously proposed aggregation pathway in [2], can be updated and incorporated with an additional parameter of surface alongside the bulk mechanism, with a schematic representation of this postulated and shown in figure 9.1.

Among the surface library investigated, it was shown that the particular surfaces exhibited strong protective effects, by significantly suppressing the aggregation tendency of the molecules. It was also shown that the general trends of protection arising from these surfaces are the same, but the levels of protection are still protein dependent. Particularly, silane A and silane B surfaces with their respective chemical agent names of APTES and HTS, enhanced the molecule stability of STT, mAb1 and WFL molecules. Silane B surface corresponds to the most protective surface, offering significant aggregation protection to the high aggregation prone WFL molecule. The particular surface is found to offer protective effects against aggregation for multiple proteins explored, as quantified by several techniques investigating the aggregation remaining in pellet, monomer fraction, and particle concentration. This finding implies that the surface modification can be an alternative strategy to enhance the molecule stability during manufacture.

By investigating particular flow regions within the extensional flow device, it was also concluded that the low shear region (syringe body), before the flow accelerates through the sudden contraction, is important for affecting the aggregation propensity of the molecules. This may partly be that the time in which the molecules interact with the surface is longer in the low shear compared to the extensional flow and high shear regions. The effect of time exposure to flow fields has been previously investigated in [2], where the aggregation propensity of WFL was affected when the time in which was exposed to shear flow was prolonged, via extended capillary lengths. Therefore, the timescale in which the molecules are exposed to flow fields, is critical and shown to be an important parameter affecting the aggregation propensity of the molecules.

The effect of shear flow events, in the absence of the constricted geometry, inducing the development of the extensional flow event was also investigated via a sliding interface system. In the particular experimental setup, the molecules were exposed into the action of plungers in the absence of the dominant extensional flow. From the results, it is shown that the sliding interface system induces similar levels of protein aggregation as with the extensional flow, highlighting the significance of the shear flow events encountered in the particular system.

To investigate whether the aggregation within the sliding interface system is mostly dominated by the effect of plunger, the addition of surfactant (PS20), indicated the aggregation suppression. From this observation, it can be concluded that if the action of the plunger is dominant, the addition of PS20 will have no effect on the aggregation. With the addition of PS20, the stability of STT is enhanced against aggregation compared to the PS20-free formulation. This suggests that the aggregation induced within the sliding interface systems is not dominated by the exclusive effect of the action of plungers, which may contribute to the development of complicated flow configurations as well possible surface scraping. Flow characterisation of the particular system, indicated the additional development of extensional flow events around the corner of the syringe, highlighting the complexity of the flow configuration. The dominance of shear flow events against any protein aggregation induced by the diffusion effects was shown by the comparison of the diffusion time of the molecules compared to the experimental time. The dominance of flow-interface interactions can be also shown by the comparison of the experimental time which corresponds to 10 minutes compared to the calculated diffusion times of $\sim$19 and $\sim$15 hours for WFL and STT molecules respectively. This suggests the dominance of flow-interface interactions compared to diffusion-driven effects.

The surface contribution into the aggregation pathway was also investigated by the covalent protein attachment of proteins on surface under flow. To the best of the author's knowledge, the effect of protein attachment on surface under extensional flow has not previously been investigated. Previous focus of literature studies around the attachment of proteins to surfaces has its application in the identification of protein-protein, protein-DNA, and protein-small molecule interactions as well as for diagnostic purposes [310]. Antibodies are often employed as recognition proteins of biological samples that are required for the antigen detection and quantification required for immunodiagnostics, protein biochips, and biosensors. The immobilisation of the capture of antibodies onto a solid support determines the sensitivity of these diagnostic assays [7]. The novelty of the protein labelling experiment, as proposed in section 6.5, indicated that the association state of the protein on the surface is significant in affecting the aggregation propensity of the molecules under flow. This conclusion is supported by the findings of the experiments highlighting that the aggregation propensity of the molecule depends on the protein attached on the surface, inducing a range of dissociation profiles. Specifically, it is shown that when the cross-linked

molecules on the surface and molecules in the bulk solution are from the same population, they interact highly with one another compared to molecules from different populations based on the slower desorption rate, in the absence of extensional flow. The desorption rates, as determined from QCMD experiments, indicate that the protein adsorption on surface is a reversible process.

Under extensional flow conditions, the aggregation is suppressed from the same population covalently attached on the surface as well as in the bulk solution. Flow induced aggregation of the molecules on the STT cross-linked surface indicated that the aggregation between same molecules is suppressed compared to the aggregation between different molecule populations. Combined with the desorption rate information, it can be concluded that the particular cross-linked surface enhances the molecule stability under flow conditions, as the desorption is also slower between the same population molecules. Suppressed aggregation can be expected in the situation where surface adsorbed molecules catalyse refolding of the native protein state in the presence of a protein attached on the surface. Alternatively, suppressed aggregation can be also induced by the full passivation STT cross-linked molecules on the surface, where it will be no molecular space for aggregation to be induced on the surface.

Under quiescent conditions, the reversible adsorption of proteins is indicated from the raw experimental QCMD data. Under extensional flow conditions, it was shown that the aggregation propensity was affected for the condition where protein molecules are already landed on surface (covalently attached). These observations indicate that there are multiple interactions of the molecules with the surface and bulk roots via multiple reversible process at a solid-liquid interface system, as indicated by the reversible arrows in the schematic shown in figure 9.1.

As mentioned in chapter 7, the suppressive aggregation at higher concentrations can be driven due to interface saturation events, with the protein molecules populating on the surface compartments of the device. The saturation effect of the molecules on the surface, highlights the contribution of solid interface in synergy with flow. This is also highlighted in [23], where the inverse dependence observed aggregation on the initial protein concentration corresponds to a surface-induced protein aggregation phenomenon. On the other hand, bulk induced aggregation corresponds to increased aggregation rate with increasing protein concentration.

At a manufacturing level, surface treatment of equipment components, such as filters, syringes, plungers, can be treated with the particular surface modifiers to alter their interaction with proteins. The surface modification of equipment components can be desirable compared to the traditional formulation strategies that require the addition of excipients in the molecule formulation. This ensures that the protein formulation is simplified, consisting of protein and buffer components, minimising the interaction of the

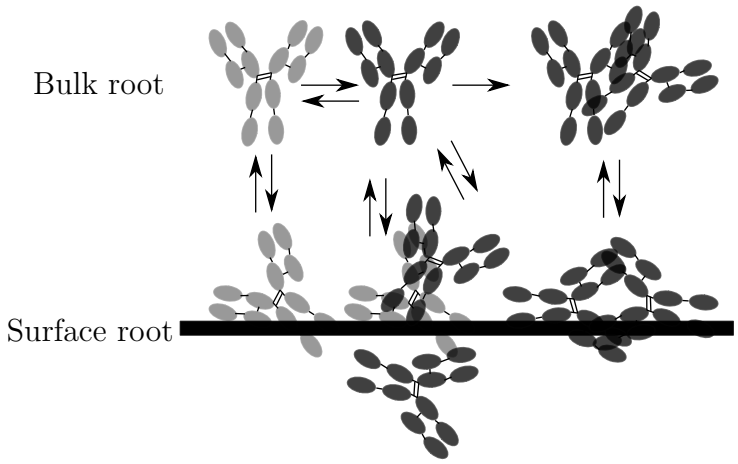

Figure 9.1: Schematic illustration of the surface and flow synergy in flow induced aggregation via potential bulk and surface roots, as adapted from Dr Leon Willis. The illustration presents the potential expansion of the bulk mediated flow induced mAb aggregation model as previously proposed in [2] including the contribution of the surface pathway. The native state of the protein (light grey) is perturbed into an aggregation-prone state (dark grey), the level of which depends on the fluid field, protein studied and surface. The aggregation prone state can either refold to the native state via bulk or surface roots or proceed along the aggregation pathway forming insoluble aggregates. The formation/refolding rates are about to be determined.

molecules with multiple interfaces.

9.2 How surfactants prevent aggregation?

As the effect of solid interface is shown to suppress the aggregation tendency of molecules, the effect of surfactants on aggregation is then investigated. The current section focuses on the formulation characterisation and analysis of two protein molecules, including MEDI3549 and MEDI8852. The aggregation propensity of higher protein concentration was investigated in a range of 0.5-40 mg/mL exceeding the maximum concentration of 10 mg/mL which was previously studied using the extensional flow device. Firstly, the rheological characterisation was conducted in their initial formulation buffer of 235 mM Sucrose, 25 mM Histidine, pH=6 showing that the solutions exhibit structural rearrangements during their exposure to shear flow, presenting a shear-thinning flow profile for a concentration range of 0.5-40 mg/mL within a range of shear rates of 2-600 s^{-1}. The shear thinning profile is as a result of the viscosity of the molecule, which decreases while the application of shear rate increases. Specifically, the shear thinning profile was observed up to shear rates of $\sim$100 s^{-1}. Relating the particular shear rates, with the actual shear rates reported in typical commercial operations, it can be found that the shear rates found in industrial applications lie within the determined experimental conditions detected in the current study. As it has been reported in [58], protein formulations are exposed to shear rates of about 50 s^{-1} during mixing processes.

To further investigate how the shear thinning effect can be linked and how it can affect the aggregation under flow, computational fluid dynamic simulations were conducted within the extensional flow device. From the simulations, it was concluded that the shear thinning effect of high concentrated protein formulations can cause flow disruption into the flow acceleration through the point of contraction. Interestingly, the shear thinning effect was shown to induce higher strain rate values up to ∼15,000 s^{-1} compared to ∼10,000 s^{-1} for a Newtonian fluid under the same flow conditions. This observation could suggest that high concentrated molecules are more susceptible to aggregation via a bulk mediated pathway under the same flow conditions. To determine the aggregation propensity of MEDI3549 and MEDI8852 experimentally, high concentrated protein formulations in the range of 0.5-40 mg/mL were exposed to the extensional flow device. Interestingly, the aggregation of both molecules was suppressed at increased concentrations, whereas the maximum aggregation was detected for both molecules at low protein concentration of 0.5 mg/mL.

Protein formulation strategies using surfactants as formulation additives are commonly found in the biopharmaceutical industry. Therefore, the aim of the second part of the project was to investigate how surfactants affect aggregation. The ability of the extensional flow device to characterise and predict the aggregation profiles of various molecules exhibiting different aggregation profiles under various surface is covered in the previous section. The current section, builds on the ability of the extensional flow device to characterise the aggregation propensity of molecules from a formulation prospective.

The extensional flow device, is then used as a formulation tool which was used to screen a range of surfactant molecules, investigating the surfactant molecules with the best protective properties against flow induced aggregation. The surfactant library was constructed based on well known and characterised molecules, including polysorbates (PS20, PS80) and poloxamers (P188). The library was also constructed to include the addition of novel surfactant molecules used in biopharmaceutical formulations (HS15 and EL). Alongside the flow conditions found during manufacture which are mimicked using the extensional flow device, the surfactant screening was also conducted in flow conditions found during the shipping process of biopharmaceuticals. The model protein selected for the conduction of the experiment was a bispecific molecule (MEDI3549), with no previous aggregation characterisation information.

The surfactant screening was also conducted using a shipping simulator mimicking the shear flow conditions in which the molecules are encountered throughout their transportation via truck and plane simulation levels. Firstly, by comparing the two types of flow configuration of shear and extensional flow, the results indicated the significance of the extensional flow to induce the aggregation of molecules, compared to the shear flow induced within the shipping simulator. From a combination of techniques, the results indicated that

the PS20 and PS80 formulations can be proposed as suitable formulation candidates to minimise aggregation. The combination of multiple techniques indicated that the selection of suitable formulation candidates is based on the balance between the total number of particles induced and the fraction of protein remaining as monomeric. The particular surfactant molecules are proposed as they have shown the minimum particle concentration whereas the aggregation is suppressed, indicating a maximum number of monomer fractions. The experiments indicated the ability of the extensional flow device to be used as a screening formulation tool for predicting suitable formulation candidates, enhancing molecule stability.

Building on these studies, the next sets of experiments, were carried out to develop a better understanding of how surfactants can act as stabilisers, and at which conditions their application can enhance the stability of molecules. The effect of the various association states of surfactants was then investigated by determining particular points of interest based on the proportionality between protein and surfactant molecules. Three points of interest have been selected, corresponding to the state where there is protein excess, protein-surfactant equivalence and surfactant excess conditions. The protein excess condition was based on the experimental determination of the critical micelle concentration (CMC) of the surfactant molecules within the formulation buffer in which the flow experiments have been conducted. To also investigate whether the effect of surfactants is protein-dependent, an IgG1 molecule (MEDI8852), compared to the previously used bispecific molecule, was used as the model protein.

The data extracted from the pelleting assay highlights the significance of the ratio between surfactant and protein molecules, which is denoted as S:P, on enhancing the molecule stability under flow. Depending on the surfactant molecule, the association state in which the aggregation of the protein is suppressed varies accordingly. In particular, the maximum suppression of aggregation, which is determined by the increase in supernatant ratio corresponds to PS20 (20:1), PS80 (20:1), and HS15 (100:1) formulations (micelle state). On the other hand, maximum supernatant ratios were determined at the equilibrium state for P188 and EL formulations between surfactant and protein molecules (1:1). By combining the pelleting assay with fluorescence spectroscopy experiments, the conditions where the aggregation is suppressed (maximum supernatant ratio) and the protein conformational state is conserved (minimum intensity and wavelength shifts) are narrowed to two formulation options.

The formulation conditions that satisfy both requirements of aggregation suppression and protein stability, correspond to the surfactant excess state, forming micelles. Specifically, it can be proposed that the suitable formulation candidates are PS80 and HS15 at surfactant to protein ratios (S:P) of 20:1 and 100:1 respectively. Overall, it can be concluded that firstly, the protective effect of surfactants is protein-dependent, as for the bispecific molecule

MEDI3549, where PS20 and PS80 are proposed as the best formulation candidates. On the other hand, when an IgG1 molecule (MEDI8852) is selected as the model protein, the most effective formulation candidates are PS80 and HS15 at the state where they form micelles.

Combining the findings of the current study where the surfactant molecules maintain the conformational state of the protein at the state in which they form micelles, with the flow induced aggregation mechanism, a schematic illustration is shown in figure 9.2. It is proposed that the aggregation is shown to be induced via bulk and surface pathways. This is based on findings where the surface activity of the protein is shown to be affected in the presence of surfactants in the absence of extensional flow. In the presence of the extensional flow, the aggregation is suppressed.

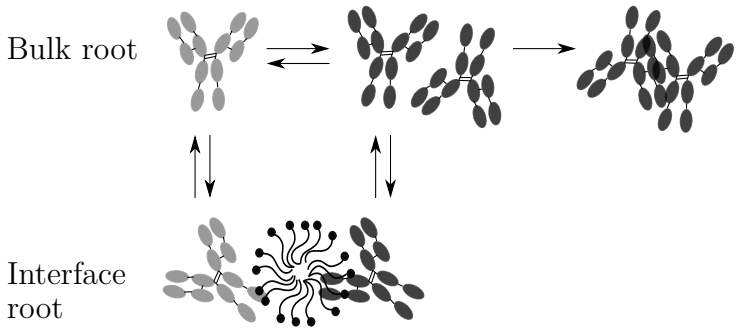

Figure 9.2: Schematic illustration of the surfactant micelle interface and flow in flow induced aggregation via potential bulk and interface roots, as adapted from Dr Leon Willis. The illustration presents the potential expansion of the bulk mediated flow induced mAb aggregation model as previously proposed in [2] including the contribution of the surfactant micelle interface pathway. The native state of the protein (light grey) is perturbed into an aggregation-prone state (dark grey), the level of which depends on the fluid field, protein studied and surfactant. The aggregation prone state can either refold to the native state via bulk or surface roots or proceed along the aggregation pathway forming insoluble aggregates. The formation/refolding rates are about to be determined.

Through developing a new technique to assess the protein state in the presence of the surfactant, the fluorescence spectroscopy, shows that surfactants can also induce conformational changes in the protein structure, as indicated from wavelength shifts and fluorescence intensity changes at particular association states. Therefore, apart from protective effects, surfactants can also impact the conformational state of proteins, facilitating protein particulates, temperature-dependent oxidation, and decreased physical stability in quiescent bulk solutions, indicating that they can exhibit dual effects on proteins [95].

The enhancement of protein stability is shown to correspond to PS80 and HS15 molecules at their CMCs which correspond to the maximum concentrations investigated. However, it has been reported that the presence of micelles could act like foreign particles, causing immunogenicity [297]. Therefore, there is a formulation dilemma to ensure that the minimum critical concentration of surfactants will be used that will avoid or reduce

surface denaturation and aggregation, whereas excluding the presence of too many micelles in the formulation [297]. For the identification of the exact mechanism of surfactants, further experiments should address flow induced aggregation in the presence of surfactants, identifying the formation/refolding rates.

9.3 Summary

The overall work presented in the current study, highlights the complexity of the flow induced aggregation of biopharmaceuticals. Firstly, the complexity refers to the multiple configurations that the protein experiences within the extensional flow device, as well as the parameter space involved. Specifically, it is shown that the flow induced aggregation is a complicated phenomenon that can be affected by the formulation conditions involving the protein molecule itself, protein concentration, choice of buffer and surfactant agents. Alongside the liquid interface space involved in the formulation, the aggregation propensity is shown to be sensitive to solid interfaces involving the equipment surface of the device. From the results, it is shown that the aggregation propensity of the molecules is driven from the synergistic action of flow and surface parameters. The study investigated a broad range of parameters, and identified the parameters and the conditions which are important in enhancing the molecule stability.

Surface modification is found to be a powerful technique in enhancing the molecule stability even at higher flow conditions for several molecules. The enhanced molecule stability as a result of surface modification was shown using a range of analytical techniques involving aggregation quantification, particle concentration, size distribution and structural perturbation or conservation of the protein structure. Based on these data, a further understanding of flow induced aggregation mechanism has been developed with the additional contribution of surface-flow synergy which is shown to be important. The current study focused on the significance of the extensional and shear flow effects on the aggregation of biopharmaceuticals, whereas the majority of the literature is focused on the effects mainly of the shear flow. Additionally, the effects of solid and liquid interfaces was investigated by the construction of surface and surfactant libraries at controlled and characterised flow conditions, which is an important aspect for the investigation of the distinct effect of these parameters.

Additionally, the development of novel methodologies involving the protein cross-linking on surface, the use of novel formulation surfactants and the stability characterisation using fluorescence spectroscopy, indicate that the study of aggregation is conducted via a broad range of perspectives including the aspects of formulation and equipment contact. It is also shown that the extensional flow device can be used as a screening formulation tool based on its ability to screen a range of surfactant molecules, and distinguishing suitable formulation candidates. The project also employed computational fluid dynamic simulations, predicting

that the formulation conditions of high concentrated protein molecules can affect the development of hydrodynamic forces. The employment of computational fluid dynamics also allows the flow characterisation, at controlled flow conditions, which is desired for the investigation of the flow induced aggregation.

9.4 Future work

The current work can be expanded in a number of areas, addressing several questions that will allow the development of further understanding of the mechanism of flow induced aggregation. In particular, the development of the microfluidic prototype device in chapter 4, section 4.5, shows that the particular device configuration is suitable for the addition of the microfluidic system onto the existing FPOP experimental setup. The particular set of experiments will allow to selectively apply fast oxidation of the protein molecules at regions of interest within the flow channel, such as the extensional flow event at the point of contraction. The fast oxidation of the protein molecule will allow distinguishing the peptide bonds that are responsible for potential structure perturbation induced by the protein unfolding under flow. This set of experiments will shed light into the early stages of protein unfolding and how the aggregation pathway can be driven by these early stages of unfolding, identifying the formation/refolding rates of aggregation mechanism. The novelty in the particular experiment is the exposure of molecules to the extensional flow and the ability to select and investigate the desired area within the flow channel, and correlate which protein building blocks are responsible for the protein unfolding.

Additionally, the expansion of surfactant screening experiments can identify the role of the presence of surfactants in the flow induced aggregation pathway for a broader range of protein molecules. From the results presented here, it was shown that the protective effect of surfactants is protein-dependent, which is important for their corresponding interaction with the protein molecules. Therefore, a more fundamental assessment of excipients can be conducted, which can help identify the mechanistic understanding of their presence in protein formulation when exposed to controlled flow conditions. The experimental methods presented in this work can be also linked to a more comprehensive formulation screening.

Building from the proof-of concept studies, previously presented in chapter 8, section 8.1, further work can be expanded on the investigation of flow interface effects compared to the diffusion-driven effects by considering the sliding interface system. From the time diffusion calculations, it is suggested that there is a dominance of flow-interface interactions compared to diffusion-driven effects, which motivates the further investigation of the flow interface interactions. The particular system allows the investigation of the parameters of interfaces in the absence of the extensional flow event induced by the sudden geometry contraction under the sliding action of plungers. This work can be further expanded on the

investigation of the role of interfaces under the action of plungers. From the second sub-study presented in section 8.2, the ability of microfluidic flow channels to expose molecules into higher extensional flow forces (strain rates), suggest the power of microfluidics to study a broader range of molecules with aggregation-resistant profiles. This set of experiments can be advantageous in the study of molecules with minimum aggregation propensity. With the use of these microfluidic systems, a further characterisation of molecules can be conducted and identifying how molecules, exposed to extremely high flow conditions, can respond. Additionally, the studies presented in the particular section, support the designing of a wider variety of flow profiles, including wait times, delays, times within various regions of the flow.

Another aspect of the project, that can be further developed, is to investigate the development of extensional flow through the application of alternative interface configurations. In the current work, the interfaces of interest are solid and liquid interfaces in combination with the application of the extensional flow. The potential aggregation pathways have been proposed based on the solid-liquid interfaces (figures 9.1 and 9.2) and may not capture all the aggregation pathways when considering the air-liquid interface. The effect of the air-liquid interface was mainly studied in literature in combination with shear flow rather than extensional flow. This implies, that with the modification of the experimental flow setup, the effect of air interface can be explored by the addition of an air interface within the syringe part.

Bibliography

[1] John Dobson, Amit Kumar, Leon F. Willis, Roman Tuma, Daniel R. Higazi, Richard Turner, David C. Lowe, Alison E. Ashcroft, Sheena E. Radford, and Nikil et al. Kapur. Inducing protein aggregation by extensional flow. *Proceedings of the National Academy of Sciences*, 114(18):4673–4678, 2017.

[2] Leon F. Willis, Amit Kumar, John Dobson, Nicholas J. Bond, David Lowe, Richard Turner, Sheena E. Radford, Nikil Kapur, and David J. Brockwell. Using extensional flow to reveal diverse aggregation landscapes for three igg1 molecules. *Biotechnology and Bioengineering*, 115(5):1216–1225, 2018.

[3] Leon F Willis, Amit Kumar, Tushar Jain, Isabelle Caffry, Yingda Xu, Sheena E Radford, Nikil Kapur, Maximiliano Vásquez, and David J Brockwell. The uniqueness of flow in probing the aggregation behavior of clinically relevant antibodies. *Engineering Reports*, 2(5):e12147, 2020.

[4] Tim J. Kamerzell, Reza Esfandiary, Sangeeta B. Joshi, C. Russell Middaugh, and David B. Volkin. Proteinexcipient interactions: Mechanisms and biophysical characterization applied to protein formulation development. *Advanced Drug Delivery Reviews*, 63(13):1118–1159, 2011. Formulating biomolecules: mechanistics insights in molecular interactions.

[5] Bilikallahalli K. Muralidhara and Marcus Wong. Critical considerations in the formulation development of parenteral biologic drugs. *Drug Discovery Today*, 25(3): 574–581, 2020.

[6] Tarik A. Khan, Hanns-Christian Mahler, and Ravuri S.K. Kishore. Key interactions of surfactants in therapeutic protein formulations: A review. *European Journal of Pharmaceutics and Biopharmaceutics*, 97:60–67, 2015.

[7] Nicholas G. Welch, Judith A. Scoble, Benjamin W. Muir, and Paul J. Pigram. Orientation and characterization of immobilized antibodies for improved immunoassays (review). *Biointerphases*, 12(2):02D301, 2017.

[8] Andrea Allmendinger, Stefan Fischer, Joerg Huwyler, Hanns-Christian Mahler, Edward Schwarb, Isidro E. Zarraga, and Robert Mueller. Rheological characterization and injection forces of concentrated protein formulations: An alternative predictive model for non-newtonian solutions. *European Journal of Pharmaceutics and Biopharmaceutics*, 87(2):318–328, 2014.

[9] Yoann Le Basle, Philip Chennell, Nicolas Tokhadze, Alain Astier, and Valérie

Sautou. Physicochemical stability of monoclonal antibodies: A review. *Journal of Pharmaceutical Sciences*, 109(1):169–190, 2020.

[10] Christopher J. Roberts. Therapeutic protein aggregation: mechanisms, design, and control. *Trends in Biotechnology*, 32(7):372–380, 2014.

[11] Moo Sun Hong, Kristen A. Severson, Mo Jiang, Amos E. Lu, J. Christopher Love, and Richard D. Braatz. Challenges and opportunities in biopharmaceutical manufacturing control. *Computers & Chemical Engineering*, 110:106–114, 2018.

[12] Jinjiang Li, Mary E. Krause, Xiaodong Chen, Yuan Cheng, Weiguo Dai, John J. Hill, Min Huang, Susan Jordan, Daniel LaCasse, and Linda et al. Narhi. Interfacial stress in the development of biologics: Fundamental understanding, current practice, and future perspective. *The AAPS Journal*, 21(3), 2019.

[13] Hanns-Christian Mahler, Wolfgang Friess, Ulla Grauschopf, and Sylvia Kiese. Protein aggregation: Pathways, induction factors and analysis. *Journal of Pharmaceutical Sciences*, 98(9):2909–2934, 2009.

[14] Ke Sherry Li, Liuqing Shi, and Michael L. Gross. Mass spectrometry-based fast photochemical oxidation of proteins (fpop) for higher order structure characterization. *Accounts of Chemical Research*, 51(3):736–744, 2018.

[15] Hyojin Lee Kim, Arnold Mcauley, and Joseph Mcguire. Protein effects on surfactant adsorption suggest the dominant mode of surfactant-mediated stabilization of protein. *Journal of Pharmaceutical Sciences*, 103(5):1337–1345, 2014.

[16] Ayoola T. Brimmo and Mohammad A. Qasaimeh. Stagnation point flows in analytical chemistry and life sciences. *RSC Advances*, 7(81):51206–51232, 2017.

[17] Innocent B. Bekard, Peter Asimakis, Joseph Bertolini, and Dave E. Dunstan. The effects of shear flow on protein structure and function. *Biopolymers*, pages n/a–n/a, 2011.

[18] Juan Jaspe and Stephen J. Hagen. Do protein molecules unfold in a simple shear flow? *Biophysical Journal*, 91(9):3415–3424, 2006.

[19] Yongzhi Qiu, Jordan Ciciliano, David R. Myers, Reginald Tran, and Wilbur A. Lam. Platelets and physics: How platelets feel and respond to their mechanical microenvironment. *Blood Reviews*, 29(6):377–386, 2015.

[20] Paul Egan, Robert Sinko, Philip R. LeDuc, and Sinan Keten. The role of mechanics in biological and bio-inspired systems. *Nature Communications*, 6(1), 2015.

[21] Shuyi Wu, Tengfei Fu, Renhui Qiu, and Luping Xu. Dna fragmentation in complicated flow fields created by micro-funnel shapes. *Soft Matter*, pages –, 2021.

[22] Yves F. Dufrene, Toshio Ando, Ricardo Garcia, David Alsteens, David Martinez-Martin, Andreas Engel, Christoph Gerber, and Daniel J. Muller. Imaging modes of atomic force microscopy for application in molecular and cell biology. *Nature Nanotechnology*, 12(4):295–307, 2017.

[23] Fulvio Grigolato and Paolo Arosio. The role of surfaces on amyloid formation. *Biophysical Chemistry*, 270:106533, 2021.

[24] Fulvio Grigolato and Paolo Arosio. Synergistic effects of flow and interfaces on antibody aggregation. *Biotechnology and Bioengineering*, 117(2):417–428, 2020.

[25] John F Douglas. *Fluid mechanics*. Pearson, 5 edition, 2007.

[26] Lauren D.C. Casa, David H. Deaton, and David N. Ku. Role of high shear rate in thrombosis. *Journal of Vascular Surgery*, 61(4):1068 – 1080, 2015.

[27] Henrik Bruus. *Theoretical microfluidics*. Oxford Univ.Press, 2011.

[28] S. Flink, F.C.J.M. van Veggel, and David Reinhoudt. Functionalization of self-assembled monolayers on glass and oxidized silicon wafers by surface reactions. *Journal of physical organic chemistry*, 14(7):407–415, 2001. 649.

[29] T Nakazumi and Y Hara. Influence of thickness of alkyl-silane coupling agent coating on separation of small dna fragments in capillary gel electrophoresis. *IOP Conference Series: Materials Science and Engineering*, 242:012034, 2017.

[30] Guisheng Zhuang and Jörg P Kutter. Anti-stiction coating of PDMS moulds for rapid microchannel fabrication by double replica moulding. *Journal of Micromechanics and Microengineering*, 21(10):105020, sep 2011.

[31] Feng Zhang, Ken Sautter, Adam M. Larsen, Daniel A. Findley, Robert C. Davis, Hussein Samha, and Matthew R. Linford. Chemical vapor deposition of three aminosilanes on silicon dioxide: Surface characterization, stability, effects of silane concentration, and cyanine dye adsorption. *Langmuir*, 26(18):14648–14654, 2010.

[32] Abraham Ulman. Formation and structure of self-assembled monolayers. *Chemical Reviews*, 96(4):1533–1554, 1996.

[33] Yuehua Yuan and T. Randall Lee. Contact angle and wetting properties. *Surface Science Techniques*, pages 3–34, 2013.

[34] Beatriz G. de la Torre and Fernando Albericio. The pharmaceutical industry in 2018. an analysis of fda drug approvals from the perspective of molecules. *Molecules*, 24(4), 2019.

[35] Ruei-Min Lu, Yu-Chyi Hwang, I-Ju Liu, Chi-Chiu Lee, Han-Zen Tsai, Hsin-Jung Li,

and Han-Chung Wu. Development of therapeutic antibodies for the treatment of diseases. *Journal of Biomedical Science*, 27(1), 2020.

[36] Dawn M Ecker, Susan Dana Jones, and Howard L Levine. The therapeutic monoclonal antibody market. *mAbs*, 7(1):9–14, 2015.

[37] Olga Obrezanova, Andreas Arnell, Ramón Gómez de la Cuesta, Maud E Berthelot, Thomas RA Gallagher, Jesús Zurdo, and Yvette Stallwood. Aggregation risk prediction for antibodies and its application to biotherapeutic development. *mAbs*, 7(2):352–363, 2015. PMID: 25760769.

[38] Melody Sauerborn, Vera Brinks, Wim Jiskoot, and Huub Schellekens. Immunological mechanism underlying the immune response to recombinant human protein therapeutics. *Trends in Pharmacological Sciences*, 31(2):53–59, 2010.

[39] Maria Vazquez-Rey and Dietmar A. Lang. Aggregates in monoclonal antibody manufacturing processes. *Biotechnology and Bioengineering*, 108(7):1494–1508, 2011.

[40] Charles Duchêne, Vasco Filipe, Sylvain Huille, and Anke Lindner. Clogging of microfluidic constrictions by monoclonal antibody aggregates: role of aggregate shape and deformability. *Soft Matter*, 16:921–928, 2020.

[41] Christopher A Ross and Michelle A Poirier. Protein aggregation and neurodegenerative disease. *Nature medicine*, 10(7):S10–S17, 2004.

[42] Lorenzo Gentiluomo, Dierk Roessner, Dillen Augustijn, Hristo Svilenov, Alina Kulakova, Sujata Mahapatra, Gerhard Winter, Werner Streicher, Åsmund Rinnan, Günther H.J. Peters, Pernille Harris, and Wolfgang Frie. Application of interpretable artificial neural networks to early monoclonal antibodies development. *European Journal of Pharmaceutics and Biopharmaceutics*, 141:81–89, 2019.

[43] Chava Kimchi-Sarfaty, Tal Schiller, Nobuko Hamasaki-Katagiri, Mansoor A. Khan, Chen Yanover, and Zuben E. Sauna. Building better drugs: developing and regulating engineered therapeutic proteins. *Trends in Pharmacological Sciences*, 34(10):534–548, 2013.

[44] Tim Dreckmann, Julien Boeuf, Imke-Sonja Ludwig, Jörg Lümkemann, and Jörg Huwyler. Low volume aseptic filling: Impact of pump systems on shear stress. *European Journal of Pharmaceutics and Biopharmaceutics*, 147:10–18, 2020.

[45] Adrian P. Defante, Cavan K. Kalonia, Emma Keegan, Steven M. Bishop, Hasige A. Satish, Steven D. Hudson, and Paul V. Santacroce. The impact of the metal interface on the stability and quality of a therapeutic fusion protein. *Molecular Pharmaceutics*, 2020.

[46] Alice R. Mazzer, Xavier Perraud, Jennifer Halley, John OHara, and Daniel G.

Bracewell. Protein a chromatography increases monoclonal antibody aggregation rate during subsequent low ph virus inactivation hold. *Journal of Chromatography A*, 1415:83–90, 2015.

[47] Wei Wang. Protein aggregation and its inhibition in biopharmaceutics. *International Journal of Pharmaceutics*, 289(1):1–30, 2005.

[48] Mary E. M. Cromwell, Eric Hilario, and Fred Jacobson. Protein aggregation and bioprocessing. *The AAPS Journal*, 8(3):E572–E579, 2006.

[49] Lisa A. Kueltzo, W.e.i. Wang, Theodore W. Randolph, and John F. Carpenter. Effects of solution conditions, processing parameters, and container materials on aggregation of a monoclonal antibody during freeze-thawing. *Journal of Pharmaceutical Sciences*, 97(5):1801–1812, 2008.

[50] Wei Wang and Satoshi Ohtake. Science and art of protein formulation development. *International Journal of Pharmaceutics*, 568:118505, 2019.

[51] Sébastien Dasnoy, Nancy Dezutter, Dominique Lemoine, Vivien Le Bras, and Véronique Préat. High-throughput screening of excipients intended to prevent antigen aggregation at air-liquid interface. *Pharmaceutical research*, 28(7):1591–1605, 2011.

[52] Tim Serno, John F Carpenter, Theodore W Randolph, and Gerhard Winter. Inhibition of agitation-induced aggregation of an igg-antibody by hydroxypropyl-β-cyclodextrin. *Journal of pharmaceutical sciences*, 99(3):1193–1206, 2010.

[53] Bin Yang, Dave J Adams, Maria Marlow, and Mischa Zelzer. Surface-mediated supramolecular self-assembly of protein, peptide, and nucleoside derivatives: From surface design to the underlying mechanism and tailored functions. *Langmuir*, 34 (50):15109–15125, 2018.

[54] Renuka Thirumangalathu, Sampathkumar Krishnan, Margaret Speed Ricci, David N. Brems, Theodore W. Randolph, and John F. Carpenter. Silicone oil- and agitation-induced aggregation of a monoclonal antibody in aqueous solution. *Journal of Pharmaceutical Sciences*, 98(9):3167–3181, 2009.

[55] LaToya S. Jones, Allyn Kaufmann, and C.Russell Middaugh. Silicone oil induced aggregation of proteins. *Journal of Pharmaceutical Sciences*, 94(4):918–927, 2005.

[56] Elena Krayukhina, Kouhei Tsumoto, Susumu Uchiyama, and Kiichi Fukui. Effects of syringe material and silicone oil lubrication on the stability of pharmaceutical proteins. *Journal of Pharmaceutical Sciences*, 104(2):527–535, 2015.

[57] Gregory V. Barnett, Vladimir I. Razinkov, Bruce A. Kerwin, Thomas M. Laue, Andrea H. Woodka, Paul D. Butler, Tatiana Perevozchikova, and Christopher J.

Roberts. Specific-ion effects on the aggregation mechanisms and proteinprotein interactions for anti-streptavidin immunoglobulin gamma-1. *The Journal of Physical Chemistry B*, 119(18):5793–5804, 2015. PMID: 25885209.

[58] Jared S. Bee, Jennifer L. Stevenson, Bhavya Mehta, Juraj Svitel, Joey Pollastrini, Robert Platz, Erwin Freund, John F. Carpenter, and Theodore W. Randolph. Response of a concentrated monoclonal antibody formulation to high shear. *Biotechnology and Bioengineering*, 103(5):936–943, 2009.

[59] Cavan K. Kalonia, Frank Heinrich, Joseph E. Curtis, Sid Raman, Maria A. Miller, and Steven D. Hudson. Protein adsorption and layer formation at the stainless steel-solution interface mediates shear-induced particle formation for an igg1 monoclonal antibody. *Molecular Pharmaceutics*, 15(3):1319–1331, 2018.

[60] Paul Roach, David Farrar, and Carole C. Perry. Interpretation of protein adsorption: Surface-induced conformational changes. *Journal of the American Chemical Society*, 127(22):8168–8173, 2005.

[61] David Richard Schmidt, Heather Waldeck, and Weiyuan John Kao. Protein adsorption to biomaterials. *Biological Interactions on Materials Surfaces*, pages 1–18, 2009.

[62] Qiang Wei, Katharina Achazi, Hendrik Liebe, Andrea Schulz, Paul-Ludwig Michael Noeske, Ingo Grunwald, and Rainer Haag. Mussel-inspired dendritic polymers as universal multifunctional coatings. *Angewandte Chemie International Edition*, 53 (43):11650–11655, 2014.

[63] B.E. Rabinow, Y.S. Ding, C. Qin, M.L. McHalsky, J.H. Schneider, K.A. Ashline, T.L. Shelbourn, and R.M. Albrecht. Biomaterials with permanent hydrophilic surfaces and low protein adsorption properties. *Journal of Biomaterials Science, Polymer Edition*, 6(1):91–109, 1995.

[64] Afsaneh Farjami, Mohammadreza Siahi-Shadbad, Parvin Akbarzadehlaleh, Khashayar Roshanzamir, and Ommoleila Molavi. Evaluation of the physicochemical and biological stability of cetuximab under various stress condition. *Journal of Pharmacy and Pharmaceutical Sciences*, 22(1):171–190, 2019.

[65] Ellen Koepf, Simon Eisele, Rudolf Schroeder, Gerald Brezesinski, and Wolfgang Friess. Notorious but not understood: how liquid-air interfacial stress triggers protein aggregation. *International journal of pharmaceutics*, 537(1-2):202–212, 2018.

[66] Mark Duerkop, Eva Berger, Astrid Dürauer, and Alois Jungbauer. Impact of cavitation, high shear stress and air/liquid interfaces on protein aggregation. *Biotechnology journal*, 13(7):1800062, 2018.

[67] Stefan Dengl, Marc Wehmer, Friederike Hesse, Florian Lipsmeier, Oliver Popp, and

Kurt Lang. Aggregation and chemical modification of monoclonal antibodies under upstream processing conditions. *Pharmaceutical research*, 30(5):1380–1399, 2013.

[68] Ulrich Brinkmann and Roland E Kontermann. The making of bispecific antibodies. In *MAbs*, volume 9, pages 182–212. Taylor & Francis, 2017.

[69] Fulvio Grigolato, Claudio Colombo, Raffaele Ferrari, Lenka Rezabkova, and Paolo Arosio. Mechanistic origin of the combined effect of surfaces and mechanical agitation on amyloid formation. *ACS Nano*, 11(11):11358–11367, 2017.

[70] James G Biddlecombe, Graeme Smith, Shahid Uddin, Sandrine Mulot, David Spencer, Chris Gee, Brendan C Fish, and Daniel G Bracewell. Factors influencing antibody stability at solid–liquid interfaces in a high shear environment. *Biotechnology progress*, 25(5):1499–1507, 2009.

[71] Marie R. G. Kopp, Umberto Capasso Palmiero, and Paolo Arosio. A nanoparticle-based assay to evaluate surface-induced antibody instability. *Molecular Pharmaceutics*, 17(3):909–918, 2020.

[72] Claire L Dobson, Paul WA Devine, Jonathan J Phillips, Daniel R Higazi, Christopher Lloyd, Bojana Popovic, Joanne Arnold, Andrew Buchanan, Arthur Lewis, Joanne Goodman, et al. Engineering the surface properties of a human monoclonal antibody prevents self-association and rapid clearance in vivo. *Scientific reports*, 6(1):1–14, 2016.

[73] Janice M Reichert, Clark J Rosensweig, Laura B Faden, and Matthew C Dewitz. Monoclonal antibody successes in the clinic. *Nature biotechnology*, 23(9):1073–1078, 2005.

[74] Janice M Reichert. Monoclonal antibodies as innovative therapeutics. *Current pharmaceutical biotechnology*, 9(6):423–430, 2008.

[75] Christine C. Lee, Joseph M. Perchiacca, and Peter M. Tessier. Toward aggregation-resistant antibodies by design. *Trends in Biotechnology*, 31(11):612–620, 2013.

[76] Nicholas APS Buss, Simon J Henderson, Mary McFarlane, Jacintha M Shenton, and Lolke de Haan. Monoclonal antibody therapeutics: history and future. *Current Opinion in Pharmacology*, 12(5):615–622, 2012. Anti-infectives New technologies.

[77] Marijn van der Neut Kolfschoten, Janine Schuurman, Mario Losen, Wim K. Bleeker, Pilar Martinez-Martinez, Ellen Vermeulen, Tamara H. den Bleker, Luus Wiegman, Tom Vink, and Lucien A. et al. Aarden. Anti-inflammatory activity of human igg4 antibodies by dynamic fab arm exchange. *Science*, 317(5844):1554–1557, 2007.

[78] Cecilia Napodano, MariaPaola Marino, Annunziata Stefanile, Krizia Pocino, Roberto Scatena, Francesca Gulli, Gian Lodovico Rapaccini, Stefano Delli Noci, Giovanna

Capozio, Donato Rigante, and Umberto Basile. Immunological role of igg subclasses. *Immunological Investigations*, 50(4):427–444, 2021.

[79] Wim Jiskoot, Theodore W. Randolph, David B. Volkin, C. Russell Middaugh, Christian Schoneich, Gerhard Winter, Wolfgang Friess, Daan J.A. Crommelin, and John F. Carpenter. Protein instability and immunogenicity: Roadblocks to clinical application of injectable protein delivery systems for sustained release. *Journal of Pharmaceutical Sciences*, 101(3):946–954, 2012.

[80] Brian Kelley. Industrialization of mab production technology: The bioprocessing industry at a crossroads. *mAbs*, 1(5):443–452, 2009.

[81] Mario Lebendiker and Tsafi Danieli. Production of prone-to-aggregate proteins. *FEBS Letters*, 588(2):236–246, 2013.

[82] Sumit Kumar Chaturvedi, Mohammad Khursheed Siddiqi, Parvez Alam, and Rizwan Hasan Khan. Protein misfolding and aggregation: Mechanism, factors and detection. *Process Biochemistry*, 51(9):1183–1192, 2016.

[83] John S. Philo. Is any measurement method optimal for all aggregate sizes and types? *The AAPS Journal*, 8(3):E564–E571, 2006.

[84] Mary E. M. Cromwell, Eric Hilario, and Fred Jacobson. Protein aggregation and bioprocessing. *The AAPS Journal*, 8(3):E572–E579, 2006.

[85] Oscar L. Ramos, Ricardo N. Pereira, Rui Rodrigues, Jose A. Teixeira, Antonio A. Vicente, and F. Xavier Malcata. Physical effects upon whey protein aggregation for nano-coating production. *Food Research International*, 66:344–355, 2014.

[86] Donald Voet, Judith G Voet, and Charlotte W Pratt. *Principles of biochemistry*. Wiley, 4 edition, 2013.

[87] Giovanni Salvi, Paolo De Los Rios, and Michele Vendruscolo. Effective interactions between chaotropic agents and proteins. *Proteins: Structure, Function, and Bioinformatics*, 61(3):492–499, 2005.

[88] Connie Lu, Dandan Liu, Hongbin Liu, and Paul Motchnik. Characterization of monoclonal antibody size variants containing extra light chains. *mAbs*, 5(1):102–113, 2013.

[89] Wei Wang, Y. John Wang, and D.Q. Wang. Dual effects of tween 80 on protein stability. *International Journal of Pharmaceutics*, 347(1):31–38, 2008.

[90] Ye Li, Vassiliy Lubchenko, and Peter G. Vekilov. The use of dynamic light scattering and brownian microscopy to characterize protein aggregation. *Review of Scientific Instruments*, 82(5):053106, 2011.

[91] John den Engelsman, Patrick Garidel, Ronald Smulders, Hans Koll, Bryan Smith, Stefan Bassarab, Andreas Seidl, Otmar Hainzl, and Wim Jiskoot. Strategies for the assessment of protein aggregates in pharmaceutical biotech product development. *Pharmaceutical Research*, 28(4):920–933, 2010.

[92] Brian C. Gau, Jiawei Chen, and Michael L. Gross. Fast photochemical oxidation of proteins for comparing solvent-accessibility changes accompanying protein folding: Data processing and application to barstar. *Biochimica et Biophysica Acta (BBA) - Proteins and Proteomics*, 1834(6):1230–1238, 2013.

[93] Shermeen A. Abbas, Greta Gaspar, Vikas K. Sharma, Thomas W. Patapoff, and Devendra S. Kalonia. Application of second-derivative fluorescence spectroscopy to monitor subtle changes in a monoclonal antibody structure. *Journal of Pharmaceutical Sciences*, 102(1):52–61, 2013.

[94] Joseph R Lakowicz. *Principles of fluorescence spectroscopy (3rd ed)*. Springer, 2006.

[95] Shujing Wang, Guoliang Wu, Xinyi Zhang, Zhou Tian, Ning Zhang, Tao Hu, Weiguo Dai, and Feng Qian. Stabilizing two igg1 monoclonal antibodies by surfactants: Balance between aggregation prevention and structure perturbation. *European Journal of Pharmaceutics and Biopharmaceutics*, 114:263–277, 2017.

[96] Mikael Lindgren, Karin Sörgjerd, and Per Hammarström. Detection and characterization of aggregates, prefibrillar amyloidogenic oligomers, and protofibrils using fluorescence spectroscopy. *Biophysical Journal*, 88(6):4200–4212, 2005.

[97] Kayoung Lee, Sang-Chul Shin, and Injoon Oh. Fluorescence spectroscopy studies on micellization of poloxamer 407 solution. *Archives of Pharmacal Research*, 26(8): 653–658, 2003.

[98] Hao Li, Danna Hu, Feiqing Liang, Xiaowei Huang, and Qiuhua Zhu. Influence factors on the critical micelle concentration determination using pyrene as a probe and a simple method of preparing samples. *Royal Society Open Science*, 7(3):192092, 2020.

[99] Stephanie K. Vargas, Aydin Eskafi, Eric Carter, and Natalie Ciaccio. A comparison of background membrane imaging versus flow technologies for subvisible particle analysis of biologics. *International Journal of Pharmaceutics*, 578:119072, 2020.

[100] Daniel Weinbuch, Wim Jiskoot, and Andrea Hawe. Light obscuration measurements of highly viscous solutions: Sample pressurization overcomes underestimation of subvisible particle counts. *The AAPS Journal*, 16(5):1128–1131, 2014.

[101] Deepak K. Sharma, Dave King, Peter Oma, and Clark Merchant. Micro-flow imaging: Flow microscopy applied to sub-visible particulate analysis in protein formulations. *The AAPS Journal*, 12(3):455–464, 2010.

[102] Constanze Helbig, Gregor Ammann, Tim Menzen, Wolfgang Friess, Klaus Wuchner, and Andrea Hawe. Backgrounded membrane imaging (bmi) for high-throughput characterization of subvisible particles during biopharmaceutical drug product development. *Journal of Pharmaceutical Sciences*, 109(1):264–276, 2020.

[103] Predrag Vujovic, Michael Chirillo, and Dee U Silverthorn. Learning (by) osmosis: an approach to teaching osmolarity and tonicity. *Advances in physiology education*, 42(4):626–635, 2018.

[104] Tsutomu Arakawa, Yoshiko Kita, and John F Carpenter. Protein–solvent interactions in pharmaceutical formulations. *Pharmaceutical research*, 8(3):285–291, 1991.

[105] Serge N. Timasheff. Control of protein stability and reactions by weakly interacting cosolvents: The simplicity of the complicated. In Enrico Di Cera, editor, *Linkage Thermodynamics of Macromolecular Interactions*, volume 51 of *Advances in Protein Chemistry*, pages 355–432. Academic Press, 1998.

[106] Aijun Wang, Andrew D Robertson, and DW Bolen. Effects of a naturally occurring compatible osmolyte on the internal dynamics of ribonuclease a. *Biochemistry*, 34 (46):15096–15104, 1995.

[107] Kelly J Frye and Catherine A Royer. The kinetic basis for the stabilization of staphylococcal nuclease by xylose. *Protein science*, 6(4):789–793, 1997.

[108] Brent S Kendrick, Byeong S Chang, Tsutomu Arakawa, Brian Peterson, Theodore W Randolph, Mark C Manning, and John F Carpenter. Preferential exclusion of sucrose from recombinant interleukin-1 receptor antagonist: role in restricted conformational mobility and compaction of native state. *Proceedings of the National Academy of Sciences*, 94(22):11917–11922, 1997.

[109] Maik Jacob and Franz X. Schmid. Protein folding as a diffusional process. *Biochemistry*, 38(42):13773–13779, 1999.

[110] Ana B. Moldes, Lorena Rodriguez-Lopez, Myriam Rincon-Fontan, Alejandro Lopez-Prieto, Xanel Vecino, and Jose M. Cruz. Synthetic and bio-derived surfactants versus microbial biosurfactants in the cosmetic industry: An overview. *International Journal of Molecular Sciences*, 22(5):2371, 2021.

[111] Bruce A. Kerwin. Polysorbates 20 and 80 used in the formulation of protein biotherapeutics: Structure and degradation pathways. *Journal of Pharmaceutical Sciences*, 97(8):2924–2935, 2008.

[112] Aadithya Kannan, Ian C. Shieh, and Gerald G. Fuller. Linking aggregation and interfacial properties in monoclonal antibody-surfactant formulations. *Journal of Colloid and Interface Science*, 550:128–138, 2019.

[113] Y. Summer Tein, Zhenhuan Zhang, and Norman J. Wagner. Competitive surface activity of monoclonal antibodies and nonionic surfactants at the airwater interface determined by interfacial rheology and neutron reflectometry. *Langmuir*, 36(27): 7814–7823, 2020.

[114] Ankit D. Kanthe, Mary Krause, Songyan Zheng, Andrew Ilott, Jinjiang Li, Wei Bu, Mrinal K. Bera, Binhua Lin, Charles Maldarelli, and Raymond S. Tu. Armoring the interface with surfactants to prevent the adsorption of monoclonal antibodies. *ACS Applied Materials & Interfaces*, 12(8):9977–9988, 2020.

[115] Meera Agarkhed, Courtney O'Dell, Ming-Ching Hsieh, Jingming Zhang, Joel Goldstein, and Arvind Srivastava. Effect of surfactants on mechanical, thermal, and photostability of a monoclonal antibody. *AAPS PharmSciTech*, 19(1):79–92, 2017.

[116] Aadithya Kannan, Ian C. Shieh, Patrick G. Negulescu, Vineeth Chandran Suja, and Gerald G. Fuller. Adsorption and aggregation of monoclonal antibodies at silicone oilwater interfaces. *Molecular Pharmaceutics*, 18(4):1656–1665, 2021. PMID: 33656340.

[117] Zhenhuan Zhang, Ann Marie Woys, Kunlun Hong, Christoph Grapentin, Tarik A. Khan, Isidro E. Zarraga, Norman J. Wagner, and Yun Liu. Adsorption of nonionic surfactant and monoclonal antibody on siliconized surface studied by neutron reflectometry. *Journal of Colloid and Interface Science*, 584:429–438, 2021.

[118] Zhenhuan Zhang, Sara Orski, Ann Marie Woys, Guangcui Yuan, Isidro E. Zarraga, Norman J. Wagner, and Yun Liu. Adsorption of polysorbate 20 and proteins on hydrophobic polystyrene surfaces studied by neutron reflectometry. *Colloids and Surfaces B: Biointerfaces*, 168:94–102, 2018. Honoring Piero Baglioni.

[119] Tsutomu Arakawa and Serge N. Timasheff. Stabilization of protein structure by sugars. *Biochemistry*, 21(25):6536–6544, 1982.

[120] Shermeen A. Abbas, Vikas K. Sharma, Thomas W. Patapoff, and Devendra S. Kalonia. Characterization of antibodypolyol interactions by static light scattering: Implications for physical stability of protein formulations. *International Journal of Pharmaceutics*, 448(2):382–389, 2013.

[121] Lu Liu, Wei Qi, Daniel K. Schwartz, Theodore W. Randolph, and John F. Carpenter. The effects of excipients on protein aggregation during agitation: An interfacial shear rheology study. *Journal of Pharmaceutical Sciences*, 102(8):2460–2470, 2013.

[122] Haripada Maity, Courtney O'Dell, Arvind Srivastava, and Joel Goldstein. Effects of arginine on photostability and thermal stability of igg1 monoclonal antibodies. *Current Pharmaceutical Biotechnology*, 10(8):761–766, 2009.

[123] Peter Hollowell, Zongyi Li, Xuzhi Hu, Sean Ruane, Cavan Kalonia, Christopher F.

van der Walle, and Jian R. Lu. Recent advances in studying interfacial adsorption of bioengineered monoclonal antibodies. *Molecules*, 25(9):2047, 2020.

[124] Benjamin Patrick Werner, Christian Schöneich, and Gerhard Winter. Silicone oil-free polymer syringes for the storage of therapeutic proteins. *Journal of Pharmaceutical Sciences*, 108(3):1148–1160, 2019.

[125] Roberto A. Depaz, Tzvetelina Chevolleau, Sébastien Jouffray, Roja Narwal, and Mariana N. Dimitrova. Cross-linked silicone coating: A novel prefilled syringe technology that reduces subvisible particles and maintains compatibility with biologics. *Journal of Pharmaceutical Sciences*, 103(5):1384–1393, 2014.

[126] Lea L. Sorret, Madison A. DeWinter, Daniel K. Schwartz, and Theodore W. Randolph. Protein-protein interactions controlling interfacial aggregation of rhil-1ra are not described by simple colloid models. *Protein Science*, 27(7):1191–1204, 2018.

[127] Shravan Sreenivasan, Wim Jiskoot, and Anurag S. Rathore. Rapid aggregation of therapeutic monoclonal antibodies by bubbling induced air/liquid interfacial and agitation stress at different conditions. *European Journal of Pharmaceutics and Biopharmaceutics*, 168:97–109, 2021.

[128] C. R. Thomas and D. Geer. Effects of shear on proteins in solution. *Biotechnology Letters*, 33(3):443–456, 2010.

[129] S. Simon, H. J. Krause, C. Weber, and W. Peukert. Physical degradation of proteins in well-defined fluid flows studied within a four-roll apparatus. *Biotechnology and Bioengineering*, 108(12):2914–2922, 2011.

[130] Innocent B. Bekard and Dave E. Dunstan. Shear-induced deformation of bovine insulin in couette flow. *The Journal of Physical Chemistry B*, 113(25):8453–8457, 2009. PMID: 19534559.

[131] S. W. Schneider, S. Nuschele, A. Wixforth, C. Gorzelanny, A. Alexander-Katz, R. R. Netz, and M. F. Schneider. Shear-induced unfolding triggers adhesion of von willebrand factor fibers. *Proceedings of the National Academy of Sciences*, 104(19): 7899–7903, 2007.

[132] Rose J. Brazilek, Francisco J. Tovar-Lopez, Angus K. T. Wong, Huyen Tran, Amanda S. Davis, James D. McFadyen, Zane Kaplan, Sanjeev Chunilal, Shaun P. Jackson, and Harshal et al. Nandurkar. Application of a strain rate gradient microfluidic device to von willebrand's disease screening. *Lab on a Chip*, 17(15):2595–2608, 2017.

[133] Johanna Wiesbauer, Massimiliano Cardinale, and Bernd Nidetzky. Shaking and stirring: Comparison of controlled laboratory stress conditions applied to the human growth hormone. *Process Biochemistry*, 48(1):33–40, 2013.

[134] Svenja Lippok, Matthias Radtke, Tobias Obser, Lars Kleemeier, Reinhard Schneppenheim, Ulrich Budde, Roland R. Netz, and Joachim O. Radler. Shear-induced unfolding and enzymatic cleavage of full-length vwf multimers. *Biophysical Journal*, 110(3):545–554, 2016.

[135] Young Bok Bae, Hye Kyeong Jang, Tae Hwan Shin, Geetika Phukan, Thanh Tinh Tran, Gwang Lee, Wook Ryol Hwang, and Ju Min Kim. Microfluidic assessment of mechanical cell damage by extensional stress. *Lab on a Chip*, 16(1):96–103, 2016.

[136] Rebecca Dylla-Spears, Jacqueline E. Townsend, Linda Jen-Jacobson, Lydia L. Sohn, and Susan J. Muller. Single-molecule sequence detection via microfluidic planar extensional flow at a stagnation point. *Lab on a Chip*, 10(12):1543, 2010.

[137] Abraham Tamir and B. Huang. Impinging stream reactors: Fundamentals and applications. *Drying Technology*, 13(1-2):503–504, 1995.

[138] Clarence G Hermansky and David V Boger. Opposing-jet viscometry of fluids with viscosity approaching that of water. *Journal of Non-Newtonian Fluid Mechanics*, 56 (1):1–14, 1995.

[139] Song L. Ng, Robert P. Mun, David V. Boger, and David F. James. Extensional viscosity measurements of dilute solutions of various polymers. *Journal of Non-Newtonian Fluid Mechanics*, 65(2-3):291–298, 1996.

[140] P. Szymczak and Marek Cieplak. Proteins in a shear flow. *The Journal of Chemical Physics*, 127(15):155106, 2007.

[141] Lorna Ashton, Jonathan Dusting, Eboshogwe Imomoh, Stavroula Balabani, and Ewan W. Blanch. Shear-induced unfolding of lysozyme monitored in situ. *Biophysical Journal*, 96(10):4231–4236, 2009.

[142] Christophe O. Chantre, Patrick H. Campbell, Holly M. Golecki, Adrian T. Buganza, Andrew K. Capulli, Leila F. Deravi, Stephanie Dauth, Sean P. Sheehy, Jeffrey A. Paten, Karl Gledhill, Yanne S. Doucet, Hasan E. Abaci, Seungkuk Ahn, Benjamin D. Pope, Jeffrey W. Ruberti, Simon P. Hoerstrup, Angela M. Christiano, and Kevin Kit Parker. Production-scale fibronectin nanofibers promote wound closure and tissue repair in a dermal mouse model. *Biomaterials*, 166:96–108, 2018.

[143] S. Rammensee, U. Slotta, T. Scheibel, and A. R. Bausch. Assembly mechanism of recombinant spider silk proteins. *Proceedings of the National Academy of Sciences*, 105(18):6590–6595, 2008.

[144] Yi Shen, Francesco Simone Ruggeri, Daniele Vigolo, Ayaka Kamada, Seema Qamar, Aviad Levin, Christiane Iserman, Simon Alberti, Peter St George-Hyslop, and Tuomas P. J. Knowles. Biomolecular condensates undergo a generic shear-mediated liquid-to-solid transition. *Nature Nanotechnology*, 15(10):841–847, 2020.

[145] Joon Seok Lee, Eujin Um, Je-Kyun Park, and Chan Beum Park. Microfluidic self-assembly of insulin monomers into amyloid fibrils on a solid surface. *Langmuir*, 24(14):7068–7071, 2008.

[146] Joon Seok Lee, Jungki Ryu, and Chan Beum Park. High-throughput analysis of alzheimer's β-amyloid aggregation using a microfluidic self-assembly of monomers. *Analytical Chemistry*, 81(7):2751–2759, 2009.

[147] T. P. J. Knowles, D. A. White, A. R. Abate, J. J. Agresti, S. I. A. Cohen, R. A. Sperling, E. J. De Genst, C. M. Dobson, and D. A. Weitz. Observation of spatial propagation of amyloid assembly from single nuclei. *Proceedings of the National Academy of Sciences*, 108(36):14746–14751, 2011.

[148] Vito Fodera, Stefano Pagliara, Oliver Otto, Ulrich F. Keyser, and Athene M. Donald. Microfluidics reveals a flow-induced large-scale polymorphism of protein aggregates. *The Journal of Physical Chemistry Letters*, 3(19):2803–2807, 2012.

[149] Lingling Shui, Johan G Bomer, Mingliang Jin, Edwin T Carlen, and Albert van den Berg. Microfluidic dna fragmentation for on-chip genomic analysis. *Nanotechnology*, 22(49):494013, 2011.

[150] Francisco Javier Tovar-Lopez, Gary Rosengarten, Erik Westein, Khashayar Khoshmanesh, Shaun P. Jackson, Arnan Mitchell, and Warwick S. Nesbitt. A microfluidics device to monitor platelet aggregation dynamics in response to strain rate microgradients in flowing blood. *Lab Chip*, 10:291–302, 2010.

[151] Yunduo Charles Zhao, Parham Vatankhah, Tiffany Goh, Rhys Michelis, Kiarash Kyanian, Yingqi Zhang, Zhiyong Li, and Lining Arnold Ju. Hemodynamic analysis for stenosis microfluidic model of thrombosis with refined computational fluid dynamics simulation. *Scientific Reports*, 11(1), 2021.

[152] Sahar Salehi, Kim Koeck, and Thomas Scheibel. Spider silk for tissue engineering applications. *Molecules*, 25(3):737, 2020.

[153] Andreas Koeppel, Nicola Stehling, Cornelia Rodenburg, and Chris Holland. Spinning beta silks requires both ph activation and extensional stress. *Advanced Functional Materials*, 31(30):2103295, 2021.

[154] Li Lu, Suna Fan, Lihong Geng, Jinyou Lin, Xiang Yao, and Yaopeng Zhang. Flow analysis of regenerated silk fibroin/cellulose nanofiber suspensions via a bioinspired microfluidic chip. *Advanced Materials Technologies*, 6(10):2100124, 2021.

[155] Nathalie Gonska, Patricia A. Lopez, Paloma Lozano-Picazo, Michael Thorpe, Gustavo V. Guinea, Jan Johansson, Andreas Barth, Jose Perez-Rigueiro, and Anna Rising. Structure-function relationship of artificial spider silk fibers produced by straining flow spinning. *Biomacromolecules*, 21(6):2116–2124, 2020.

[156] Jonathan W. Larson, Gregory R. Yantz, Qun Zhong, Rebecca Charnas, Christina M. DAntoni, Michael V. Gallo, Kimberly A. Gillis, Lori A. Neely, Kevin M. Phillips, Gordon G. Wong, Steven R. Gullans, and Rudolf Gilmanshin. Single dna molecule stretching in sudden mixed shear and elongational microflows. *Lab Chip*, 6:1187–1199, 2006.

[157] H. Dakhil, S. K. Basu, S. Steiner, Y. Gerlach, A. Soller, Sharadwata Pan, Natalie Germann, M. Leidenberger, B. Kappes, and A. Wierschem. Buffered λ-dna solutions at high shear rates. *Journal of Rheology*, 65(2):159–169, 2021.

[158] Elena Paslaru, Mihaela Cristina Baican, Elena Gabriela Hitruc, Manuela Tatiana Nistor, Fabienne Poncin-Epaillard, and Cornelia Vasile. Immunoglobulin g immobilization on pvdf surface. *Colloids and Surfaces B: Biointerfaces*, 115:139–149, 2014.

[159] Nicholas G. Welch, Robert M.T. Madiona, Thomas B. Payten, Christopher D. Easton, Luisa Pontes-Braz, Narelle Brack, Judith A. Scoble, Benjamin W. Muir, and Paul J. Pigram. Surface immobilized antibody orientation determined using tof-sims and multivariate analysis. *Acta Biomaterialia*, 55:172–182, 2017.

[160] Nicholas G. Welch, Christopher D. Easton, Judith A. Scoble, Charlotte C. Williams, Paul J. Pigram, and Benjamin W. Muir. A chemiluminescent sandwich elisa enhancement method using a chromium (iii) coordination complex. *Journal of Immunological Methods*, 438:59–66, 2016.

[161] Nicholas G. Welch, Judith A. Scoble, Christopher D. Easton, Charlotte C. Williams, Barry J. Bradford, Laman K. Mamedova, Paul J. Pigram, and Benjamin W. Muir. High-throughput production of chromium(iii) complexes for antibody immobilization. *Analytical Chemistry*, 88(20):10102–10110, 2016.

[162] Adarsh D. Radadia, Courtney J. Stavis, Rogan Carr, Hongjun Zeng, William P. King, John A. Carlisle, Aleksei Aksimentiev, Robert J. Hamers, and Rashid Bashir. Control of nanoscale environment to improve stability of immobilized proteins on diamond surfaces. *Advanced Functional Materials*, 21(6):1040–1050, 2011.

[163] Sandipan Ray, Gunjan Mehta, and Sanjeeva Srivastava. Label-free detection techniques for protein microarrays: Prospects, merits and challenges. *PROTEOMICS*, 10(4):731–748, 2010.

[164] Hans Elwing. Protein absorption and ellipsometry in biomaterial research. *Biomaterials*, 19(4-5):397–406, 1998.

[165] Zigmas Balevicius, Almira Ramanaviciene, Ieva Baleviciute, Asta Makaraviciute, Lina Mikoliunaite, and Arunas Ramanavicius. Evaluation of intact- and fragmented-

antibody based immunosensors by total internal reflection ellipsometry. *Sensors and Actuators B: Chemical*, 160(1):555–562, 2011.

[166] Young Min Bae, Byung-Keun Oh, Woochang Lee, Won Hong Lee, and Jeong-Woo Choi. Study on orientation of immunoglobulin g on protein g layer. *Biosensors and Bioelectronics*, 21(1):103–110, 2005.

[167] Zhanhui Wang and Gang Jin. Feasibility of protein a for the oriented immobilization of immunoglobulin on silicon surface for a biosensor with imaging ellipsometry. *Journal of Biochemical and Biophysical Methods*, 57(3):203–211, 2003.

[168] Zhan-Hui Wang and Gang Jin. Silicon surface modification with a mixed silanes layer to immobilize proteins for biosensor with imaging ellipsometry. *Colloids and Surfaces B: Biointerfaces*, 34(3):173–177, 2004.

[169] Hong Yan Song, Jonathan Hobley, Xiaodi Su, and Xiaodong Zhou. End-on covalent antibody immobilization on dual polarization interferometry sensor chip for enhanced immuno-sensing. *Plasmonics*, 9(4):851–858, 2014.

[170] Jorge Escorihuela, Miguel Angel Gonzalez-Martinez, Jose Luis Lopez-Paz, Rosa Puchades, Angel Maquieira, and David Gimenez-Romero. Dual-polarization interferometry: A novel technique to light up the nanomolecular world. *Chemical Reviews*, 115(1):265–294, 2014.

[171] Hong Yan Song, Xiaodong Zhou, Jonathan Hobley, and Xiaodi Su. Comparative study of random and oriented antibody immobilization as measured by dual polarization interferometry and surface plasmon resonance spectroscopy. *Langmuir*, 28 (1):997–1004, 2011.

[172] E. Mauriz, M.C. Garcia-Fernandez, and L.M. Lechuga. Towards the design of universal immunosurfaces for spr-based assays: A review. *TrAC Trends in Analytical Chemistry*, 79:191–198, 2016.

[173] Sandeep Kumar Vashist, Chandra Kumar Dixit, Brian D. MacCraith, and Richard O'Kennedy. Effect of antibody immobilization strategies on the analytical performance of a surface plasmon resonance-based immunoassay. *The Analyst*, 136(21): 4431, 2011.

[174] Jia Zhang, Ying Sun, Qiong Wu, Hua Zhang, Yu Bai, and Daqian Song. A protein a modified au-graphene oxide composite as an enhanced sensing platform for spr-based immunoassay. *The Analyst*, 138(23):7175, 2013.

[175] Hongxia Chen, Junyi Huang, Jaebeom Lee, Sungu Hwang, and Kwangnak Koh. Surface plasmon resonance spectroscopic characterization of antibody orientation and activity on the calixarene monolayer. *Sensors and Actuators B: Chemical*, 147 (2):548–553, 2010.

[176] Hai Xu, Xiubo Zhao, Colin Grant, Jian R. Lu, David E. Williams, and Jeff Penfold. Orientation of a monoclonal antibody adsorbed at the solid/solution interface: A combined study using atomic force microscopy and neutron reflectivity. *Langmuir*, 22(14):6313–6320, 2006.

[177] Xiubo Zhao, Fang Pan, Luis Garcia-Gancedo, Andrew J. Flewitt, Gregory M. Ashley, Jikui Luo, and Jian R. Lu. Interfacial recognition of human prostate-specific antigen by immobilized monoclonal antibody: effects of solution conditions and surface chemistry. *Journal of The Royal Society Interface*, 9(75):2457–2467, 2012.

[178] Xiubo Zhao, Fang Pan, Ben Cowsill, Jian R. Lu, Luis Garcia-Gancedo, Andrew J. Flewitt, Gregory M. Ashley, and Jikui Luo. Interfacial immobilization of monoclonal antibody and detection of human prostate-specific antigen. *Langmuir*, 27(12): 7654–7662, 2011.

[179] Emanuel Schneck, Ida Berts, Avraham Halperin, Jean Daillant, and Giovanna Fragneto. Neutron reflectometry from poly (ethylene-glycol) brushes binding anti-peg antibodies: Evidence of ternary adsorption. *Biomaterials*, 46:95–104, 2015.

[180] R. Funari, B. Della Ventura, C. Altucci, A. Offenhausser, D. Mayer, and R. Velotta. Single molecule characterization of uv-activated antibodies on gold by atomic force microscopy. *Langmuir*, 32(32):8084–8091, 2016.

[181] Xudong Deng, Mengsu Chen, Qiang Fu, Niels M. B. Smeets, Fei Xu, Zhuyuan Zhang, Carlos D. M. Filipe, and Todd Hoare. A highly sensitive immunosorbent assay based on biotinylated graphene oxide and the quartz crystal microbalance. *ACS Applied Materials & Interfaces*, 8(3):1893–1902, 2016.

[182] Rashida Akter, Choong Kyun Rhee, and Md. Aminur Rahman. A highly sensitive quartz crystal microbalance immunosensor based on magnetic bead-supported bi-enzymes catalyzed mass enhancement strategy. *Biosensors and Bioelectronics*, 66: 539–546, 2015.

[183] V. Lebec, S. Boujday, C. Poleunis, C.-M. Pradier, and A. Delcorte. Time-of-flight secondary ion mass spectrometry investigation of the orientation of adsorbed antibodies on sams correlated to biorecognition tests. *The Journal of Physical Chemistry C*, 118(4):2085–2092, 2014.

[184] Rami N. Foster, Elisa T. Harrison, and David G. Castner. Tof-sims and xps characterization of protein films adsorbed onto bare and sodium styrenesulfonate-grafted gold substrates. *Langmuir*, 32(13):3207–3216, 2016.

[185] Newton T. Samuel, M. S. Wagner, K. D. Dornfeld, and David G. Castner. Analysis of poly(amino acids) by static time-of-flight secondary ion mass spectrometry (tof-sims). *Surface Science Spectra*, 8(3):163–184, 2001.

[186] Young-Pil Kim, Mi-Young Hong, Jinmo Kim, Eunkeu Oh, Hyun Kyong Shon, Dae Won Moon, Hak-Sung Kim, and Tae Geol Lee. Quantitative analysis of surface-immobilized protein by tof-sims: Effects of protein orientation and trehalose additive. *Analytical Chemistry*, 79(4):1377–1385, 2007.

[187] Loren Baugh, Tobias Weidner, J. E. Baio, Phuong-Cac T. Nguyen, Lara J. Gamble, Patrick S. Stayton, and David G. Castner. Probing the orientation of surface-immobilized protein g b1 using tof-sims, sum frequency generation, and nexafs spectroscopy. *Langmuir*, 26(21):16434–16441, 2010.

[188] Hua Wang, David G. Castner, Buddy D. Ratner, and Shaoyi Jiang. Probing the orientation of surface-immobilized immunoglobulin g by time-of-flight secondary ion mass spectrometry. *Langmuir*, 20(5):1877–1887, 2004.

[189] Nicholas G. Welch, Robert M. T. Madiona, Thomas B. Payten, Robert T. Jones, Narelle Brack, Benjamin W. Muir, and Paul J. Pigram. Surface adsorbed antibody characterization using tof-sims with principal component analysis and artificial neural networks. *Langmuir*, 32(34):8717–8728, 2016.

[190] Nicholas G. Welch, Robert M. T. Madiona, Judith A. Scoble, Benjamin W. Muir, and Paul J. Pigram. Tof-sims and principal component analysis investigation of denatured, surface-adsorbed antibodies. *Langmuir*, 32(42):10824–10834, 2016.

[191] Andrew G. Richter and Ivan Kuzmenko. Using in situ x-ray reflectivity to study protein adsorption on hydrophilic and hydrophobic surfaces: Benefits and limitations. *Langmuir*, 29(17):5167–5180, 2013.

[192] Gunnar Dunér, Esben Thormann, and Andra Ddinait. Quartz crystal microbalance with dissipation (qcm-d) studies of the viscoelastic response from a continuously growing grafted polyelectrolyte layer. *Journal of Colloid and Interface Science*, 408: 229–234, 2013.

[193] Matthew C. Dixon. Quartz crystal microbalance with dissipation monitoring: Enabling real-time characterization of biological materials and their interactions. *Journal of biomolecular techniques : JBT*, 19(3):151–158, 2008.

[194] Leopoldo Laricchia-Robbio and Roberto P Revoltella. Comparison between the surface plasmon resonance (spr) and the quartz crystal microbalance (qcm) method in a structural analysis of human endothelin-1. *Biosensors and Bioelectronics*, 19 (12):1753–1758, 2004.

[195] Jenny Malmstrom, Hossein Agheli, Peter Kingshott, and Duncan S. Sutherland. Viscoelastic modeling of highly hydrated laminin layers at homogeneous and nanostructured surfaces:? quantification of protein layer properties using qcm-d and spr. *Langmuir*, 23(19):9760–9768, 2007.

[196] Jacob L. Jordan and Erik J. Fernandez. Qcm-d sensitivity to protein adsorption reversibility. *Biotechnology and Bioengineering*, 101(4):837–842, 2008.

[197] Sebastian J. Kapp, Iben Larsson, Marco Van De Weert, Marité Cárdenas, and Lene Jorgensen. Competitive adsorption of monoclonal antibodies and nonionic surfactants at solid hydrophobic surfaces. *Journal of Pharmaceutical Sciences*, 104 (2):593–601, 2015.

[198] David J. Brockwell, Godfrey S. Beddard, Emanuele Paci, Dan K. West, Peter D. Olmsted, D. Alastair Smith, and Sheena E. Radford. Mechanically unfolding the small, topologically simple protein l. *Biophysical Journal*, 89(1):506–519, 2005.

[199] Marzia Marciello, Marco Filice, David Olea, Marisela Velez, Jose M. Guisan, and Cesar Mateo. Useful oriented immobilization of antibodies on chimeric magnetic particles: Direct correlation of biomacromolecule orientation with biological activity by afm studies. *Langmuir*, 30(49):15022–15030, 2014.

[200] Jiangtao Zhou, Francesco S. Ruggeri, Manuela R. Zimmermann, Georg Meisl, Giovanni Longo, Sergey K. Sekatskii, Tuomas P. J. Knowles, and Giovanni Dietler. Effects of sedimentation, microgravity, hydrodynamic mixing and air-water interface on a-synuclein amyloid formation. *Chemical Science*, 11(14):3687–3693, 2020.

[201] Jiangtao Zhou, Leonardo Venturelli, Ludovic Keiser, Sergey K. Sekatskii, Francois Gallaire, Sandor Kasas, Giovanni Longo, Tuomas P. J. Knowles, Francesco S. Ruggeri, and Giovanni Dietler. Environmental control of amyloid polymorphism by modulation of hydrodynamic stress. *ACS Nano*, 15(1):944–953, 2020.

[202] Joe A. Adam, Hannah R. Middlestead, Nicholas E. Debono, and Amir H. Hirsa. Effects of shear rate and protein concentration on amyloidogenesis via interfacial shear. *The Journal of Physical Chemistry B*, 125(36):10355–10363, 2021.

[203] Yuh-Fun Maa and Chung C. Hsu. Protein denaturation by combined effect of shear and air-liquid interface. *Biotechnology and Bioengineering*, 54(6):503–512, 1997.

[204] Matthew Hoehne, Fauna Samuel, Aichun Dong, Christine Wurth, Hanns-Christian Mahler, John F. Carpenter, and Theodore W. Randolph. Adsorption of monoclonal antibodies to glass microparticles. *Journal of Pharmaceutical Sciences*, 100(1): 123–132, 2011.

[205] Jared S. Bee, Michele Davis, Erwin Freund, John F. Carpenter, and Theodore W. Randolph. Aggregation of a monoclonal antibody induced by adsorption to stainless steel. *Biotechnology and Bioengineering*, 105(1):121–129, 2010.

[206] Sanli Movafaghi, Hao Wu, Irene M. Francino Urdániz, David S. Bull, Mary D. Kelly, Theodore W. Randolph, and Andrew P. Goodwin. The effect of container surface

passivation on aggregation of intravenous immunoglobulin induced by mechanical shock. *Biotechnology Journal*, 15(9):2000096, 2020.

[207] Shih-Hang Chang and Yuan-Chien Hsiao. Surface and protein adsorption properties of 316l stainless steel modified with polycaprolactone film. *Polymers*, 9(12):545, 2017.

[208] Cheng Her, Laura M. Tanenbaum, Swati Bandi, Theodore W. Randolph, Renuka Thirumangalathu, Krishna M.G. Mallela, John F. Carpenter, and Yannick Elias. Effects of tubing type, operating parameters, and surfactants on particle formation during peristaltic filling pump processing of a mab formulation. *Journal of Pharmaceutical Sciences*, 109(4):1439–1448, 2020.

[209] Kirk Roffi, Li Li, and Jacob Pantazis. Adsorbed protein film on pump surfaces leads to particle formation during fill-finish manufacturing. *Biotechnology and Bioengineering*, 118(8):2947–2957, 2021.

[210] Tetsuo Torisu, Takahiro Maruno, Yoshinori Hamaji, Tadayasu Ohkubo, and Susumu Uchiyama. Synergistic effect of cavitation and agitation on protein aggregation. *Journal of Pharmaceutical Sciences*, 106(2):521–529, 2017.

[211] Jared S. Bee, David Chiu, Suzanne Sawicki, Jennifer L. Stevenson, Koustuv Chatterjee, Erwin Freund, John F. Carpenter, and Theodore W. Randolph. Monoclonal antibody interactions with micro- and nanoparticles: Adsorption, aggregation, and accelerated stress studies. *Journal of Pharmaceutical Sciences*, 98(9):3218–3238, 2009.

[212] K. A Athanasiou and Roman M Natoli. *Introduction to continuum biomechanics*. Morgan and Claypool Publishers, 2009.

[213] Paul Yager. Basic microfluidic concepts, 2017. URL `http://faculty.washington.edu/yagerp/microfluidicstutorial/basicconcepts/basicconcepts.htm`.

[214] N. D. Sylvester and S. L. Rosen. Laminar flow in the entrance region of a cylindrical tube: Part i. newtonian fluids. *AIChE Journal*, 16(6):964–966, 1970.

[215] Jiyuan Tu, Guan-Heng Yeoh, and Chaoqun Liu. Chapter 1 - introduction. In Jiyuan Tu, Guan-Heng Yeoh, and Chaoqun Liu, editors, *Computational Fluid Dynamics (Second Edition)*, pages 1 – 29. Butterworth-Heinemann, second edition edition, 2013. ISBN 978-0-08-098243-4.

[216] *COMSOL Multiphysics Reference Manual*. 2019. URL `https://doc.comsol.com/5.5/doc/com.comsol.help.comsol/COMSOL_ReferenceManual.pdf`.

[217] William L. Oberkampf and Timothy G. Trucano. Verification and validation in computational fluid dynamics. *Progress in Aerospace Sciences*, 38(3):209–272, 2002.

[218] Jun Liu, Mary D.H. Nguyen, James D. Andya, and Steven J. Shire. Reversible self-association increases the viscosity of a concentrated monoclonal antibody in aqueous solution. *Journal of Pharmaceutical Sciences*, 94(9):1928–1940, 2005.

[219] Nitin Rathore, Pratik Pranay, Joseph Bernacki, Bruce Eu, Wenchang Ji, and Ed Walls. Characterization of protein rheology and delivery forces for combination products. *Journal of Pharmaceutical Sciences*, 101(12):4472–4480, 2012.

[220] Dheeraj S. Tomar, Sandeep Kumar, Satish K. Singh, Sumit Goswami, and Li Li. Molecular basis of high viscosity in concentrated antibody solutions: Strategies for high concentration drug product development. *mAbs*, 8(2):216–228, 2016.

[221] Alfredo Lanzaro, Aisling Roche, Nicole Sibanda, Daniel Corbett, Peter Davis, Maryam Shah, Jai A Pathak, Shahid Uddin, Christopher F van der Walle, Xue-Feng Yuan, et al. Cluster percolation causes shear thinning behavior in concentrated solutions of monoclonal antibodies. *Molecular Pharmaceutics*, 2021.

[222] Teddy J. Zbacnik, Ryan E. Holcomb, Derrick S. Katayama, Brian M. Murphy, Robert W. Payne, Richard C. Coccaro, Gabriel J. Evans, James E. Matsuura, Charles S. Henry, and Mark Cornell Manning. Role of buffers in protein formulations. *Journal of Pharmaceutical Sciences*, 106(3):713–733, 2017.

[223] M. Lessel, O. Bäumchen, M. Klos, H. Hähl, R. Fetzer, M. Paulus, R. Seemann, and K. Jacobs. Self-assembled silane monolayers: an efficient step-by-step recipe for high-quality, low energy surfaces. *Surface and Interface Analysis*, 47(5):557–564, 2015.

[224] Malgorzata Adamkiewicz, Tony O'Hara, David O'Hagan, and Georg Hahner. A vapor phase deposition of self-assembled monolayers: Vinyl-terminated films of volatile silanes on silicon oxide substrates. *Thin Solid Films*, 520(22):6719–6723, 2012.

[225] Hiroyuki Sugimura, Atsushi Hozumi, Tetsuya Kameyama, and Osamu Takai. Organosilane self-assembled monolayers formed at the vapour/solid interface. *Surface and Interface Analysis*, 34(1):550–554, 2002.

[226] Amol Chandekar, Sandip K. Sengupta, and James E. Whitten. Thermal stability of thiol and silane monolayers: A comparative study. *Applied Surface Science*, 256(9): 2742–2749, 2010.

[227] H.-J. Himmel, Ch. Woll, R. Gerlach, G. Polanski, and H.-G. Rubahn. Structure of heptanethiolate monolayers on au(111): Adsorption from solution vs vapor deposition. *Langmuir*, 13(4):602–605, 1997.

[228] Hisham M Abourayana, Nuri A Zreiba, and Abdulkader M Elamin. Synthesis

and characterization of plasma polymerized thin films deposited from benzene and hexamethyldisiloxane using (pecvd) method. *Eng. and tech*, 74:295–300, 2011.

[229] Jay W Grate, Marvin G Warner, Jonathan W Pittman, Karl J Dehoff, Thomas W Wietsma, Changyong Zhang, and Mart Oostrom. Silane modification of glass and silica surfaces to obtain equally oil-wet surfaces in glass-covered silicon micromodel applications. *Water Resources Research*, 49(8):4724–4729, 2013.

[230] Htet H Kyaw, Salim H Al-Harthi, Azzouz Sellai, and Joydeep Dutta. Self-organization of gold nanoparticles on silanated surfaces. *Beilstein journal of nanotechnology*, 6: 2345, 2015.

[231] J Li and XZ Li. Tribological characteristics of self-assembled nanometer film deposited on phosphorylated 3-aminopropyltriethoxysilane. *Bulletin of Materials Science*, 34 (3):583–588, 2011.

[232] Luc Sero, Lionel Sanguinet, Severine Derbre, Frank Boury, Guillaume Brotons, Sylvie Dabos-Seignon, Pascal Richomme, and Denis Seraphin. Fluorescent self-assembled monolayers of umbelliferone: A relationship between contact angle and fluorescence. *Langmuir*, 29(33):10423–10431, 2013.

[233] Gelest. Hydrophobicity, hydrophilicity and silane surface modification, 2006. URL `https://www.gelest.com/wp-content/uploads/Hydrophobicity.pdf`. Accessed: 5-3-2019.

[234] Remi Courson, Marc Fouet, Pierre Joseph, Fabien Mesnilgrente, Veronique Conedera, and Anne-Marie Gue. Sams vapor deposition: A ready to use functionalization technology for monitoring wettability properties in microfluidic devices. 10 2014.

[235] Shohei Kaneda, Koichi Ono, Tatsuhiro Fukuba, Takahiko Nojima, Takatoki Yamamoto, and Teruo Fujii. Modification of the glass surface property in pdms-glass hybrid microfluidic devices. *Analytical Sciences*, 28(1):39–39, 2012.

[236] J Fan, MCT Wilson, and N Kapur. Displacement of liquid droplets on a surface by a shearing air flow. *Journal of colloid and interface science*, 356(1):286–292, 2011.

[237] Alfa A Widati, Nuryono Nuryono, Indriana Kartini, and Noah D Martino. Silica-methyltrimethoxysilane based hydrophobic coatings on a glass substrate. *Journal of Chemical Technology and Metallurgy*, 52(6):1123–1128, 2017.

[238] Agnieszka Witecka, Akiko Yamamoto, Henryk Dybiec, and Wojciech Swieszkowski. Surface characterization and cytocompatibility evaluation of silanized magnesium alloy az91 for biomedical applications. *Science and technology of advanced materials*, 13(6):064214, 2012.

[239] Jan-Niklas Klatt, Tobias Hutzenlaub, Thomas Subkowski, Tanja Muller, Stefan

Hennig, Roland Zengerle, and Nils Paust. Blocking protein adsorption in microfluidic chips by a hydrophobin coating. *ACS Applied Polymer Materials*, 2021.

[240] Brian Seed. Silanizing glassware. *Current Protocols in Molecular Biology*, 28(1): A.3B.1–A.3B.2, 1994.

[241] Lilyan Chan, Hannah F. Cross, Joseph K. She, Gabriel Cavalli, Hugo F. P. Martins, and Cameron Neylon. Covalent attachment of proteins to solid supports and surfaces via sortase-mediated ligation. *PLoS ONE*, 2(11):e1164, 2007.

[242] Srivatsa V. Rao, Kimberly W. Anderson, and Leonidas G. Bachas. Oriented immobilization of proteins. *Mikrochimica Acta*, 128(3-4):127–143, 1998.

[243] Yongwon Jung, Jin Young Jeong, and Bong Hyun Chung. Recent advances in immobilization methods of antibodies on solid supports. *The Analyst*, 133(6):697, 2008.

[244] Yingshuai Liu and Jie Yu. Oriented immobilization of proteins on solid supports for use in biosensors and biochips: a review. *Microchimica Acta*, 183(1):1–19, 2015.

[245] Malgorzata Baranowska, Agata J. Slota, Pinkie J. Eravuchira, Maria Alba, Pilar Formentin, Josep Pallarès, Josep Ferré-Borrull, and Lluís F. Marsal. Protein attachment to silane-functionalized porous silicon: A comparison of electrostatic and covalent attachment. *Journal of Colloid and Interface Science*, 452:180–189, 2015.

[246] Sean X. Liu and Jun-Tae Kim. Application of kevin-voigt model in quantifying whey protein adsorption on polyethersulfone using qcm-d. *JALA: Journal of the Association for Laboratory Automation*, 14(4):213–220, 2009.

[247] M V Voinova, M Rodahl, M Jonson, and B Kasemo. Viscoelastic acoustic response of layered polymer films at fluid-solid interfaces: Continuum mechanics approach. *Physica Scripta*, 59(5):391–396, may 1999.

[248] Michael F. Ashby. Chapter 15 - material profiles. In Michael F. Ashby, editor, *Materials and the Environment (Second Edition)*, pages 459–595. Butterworth-Heinemann, Boston, second edition edition, 2013.

[249] Antonio N Calabrese, James R Ault, Sheena E Radford, and Alison E Ashcroft. Using hydroxyl radical footprinting to explore the free energy landscape of protein folding. *Methods*, 89:38–44, 2015.

[250] Sharma T Sanjay, Meihan Li, Wan Zhou, Xiaochun Li, and XiuJun Li. A reusable pmma/paper hybrid plug-and-play microfluidic device for an ultrasensitive immunoassay with a wide dynamic range. *Microsystems & Nanoengineering*, 6(1):1–11, 2020.

[251] RR Richardson Jr, JA Miller, and William M Reichert. Polyimides as biomaterials: preliminary biocompatibility testing. *Biomaterials*, 14(8):627–635, 1993.

[252] Abdallah Chahadih, Pierre Yves Cresson, Zahir Hamouda, Sijia Gu, Colin Mismer, and Tuami Lasri. Microwave/microfluidic sensor fabricated on a flexible kapton substrate for complex permittivity characterization of liquids. *Sensors and Actuators A: Physical*, 229:128–135, 2015.

[253] FX Schmid. Optical spectroscopy to characterize protein conformation and conformational changes. *Protein structure: A practical approach*, 11, 1997.

[254] Ashlesha S. Raut and Devendra S. Kalonia. Pharmaceutical perspective on opalescence and liquidliquid phase separation in protein solutions. *Molecular Pharmaceutics*, 13(5):1431–1444, 2016.

[255] Wyatt Technology Corporation. *Hardware Manual for the miniDAWN TREOS Light Scattering Instrument*. 2010. URL `https://physiology.case.edu/media/eq_manuals/eq_manual_miniDAWN_TREOS_Hardware_Manual_M3000_Rev_B.pdf`.

[256] Wyatt Technology Corporation. *Astra V User's Guide*. 2008.

[257] Renliang Xu. Light scattering: A review of particle characterization applications. *Particuology*, 18:11–21, 2015.

[258] Jörg Stetefeld, Sean A. McKenna, and Trushar R. Patel. Dynamic light scattering: a practical guide and applications in biomedical sciences. *Biophysical Reviews*, 8(4): 409–427, 2016.

[259] Jan Jezek, Martin Rides, Barry Derham, Jonathan Moore, Elenora Cerasoli, Robert Simler, and Bernardo Perez-Ramirez. Viscosity of concentrated therapeutic protein compositions. *Advanced drug delivery reviews*, 63(13):1107–1117, 2011.

[260] Leon Fitzroy Willis. The effects of flow on therapeutic protein aggregation. September 2018. URL `https://etheses.whiterose.ac.uk/21963/`.

[261] Rixiang Huang, Peng Yi, and Yuanzhi Tang. Probing the interactions of organic molecules, nanomaterials, and microbes with solid surfaces using quartz crystal microbalances: methodology, advantages, and limitations. *Environmental Science: Processes & Impacts*, 19(6):793–811, 2017.

[262] Fredrik Höök, Bengt Kasemo, Tommy Nylander, Camilla Fant, Kristin Sott, and Hans Elwing. Variations in coupled water, viscoelastic properties, and film thickness of a mefp-1 protein film during adsorption and cross-linking: a quartz crystal microbalance with dissipation monitoring, ellipsometry, and surface plasmon resonance study. *Analytical chemistry*, 73(24):5796–5804, 2001.

[263] Masoumeh Mousavi and Elham Fini. Silanization mechanism of silica nanoparticles in bitumen using 3-aminopropyl triethoxysilane (aptes) and 3-glycidyloxypropyl

trimethoxysilane (gptms). *ACS Sustainable Chemistry & Engineering*, 8(8): 3231–3240, 2020.

[264] ALAIN CARRE and VALERIE LACARRIERE. Study of surface charge properties of minerals and surface-modified substrates by wettability. *Contact Angle, Wettability and Adhesion, Volume 4*, 4:267, 2006.

[265] Koen van der Maaden, Karen Sliedregt, Alexander Kros, Wim Jiskoot, and Joke Bouwstra. Fluorescent nanoparticle adhesion assay: a novel method for surface pka determination of self-assembled monolayers on silicon surfaces. *Langmuir*, 28(7): 3403–3411, 2012.

[266] Tadesse Z. Mengistu, Vishya Goel, J. Hugh Horton, and Sylvie Morin. Chemical force titrations of functionalized si(111) surfaces. *Langmuir*, 22(12):5301–5307, 2006.

[267] Curtiss P Schneider, Diwakar Shukla, and Bernhardt L Trout. Arginine and the hofmeister series: the role of ion–ion interactions in protein aggregation suppression. *The Journal of Physical Chemistry B*, 115(22):7447–7458, 2011.

[268] Wei Wang and Satoshi Ohtake. Science and art of protein formulation development. *International journal of pharmaceutics*, 568:118505, 2019.

[269] Narendra B Bam, Jeffrey L Cleland, Janet Yang, Mark C Manning, John F Carpenter, Robert F Kelley, and Theodore W Randolph. Tween protects recombinant human growth hormone against agitation-induced damage via hydrophobic interactions. *Journal of pharmaceutical sciences*, 87(12):1554–1559, 1998.

[270] Yingda Xu, Dongdong Wang, Bruce Mason, Tony Rossomando, Ning Li, Dingjiang Liu, Jason K Cheung, Wei Xu, Smita Raghava, Amit Katiyar, et al. Structure, heterogeneity and developability assessment of therapeutic antibodies. In *MAbs*, volume 11, pages 239–264. Taylor & Francis, 2019.

[271] Justyna Łuczak, Anna Latowska, and Jan Hupka. Micelle formation of tween 20 nonionic surfactant in imidazolium ionic liquids. *Colloids and Surfaces A: Physicochemical and Engineering Aspects*, 471:26–37, 2015.

[272] Zsóka Weiszhár, Judit Czúcz, Csaba Révész, László Rosivall, János Szebeni, and Zoltán Rozsnyay. Complement activation by polyethoxylated pharmaceutical surfactants: Cremophor-el, tween-80 and tween-20. *European Journal of Pharmaceutical Sciences*, 45(4):492–498, 2012.

[273] Tsutomu Arakawa, Daisuke Ejima, Kouhei Tsumoto, Noriyuki Obeyama, Yoshikazu Tanaka, Yoshiko Kita, and Serge N. Timasheff. Suppression of protein interactions by arginine: A proposed mechanism of the arginine effects. *Biophysical Chemistry*, 127(1):1–8, 2007.

[274] Mariya Pindrus, Steven J Shire, Robert F Kelley, Barthelemy Demeule, Rita Wong, Yiren Xu, and Sandeep Yadav. Solubility challenges in high concentration monoclonal antibody formulations: relationship with amino acid sequence and intermolecular interactions. *Molecular pharmaceutics*, 12(11):3896–3907, 2015.

[275] V. Burckbuchler, G. Mekhloufi, A. Paillard Giteau, J.L. Grossiord, S. Huille, and F. Agnely. Rheological and syringeability properties of highly concentrated human polyclonal immunoglobulin solutions. *European Journal of Pharmaceutics and Biopharmaceutics*, 76(3):351–356, 2010.

[276] Yang Yang, Ajoy Velayudhan, Nina F. Thornhill, and Suzanne S. Farid. Multi-criteria manufacturability indices for ranking high-concentration monoclonal antibody formulations. *Biotechnology and Bioengineering*, 114(9):2043–2056, 2017.

[277] Vânia Regina Nicoletti Telis, Javier Telis-Romero, HB Mazzotti, and Ana Lúcia Gabas. Viscosity of aqueous carbohydrate solutions at different temperatures and concentrations. *International Journal of food properties*, 10(1):185–195, 2007.

[278] Camille Gleason, Chanel Yee, Peter Masatani, C Russell Middaugh, and Aylin Vance. Probing shear thinning behaviors of igg molecules at the air–water interface via rheological methods. *Langmuir*, 32(2):496–504, 2016.

[279] Mahlet A Woldeyes, Wei Qi, Vladimir I Razinkov, Eric M Furst, and Christopher J Roberts. How well do low-and high-concentration protein interactions predict solution viscosities of monoclonal antibodies? *Journal of pharmaceutical sciences*, 108(1): 142–154, 2019.

[280] Walter Schwenger, Charlotte Pellet, Delphine Attonaty, and Jean-René Authelin. An empirical quantitative model describing simultaneously temperature and concentration effects on protein solution viscosity. *Journal of Pharmaceutical Sciences*, 109 (3):1281–1287, 2020.

[281] Michael J Treuheit, Andrew A Kosky, and David N Brems. Inverse relationship of protein concentration and aggregation. *Pharmaceutical research*, 19(4):511–516, 2002.

[282] Marianna L. Fleischman, Jonathan Chung, Eden P. Paul, and Rachael A. Lewus. Shipping-induced aggregation in therapeutic antibodies: Utilization of a scale-down model to assess degradation in monoclonal antibodies. *Journal of Pharmaceutical Sciences*, 106(4):994–1000, 2017.

[283] Hyo Jin Lee, Arnold McAuley, Karl F. Schilke, and Joseph McGuire. Molecular origins of surfactant-mediated stabilization of protein drugs. *Advanced Drug Delivery Reviews*, 63(13):1160–1171, 2011. Formulating biomolecules: mechanistics insights in molecular interactions.

[284] Alana Gerhardt, Aaron C. Mcumber, Bao H. Nguyen, Rachael Lewus, Daniel K. Schwartz, John F. Carpenter, and Theodore W. Randolph. Surfactant effects on particle generation in antibody formulations in pre-filled syringes. *Journal of Pharmaceutical Sciences*, 104(12):4056–4064, 2015.

[285] Estelle JA Suys, Dallas B Warren, Anna C Pham, Cameron J Nowell, Andrew J Clulow, Hassan Benameur, Christopher JH Porter, Colin W Pouton, and David K Chalmers. A nonionic polyethylene oxide (peo) surfactant model: experimental and molecular dynamics studies of kolliphor el. *Journal of pharmaceutical sciences*, 108 (1):193–204, 2019.

[286] Liya Zeng, Xin Xin, and Yalin Zhang. Development and characterization of promising cremophor el-stabilized o/w nanoemulsions containing short-chain alcohols as a cosurfactant. *RSC advances*, 7(32):19815–19827, 2017.

[287] Estefanía Grotz, Ezequiel Bernabeu, Monica Pappalardo, Diego A. Chiappetta, and Marcela A. Moretton. Nanoscale kolliphor hs 15 micelles to minimize rifampicin self-aggregation in aqueous media. *Journal of Drug Delivery Science and Technology*, 41:1–6, 2017.

[288] Russell E Madsen, Roy T Cherris, John G Shabushnig, and DG Hunt. Visible particulates in injectionsa history and a proposal to revise usp general chapter injections< 1. In *Pharmacopeial Forum*, volume 35, pages 1383–1387, 2009.

[289] Stephen E Langille. Particulate matter in injectable drug products. *PDA J Pharm Sci Technol*, 67(3):186–200, 2013.

[290] Caitlin V. Wood, Vladimir I. Razinkov, Wei Qi, Eric M. Furst, and Christopher J. Roberts. A rapid, small-volume approach to evaluate protein aggregation at air-water interfaces. *Journal of Pharmaceutical Sciences*, 110(3):1083–1092, 2021.

[291] Adam Dariusz Grabarek, Ula Bozic, Jannik Rousel, Tim Menzen, Wendelin Kranz, Klaus Wuchner, Wim Jiskoot, and Andrea Hawe. What makes polysorbate functional? impact of polysorbate 80 grade and quality on igg stability during mechanical stress. *Journal of Pharmaceutical Sciences*, 109(1):871–880, 2020.

[292] Florian Johann, Steffen Wöll, Matthias Winzer, Jared Snell, Bernhard Valldorf, and Henning Gieseler. Miniaturized forced degradation of therapeutic proteins and adcs by agitation-induced aggregation using orbital shaking of microplates. *Journal of Pharmaceutical Sciences*, 2021.

[293] Mokhtar M. Mabrouk, Nouran A. Hamed, and Fotouh R. Mansour. Spectroscopic methods for determination of critical micelle concentrations of surfactants; a comprehensive review. *Applied Spectroscopy Reviews*, 0(0):1–29, 2021.

[294] KS Birdi, HN Singh, and SU Dalsager. Interaction of ionic micelles with the

hydrophobic fluorescent probe 1-anilino-8-naphthalenesulfonate. *Journal of Physical Chemistry*, 83(21):2733–2737, 1979.

[295] Emmanuele De Vendittis, Giuseppe Palumbo, Giuseppe Parlato, and Vincenzo Bocchini. A fluorimetric method for the estimation of the critical micelle concentration of surfactants. *Analytical biochemistry*, 115(2):278–286, 1981.

[296] Yoshio Nakahara, Toshiyuki Kida, Yohji Nakatsuji, and Mitsuru Akashi. New fluorescence method for the determination of the critical micelle concentration by photosensitive monoazacryptand derivatives. *Langmuir*, 21(15):6688–6695, 2005.

[297] Shohei Horiuchi and Gerhard Winter. Cmc determination of nonionic surfactants in protein formulations using ultrasonic resonance technology. *European Journal of Pharmaceutics and Biopharmaceutics*, 92:8–14, 2015.

[298] Saif Shubber, Driton Vllasaliu, Cyril Rauch, Faron Jordan, Lisbeth Illum, and Snjezana Stolnik. Mechanism of mucosal permeability enhancement of critical-sorb®(solutol® hs15) investigated in vitro in cell cultures. *Pharmaceutical research*, 32(2):516–527, 2015.

[299] Aba Priev, Samuel Zalipsky, Rivka Cohen, and Yechezkel Barenholz. Determination of critical micelle concentration of lipopolymers and other amphiphiles: comparison of sound velocity and fluorescent measurements. *Langmuir*, 18(3):612–617, 2002.

[300] Matías Möller and Ana Denicola. Protein tryptophan accessibility studied by fluorescence quenching. *Biochemistry and Molecular Biology Education*, 30(3): 175–178, 2002.

[301] Bret A Shirley. *Protein stability and folding: Theory and practice*, volume 21. Springer, 1995.

[302] John Andrew Dobson. Biophysical characterisation of biopharmaceuticals under defined flow fields. November 2017. URL `https://etheses.whiterose.ac.uk/20779/`.

[303] Yuchen Zhang, Dingding Han, Zhongwang Dou, Jean-Christophe Veilleux, Galen H Shi, David S Collins, Pavlos P Vlachos, and Arezoo M Ardekani. The interface motion and hydrodynamic shear of the liquid slosh in syringes. *Pharmaceutical Research*, 38(2):257–275, 2021.

[304] Takahiro Maruno, Hiroki Watanabe, Saki Yoneda, Takayuki Uchihashi, Satoru Adachi, Kunihito Arai, Taichi Sawaguchi, and Susumu Uchiyama. Sweeping of adsorbed therapeutic protein on prefillable syringes promotes micron aggregate generation. *Journal of pharmaceutical sciences*, 107(6):1521–1529, 2018.

[305] Katia Boven, Scott Stryker, John Knight, Adrian Thomas, Marc van Regenmortel,

David M Kemeny, David Power, Jerome Rossert, and Nicole Casadevall. The increased incidence of pure red cell aplasia with an eprex formulation in uncoated rubber stopper syringes. *Kidney international*, 67(6):2346–2353, 2005.

[306] Sumit Majumdar, Brandi M Ford, Kevin D Mar, Vince J Sullivan, Robert G Ulrich, and Ajit Joseph M D'souza. Evaluation of the effect of syringe surfaces on protein formulations. *Journal of pharmaceutical sciences*, 100(7):2563–2573, 2011.

[307] Caitlin V Wood, Sean McEvoy, Vladimir I Razinkov, Wei Qi, Eric M Furst, and Christopher J Roberts. Kinetics and competing mechanisms of antibody aggregation via bulk-and surface-mediated pathways. *Journal of pharmaceutical sciences*, 109(4): 1449–1459, 2020.

[308] Claire L Dobson, Paul WA Devine, Jonathan J Phillips, Daniel R Higazi, Christopher Lloyd, Bojana Popovic, Joanne Arnold, Andrew Buchanan, Arthur Lewis, Joanne Goodman, et al. Engineering the surface properties of a human monoclonal antibody prevents self-association and rapid clearance in vivo. *Scientific reports*, 6(1):1–14, 2016.

[309] Lucas H. Ting, Shirin Feghhi, Nikita Taparia, Annie O. Smith, Ari Karchin, Esther Lim, Alex St. John, Xu Wang, Tessa Rue, and Nathan J. et al. White. Contractile forces in platelet aggregates under microfluidic shear gradients reflect platelet inhibition and bleeding risk. *Nature Communications*, 10(1), 2019.

[310] Benjamin P Duckworth, Juhua Xu, T Andrew Taton, Athena Guo, and Mark D Distefano. Site-specific, covalent attachment of proteins to a solid surface. *Bioconjugate chemistry*, 17(4):967–974, 2006.

Appendices

Appendix A

FPOP microfluidic design drawings

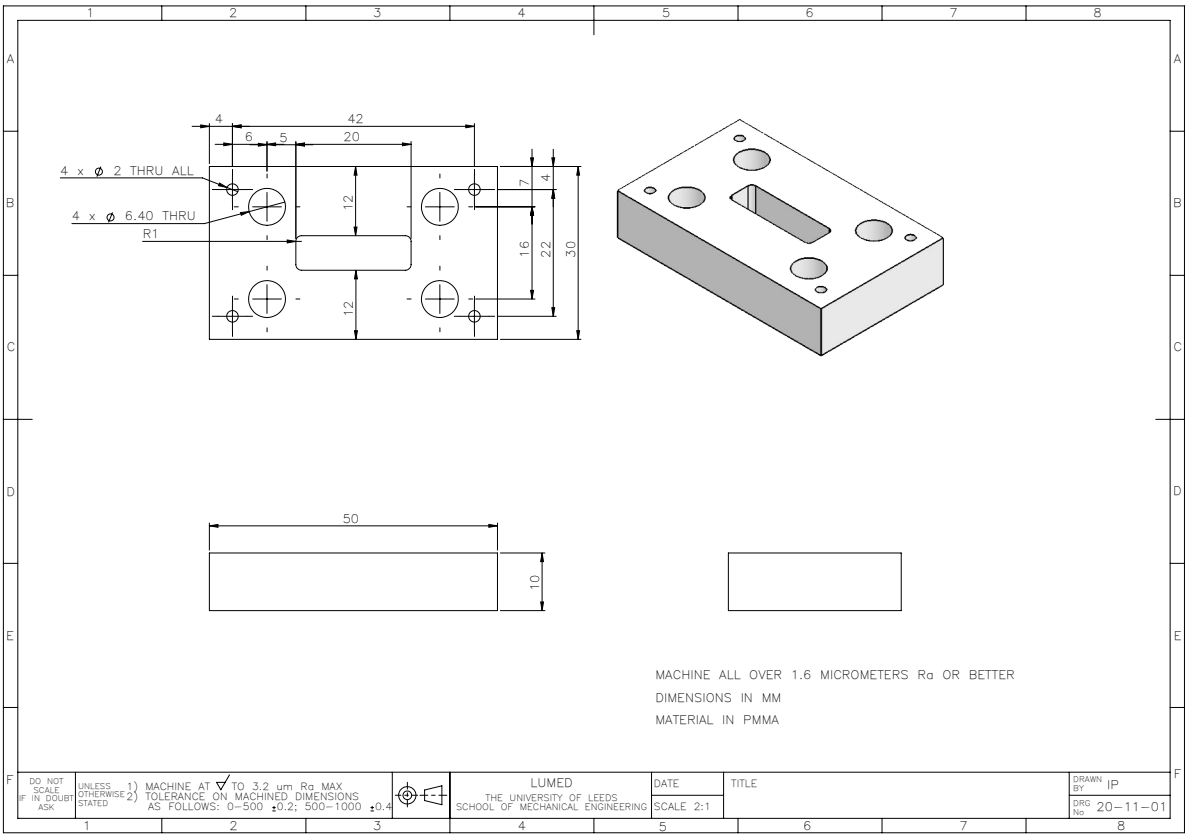

(a)

Figure A.1: Engineering drawings indicating the FPOP microfluidic device components including the upper plate (A.1a), sandwiched with the glass slides A.1b, flow channel (A.1c) and the bottom plate with a 6 mm optical window opening (A.1d).

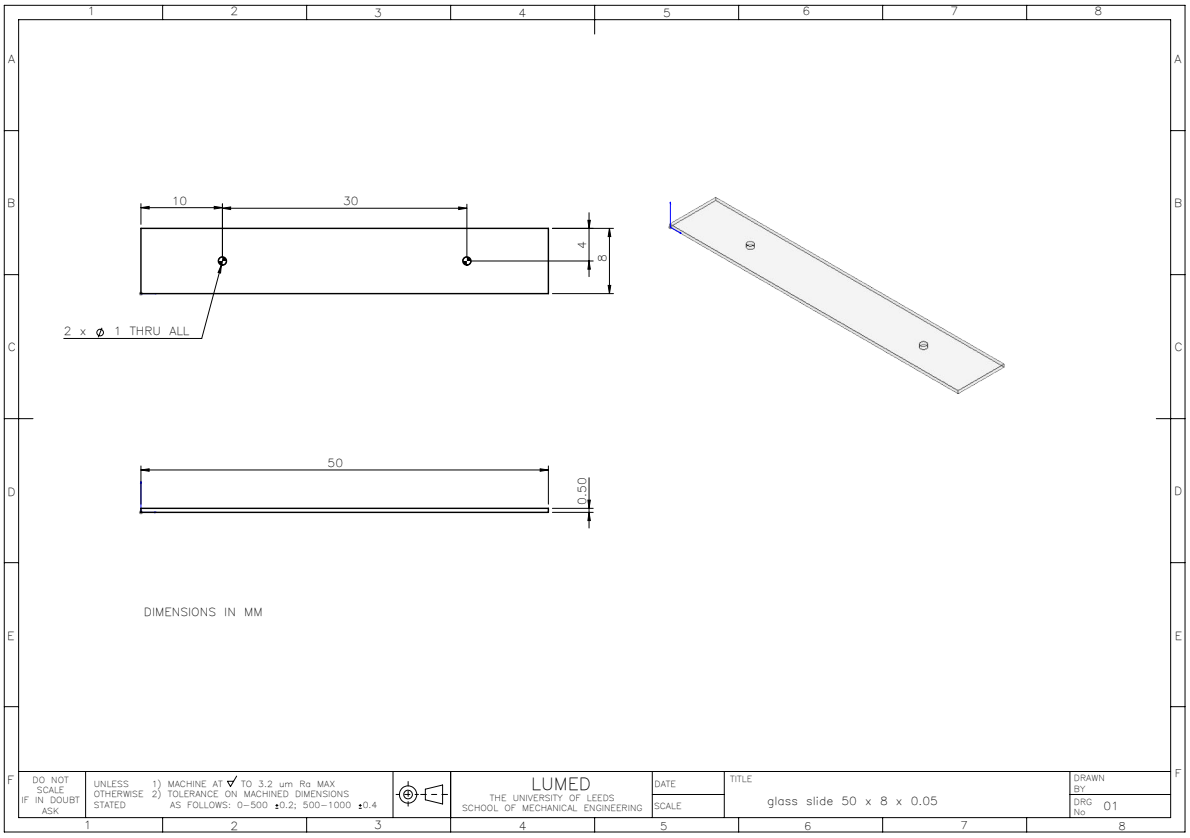

(b)

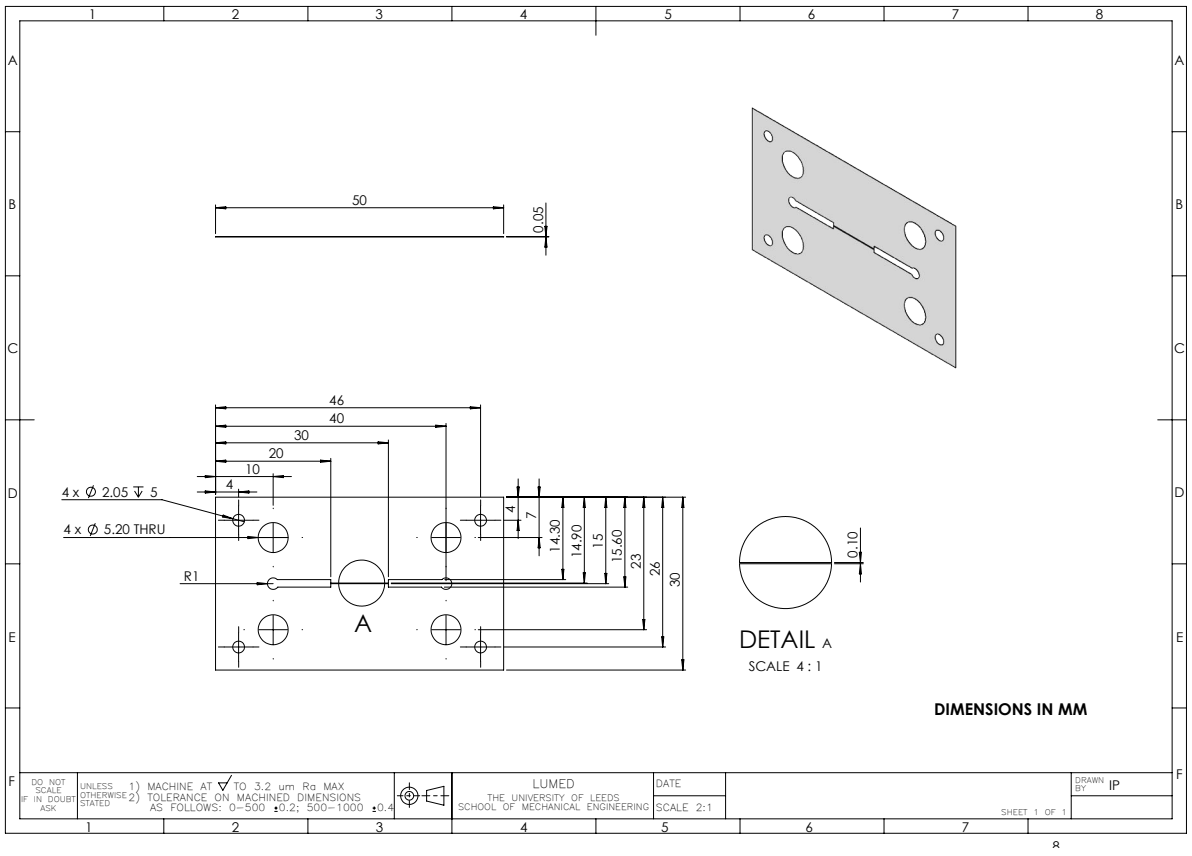

(c)

Figure A.1: Engineering drawings indicating the FPOP microfluidic device components including the upper plate (A.1a), sandwiched with the glass slides A.1b, flow channel (A.1c) and the bottom plate with a 6 mm optical window opening (A.1d) (cont.).

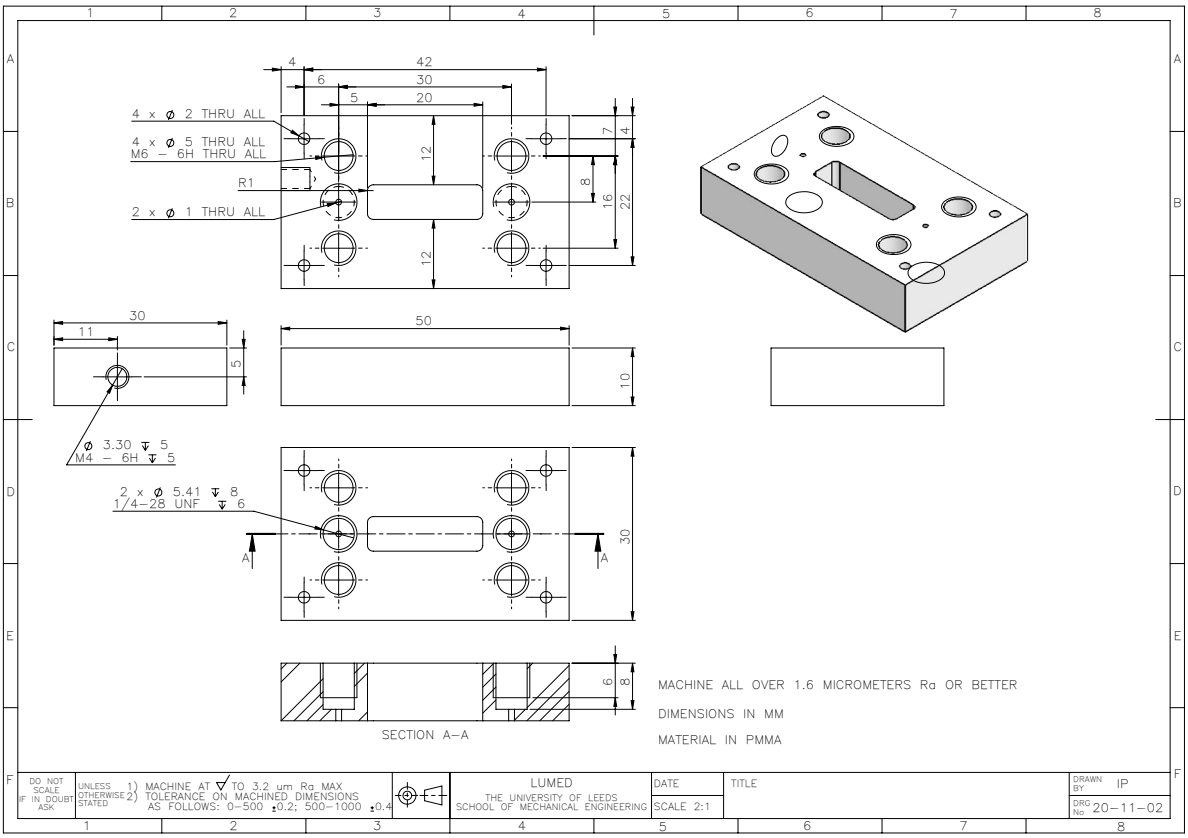

(d)

Figure A.1: Engineering drawings indicating the FPOP microfluidic device components including the upper plate (A.1a), sandwiched with the glass slides A.1b, flow channel (A.1c) and the bottom plate with a 6 mm optical window opening (A.1d) (cont.).

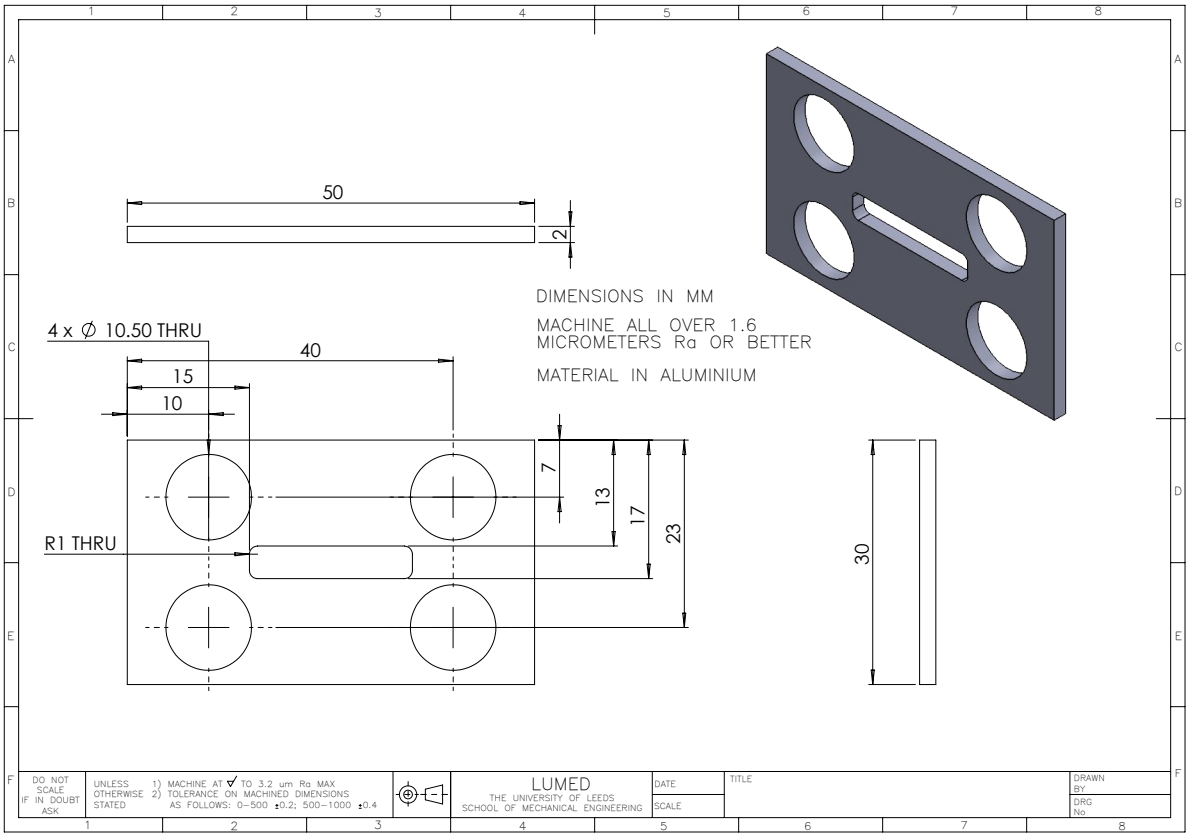

(a)

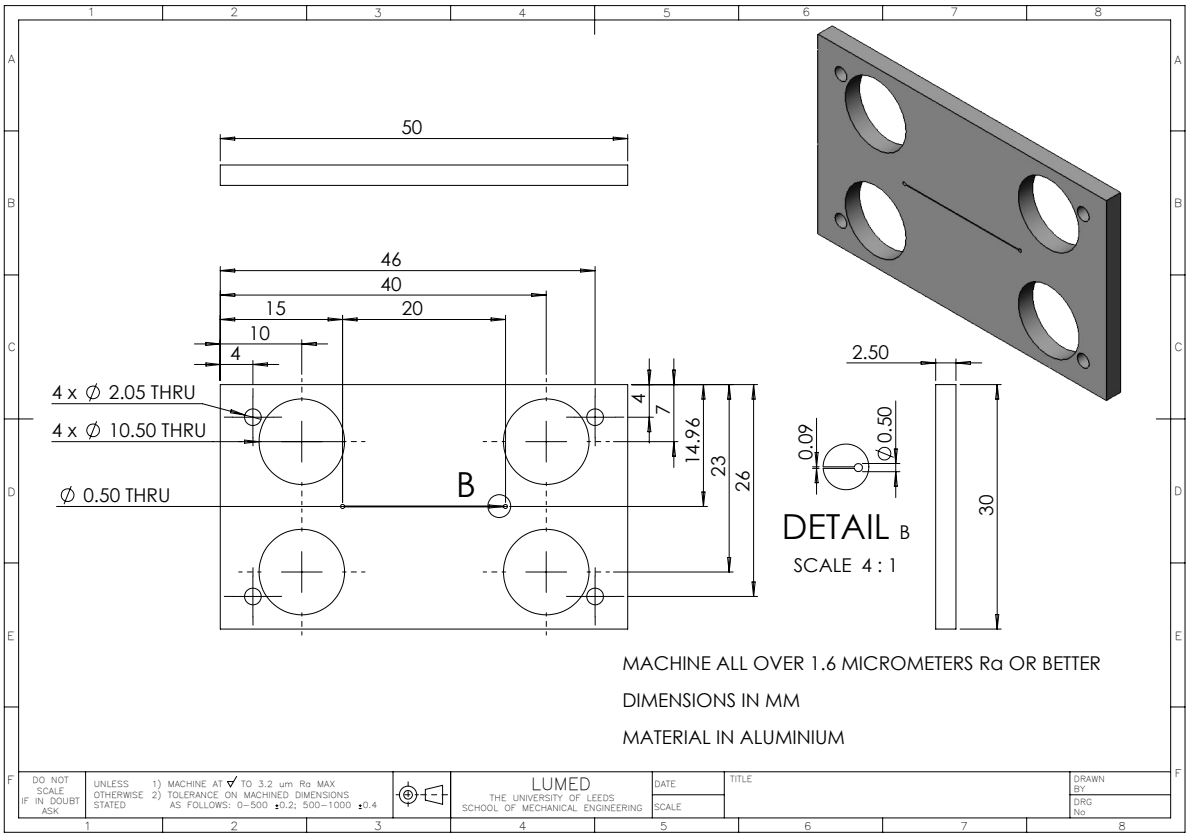

(b)

Figure A.2: Engineering drawing for the aluminium exterior mask for the FPOP microfluidic device with a 4 mm (A.2a) and 90 μm (A.2b) optical window openings.

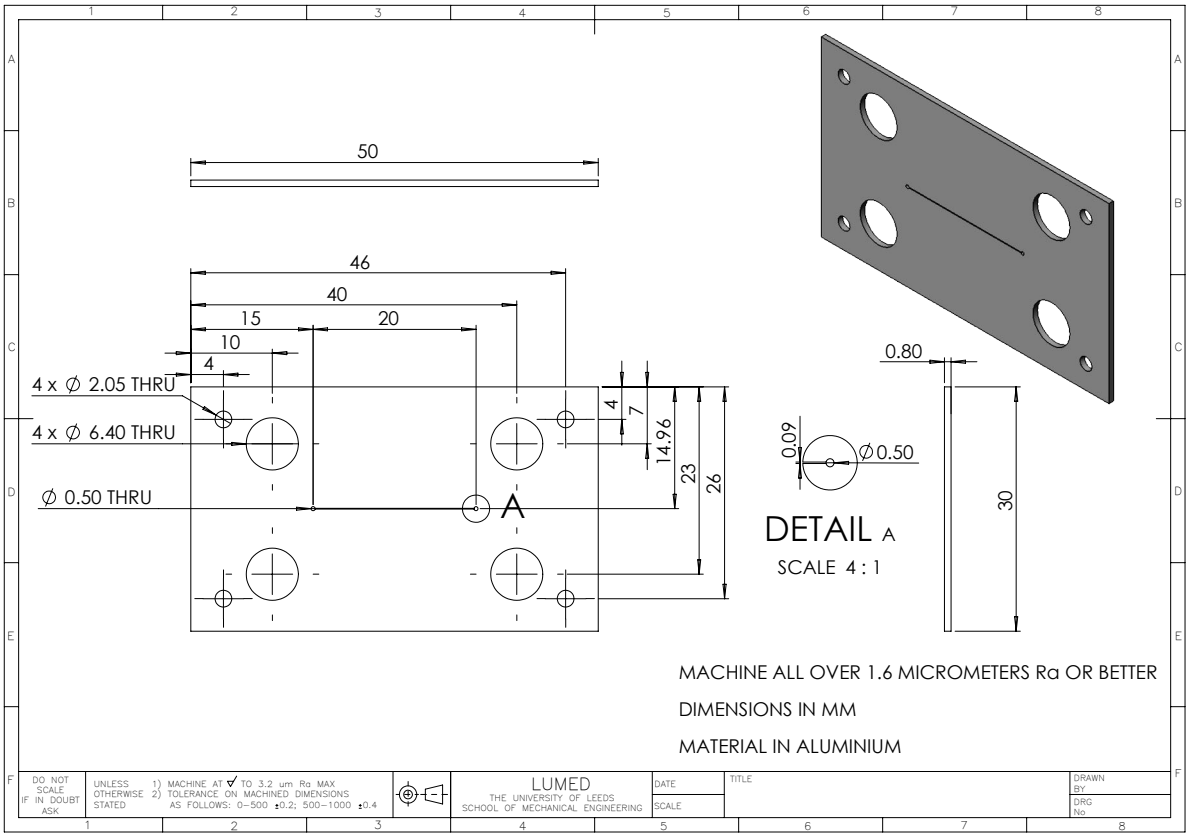

Figure A.3: Engineering drawing for the aluminium interior mask for the FPOP microfluidic device flow channel with a 90 μm optical window opening.

Appendix B

Proof-of-concept microfluidic design drawings

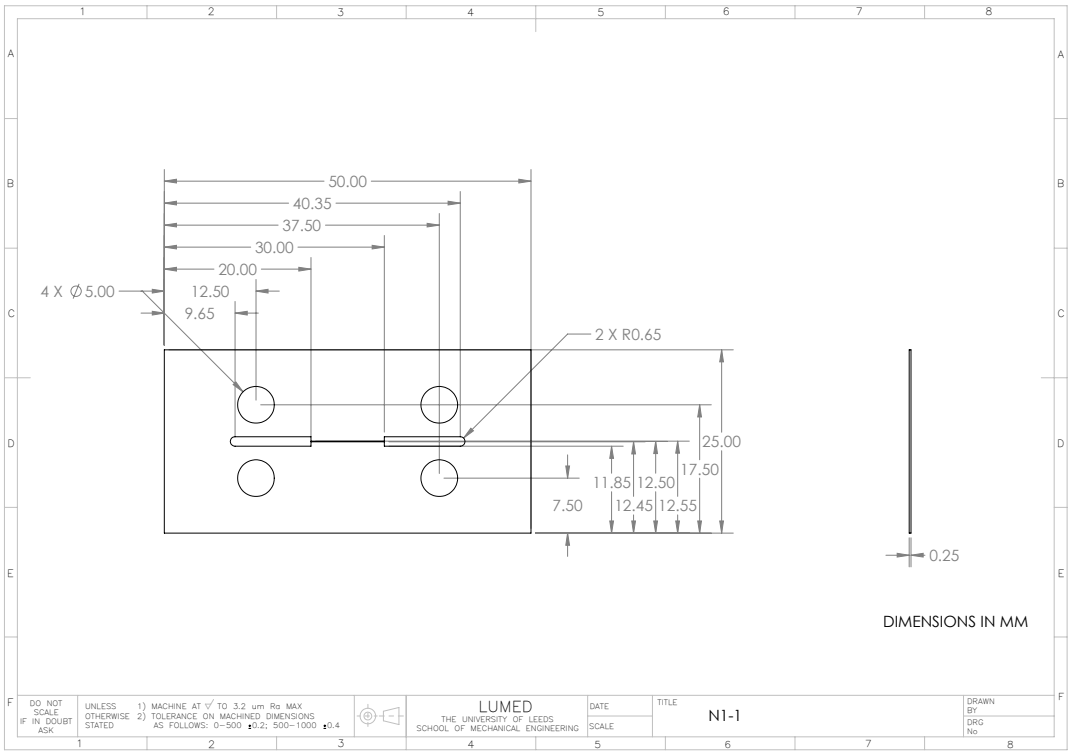

(a)

Figure B.1: Engineering drawings indicating the microfluidic channels with multiple number of constrictions used for the conduction of computational fluid dynamics simulations, as presented in chapter 8. Flow channels consist of contractions in series such as one N1-1 (B.1a), two N1-2 (B.1b) and four N1-4 (B.1c) contractions, channels consisting of 21 contractions with rectangular O1-21 (B.1d), triangular P1-21 (B.1e) shapes and channels with 10 contractions in series, R1-10 (B.1f) and S1-10 (B.1g).

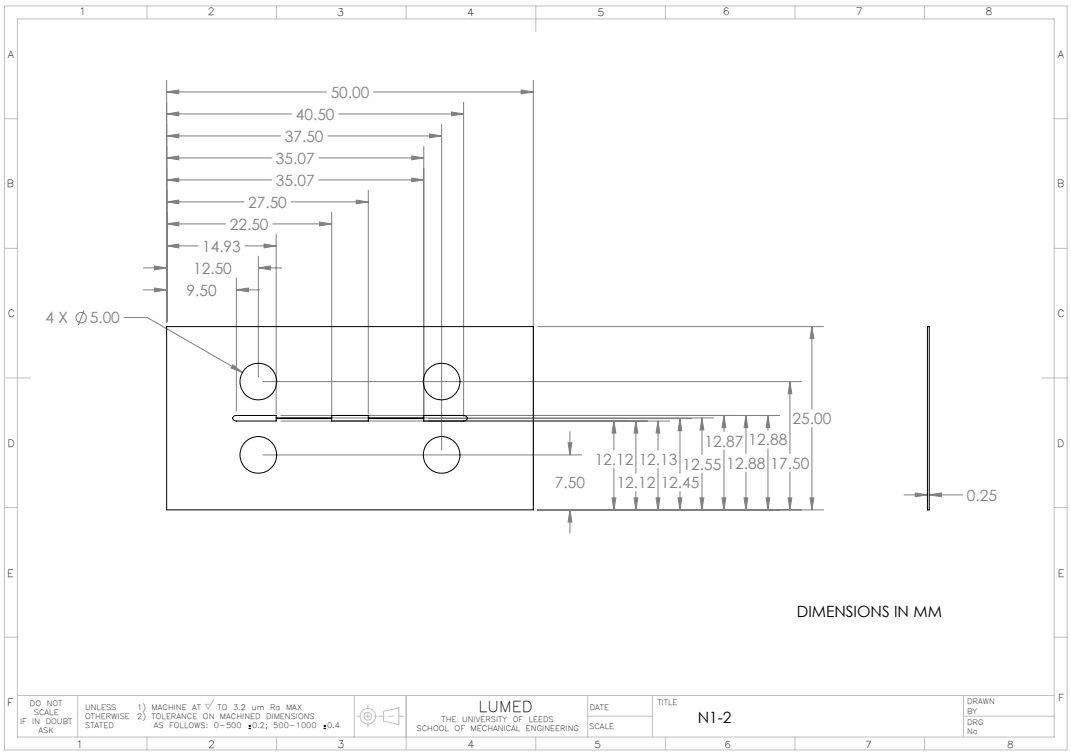

(b)

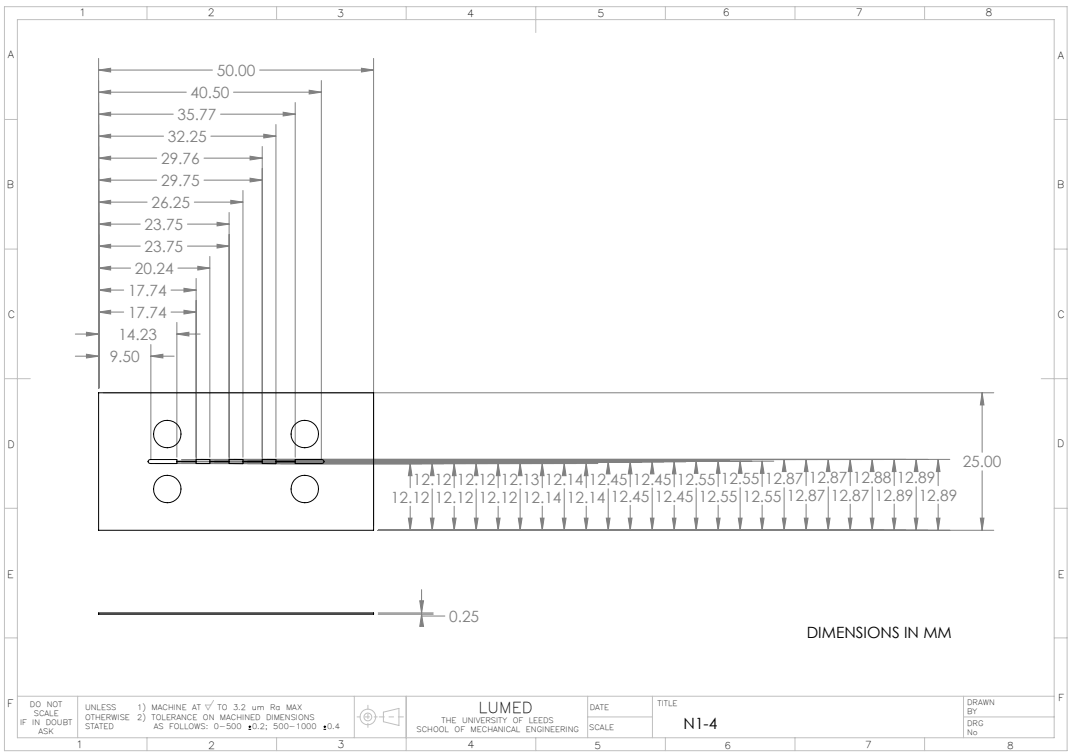

(c)

Figure B.1: Engineering drawings indicating the microfluidic channels with multiple number of constrictions used for the conduction of computational fluid dynamics simulations, as presented in chapter 8. Flow channels consist of contractions in series such as one N1-1 (B.1a), two N1-2 (B.1b) and four N1-4 (B.1c) contractions, channels consisting of 21 contractions with rectangular O1-21 (B.1d), triangular P1-21 (B.1e) shapes and channels with 10 contractions in series, R1-10 (B.1f) and S1-10 (B.1g) (cont.).

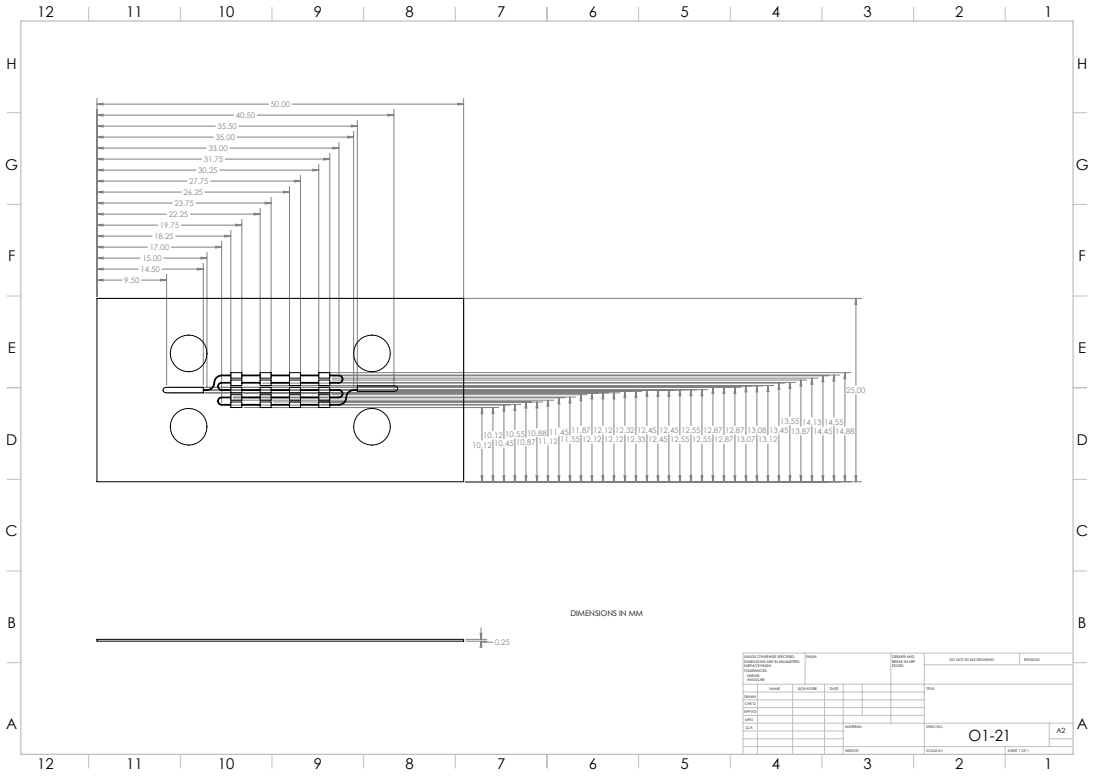

(d)

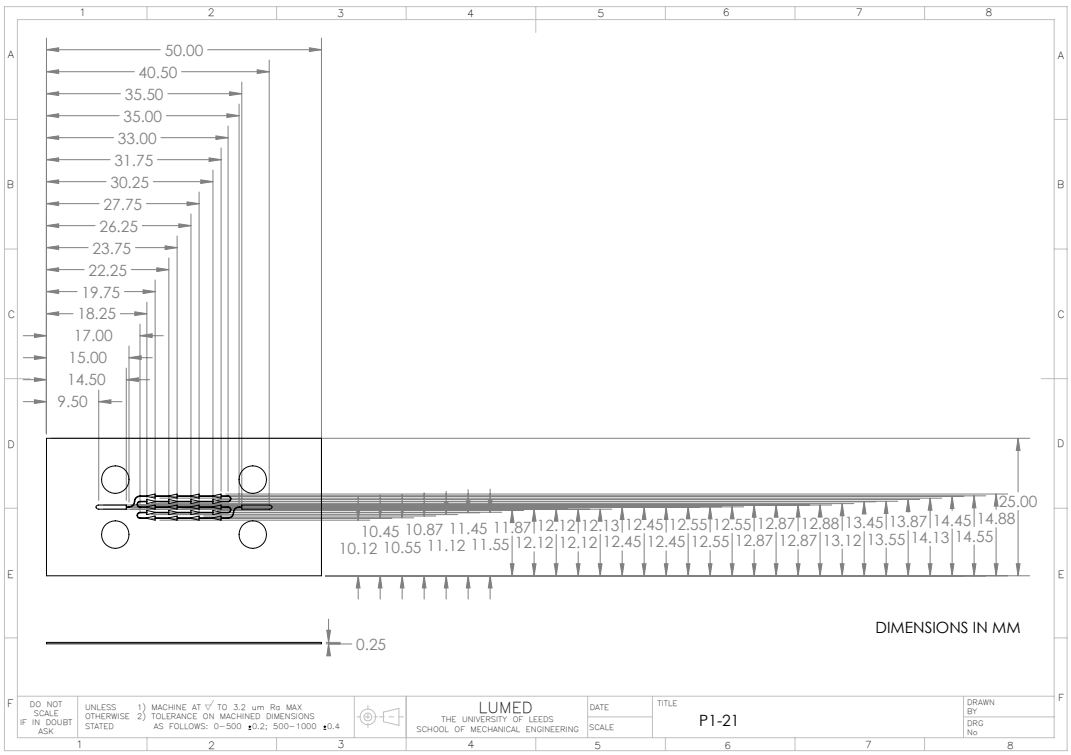

(e)

Figure B.1: Engineering drawings indicating the microfluidic channels with multiple number of constrictions used for the conduction of computational fluid dynamics simulations, as presented in chapter 8. Flow channels consist of contractions in series such as one N1-1 (B.1a), two N1-2 (B.1b) and four N1-4 (B.1c) contractions, channels consisting of 21 contractions with rectangular O1-21 (B.1d), triangular P1-21 (B.1e) shapes and channels with 10 contractions in series, R1-10 (B.1f) and S1-10 (B.1g) (cont.).

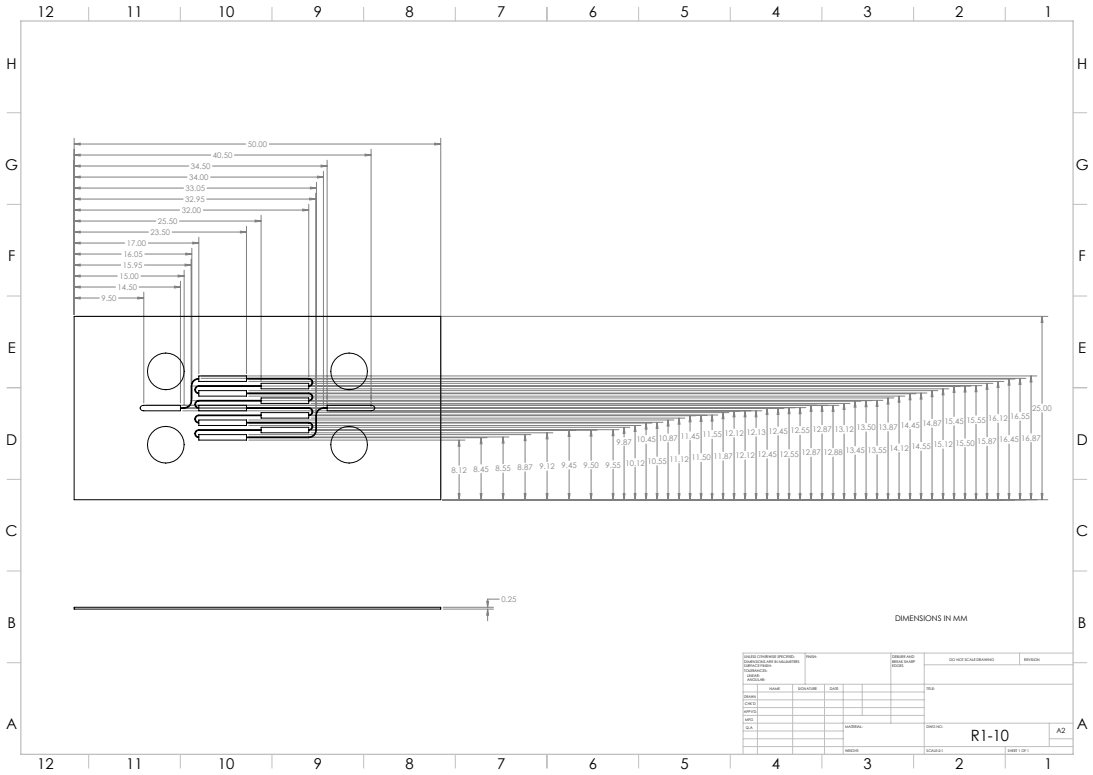

(f)

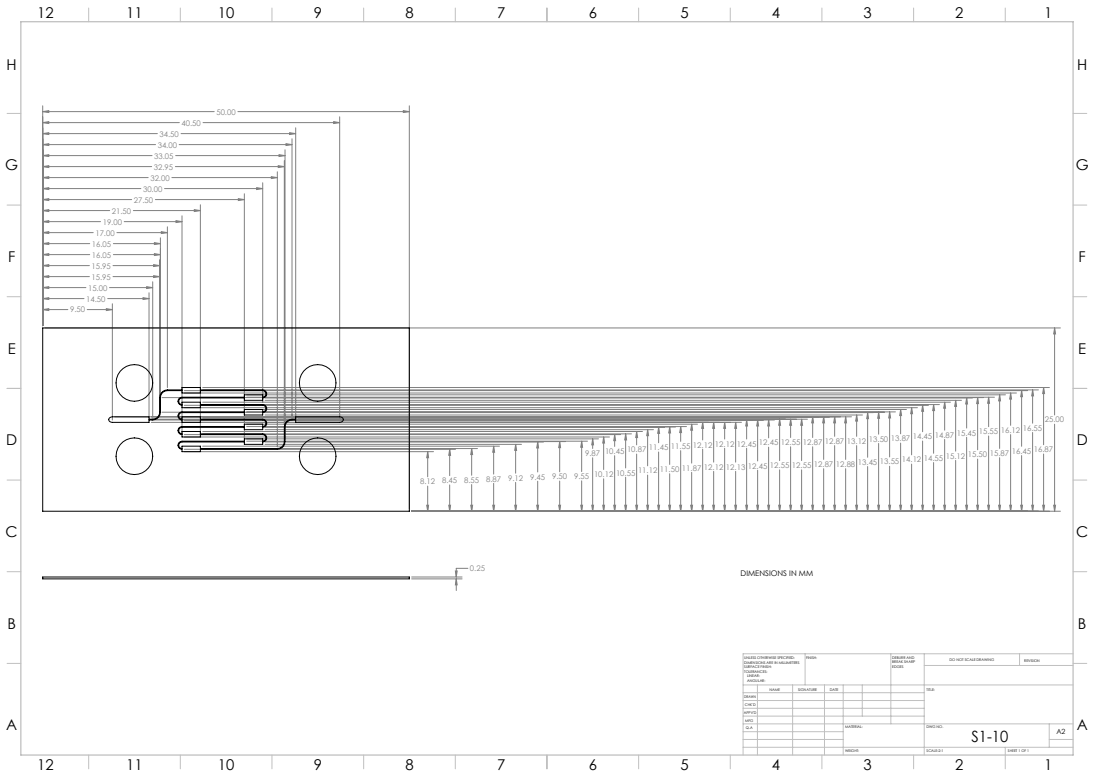

(g)

Figure B.1: Engineering drawings indicating the microfluidic channels with multiple number of constrictions used for the conduction of computational fluid dynamics simulations, as presented in chapter 8. Flow channels consist of contractions in series such as one N1-1 (B.1a), two N1-2 (B.1b) and four N1-4 (B.1c) contractions, channels consisting of 21 contractions with rectangular O1-21 (B.1d), triangular P1-21 (B.1e) shapes and channels with 10 contractions in series, R1-10 (B.1f) and S1-10 (B.1g) (cont.).